# Modeling of Large Megathrust Earthquakes and Tsunami Generation using High-performance Computing

**Sara Aniko Wirp**




München 2025

# Modeling of Large Megathrust Earthquakes and Tsunami Generation using High-performance Computing

**Sara Aniko Wirp**

Dissertation zur Erlangung des
Doktorgrades an der Fakultät für Geowissenschaften
der Ludwig–Maximilians–Universität
München

vorgelegt von
Sara Aniko Wirp

München, den 03.07.2025

Erstgutachter: Prof. Dr. Heiner Igel
Zweitgutachter: Prof. Dr. Alice–Agnes Gabriel
Tag der mündlichen Prüfung: 10.12.2025

# Contents

**Summary** **xxiii**

**1 Introduction** **1**
1.1 General structure of subduction zones . . . 2
1.1.1 Subduction zone types . . . 4
1.2 Occurrence of megathrust earthquakes . . . 4
1.2.1 Sediment control of earthquake size . . . 5
1.3 Seismogenic coupling of subduction zones . . . 6
1.3.1 Slip deficit and asperities . . . 6
1.4 Hazard caused by megathrust earthquakes . . . 7
1.4.1 Tsunami earthquakes . . . 8
1.5 Research gap . . . 9
1.6 Dynamic rupture modeling of subduction zones . . . 10
1.7 Thesis outline . . . 11
1.7.1 Publications . . . 12

**2 Methods** **15**
2.1 Earthquake dynamic rupture modeling with SeisSol . . . 15
2.2 Tsunami modeling with sam(oa)$^2$ and GeoClaw . . . 16
2.3 Workflow for one-way linking between models of different scales . . . 17
2.3.1 Linking geodynamic models to dynamic rupture . . . 17
2.3.2 Linking dynamic rupture simulations to tsunami models . . . 19
2.4 Fully-coupled dynamic rupture-tsunami simulations . . . 21
2.4.1 Meshing workflow . . . 21

**3 3D linked subduction, dynamic rupture, tsunami and inundation modeling: dynamic effects of supershear and tsunami earthquakes, hypocenter location and shallow fault slip** **25**
3.1 Introduction . . . 27
3.2 Methods . . . 31
3.2.1 3D earthquake dynamic rupture modeling with SeisSol . . . 31
3.2.2 Subduction seismic cycle modeling for earthquake initial conditions 32
3.2.3 Tsunami and inundation modeling with Samoa . . . 34
3.2.4 Dynamic rupture modeling for tsunami initial conditions . . . 35

3.3 Earthquake and tsunami model setup . . . 36
3.3.1 3D heterogeneous megathrust dynamic rupture models . . . 36
3.3.2 Tsunami model setup . . . 37
3.4 Results . . . 38
3.4.1 Dynamic rupture models . . . 38
3.4.2 Tsunami simulations . . . 45
3.4.3 Tsunami simulation with complex coastal topo-bathymetry . . . 47
3.4.4 Simulations with increased fracture energy and Poisson's ratio . . . 49
3.4.5 Dynamic effects during tsunami generation by supershear and tsunami earthquakes . . . 51
3.5 Discussion . . . 54
3.5.1 Simplifying model assumptions . . . 54
3.5.2 Hypocentral depth and up-dip versus down-dip supershear rupture propagation . . . 56
3.5.3 Bilateral versus unilateral rupture on a complex bimaterial megathrust 56
3.5.4 Comparison of tsunami behaviour for linear and complex coastline . 57
3.5.5 Large shallow slip . . . 57
3.6 Conclusion . . . 60

**Appendices** **63**
3.A Supplementary Tables and Figures . . . 63

**4 Dynamic rupture modeling of large earthquake scenarios at the Hellenic Arc towards physics-based seismic and tsunami hazard assessment 81**
4.1 Introduction . . . 83
4.1.1 Historic tsunamigenic earthquakes: the AD 365 & 1303 events . . . 85
4.1.2 Seismic-tsunami hazard assessment in the Hellenic Arc region . . . 87
4.2 Reference 3D dynamic rupture model setup . . . 89
4.2.1 Geometric model, mesh, and resolution . . . 89
4.2.2 Ambient prestress and relative fault strength . . . 90
4.2.3 Depth-dependent fault friction and rupture nucleation . . . 92
4.2.4 Off-fault plasticity . . . 92
4.3 Increasingly complex initial conditions . . . 94
4.3.1 Reference laterally homogeneous prestress and friction parameters . 96
4.3.2 Single-asperity prestress model (HEA) . . . 96
4.3.3 Segmented stress models (HMS and HES) . . . 97
4.3.4 Multi-scale asperity models (DCA and DCAS) . . . 97
4.4 Results . . . 98
4.4.1 Margin-wide 3D dynamic rupture scenarios . . . 98
4.4.2 Single prestress asperity model (HEA) . . . 105
4.4.3 Dynamic rupture models with along-arc segmented prestress (models HMS and HES) . . . 107

4.4.4 Combining a multi-scale $D_c$-asperity model with laterally homogeneous prestress (model DCA) . . . 108
4.4.5 Model combining the multi-scale asperity model and the segmented stress model (DCAS) . . . 109
4.4.6 Shake maps . . . 109
4.5 Discussion . . . 112
4.5.1 The AD 365 earthquake and tsunami . . . 112
4.5.2 Modeling the 1303 earthquake as constrained by a single asperity versus stress segmentation . . . 115
4.5.3 Shake maps . . . 116
4.5.4 Implications for regional earthquake and tsunami hazard assessments 116
4.5.5 Limitations of this work . . . 117
4.6 Conclusions . . . 118

**Appendices 121**
4.A Computational mesh used for all ten dynamic rupture simulations . . . 121
4.B Close-up views of dynamic rupture simulation results . . . 122

**5 Hellenic Arc tsunami generation from $M_W8+$ 3D margin-wide dynamic rupture earthquake scenarios 127**
5.1 Introduction . . . 129
5.1.1 The tectonic setting of the Hellenic Arc Subduction Zone . . . 129
5.1.2 Hellenic Arc tsunamigenic earthquakes . . . 129
5.1.3 Earthquake sources in tsunami models . . . 130
5.1.4 Overview of this study . . . 131
5.2 Methods . . . 133
5.2.1 Dynamic rupture modeling with SeisSol . . . 134
5.2.2 One-way linked tsunami modeling with GeoClaw . . . 134
5.2.3 3D fully-coupled earthquake-tsunami modeling . . . 135
5.2.4 Computational domain and meshing . . . 135
5.2.5 Initial stresses and fault friction . . . 136
5.2.6 Off-fault plasticity . . . 137
5.3 Results . . . 138
5.3.1 One-way linked dynamic rupture earthquake-tsunami scenarios . . . 138
5.3.2 3D fully-coupled scenario . . . 144
5.4 Discussion . . . 146
5.4.1 Comparison with historic tsunamis . . . 146
5.4.2 Implications for regional and transnational tsunami hazard assessment 149
5.4.3 Source spectrum analysis of oceanic acoustic and tsunami waves . . . 150
5.4.4 Limitations . . . 152
5.5 Conclusions . . . 153

**Appendices 155**

5.A Meshing challenges . . . . . 155
5.B Dynamic rupture modeling results . . . . . 157
5.C One-way linked tsunami results . . . . . 158
5.D Fully-coupled model: tsunami results . . . . . 169

**6 Conclusion and Outlook** **177**
6.1 Summary of presented work . . . . . 177
6.2 Future perspectives . . . . . 179

**Acknowledgments** **231**

# List of Figures

2.1 **Failure analysis of material properties exported from the SC model:** a) Static (red) and dynamic (blue) friction coefficient ($\mu_s$ and $\mu_d$) displayed with depth. b) Critical slip weakening distance $D_c$, and c) on-fault cohesion plotted with depth. d) Fault strength (red), shear traction (red), and failure (green) with distance from the trench. Failure occurs when the shear traction exceeds the fault strength. . . . . 18

2.2 **Filtering process for one-way linking of the dynamic rupture to shallow-water tsunami modeling.** The figure is adapted from Wirp et al. (2021). a) Unfiltered seafloor displacement at 149 s simulation time. b) Wavenumber representation of the displacement field. The red line represents the smooth filter kernel that is applied to the data. c) Filtered signal after applying the Fourier filter. d) Difference between the unfiltered (a) and filtered (c) wavefield. . . . . 20

2.3 **Meshing process:** Snapshots of the meshing process in the SimModeler GUI (`http://www.simmetrix.com/index.php`). a) Intersection of the water layer with the topobathymetry for the Hellenic Arc region. b) and d) Zoom into the region where the intersection causes an error. c) Successful union of the water layer and topography, showing the small mesh space of both regions and the megathrust below. e) Meshing face that requires manual correction. For a) and d), the water layer is colored yellow, the topobathymetry grey. . . . . 22

3.1 **Left:** adapted from Madden et al., 2020 (a) sketch and dimensions of the one-way linked 2D geodynamic subduction model, (b) the 3D dynamic rupture earthquake model, (c) the dynamic rupture seafloor displacement and (d) the 2D tsunami model, modified from Madden et al. (2020). The 3D unstructured tetrahedral mesh of the dynamic rupture model (b) is shown in grey. **Right:** Snapshot of slip rate across the 3D subducting interface (greenish colors) and the seismic wavefield recorded at the free surface in terms of absolute velocity (warm colors). This snapshot is extracted from model 3B after 40 s simulation time. . . . . 30

3.2 Subduction model initial conditions for the dynamic rupture earthquake simulations. **a)** Snapshot of stresses evolving during the 2D long-term geodynamic subduction and seismic cycle simulation at the time-step right before a slip event occurs (adapted from (van Zelst et al., 2019)). The stresses are expanded to the third dimension assuming plane strain conditions. **b)** On-fault shear stress and fault strength in the SC model at the coupling time-step. The fault yields and failure occurs when both align. **c)** Pre-processed (see text) initial shear stress in the three-dimensional dynamic rupture model at timestep t=0 s in the DR model. The black squares indicate nucleation locations that are used for model families 1–4. The hypocenter of the reference model 3B is marked. **d)** Fault geometry in 2D and dip angle of the fault. Regions of increasing dip are highlighted in blue and indicate local topographic highs (1 and 2) in the fault plane. 33

3.3 **Left:** Sketch of the tsunami model setup for most scenarios for sam(oa)$^2$-flash with a linearly sloping beach starting at x = 500 km. Red and blue colors are an exemplary snapshot of seafloor uplift and subsidence resulting from a DR model that are used to source the tsunami model. **Right:** Zoom-in of the non-linear height profile of the complex beach used in one tsunami scenario (model 4.D) adapted from the Okushiri benchmark. The position and slope are designed to be comparable to the linear beach (left). The depth profile is illustrated by blue and red colors. Contour lines are shown every 500m. . . . . 39

3.4 Slip rate at the timestep t=12 s (model 1), t=16 s (model 2), t=10 s (model 3) and t=14 s (model 4), capuring down-dip and up-dip propagating supershear rupture being triggered by one of the two topographic highs in the fault geometry depending on hypocentral depth. The white reflections highlight the uneven geometry of the fault. The hypocentral locations vary with depth (25 km, 30 km, 40km and 45km) and laterally on the fault (y=-78.25 km, y=-156.5 km, y=-234.75 km). For model 1 and 2 supershear rupture evolves in downdip direction, whereas for model 3 and 4 in updip direction. . . . . 40

3.5 Rupture velocity for 12 dynamic rupture simulations with varying hypocenter locations. Note the difference in nucleation radii according to Table 3.1. Most parts of the fault rupture at speeds around 3000m/s. Much lower velocities are visible in the shallower fault part. Supershear rupture is visible as dark blue areas in downdip direction for nucleation locations at a depth of 25 km and 30 km and in updip direction for nucleation depths of 40 km and 45 km. The rupture velocity is very inhomogeneous due to the complex and heterogeneous material properties on the fault. . . . . 41

3.6 Accumulated fault slip at the end of the simulation, after 200s for 12 dynamic rupture models. The hypocenter locations vary with depth (25 km, 30 km, 40 km and 45 km) and laterally on the fault (y=-78.25 km, y=-156.5 km, y=-234.75 km). . . . . 44

3.7 **Top:** Comparison of sea surface height (ssh) for tsunami fronts arriving at the coast for the models 2A-2C (upper row). The difference in arrival times between the models is shown as $\Delta$ssh (lower row). **Bottom:** Inundation comparison for models 3A-3C. The green to white colour scale shows the time delay for the tsunami fronts arriving at the coast (upper row). The difference in inundation between respective models is plotted as $\Delta$t (lower row). . . . . 46

3.8 Seasurface height of the waves at the coast (**left**) and inundation area and time (**right**) for the tsunami scenario with a complex coast (Fig. 3.3, right). Note the different x-axis scale compared to Fig. 3.7 which is necessary to resolve the complex coastline at the beginning of the simulation (solid black line) accurately. The dotted line illustrates how far in-land the tsunami inundates. . . . . 48

3.9 Fault slip, peak slip rate and rupture velocity for the dynamic rupture models 3, 5 (increased fracture energy) and 6 (higher Poisson's ratio) after 200 s at the end of the DR simulation. . . . . 50

3.10 **Top** Sea surface height (ssh) for models 5 and 6 at t=200 s with contours at -0.5, 0.5 1.0 and 1.5 m, at the end of the DR earthquake simulations. **Bottom:** Trajectories of the sea surface height for dynamically sourced tsunami (model 5 and 6) measured at y=0.0 km, -156.5 km and -313.0 km. Directly after the earthquake at t=200 s (top), during the wave propagation at 1400 s (middle) and at the time of coastal inundation at t=2,220 s (bottom). . . . . 52

3.11 **Top:** Comparison of sea surface height for tsunami fronts arriving at the coast for the models 3B, 5 and 6. The difference between the models is shown as Δssh. In contrast to Fig. 3.7 the x-axis (distance from coast) indicates higher values. This is due to the greater inundation area of model 5 which exceeds 161m distance. **Bottom:** Inundation comparison for models 3B, 5 and 6. The green to white colour scale shows the time delay for the wave fronts arriving at the coast. The difference between the models is plotted as Δt with a blue (negative values) to red (p color-scale respectively. . . . . 53
3.12 **Top:** Unfiltered seafloor displacements from dynamic rupture model 1B (supershear rupture in downdip direction), 3B (supershear rupture in updip direction) and 5 (tsunami earthquake) at a simulation time of 100 s. **Bottom:** Tsunami generation sea surface height timeseries for model 1B, 3B and 5 at x=-100 km, y=-150 km. . . . . 54
3.A.1 Fourier-filtering process to remove seismic waves: Exemplary wavenumber representation (left) of the displacement field of model 5: Seismic waves are represented by radial symmetric lines. The coefficients are removed by the developed smooth filter kernel (middle), which results in a filtered wavenumber representation (right). . . . . 63
3.A.2 The earthquake model seafloor displacement of model 5 at t=149 s (left). The filtered displacement (middle) and the difference between both (right). 64
3.A.3 Final slip, peak slip rate, and rupture velocity for higher resolution (h=500m, p=5) dynamic rupture models 1B and model 3B (reference model) after 200 s at the end of the DR simulation. . . . . 65
3.A.4 Peak slip rate (PSR) in m/s on the fault plane at the end of all dynamic rupture models. The highest PSR is located at the same depth for all earthquakes and the overall pattern of the PSR is similar. Lateral extending bands are visible due to lateral extending material properties on the fault. The shallower the hypocenter location, the higher the PSR. Even though the material properties and stresses along strike are the same, we see along arc differences of the PSR distribution at same depths. . . . . 66
3.A.5 Seasurface height at t=200 s with contours at -0.5 0.5 1.0 and 1.5 m, at the end of the earthquake simulation. . . . . 67
3.A.6 Trajectories of the sea surface height for dynamically sourced tsunamis at y=-313.o,-156.0 and 0 km. Directly after the earthquake at t=200 s, during the wave propagation at t=1400 s and at the time of inundation at t=2200 s. . . . . 68
3.A.7 Inundation comparison for model 1.A-1.C. The hypocenter locations for the dynamic rupture simulations vary along strike. . . . . 69
3.A.8 Inundation comparison for model 2.A-2.C. The hypocenter locations for the dynamic rupture simulations vary along strike. . . . . 70
3.A.9 Inundation comparison for model 4.A-4.C. The hypocenter locations for the dynamic rupture simulations vary along strike. . . . . 71

3.A.10 Inundation comparison for model 1.A-4.A. The hypocenter locations for the dynamic rupture simulations vary with depth. . . . . 72

3.A.11 Inundation comparison for model 1.B-4.B. The hypocenter locations for the dynamic rupture simulations vary with depth. . . . . 73

3.A.12 Inundation comparison for model 1.C-4.C. The hypocenter locations for the dynamic rupture simulations vary with depth. . . . . 74

3.A.13 Comparison of the seasurface height at the moment when the tsunami arrives the coast for model 1A-C. The hypocenter locations for the dynamic rupture simulations vary along strike. . . . . 75

3.A.14 Comparison of the seasurface height at the moment when the tsunami arrives the coast for model 3A-C. The hypocenter locations for the dynamic rupture simulations vary along strike. . . . . 76

3.A.15 Comparison of the seasurface height at the moment when the tsunami arrives the coast for model 4A-C. The hypocenter locations for the dynamic rupture simulations vary along strike. . . . . 77

3.A.16 Comparison of sea surface height for wave fronts arriving at the coast for the models 1.A-4.A. The difference between the models is shown as $\Delta$ssh. 78

3.A.17 Comparison of the seasurface height at the moment when the tsunami arrives the coast for model 1.B-4.B. The hypocenter locations for the dynamic rupture simulations vary with depth . . . . . 79

3.A.18 Comparison of the seasurface height at the moment when the tsunami arrives the coast for model 1.C-4.C. The hypocenter locations for the dynamic rupture simulations vary with depth. . . . . 80

4.1.1 **Tectonic constraints for 3D dynamic rupture scenarios in the Hellenic Arc area: a)** Hellenic Arc megathrust geometry (Basili et al., 2013) and modeled domain extent. Depth is colored from shallow (white) to deep (purple). The red stars mark the hypocenters of the historical $M_W$∼8 AD 365 and 1303 Crete earthquakes that generated destructive tsunamis. **b)** Zoomed-in view of **a)** focusing on the northern trench as the main tectonic feature including plate boundaries and motions of the African and Eurasian Plates, and subduction zone domains. The main plate boundaries (Bird, 2003) are marked with black lines. Subduction zones are also labeled with black triangles, pointing toward subduction. Red arrows indicate the Aegean (30.5 mm/yr Reilinger et al. (2006)) and the African (5 mm/yr Ganas and Parsons (2009); Vernant et al. (2014)) plate motions resulting in a convergence rate of ∼35 mm/yr. A grey line frames the outer Hellenic Arc, a blue line frames the Sedimentary Arc, and the Volcanic Arc is framed by a red line (Kkallas et al., 2021). In-slab events lay below the transition from Sedimentary to Volcanic Arc. **c)** 3D views of the modeled Hellenic arc megathrust. **d)** Modeled absolute particle velocity [m/s] across the Earth's surface with topo-bathymetry in the reference scenario at simulation time 100 s. High-amplitude surface waves extend from Greece and Turkey until the coast of Lybia and Egypt, suggesting that the ground shaking from a margin-wide megathrust event on the Hellenic Arc could directly affect large parts of the eastern Mediterranean. . . . . 86

4.2.1 Ratio of initial shear stress ($\tau$) to effective normal stress ($\sigma_n'$) illustrating closeness to failure prior dynamic rupture onset. In our linear slip-weakening friction framework, frictional failure occurs when $\frac{\tau}{\sigma_n'} = 0.6 = \mu_s$. We here show $\frac{\tau}{\sigma_n'}$ for: **a)** the reference model setup with Eastern (HE), Central (HM), and Western (HW) hypocenters, and the model allowing for off-fault plasticity (HEP). In all of these models, the fault is close to optimally prestressed, which can lead to margin-wide earthquake scenarios of $M_W$∼9.0. The bottom-right inset illustrates the plunge of the maximum ($\sigma_1$, black, 10 °) and minimum ($\sigma_3$, red) principal stresses; **b)** the rotated stress model (HER), characterized by a slightly shallower $\sigma_1$ plunge (5 °). Here, the shallower fault portion is less optimally prestressed, which prevents shallow rupture, resulting in a dynamic rupture scenario of $M_W$∼8.9; **c)** the single-asperity model (HEA) for a dynamic rupture earthquake scenario resembling the 1303 Crete earthquake, described in Sec. 4.3.2; **d)** the segmented prestress model (HES, DCAS) informed by the regional stress inversion of Kkallas et al. (2021) described in Sec.4.3.3. **e)** the $D_c$-asperity model (DCA), characterized by a slightly steeper $\sigma_1$ plunge (15 °). Here, the deeper fault portion is less optimally prestressed. **(*):** The names of the models are defined in detail in Section 4.3. . . . . 93

4.2.2 **a)** Depth-dependent plastic cohesion and bulk friction for model HEP with off-fault plasticity. **b)** Depth-dependence of friction coefficients in all models. We assume a constant static friction coefficient $\mu_s$, while the dynamic friction coefficient $\mu_d$ varies with depth. Slip-strengthening ($\mu_d > \mu_s$) is assumed in the upper 15 km and at depths lower than 43.3 km, and slip-weakening ($\mu_d < \mu_s$) is assumed within the seismogenic zone. **c)** Multiscale asperity models, with scale-dependent critical slip-weakening distance ($D_c$), following Ide and Aochi (2005) and described in Sec. 4.3.4. 95

4.4.1 **Rupture characteristics of modeled counterfactual margin-wide 3D dynamic rupture scenarios HE, HM, HW, and HEP:** Fault slip ([m], left), peak slip rate ([m/s], middle), and vertical seafloor uplift ([m], right) distributions. Changing the hypocenter location (white star) in **a), b)** and **c)** impacts shallow fault slip, generating localized near-trench uplift visible in the vertical seafloor displacements (right). We account for the possibility of off-fault plasticity in model HEP (**d)**), extending the eastern hypocenter reference (HE) scenario in **a)**. This restricts slip to the deeper fault areas but generates increased slip amplitudes, which, combined with off-fault plastic strain, increases vertical seafloor displacements. The color scales are saturated. See Table 4.4.1 for absolute maximum values. See Animations S1-S4 for illustrations of slip rate evolution across the megathrust. . . . . 100

4.4.2 **Slip rate evolution of four margin-wide rupture scenarios:** Absolute slip rate [m/s] after 25 s, 50 s, 75 s, 100 s, 125 s, and 150 s simulation time (Movies S1-S4): **a)** Reference scenario: Hypocenter East (HE), **b)** Hypocenter Middle (HM), **c)** Hypocenter West (HW), and **d)** Hypocenter East with off-fault Plasticity (HEP) scenarios. The color scale is saturated. For absolute maximum slip rate values see Table 4.4.1. . . . . 102

4.4.3 **Stress drop of the ten dynamic rupture scenarios presented in this study: a) - c)** Margin-wide dynamic rupture scenarios based on laterally-homogeneous initial stress conditions (HE, HM, HW), **d)** HEP dynamic rupture scenario incorporating off-fault plastic yielding, **e)** HER model with a less steeply dipping maximum principal stress $\sigma_1$ than in HE (HER), **f)** single-asperity model (HEA), **g)** and **h)** segmented stress models (HMS and HES), **i)** multiscale asperity model based on the reference laterally-homogeneous stress (DCA), and **j)** multiscale asperity model based on the segmented stress model (DCAS). The highest stress drop for **a) - e)** can be observed near the slab's deep, steeper dipping edge. In **g)**, the stress drop is highly inhomogeneous and follows the heterogeneous initial stress conditions (Fig. 4.2.1). For **i)**, the stress drop is particularly high, compared to the other models. A closeup of **f)**, **h)**, and **j)** can be found in the Appendix Fig. 4.B.2. We measure stress drop as the difference in fault stress before and after dynamic rupture. We caution that shallow rupture propagation into the slip-strengthening region of the slab, which is associated with small or negative stress drops, appears as locally apparently elevated stress drops. . . . . 103

4.4.4 Accumulated off-fault plastic strain quantified as $\eta$ in scenario HEP (Sec. 4.2.4): **a)** Map view of the fault and free surface showing $\eta$ and the location of the cutting plane used for the vertical slice in **b), c)** and **d)**. **b)** Close-up cut-away view combining a map view and a vertical slice through the damage zone. The megathrust interface is transparent dark grey. $\eta$ is displayed from above and on the cutting plane. **c)** Same as in **b)**, but from another viewing direction. **d)** Cut-away view from NW combining the megathrust interface, displayed as transparent dark grey, and a vertical slice showing $\eta$. The unstructured tetrahedral mesh is refined around the slab and coarsens with distance. . . . . 104

4.4.5 **Rupture characteristics for the six non-margin-wide spontaneously arresting dynamic scenarios:** Fault slip [m], peak slip rate [m/s], and vertical displacement distribution for **a)** model HER using a less steeply oriented maximum principal stress $\sigma_1$ than in HE,**b)** the single-asperity model (HEA), **c)** and **d)** models HMS and HES based on a segmented stress model with two different epicenter locations, **e)** the multiscale asperity model DCA using the reference laterally-homogeneous stress and **f)** the multi-scale asperity model DCAS using the segmented stress. White stars mark the respective hypocenters. Note the significant differences in fault slip across the scenarios and varying seafloor uplift patterns. The color scales are saturated. For absolute maximum values and other characteristics such as moment magnitudes, see Table 4.4.1. A closeup of **b)**, **d)** and **f)** is shown in Appendix Fig. 4.B.1 and 4.B.4. . . . . 106

4.4.6 **Slip rate [m/s] snapshots for the six non-margin-wide spontaneously arresting dynamic rupture scenarios (Movies S5-S10):** **a)** HER, based on a less steeply oriented maximum principal stress $\sigma_1$ than in HE, **b)** HEA, the single prestress asperity model, **c)** and **d)** HMS and HES, combining along-arc heterogeneous, segmented prestress with two different hypocenter locations, **e)** DCA, the multi-scale $D_c$-asperity model combined with the reference laterally-homogeneous prestress and **f)** DCAS, the multi-scale $D_c$-asperity model combined with along-arc heterogeneous prestress. Slip rates [m/s] are shown at 20 s, 30 s, 40 s, 50 s, 60 s and 70 s simulation time. The rupture evolution model DCAS after 5 s, 10 s, 15 s, 20 s and 25 s can be found in Appendix Fig. 4.B.4. A closeup of the rupture evolution for all models at 20 s simulation time can be found in Appendix Fig. 4.B.3. . . . . 110

4.4.7 Horizontal peak ground velocities (PGVs) (resolved up to 2.7 Hz in the vicinity of the slab but with spatially decreasing accuracy away from it) for **a)** Reference model (HE), **b)** model with western hypocenter location (HW), **c)** single stress-asperity model (HEA), **d)** model including off-fault plastic yielding (HEP), **e)** the model based on the multi-scale asperity model and the reference laterally-homogeneous stress (DCA) and **f)** the model based on the multi-scale asperity model and the segmented stress model (DCAS). Note the different scales for **c)** and **f)**. In **a)** (model HE), the highest PGV is located above the western Hellenic Arc. The PGV in **d)** (model HEP) has a similar pattern but high PGVs (e.g., >0.5 m/s) affect a smaller area than in model HE. **b)** (model HW) shows the highest PGVs (∼1.0 m/s) and also the largest spatial extent of high PGV values, with PGVs higher than 0.5 m/s extending up to the northern coast of Africa. Models HEA, DCA, and DCAS are characterized by locally smaller and more localized PGVs due to their smaller rupture extent (Fig. 4.4.5) and moment magnitude (**c)** max. PGVs of model HEA ∼0.02 m/s, which is ∼2% of max. PGVs of model HW, **e)** PGVs of model DCA, restricted to a small area east of Crete, **f)** max. PGVs of model DCAS ∼0.06-0.2 m/s, which is ∼6-20% of max. PGVs of model HW). The color scale is saturated. For absolute maximum values see Table 4.4.1. . . . . 113

4.A.1 Top view on the wireframe of the computational mesh used to run the DR models of this study. Note the fine mesh resolution above the fault and the mesh coarsening to the simulation boundaries. . . . . 121

4.B.1 **Close-up of rupture characteristics of model HEA, HES and DCAS:** Zoom in of Fig. 4.4.5b,d, and e showing the final fault slip, peak slip rate, and vertical seafloor displacement. The color scales are saturated. For absolute maximum values see Table 4.4.1. Areas of high PSR do not coincide with areas of high fault slip. The vertical seafloor displacement mirrors the final on-fault slip. The seafloor subsidence for HES is more pronounced than for HEA and DCAS. . . . . 123

4.B.2 **Stress drop for model HEA, HES, and DCAS:** Close-up of Fig. 4.4.3f,h and j. For HES, the stress drop is highest at the steeper dipping fault, whereas the stress drop of HEA and DCAS is homogeneously distributed. . . . . 124
4.B.3 **Close-up of Fig. 4.4.6:** Slip rate in dip direction for simulations HER **a)**, HEA **b)**, HMS **c)**, HES **d)**, DCA **e)**, and DCAS **f)** at 20 s simulation time. Note the bilateral rupture evolution for models HER, HEA, and HMS. For DCA, the slip rate is highest, whereas the smaller moment magnitude DCAS scenario experiences a lower slip rate than all other models. . . . . 124
4.B.4 **Close-up of Fig. 4.4.6f:** Slip rate in dip direction for simulation DCAS at 5 s, 10 s, 15 s, 20 s, and 25 s simulation time. Note the changed color scale compared to Figs. 4.4.6 and 4.B.3. . . . . 125

5.1.1 **Dynamic rupture modeling domain:** a) The Hellenic Arc megathrust by Scala et al. (2020); Basili et al. (2021) used in this study. The dark red color indicates deeper fault depths. Note that the tsunami modeling computational domain extends beyond the dynamic rupture modeling domain (Figs. 5.3.2 and 5.3.3). b) Zoom into the Hellenic Arc region with $M_W$ >5.4 earthquakes (red stars) related to the Hellenic Arc subduction or surrounding tectonics (Papadopoulos et al., 2010; Bocchini et al., 2020; Cirella et al., 2020; Coban and Sayil, 2020). Plate boundaries are indicated by black lines (Bird, 2003), and the convergent subduction margin is marked with triangles. . . . . 132
5.3.1 **Accumulated fault slip at the end of five SeisSol dynamic rupture simulations** for models a) HE, b) HM, c) HW, d) HEP, e) HEA. Depending on the hypocentral location, fault slip penetrates the shallow slip-strengthening fault portion, causing a pronounced band of near-trench uplift. Yellow stars mark the hypocenters. **Computed bathymetry perturbation** used as input in the tsunami models associated with the earthquake dynamic rupture simulations for margin-wide rupture scenarios based on laterally homogeneous initial stress conditions f) HE, g) HM, h) HW, i) HEP including off-fault plastic strain and j) the single initial stress asperity approach (HEA). It combines the vertical surface displacement with the contribution from the horizontal displacement from the Tanioka filter (Tanioka and Satake, 1996). Max. dZ refers to the maximum bathymetry perturbation of each scenario. Note the thin band of near-trench uplift in panels f), g), and h) produced by slip penetrating the shallow slip-strengthening fault region (see a), b), c)). . . . . 140
5.3.2 Sea surface height anomaly (ssha) of all five one-way linked earthquake-tsunami scenarios at 0.5 h (first column), 1.5 h (second column), and 2.5 h (third column) simulation time. The initial coarse grid in the North (see 0.5 h simulation time) is refined with increasing simulation time. Note the different color scale for panel **e)**. . . . . 142

5.3.3 Maximum sea surface height anomaly (ssha [m]) in the Mediterranean during the simulation time of 8 h for five non-linear shallow water equation tsunami simulations induced by static bathymetry perturbations computed from the coseismic displacement of five dynamic rupture scenarios. The contour lines show the tsunami propagation expansion after 1 h, 2 h, 3 h, 4 h, 5 h, and 6 h, respectively. In **a)** model HE, **b)** model HM, and **c)** model HW, the epicenter location in the dynamic rupture models is varied (Fig. 5.3.1), **d)** model HEP allows for off-fault plastic deformation in the upper 15 km, and **e)** model HEA uses a single initial stress asperity. Note the different color scale for panel **e)**. See Animations S1, S2, S3, S4, and S5 for illustrations of the time-dependent evolution of ssha. . . . . 143

5.3.4 Large-scale 3D fully-coupled earthquake-tsunami scenario (HE). a) Sea surface height anomaly (ssha) after $t$ =150 s simulation time. b) Sea surface vertical velocity (ssvv) after $t$ =150 s simulation time. c) Sea surface height anomaly (ssha) along three selected cross-sections (profiles 1–3). See Animations S6 and S7 for illustrations of the time-dependent evolution of ssha and ssvv. . . . . 145

5.3.5 a) Spectrograms of acoustic signals recorded at the 11 tide gauge stations (b) in the fully-coupled earthquake-tsunami simulation. The signature of direct acoustic waves can be identified in the high-frequency leading waves. This signal is followed at stations 13, 17, and 18 by dispersive waves, which we identify as oceanic Rayleigh waves (Oliver and Major, 1960). b) Map showing the tide gauge locations used in this study. Blue triangles mark the tide gauge stations from Wang et al. (2020), while red triangles are the stations added in this study. . . . . 147

5.4.1 Space-time evolution of the sea surface vertical velocity (ssvv) for profiles 1, 2, and 3 of Fig. 5.3.4 for the full duration of the fully-coupled simulations. Dashed lines indicate velocities of 3000 m/s (seismic), 1500 m/s (acoustic waves), and 80 m/s (tsunami). . . . . 152

5.A.1 a) Computational mesh of the fully-coupled earthquake-tsunami model, including the water layer. The sea surface vertical velocity after 200 s simulation time ranges from -2 to 2 m/s to highlight complexities in the early stage of tsunami generation. Note that the modeling domain of the fully-coupled tsunami model is smaller than the one used with GeoClaw (Figs. 5.3.2 and 5.3.3). b) Map view and c) perspective view of the modeling domain of the fully-coupled model. The water layer is colored light blue, the free surface and absorbing boundary conditions are colored dark blue and red, respectively. d) Zoom into the connection of the water layer (red) and surroundings (blue). Note the finer mesh resolution of the water layer and the mesh size coarsening away from the water layer. . . . . 156

5.B.1 **SeisSol dynamic rupture results:** a) Peak slip rate and b) rupture velocity for models HE, HM, HW, HEP, and HEA, respectively. Depending on the hypocentral location, fault slip penetrates the shallow slip-strengthening fault portion, causing a pronounced band of near-trench uplift. White stars mark the hypocenter. . . . . 157
5.C.1 Tsunami evolution (ssha [m]) for model HE (eastern hypocenter) after 1 h, 2 h, 3 h, 4 h, 4.5 h, 5 h, 5.5 h, 6 h, 6.5 h, 7 h, 7.5 h, 8 h simulation time. Red marks elevation, and blue marks depression from the sea surface at rest. 159
5.C.2 Tsunami evolution (ssha [m]) for model HM (middle hypocenter) after 1 h, 2 h, 3 h, 4 h, 4.5 h, 5 h, 5.5 h, 6 h, 6.5 h, 7 h, 7.5 h, 8 h simulation time. Red marks elevation, and blue marks depression from the sea surface at rest. 160
5.C.3 Tsunami evolution (ssha [m]) for model HW (western hypocenter) after 1 h, 2 h, 3 h, 4 h, 4.5 h, 5 h, 5.5 h, 6 h, 6.5 h, 7 h, 7.5 h, 8 h simulation time. Red marks elevation, and blue marks depression from the sea surface at rest. . . . . 161
5.C.4 Tsunami evolution (ssha [m]) for model HEP (eastern hypocenter, including plastic deformation) after 1 h, 2 h, 3 h, 4 h, 4.5 h, 5 h, 5.5 h, 6 h, 6.5 h, 7 h, 7.5 h, 8 h simulation time. Red marks elevation, and blue marks depression from the sea surface at rest. . . . . 162
5.C.5 Tsunami evolution (ssha [m]) for model HEA (eastern hypocenter with initial stress asperity) after 1 h, 2 h, 3 h, 4 h, 4.5 h, 5 h, 5.5 h, 6 h, 6.5 h, 7 h, 7.5 h, 8 h simulation time. Red marks elevation, and blue marks depression from the sea surface at rest. . . . . 163
5.C.6 Synthetic tide gauges showing the sea surface height anomaly (ssha [m]) vs simulation time (8 h) for the one-way-linked model HE (eastern hypocenter) at 23 stations (Fig. 5.3.5 b). . . . . 164
5.C.7 Synthetic tide gauges showing the sea surface height anomaly (ssha [m]) vs simulation time (8 h) for the one-way-linked model HM (middle hypocenter) at 23 stations (Fig. 5.3.5 b). . . . . 165
5.C.8 Synthetic tide gauges showing the sea surface height anomaly (ssha [m]) vs simulation time (8 h) for the one-way-linked model HW (western hypocenter) at 23 stations (Fig. 5.3.5 b). . . . . 166
5.C.9 Synthetic tide gauges showing the sea surface height anomaly (ssha [m]) vs simulation time (8 h) for the one-way-linked model HEP (eastern hypocenter, including plastic deformation) at 23 stations (Fig. 5.3.5 b). . . . . 167
5.C.10 Synthetic tide gauges showing the sea surface height anomaly (ssha [m]) vs simulation time (8 h) for the one-way-linked model HEA (eastern hypocenter with initial stress asperity) at 23 stations (Fig. 5.3.5 b). . . . . 168
5.D.1 Results of the fully-coupled earthquake-tsunami simulation: a) ssha [m], b) ssvv [m/s], and c) cross-sections of ssha [m] after 50 s simulation time. 169
5.D.2 Results of the fully-coupled earthquake-tsunami simulation: a) ssha [m], b) ssvv [m/s], and c) cross-sections of ssha [m] after 100 s simulation time. 170

5.D.3 Results of the fully-coupled earthquake-tsunami simulation: a) ssha [m], b) ssvv [m/s], and c) cross-sections of ssha [m] after 200 s simulation time. 171

5.D.4 Results of the fully-coupled earthquake-tsunami simulation: a) ssha [m], b) ssvv [m/s], and c) cross-sections of ssha [m] after 250 s simulation time. 172

5.D.5 Results of the fully-coupled earthquake-tsunami simulation: a) ssha [m], b) ssvv [m/s], and c) cross-sections of ssha [m] after 300 s simulation time. 173

5.D.6 Synthetic tide gauges showing the sea surface vertical velocity (ssvv [m/s]) vs simulation time (300 s) for the fully-coupled earthquake-tsunami model HE (eastern hypocenter) at stations 13 to 23 (Fig. 5.3.5 b). . . . . 174

6.2.1 SimModeler (Simmetrix Inc., 2017) snapshot of the intersection of bathymetry with a water surface for the Mediterranean. The rectangular part would form the modeling domain for a fully-coupled earthquake-tsunami model. The yellow color represents the water layer, and grey represents the solid. Note the many small-scale islands in Greece where the water layer intersects with the topobathymetry. . . . . 180

6.2.2 **Deep subducting seamount in seismo-thermo-mechanical geodynamic seismic cycle model:** Figure is adapted from Fonteijn et al., Tectonophysics (in prep.). a) Subducting interface with imposed deep subducting seamount. Seismic events are displayed as red stars. The events accumulate on top of the seamount. b) Event density in the geodynamic seismic cycling model. High event density is colored dark blue. The event density is high on top of the seamount. Splay faults (white lines) branch the main megathrust. This model could be converted into initial conditions for DR modeling. . . . . 181

# List of Tables

3.1 Model families 1 - 4 defined by hypocentral location. Each model family includes three dynamic rupture scenarios with varying lateral hypocenter location (A - C). Nucleation characteristics vary between the dynamic rupture model families. The material properties that are imported from the seismic cycle model and used as initial conditions vary with depth. Thus, different static friction coefficients and radii have to be chosen to enable nucleation at different depths. Model 5 is adapted from the reference model 3B friction law with higher fracture energy. Model 6 is the reference model 3B with a higher Poisson's ratio of 0.3. . . . . 42

3.2 Dynamic rupture and tsunami characteristics for model 1 to 4 with centered and lateral varying hypocenter locations. . . . . 43
3.3 Dynamic rupture and tsunami characteristics for model 3B, 5 and 6 with centered hypocenter locations. . . . . 49

4.2.1 Dynamic rupture parameters common to all ten models. The names of the models are defined in Figure 4.2.1 and in Sections 4.1 and 4.3. . . . . 94
4.4.1 Rupture characteristics for all 10 dynamic rupture simulations. . . . . 112

5.2.1 Dynamic rupture parameters for five dynamic rupture models HE, HM, HW, HEP, and HEA, selected from the ensemble in Wirp et al. (2024). [a] The orientation of the maximum horizontal stress is $SH_{\max}$ =280 ° for models HE (eastern hypocenter), HM (middle hypocenter), HW (western hypocenter), and HEP (model HE including off-fault plasticity) but $SH_{\max}$ =290 ° for HEA (single-asperity model). [b] The seismogenic depth is 15–43.3 km for models HE, HM, HW, and HEP but 10–43.3 km for HEA. [c] The hypocenter depth is ∼30 km for models HE, HM, HW, and HEP but ∼7 km for model HEA. . . . . 137
5.3.1 Key results of our here considered five earthquake dynamic rupture scenarios, see also Wirp et al. (2024). . . . . 139
5.4.1 Non-dimensional parameters for our model setup, as introduced by Abrahams et al. (2023). $c_0$ =1500 m/s is the acoustic wave speed $g$ =9.81 m/s$^2$ the gravitational acceleration and $H$ is the maximum water depth of the Aegean east of Crete (∼3,544 m). . . . . 150

# Summary

Subduction zones, such as the Hellenic Arc, are seismically active and highly earthquake-prone regions, capable of generating destructive tsunamis. For seismic and tsunami hazard assessment, it is crucial to better understand and characterize these earthquakes. Due to their location, subduction zones are usually inaccessible for direct observations. Physics-based dynamic rupture (DR) models use scaled friction constitutive relations derived from laboratory experiments to capture the variability of earthquake rupture in both space and time. DR models can also account for the structural complexity of subduction zones. In this thesis, I utilize high-performance computing and access to supercomputers, which are essential for running these highly complex simulations.

In the first study of this thesis, I use a 2D geodynamic model that simulates long-term subduction and seismic cycles to initialize 3D DR models, which vary in hypocentral location, Poisson's ratio, and fracture energy. The resulting seafloor perturbation is then used to source tsunami models. This linkage between spatial and temporal scales is a means of imposing model initial conditions for inaccessible regions, thereby ensuring physical consistency. I show that increasing Poisson's ratio and tripling fracture energy lead to significantly higher tsunami amplitudes, potentially generating a "tsunami earthquake".

The second part of this dissertation presents an alternative method for constraining DR initial conditions in subduction zones. I present ten 3D DR simulations exploring scenarios with different hypocentral positions and increasing complexity, ranging from a uniform stress environment to along-arc variations in shear stress, and multiple asperities of varying critical slip-weakening distances. These models produce different levels of shallow slip that penetrate the slip-strengthening region of the fault, creating small bands of near-trench uplift. Incorporating off-fault plasticity doubles the vertical co-seismic seafloor uplift, and increasing initial shear stress complexities tend to limit rupture propagation.

In the third study, I use the static seafloor perturbation of five DR models from the previous research to analyze how hypocentral location and off-fault plasticity influence tsunami propagation, amplitude, and arrival times. Off-fault plasticity may have been crucial in generating historical tsunami earthquakes, because it amplifies wave amplitudes. I extend one scenario into a fully-coupled large-scale 3D earthquake-tsunami simulation. This simulation captures earthquake rupture, the propagation, superimposition, and conversion of elastic and acoustic waves, as well as dispersion and the initial phase of tsunami generation. The high amplitudes of the seismo-acoustic waves can be recorded at synthetic tide gauge stations and could serve as an early warning for tsunami hazards.

# Chapter 1

# Introduction

The Earth's lithosphere consists of the Earth's crust and the uppermost rigid mantle (e.g., White, 1988). It is divided into continental and oceanic plates that move relative to each other because of gravity-driven mantle convection and slab-pull of subducting plates (Davies and Richards, 1992; Conrad and Lithgow-Bertelloni, 2002; Iaffaldano and Bunge, 2009; Stadler et al., 2010). The movement of the plates creates divergent, convergent, and transform plate boundaries, which, because of their movement and interplate interaction, cause earthquakes. The most notable divergent plate boundaries include the oceanic ridge of Iceland (Sigmundsson, 2006) and the "Afar triple junction" (Ebinger et al., 2010). Transform plate boundaries (Stoddard, 1992) are areas where the plates slide parallel to each other, causing dislocations. If two plates converge, a subduction zone forms where the heavier plate bends down and subducts beneath the other plate (underthrusting). 55,000km of all Earth's convergent plate margins form subduction zones (Lallemand and Lallemand, 1999; Stern, 2002).

The plate's subduction rate varies between 2 cm–12 cm per year (Kopp, 2013) and is determined by the downward movement of the subducting plate (megathrust) and the convergence rate between the lower and upper plate (Doglioni et al., 2007; Ficini et al., 2020). Due to the rapid relative movement of plates and the brittle behavior of lithospheric rocks, plate collision causes cycles of interplate locking. This results in stress buildup and sudden release of frictional energy during earthquake ruptures, which occurs from the seismic breaking of fragile lithospheric rocks (e.g., Lockner and Beeler, 2002). As a result, more than 90% of the total seismic energy released worldwide happens at large shallow subduction interfaces (e.g., Pacheco and Sykes, 1992). The most significant and destructive seismic events on Earth, such as the 1960 $M_W$9.5 Valdivia Chile earthquake, the 2004 $M_W$9.0 Sumatra-Andaman, the 2010 $M_W$8.8 Maule, and the 2011 $M_W$9.0 Tōhoku-Oki earthquakes, among others, occurred in subduction zone regions and were recorded by global seismic networks, GPS, or InSAR (Interferometric Synthetic Aperture Radar) data (e.g., Cifuentes and Silver, 1989; Delouis et al., 2010; Shearer and Bürgmann, 2010; Contreras-Reyes and Carrizo, 2011; Simons et al., 2011). Overall, more than 80 % of earthquakes with $M_W \geq 8.0$ are associated with interplate dip-slip events in subduction zones.

Often, these megathrust earthquakes are followed by massive tsunami waves and pose an increasing threat to civilization as the population in coastal regions grows (Stern, 2002; Kopp, 2013; Bilek and Lay, 2018).

The rupture characteristics of megathrust earthquakes strongly depend on the composition and material properties of both converging plates, the plate interface and margin geometry, temperature profile, stress accumulation, and other factors, and are highly unique (e.g., Richardson et al., 1979; Ohnaka, 2004; Park, 2013; Tarasov, 2014; Zheng and Chen, 2016; Klinger et al., 2018). Therefore, it is crucial to map subduction zones as detailed as possible and to gain a better understanding of what influences the rupture process, what causes strong ground accelerations, and what produces tsunamis associated with earthquakes. The following sections present current knowledge about subduction zone structures and the scientific methods used to study seismic and tsunami hazards in coastal areas.

## 1.1 General structure of subduction zones

The Slab 2.0 interactive geographic map (Hayes et al., 2018) is a model of the three-dimensional geometries of all seismically active subducting slabs worldwide. The model is based on seismic data from global, local, and regional scales, including receiver functions, relocation studies, and seismic tomography, providing a comprehensive overview of the shapes and extents of the megathrust in both lateral and vertical directions. In some convergent margins, the subducting plate extends to depths greater than the 660 km discontinuity (Stern, 2002).

However, not only is the shape of the subducting interface important for understanding where, why, and how earthquakes occur at convergent margins, but the composition of the convergent plates also influences the structure of each subduction zone in a unique manner (Zheng and Chen, 2016). Oceanic crust is mainly made up of dense mafic rocks like basalt and gabbro, which are covered by sediments on the seafloor. Continental crust, however, mainly consists of lighter and less dense felsic rocks, such as gneiss or granite, which are often overlain by sedimentary rocks. The oceanic slab dehydrates during subduction at the slab-mantle interface at depths between 75 and 300 km and temperatures of 600–800 °C, leading to the process known as dehydration embrittlement of rocks (e.g., Green and Houston, 1995; Peacock, 2001; Wang et al., 2017). This process creates partial melts made of crustal elements that rise and form volcanic arcs. The temperature profile of the subducting slab determines the depth where seismic activity and rupture propagation occur (Stern, 2002; Jia et al., 2020; Liu et al., 2021; van Zelst et al., 2023) (Sec. 1.2).

The overall characteristic profile of a subduction zone can be described as follows (Kopp, 2013):

The outer rise forms a ridge next to the oceanic trench on the side of the subducting plate. Adjacent to it lies the trench itself, followed by the frontal accretionary prism, the

outer wedge, and the inner wedge, where the material of the incoming continental plate accumulates and forms a forearc high.

The accretionary frontal prism consists of ocean sediments and upper plate material that accumulate during plate convergence (Moore and Silver, 1987; Maravelis et al., 2015). Its lateral size varies and can reach up to 30 km (Von Huene et al., 2009). The frontal prism experiences periods of erosion leading to scar formation, followed by a healing phase where the basement topography is subducted deeper and the pre-collisional structure is rebuild (Brizzi et al., 2021). These processes directly affect the subduction rate and the stresses on the megathrust. The sediment thickness indirectly decreases plate friction by increasing the weight on the interplate shear zone and rising pore fluid pressure (Von Huene et al., 2009).

The frontal prism transitions into the outer wedge. A seismic velocity increase characterizes this transition. Off the central Chilean coast, for instance, velocities shift from approximately 3.2 km/s to about 4.2 km/s (e.g., Kopp et al., 2002). This velocity change toward the outer wedge results from an increase in material strength and rigidity (e.g., Gailler et al., 2007; Contreras-Reyes et al., 2008), which can be mapped using seismic refraction methods.

A contrast in the strain rate defines the inner wedge. It is the strongest segment of the subduction zone and acts as a mechanical barrier (Byrne et al., 1993). The inner wedge can be of either continental or oceanic origin and is composed of igneous or metamorphic material. A depression in the inner wedge forms the several-kilometer-thick forearc basin, which is filled with sediments derived from the arc (e.g., Fisher, 1979; McNeill et al., 2000; Schlüter et al., 2002; Chapp et al., 2008). The mechanics of the forearc basin are still debated, but may include interseismic subsidence or erosional processes (e.g., Wells et al., 2003; Fuller et al., 2006).

For the study and prevention of seismic hazards caused by megathrust earthquakes near coastal regions, it is crucial to analyze the dynamics of the so-called “subduction channel" (e.g., Cloos and Shreve, 1988). This area presents the space between two colliding plates, the interface where the subducting oceanic slab meets the overlying oceanic or continental mantle (Zheng et al., 2013). The thickness of the subduction channel varies from approximately 0.5 to 1.5 kilometers for accretionary and erosive margins and depends on the incoming plate structure (Wallace et al., 2003; Sage et al., 2006). This interface forms a large shear zone that can be detected with seismic methods and features a low-velocity zone in seismic data (e.g., Calahorrano B. et al., 2008). The physical properties, such as rigidity, compaction, and frictional behavior, along the subduction channel change with increasing depth due to rising temperature and pressure. The shape of the plates' interface depends on factors like the thickness of incoming sediments, decomposition of the mantle wedge, fluid intrusions, and the subduction of geometric features, such as seamounts (McIntosh et al., 2007; Ranero et al., 2008), making it highly complex.

### 1.1.1 Subduction zone types

Subduction zones can be classified into two main types: the Chilean and the Mariana types.

The Chilean type features a young and light weight subducting plate, which causes low-angle ($\leq$30 °) subduction at high rates (Zheng et al., 2013). Young lithospheres tend to be more buoyant, leading to stronger coupling and larger earthquakes (Stern, 2002; Zheng and Chen, 2016). This explains why nearly all of the Earth's largest $M_W \geq 7.6$ earthquakes occur in Chilean-type subduction zones (e.g., Cloos and Shreve, 1988). In ocean-continental subduction zones, this effect is amplified due to the greater strength of the continental crust compared to oceanic lithosphere, combined with the wet, cold forearc environment (e.g., McCaffrey, 1997b).

Mariana-type subduction zones, on the other hand, are characterized by older subducting lithosphere that gradually bends downward at steeper angles of $\geq$40 ° (Cloos and Shreve, 1988), resulting in lower coupling and generally smaller magnitude earthquakes (Stern, 2002). As depth increases, the angle of the subducting plate also becomes steeper (Zheng and Chen, 2016). A narrow trench covers Mariana-type subduction zones, whereas Chilean-type subduction zones are overlain by thick sediment layers (Cloos and Shreve, 1988).

## 1.2 Occurrence of megathrust earthquakes

The occurrence of great megathrust earthquakes is related to the accumulation of elastic strain during the interseismic phase (Kopp et al., 2002; Fialko, 2006). As two plates move toward each other, stress builds up at the locked portions of the plates' interface, and elastic potential energy is stored in the rocks (Reid, 1929). Strong plate locking in large areas, followed by high strain accumulation, is favored in areas with smooth and homogeneous plate interfaces (e.g., Ruff and Kanamori, 1983; Scholl et al., 2015; Olsen et al., 2020). Additionally, the orientation of maximum compressive stress plays an important role in the generating large megathrust events. The stress state at seismogenic depths cannot be measured directly (Hardebeck, 2015) but may be inferred from density variations (Whittaker et al., 1992).

If the accumulated stresses and strains overcome the fault's frictional strength during the co-seismic phase, stored potential energy is released. This leads to elastic and plastic deformation of the rocks, rupture propagates spontaneously along the megathrust, and pore-fluid pressure in the frontal prism increases (Kopp, 2013). This process can be studied through dynamic rupture (DR) models, which simulate the propagation of rupture along a predefined fault interface (Sec. 2.1).

The upper and lower boundaries of this seismogenic depth are defined by the transition from frictionally stable to frictionally unstable sliding (Sakaguchi et al., 2011).For most

subduction zones, the seismogenic zone exist at depths between 10–15 km and 35–45 km (Lay et al., 2012). The up-dip limit is defined by the transition from the outer wedge to the frontal prism and can be associated with to material weakness (Krabbenhoeft et al., 2010; Wells et al., 2003; Song and Simons, 2003). Material deforms continuously, and no high strain can be accumulated.

At depths of ≥45 km, the temperature reaches about 350 °C, and pressure rises. The subducted lithospheric rocks lose their frictional properties, and thermally activated stable-sliding of the crustal rocks begins (Oleskevich et al., 1999). If such high temperatures are not reached at that depth, the intersection of the subducting slab and the Moho (Bostock, 2013) marks the downdip seismogenic limit.

The world stress map (Heidbach et al., 2018) provides an overview of the global distribution of tectonic stresses. It includes first-order plate-scale stress fields that arise from plate forces, second-order regional stress fields, and third-order stress fields that can only be obtained for high data density.

### 1.2.1 Sediment control of earthquake size

Numerous recent scientific studies have examined how sediments influence subduction megathrust earthquakes (Heuret et al., 2012; Brizzi et al., 2020; Olsen et al., 2020; Brizzi et al., 2021). Thick sediments slow down the subduction process because they cause a wider accretionary wedge and thickening of the overriding plate. This results in larger shear stresses and slab buoyancy, which again leads to shallower plate subduction. This decrease in dip (Sec. 1.1.1) broadens the seismogenic zone and promotes the occurrence of giant ($M_W \geq 8.5$) subduction earthquakes, as the potential area for rupture propagation increases. Additionally, the subducted sediments smooth the plate interface (Contreras-Reyes and Carrizo, 2011; Wang and Bilek, 2014) and control the frictional properties of the subducted material (Ruff, 1989; Brizzi et al., 2020). This, in turn, directly affects the seismogenic behavior of the megathrust (Wang and Bilek, 2014; Brizzi et al., 2020). Furthermore, subducted sediments contain fluids that decrease the effective normal stress on the plate interface, thereby weakening the megathrust.

The subduction of a thick sediment layer also favors the formation of splay faults, which are smaller reverse faults that connect the shallow megathrust with the ocean floor (Park et al., 2002; Sibuet et al., 2007; Collot et al., 2008; Brizzi et al., 2020). These faults can increase uplift caused by an earthquake because of their high fault angle and can trigger large tsunami amplitudes. In many subduction zone regions, splay faults have already been identified as the main factor controlling maximum tsunami amplitudes (Melnick et al., 2012).

## 1.3 Seismogenic coupling of subduction zones

The seismic coupling coefficient $\chi_s$ (McCaffrey, 1997a) describes how much slip on the subduction plate interface is accommodated as earthquake rupture (Bird et al., 2002; Frohlich and Wetzel, 2007). It is the ratio between the relative tectonic plate velocities $\dot{M}_0^T$ and the slip rate (Pacheco et al., 1993), which can be classified by the observed seismic moment rate release $\dot{M}_0^s$:

$$\chi_s = \frac{\dot{M}_0^s}{\dot{M}_0^T} \,. \tag{1.1}$$

Defining the correct seismic coupling coefficient is difficult because the largest earthquakes, which happen rarely, release most of the moment rates. Therefore, there are significant uncertainties in seismic coupling. If oceanic lithosphere subducts beneath continental lithosphere, the seismic coupling is relatively high ($\geq$0.7) at shallow depths. In contrast, oceanic-oceanic collision have much lower coupling, estimated not to exceed $\sim$0.4. At depths beyond 100 km, the seismic coupling coefficient decreases (to less than 0.2) due to rising temperatures and pressures. Generally, variations in the frictional behavior of rocks at the plate interface cause changes in the coupling coefficient (Pacheco and Sykes, 1992). However, a clear correlation between the seismic coupling coefficient and the width of the seismogenic zone has yet to be identified (Stern, 2002).

### 1.3.1 Slip deficit and asperities

The slip distribution of megathrust earthquakes primarily depends on the spatial distribution of strain buildup and the slip deficit on the plate interface that develops during the locking period (Herman et al., 2018) (Sec.1.2). The seismicity distribution of megathrust events is highly heterogeneous in both space and time (Bilek, 2010). Typically, regions with little or no spatiotemporal seismic activity, known as seismic gaps (McNally, 1983), are used to estimate the locations of future megathrusts earthquakes. Recurrence times of past events in the locked area are used to predict where and when earthquakes may happen (Kagan and Jackson, 1991; McCann et al., 1979). Some earthquakes, such as the 2011 Maule event offshore of Chile, fit these assumptions (Moreno et al., 2010; Vigny et al., 2011). However, rupture propagation might extend to much larger areas than the seismic gap (Lay et al., 2011; Lorito et al., 2011), and the co-seismic slip might be unevenly distributed (Kennett et al., 2011; Moreno et al., 2012). Areas with high slip can be right next to areas with low or no slip (Kanamori, 1994; Bürgmann et al., 2005).

To better understand how rupture propagates along a fault interface, it is important to study earthquakes that do not fit the seismic gap, such as the 2011 Tohoku Oki earthquake (e.g., Heki, 2011; Loveless and Meade, 2011; Ulrich and Aochi, 2015). Here, earthquake nucleation was influenced by structural heterogeneities on the plate interface (Zhao et al., 2011) and a slip deficit up-dip of the seismogenic zone.

Herman et al. (2018) investigate in 3D finite element models how locked regions may limit the rupture propagation process. They distinguish between multi- and single-asperity

ruptures. For a single-asperity rupture, the maximum slip is accumulated within one asperity, and the asperity geometry restricts shallow slip. For multi-asperity ruptures, high slip may also occur up-dip of the asperities. Outside the main slip deficit asperity, they exhibit high pseudo-coupling, which results in additional slip accumulation in areas believed to have a low interseismic slip deficit on the shallow fault. Even in single asperities, these pseudo-coupled regions are crucial, as different patches can overlap and influence rupture propagation and, consequently, earthquake size.

Besides heterogeneous slip deficit distributions, geometric or anatomical features on the subducting plate may also act as asperities or barriers to rupture propagation (e.g., Tanioka et al., 1997; Bilek et al., 2003; von Huene et al., 2012). Different subduction zones often have unique geometries. However, a study by Sparkes et al. (2010) found a connection between topographic heights over 1 km and segmentation of rupture propagation along the South American trench system. Topographic heights in the subducting plate often result from subducted seamounts or oceanic plateaus, which create high-strain contact zones (e.g., Cloos, 1992). When the height of a seamount exceeds the thickness of the décollement zone, there is direct contact between the seamount and the overriding plate, which limits the lateral propagation of rupture (Singh et al., 2011). Additionally, subducted topographic heights may hinder elastic strain buildup during subduction, thereby preventing rupture propagation and slip accumulation during the coseismic phase (Kopp et al., 2006; Mochizuki et al., 2008).

## 1.4 Hazard caused by megathrust earthquakes

The population in coastal areas continues to increase. For global trading partners, suitable harbor locations are crucial. Harbor cities grow and become vital for international commercial networks. In terms of tourism, coastal areas are also attractive, as they often serve as preferred international vacation spots. Therefore, it is in everyone's interest to protect coastal regions and to invest in research and study of seismic and tsunami dangers for areas that could be impacted by subduction megathrust earthquakes and related events tsunamis.

Earthquake hazard maps (e.g., Shedlock et al., 2000) show which areas are likely or unlikely to be affected by a potential earthquake. These maps often rely on historical earthquake catalogs for a specific area or geological assumptions to identify seismically active regions (Mulargia, 2019) and its potential effects on the surrounding area. They describe the average occurrence rate for specific events, predicting an exceedance probability of certain peak ground motion and acceleration values, which are weighted and combined for different sources (Volpe et al., 2019).Past events help determine the area of shaking and ground deformation based on distance from the epicenter.

There are two types of strategies for creating such hazard maps: the probabilistic approach and the deterministic approach (Stein et al., 2012). In the deterministic seismic

hazard assessment approach (DSHA), the most significant event for a specific area is identified, and the shaking associated with the maximum magnitude is estimated. In contrast, probabilistic seismic hazard assessment (PSHA, e.g., Marzocchi et al. (2015)), considers all possible earthquakes and magnitudes that could cause significant ground shaking in a particular area. It assigns a probability to each shaking intensity, based on uncertainty factors related to location and time (Cornell, 1968; Hanks and Cornell, 1994).

Probabilistic tsunami hazard assessment (PTHA) uses this information to inform tsunami models, creating simulations for each scenario (e.g., Davies et al., 2018; Volpe et al., 2019; Lorito et al., 2021; Abbate et al., 2025). Tsunami hazard maps are produced to show the probability of specific wave heights along coastal regions.

Government decisions regarding civil protection are often based on these seismic and tsunami hazard maps. Nevertheless, these hazard maps depend on many assumptions, since earthquake hazard is not a physically measurable unit (Stein et al., 2012). The past has shown, however, that earthquakes can also happen in areas where hazard maps did not predict major destructive earthquakes, for example, during the 2010 Haiti earthquake (ten Brink et al., 2020). Additionally, the seismic history is often too short to make reliable predictions for future (megathrust) events that cause destructive tsunamis.

### 1.4.1 Tsunami earthquakes

Tsunami earthquakes were first defined by Kanamori (1972) and describe earthquakes that cause tsunami amplitudes much larger than expected based on the earthquakes' surface-wave magnitude $M_S$. These earthquakes have larger moment magnitudes $M_W$ than other events with the same $M_S$. While $M_S$ measures the energy released by surface waves over a short period of 1–20 s, $M_W$ determines the energy release over a longer duration. The difference between $M_S$-$M_W$ highlights the slow rupture propagation of these earthquakes, which is typical of “tsunami earthquakes" (Kanamori and Kikuchi, 1993).

Tsunami earthquakes typically nucleate at very shallow depths, where the frontal prism meets the outer wedge (Sec. 1.1), and propagate up-dip to the surface, leading to large displacements of the water column (Kanamori and Kikuchi, 1993; Ammon et al., 2006; Bilek and Engdahl, 2007; Lay et al., 2012). Generally, the size of the earthquake is one of the most important factors influencing the generation of tsunami earthquakes (Polet and Kanamori, 2000).

Kanamori and Kikuchi (1993) further classify tsunami earthquakes into two different types: the ones that occur in regions with large amounts of accretionary sediments overlying the trench, or those that happen in subduction zones where the deposits are completely subducted. In the first case, the displacement, slipping, and collapse of accretionary sediments during the earthquake cause exceptionally large tsunami amplitudes. In the second case, the plate interface is weak because it is filled with subducted soft sediments, while sediments in the accretionary prism are either absent or very thin. In this case, the earthquake

rupture propagates up-dip until it reaches the surface, causing significant displacements of the water column (e.g., Ide et al., 2011). At shallow depths, the rupture passes through the low-velocity region composed of soft, low-rigidity material that reduces the rupture velocity (Polet and Kanamori, 2000). This type of tsunami earthquake is therefore referred to as a “slow tsunami earthquake".

## 1.5 Research gap

To improve the quantification of seismic and tsunami hazards in megathrust regions, it is crucial to understand what influences earthquake recurrence and magnitude. Often, highly complex rupture processes are poorly understood because many subduction zones are submerged in deep water and are difficult to access for direct measurements. If accessible, direct observations are restricted to the uppermost part of the subduction zone (Chester et al., 2012; Brizzi et al., 2020) due to the physical constraints of borehole depths. However, most megathrust earthquakes and faulting processes occur at greater depths. They are governed by the stress and strength conditions of the fault zone (Hardebeck, 2015) that accumulate during the interseismic phase (Sec. 1.2). To better understand these processes, marine geophysical techniques are employed to accurately image the complex structures of the subduction zone and produce high-resolution local bathymetry maps (Jones et al., 2008). Additionally, dense seismic land and offshore networks, satellite data, and GPS networks shed light on rupture processes and help characterize smaller-scale source properties (e.g., Smith and Sandwell, 1997; Ishii et al., 2005).

Despite recent advances in earthquake monitoring and geophysical seagoing measurements, it remains poorly understood where large $M_W \geq 8$ subduction zone earthquakes are likely to happen (Kopp, 2013), what factors influence earthquake nucleation or rupture arrest, and how the rupture propagates along the megathrust interface.

The rarity of great earthquakes presents an additional challenge for probabilistic seismic and tsunami hazard assessment. Hazard maps often depend on poorly constrained parameters and limited understanding of the rupture process itself (Stein et al., 2012). These discretionary assumptions alone do not demonstrate the likelihood of future earthquakes. Since the devastating Tohoku-Oki (e.g., Løvholt et al., 2012; Kozdon and Dunham, 2013; Goda, 2015; Galvez et al., 2016) and Sumatra (e.g., Bletery et al., 2016; Ulrich et al., 2021) earthquakes, it is evident that many assumptions and hypotheses that guided the understanding of occurrence rates (Ruff and Kanamori, 1980; Kanamori, 2006), possible earthquake magnitudes, and damage are only partially accurate. The entire earthquake process itself must be much more complex than previously believed.

Therefore, more observations and numerical models that examine rupture evolution, propagation, extent, recurrence intervals, and potential locations of $M_W \geq 8.0$ earthquakes, which could generate strong ground motions and source tsunamis, are necessary to accurately assess the overall seismic and tsunami hazard impact (Wirth et al., 2022). This

highlights the need to compare and connect different geological data and to bridge models across disciplines and timescales (e.g., Madden et al., 2020; Wirp et al., 2021) both on- and offshore. This connection may help enhance the overall understanding of subduction zone mechanics, megathrust earthquakes, and the processes of tsunami generation and propagation, thereby aiding in tsunami early warning.

## 1.6 Dynamic rupture modeling of subduction zones

New earthquakes often change our understanding of the depth-related processes (Lay et al., 2012) behind how rupture initiates and propagate, the estimation of where earthquakes could happen, and the hazard intensity in specific areas. Dynamic rupture is highly unique and can propagate as pulse-like (e.g., Gabriel et al., 2012; Meier et al., 2016) or crack-like (e.g., Yomogida, 1988) rupture, depending on the slip duration at each fault point. For pulse-like ruptures, the slip duration is shorter than the overall rupture duration, whereas for crack-like ruptures, it is similar. The rupture on the fault interface can be slow or fast and can propagate at subshear or supershear speeds (Andrews, 1976b; Dunham, 2007; Kaneko and Shearer, 2014; Socquet et al., 2019; Wang and Zhang, 2025).

The types of rupture depend on the geological characteristics of the upper and lower plates, such as stress state, fault strength, pore pressure, off-fault damage zones (Templeton and Rice, 2008; Gabriel et al., 2013; Dal Zilio and Gerya, 2022), and fault roughness (e.g., Dunham et al., 2011b; Shi and Day, 2013; Taufiqurrahman et al., 2022). Bi-material effects (e.g., Ampuero and Ben-Zion, 2008), heterogeneities in stress and strength (Ripperger, 2007; Langer et al., 2013), thermal pressurization (Andrews, 2002; Bizzarri and Cocco, 2006; Schmitt et al., 2015), flash heating and frictional melting (Rice, 2006, 2017), as well as low velocity zones (Harris and Day, 1997; Huang and Ampuero, 2011; Thakur et al., 2020) and geometrical variations of the fault may influence the rupture evolution and can directly be included as initial condition in numerical DR simulations.

Given the inaccessibility of subducting megathrusts, numerical earthquake simulations help enhance our understanding of faulting mechanisms. DR models (e.g., Madariaga et al., 1998; de la Puente et al., 2009; Ramos et al., 2022) utilize physical equations to replicate the rupture propagation process and the interaction of the rupture front with the surrounding Earth and radiated seismic waves, or to simulate possible future earthquake scenarios for a specific area of interest. The numerical models deepen our understanding of what governs subduction zone mechanics at convergent margins and what controls the location and size of the rupture.

Especially for probabilistic seismic and tsunami hazard assessment (Knighton and Bastidas, 2015; Selva et al., 2016; Grezio et al., 2017; Park et al., 2017), more data and observations are needed to reduce risks. Dynamic rupture modeling can complement these common hazard studies, as understanding the entire rupture process is essential for estimating the probabilities of ground motion exceeding certain levels. A combination of seismic and geodetic monitoring, along with modern numerical modeling techniques is crucial for

advancing the understanding of megathrust subduction and tsunami-generic earthquakes (e.g., Wirth et al., 2022) and to reduce risks that are associated with convergent margins.

This dissertation focuses on the dynamics of large ($M_W \geq 7.5$) subduction zone earthquakes and their associated tsunamis. I use the dynamic rupture modeling software SeisSol (Uphoff et al., 2024) (Sec. 2.1) to simulate rupture on predefined megathrusts. I present various options for constraining the initial conditions of these DR models. I further use the resulting seafloor uplift and subsidence to model the related tsunami generation, propagation, and inundation with the hydrostatic shallow-water solvers sam(oa)$^2$-flash (`https://gitlab.lrz.de/samoa/samoa`) and GeoClaw (Berger et al., 2011) (Sec. 2.2). Additionally, I use fully-coupled models that include both earthquake rupture and tsunami generation and propagation (Sec . 2.4). I analyze the results and highlight implications for understanding earthquake dynamics and tsunami generation in general, as well as for seismic and tsunami hazards in the Hellenic Arc region.

## 1.7 Thesis outline

Each study in this thesis examines the dynamics of subduction zones and aims to connect models and scales to better understand the interaction between long-term subduction, dynamic earthquake rupture, and the generation and propagation of tsunamis.

Chapter 3 connects all the previous points using a long-term geodynamic subduction and seismic cycling model to source dynamic rupture, which is then linked to tsunami simulations analyzing the impact of hypocentral location, Poisson's ratio, and fracture energy on co-seismic seafloor uplift and tsunami amplitudes.

Chapter 4 explores how increasing the complexity of ten potential earthquake rupture scenarios on the Hellenic Arc megathrust, located in Greece, influences rupture behavior, moment magnitude, and co-seismic seafloor uplift, thereby reconstructing historic tsunami-generic events.

The study in Chapter 5 models tsunamis in the Hellenic Arc region, using five DR scenarios from Chapter 4 to examine how epicenter location and off-fault plasticity influence maximum tsunami amplitudes and to identify regions with high tsunami impact. One scenario is also expanded into a large-scale, fully-coupled 3D earthquake-tsunami model to capture the complexities of the early tsunami generation phase.

Chapter 6 gives a final outlook by summarizing the key results of this thesis and discussing ideas for future research.

### 1.7.1 Publications

Chapter 3 has been published in a slightly altered form in Frontiers in Earth Sciences as:

- **Wirp** S A, Gabriel A-A, Schmeller M, H. Madden E, van Zelst I, Krenz L, van Dinther Y and Rannabauer L (2021). 3D Linked Subduction, Dynamic Rupture, Tsunami, and Inundation Modeling: Dynamic Effects of Supershear and Tsunami Earthquakes, Hypocenter Location, and Shallow Fault Slip. Front. Earth Sci. 9:626844. `https://doi.org/10.3389/feart.2021.626844`

Chapter 4 has been published by the Journal of Geophysical Research: Solid Earth in a slightly altered form with minor revision as:

- **Wirp**, S. A., Gabriel, A.-A., Ulrich, T., & Lorito, S. (2024). Dynamic rupture modeling of large earthquake scenarios at the Hellenic Arc toward physics-based seismic and tsunami hazard assessment. Journal of Geophysical Research: Solid Earth, 129, e2024JB029320. `https://doi.org/10.1029/2024JB029320`

Chapter 5 has shortly been submitted for publication in a slightly altered form as:

- **Wirp**, S. A., Kutschera, F., Gabriel, A.-A., Ulrich, T., Bader, M., Lorito, S. (2025). Hellenic Arc tsunami generation from $M_W8+$ 3D margin-wide dynamic rupture earthquake scenarios, submitted to Journal of Geophysical Research: Solid Earth. Preprint: `https://doi.org/10.31223/X52X6M`

During my Ph.D. thesis, I co-supervised two Bachelor's and one Master's thesis:

- Fabian Kutschera, Physics-based earthquake-tsunami modelling for North Iceland using supercomputing (2020)
- Janina Moser, The Hellenic Arc: Modelling subduction earthquakes and Tsunami hazard (2021)
- Fabian Kutschera, 3D fully-coupled earthquake-tsunami modeling of the 2020 Mw 7.0 Samos earthquake (2023)

An extended version of F. Kutscheras Bachelor thesis has been published as:

- Kutschera, F., Gabriel, A.-A., **Wirp**, S. A., Li, B., Ulrich, T., Abril, C., and Halldórsson, B. (2024). Linked and fully coupled 3D earthquake dynamic rupture and tsunami modeling for the Húsavík–Flatey Fault Zone in North Iceland, Solid Earth, 15, 251–280. `https://doi.org/10.5194/se-15-251-2024`

An extension of F. Kutscheras Master thesis will be submitted for publication shortly as well.

I have also been involved in collaborations during my Ph.D. that are not part of this dissertation. I specifically contributed to two published conference abstracts and two additional papers:

- Li, B., **Wirp**, S. A., Gabriel, A.-A., Bader, M., Halldórsson, B. (2019). Towards Physics-based probabilistic seismic hazard assessement in complex fault networks - The ChEESE project. Útgefandi/Publisher: Þekkingarnet ingeyinga/Husavik Academic Centre, 45.

- Kutschera, F., Gabriel, A. A., **Wirp**, S. A., Li, B., Ulrich, T., Abril, C., & Halldórsson, B. (2022). Modeling potential earthquake-tsunami scenarios from earthquake rupture simulations on the Húsavík-Flatey Fault Zone, North Iceland. Útgefandi/Publisher: Þekkingarnet ingeyinga/Husavik Academic Centre, 45.

- Folch, A., Abril, C., Afanasiev, M., Amati, G., Bader, M., Badia, R. M., ..., **Wirp**, S. A. & Wössner, U. (2023). The EU Center of Excellence for Exascale in Solid Earth (ChEESE): Implementation, results, and roadmap for the second phase. Future Generation Computer Systems, 146, 47-61. `https://doi.org/10.1016/j.future.2023.04.006`

- Saki, M., **Wirp**, S. A., Billen, M., Thomas, C. (2024). Seismic evidence for possible entrainment of rising plumes by subducting slab induced flow in three subduction zones surrounding the Caribbean Plate. Physics of the Earth and Planetary Interiors, 352, 107212. `https://doi.org/10.1016/j.pepi.2024.107212`

# Chapter 2

# Methods

## 2.1 Earthquake dynamic rupture modeling with SeisSol

All physics-based dynamic rupture earthquake models of this thesis are simulated using the open-source software SeisSol (Uphoff et al. (2022); de la Puente et al. (2009); Pelties et al. (2012, 2014), `https://seissol.org`). SeisSol simulates frictional failure across prescribed fault surfaces, capturing the detailed evolution and propagation of slip. At the same time, it simulates the seismic waves radiated by the rupture front, solving the high-order accurate 3D seismic wave propagation in space and time. It accounts for (visco-)plastic Drucker-Prager off-fault plastic deformation (Andrews, 2005; Wollherr et al., 2018) and models the resulting ground motion of the earthquake.

The software is highly optimized for current petascale supercomputers (Breuer et al., 2014; Heinecke et al., 2014; Rettenberger et al., 2016; Uphoff and Bader, 2020; Dorozhinskii and Bader, 2021). It includes the parallel implementation of the discontinuous Galerkin (DG) scheme with an efficient Arbitrary high-order DERivative (ADER) local time-stepping algorithm (Dumbser and Käser, 2006; Käser and Dumbser, 2006; Breuer et al., 2016; Uphoff et al., 2017; Wolf et al., 2020). It uses a simulation domain discretized by unstructured tetrahedral grids with static mesh adaptivity (Dumbser and Käser, 2006; Käser and Dumbser, 2006) which is suited to model complex slab geometries as used in the following studies of Chapters 3, 4, and 5. The software's accuracy is verified against a wide range of community benchmarks (Harris et al., 2011, 2018).

Dynamic rupture modeling has been used to study essential aspects of earthquake physics (e.g., Gabriel et al., 2012; Shi and Day, 2013), to evaluate earthquake hazard (e.g., Hok et al., 2011; Aochi and Ulrich, 2015; Wirp et al., 2024), or to analyze previous earthquakes (e.g., Ma and Beroza, 2008; Kozdon and Dunham, 2013; Taufiqurrahman et al., 2023).

Commonly, the static failure on the fault is defined as:

$$|\tau_s| = c - \mu_s \tau_n' \,, \tag{2.1}$$

with $\tau_s$ being the on-fault shear traction, $c$ the on-fault cohesion, $\mu_s$ defining the static friction coefficient, and $\tau_n'$ the effective normal traction. When the on-fault shear stress

exceeds the fault's static strength (right-hand side of Eq. 2.1), the fault weakens, rupture initiates, and seismic waves are emitted.

All earthquake models of this dissertation are simulated using the constitutive law of linear slip weakening friction (e.g., Ida, 1972; Andrews, 1976a) describing the fault rheology as follows:

$$f(s) = \begin{cases} \mu_s - \frac{\mu_s - \mu_d}{D_c} \cdot s, & s \leq D_c \,, \\ \mu_d, & s > D_c \end{cases} \quad . \tag{2.2}$$

The fault weakening is described as a simplified linear decrease of the friction coefficient from its static value $\mu_s$ to the dynamic friction coefficient $\mu_d$ over the characteristic slip-weakening distance $D_c$. As the slip $s$ exceeds $D_c$, the friction remains at its dynamic coefficient.

More complex friction laws, such as rate-and-state friction, were derived from laboratory experiments (Dieterich, 1979; Ruina, 1983). They account for a time-dependent friction evolution and secondary effects, such as fault reactivation (e.g., Gabriel et al., 2012), but are not used in this thesis.

Dynamic rupture simulations require a set of initial conditions. These are crucial assumptions about fault geometry, initial stress state, and rock properties that directly affect the simulation results. Especially in subduction zones, obtaining accurate values for frictional strength, fault loading stresses, fault geometry, and subsurface material properties can be challenging due to limited accessibility. The following Chapters 3 and 4 illustrate different methods for constraining initial conditions for subduction zones. One approach involves geodynamic long-term subduction and seismic cycling models (van Zelst et al., 2019; Madden et al., 2020; Wirp et al., 2021; van Zelst et al., 2022) since they provide physically self-consistent values that fit subduction and deformation over geological timescales. Another approach is to constrain the tectonic background stresses and fault strength on the subduction scale using a regional stress tensor approach (Ulrich et al., 2022) and the Mohr-Coulomb theory of frictional failure combined with seismo-tectonic observations (Wirp et al., 2024).

## 2.2 Tsunami modeling with sam(oa)$^2$ and GeoClaw

In this thesis, I use the tsunami modeling softwares sam(oa)$^2$-flash (`https://gitlab.lrz.de/samoa/samoa`, Meister et al. (2016)) (Chapter 3) and GeoClaw (Clawpack Development Team (2023), Berger et al. (2011); LeVeque and George (2008); LeVeque et al. (2011)) (Chapter 5). Both codes utilize the two-dimensional depth-averaged hydrostatic non-linear Shallow Water Equations (SWE, LeVeque et al. (2011)) and incorporate adaptive mesh refinement (e.g., Meister et al., 2016), enabling the refinement of the wavefront for small-scale inundation modeling at the coast. The SWE imply that vertical scales (water depth) can be ignored compared to horizontal scales (tsunami wavelength). For tsunami modeling of subduction zone earthquakes, this approximation is sufficient. Both tsunami software programs can use either the static seafloor displacement or the full spatio-temporal seafloor

perturbation from a DR earthquake simulation to source the tsunami. Sam(oa)$^2$-flash has been validated against various benchmarks (Synolakis et al., 2008), and the GeoClaw code was approved by the US National Tsunami Hazard Mitigation Program (Gonzalez et al., 2011).

## 2.3 Workflow for one-way linking between models of different scales

Linking geophysical models is a helpful way to constrain suitable initial conditions and ensure physical consistency between the models (Madden et al., 2020; Wirp et al., 2021). Long-term geodynamic models can inform smaller-scale dynamic rupture models, and the results of these rupture models can then provide initial conditions for tsunami simulations. In the following, I will describe the one-way linking workflow from large-scale geodynamics to short-term dynamic rupture and tsunami modeling.

### 2.3.1 Linking geodynamic models to dynamic rupture

2D seismo-thermo-mechanical geodynamic (SC) models simulate large-scale long-term subduction zone processes along with smaller timescale frictional slip events. The evolution of the subduction zone is modeled over millions of years, accounting for complex rheology and temperature variations. The SC model combines these large-scale processes with seismic cycling over a period of 5 years (e.g., Van Dinther et al., 2014; Dal Zilio and Gerya, 2022; van Zelst et al., 2022). It provides information about megathrust geometry, material properties, and the stresses and strength that develop during the interseismic phase. This data can be extracted from the SC model at the timestep just before a megathrust event and used as physically consistent initial conditions for dynamic rupture modeling SeisSol.

The SC models include several seismic events for each simulation. Necessary for coupling the geodynamic model to SeisSol is choosing the right linking timestep. For that, every timestep (5 years) of the SC model needs to be printed. Typically, 5000 years of modeling time (1,000 timesteps) and earthquake cycling are used, as it provides approximately 70 megathrust events that rupture the entire fault and are sufficient to choose from. Each timestep is plotted, and the strain rate is analyzed (Madden et al., 2020; Wirp et al., 2021). Depending on the purpose of the investigation, a specific model with or without splay-fault evolution and with particular rupture propagation characteristics is selected. It is essential to choose the coupling timestep just before a slip event occurs, meaning obtaining initial conditions for a fault that is close to but not yet at failure.

For this specific timestep, all information (material properties, fault geometry, stresses, and strength) is extracted from the SC model. Fig. 2.1 a,b,c show the static and dynamic friction coefficients, the critical slip-weakening distance $D_c$, and the on-fault cohesion at this timestep. The on-fault conditions would cause instantaneous failure in SeisSol, such

that a failure analysis of the stresses on the fault is essential. In Fig. 2.1 d, fault strength and shear traction are shown. Wherever the initial shear traction ($\tau_s$, blue) exceeds the static fault strength (red), failure occurs (green). In this example, failure would occur instantaneously at the upper part of the fault near the trench (∼5–10 km depth, sediments), at ∼250 km distance from the trench which corresponds to an intermediate depth of ∼30–45 km (nucleation region in the SC model), and at individual points at a greater depth of approximately 70–80 km at roughly ∼340 km distance from the trench. At these on-fault locations, the material properties must be adjusted to prevent multiple points of failure in the dynamic rupture simulation.

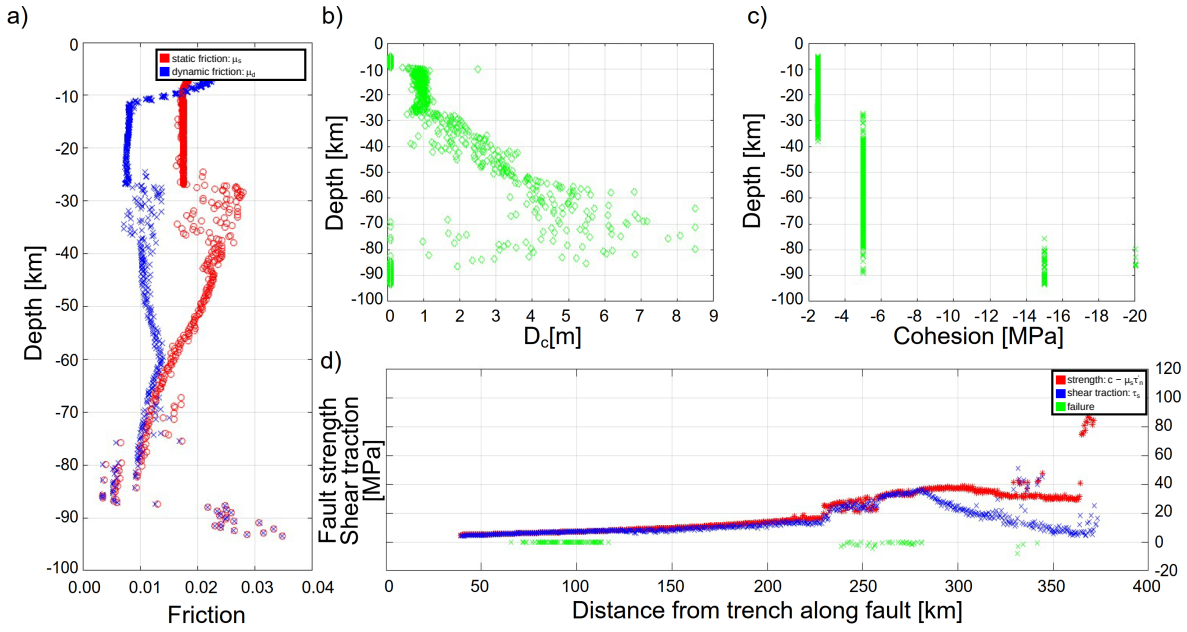



Figure 2.1: **Failure analysis of material properties exported from the SC model:** a) Static (red) and dynamic (blue) friction coefficient ($\mu_s$ and $\mu_d$) displayed with depth. b) Critical slip weakening distance $D_c$, and c) on-fault cohesion plotted with depth. d) Fault strength (red), shear traction (blue), and failure (green) with distance from the trench. Failure occurs when the shear traction exceeds the fault strength.

Figure 2.1a shows the on-fault static and dynamic friction coefficients ($\mu_d$ and $\mu_s$) that can be directly imported as initial conditions in the DR model. Most of the values follow predominantly traces indicating a logical on-fault distribution of $\mu_s$ and $\mu_d$ with increasing distance from the trench. Additionally, there are "outliers" of both values at distances where we observe instantaneous failure. For distances of approximately 240-280 km, these values can be corrected and adjusted to align with the main distribution. For the shallow sediments (distance from trench ∼100 km), the cohesion is instead changed to 5 MPa,

which is the value that equals the material right below the sediments. This prevents failure on the shallow fault section. Failures at approximately 330–350 km distance from the trench are addressed similarly by setting a very high cohesion of 15 MPa and adjusting the $\mu_s$ values. The outcome is a fault that does not undergo instantaneous failure, and all corrected material properties can be imported into SeisSol.

The dynamic rupture simulations in SeisSol are usually conducted in a 3-dimensional domain. Therefore, all output from the SC model must be extended into the third dimension. The SC model is two-dimensional and does not include information about along-strike stress, strength, or material properties variations. For simplicity, all on-fault variables can be kept constant and copied to the third dimension (Wirp et al., 2021). If a more complex model is preferred, advanced research on along-strike heterogeneities in subduction zones and specific regions must be conducted, and corresponding assumptions and adaptations of the modeling parameters need to be made (Ulrich et al., 2022; Wirp et al., 2024).

### 2.3.2 Linking dynamic rupture simulations to tsunami models

The difficulty in linking DR models to tsunami models is similar to the SC-DR connection: bridging the different spatial and temporal scales of the models. For DR modeling in SeisSol, having high on-fault resolution is especially crucial to capture the rupture process accurately. Away from the fault, the computational mesh and thus the resolution can be reduced to save computational costs. Additionally, it may be sufficient to plot timesteps of 1 s or more to analyze rupture propagation and simulation results. For tsunami modeling, it is crucial to accurately resolve the seafloor (free surface) perturbation in both space and time to capture the desired wavelength and frequency accurately. Madden et al. (2020) find that a free surface perturbation sampling rate of 1 Hz is sufficient because it adequately resolves the tsunami waves. For an average water depth of 2 km, the maximum wave propagation speed is approximately 140 m/s.

While SeisSol uses a tetrahedral mesh to accurately depict complex fault structures and geometries, including mesh coarsening away from areas of interest, the tsunami codes sam(oa)$^2$-flash and GEOClaw (Sec. 2.2) utilize a uniform Cartesian grid mesh. Therefore, the free surface perturbation of SeisSol must be bilinearly interpolated using a nearest-neighbor approach (Madden et al., 2020; Wirp et al., 2021) to produce a logically regular (e.g. rectangular) latitude-longitude grid on a sphere that is readable by the codes.

The seafloor deformation caused by a dynamic rupture event is usually represented as a 3-dimensional vector in SeisSol, which includes vertical and horizontal displacement components in all directions ($\Delta x$, $\Delta y$, and $\Delta z$). The tsunami model, in contrast, utilizes a 2D initial seafloor disturbance to generate the tsunami, including only the horizontal east-west ($\Delta x$) and north-south ($\Delta y$) components. Since the water column is expected to be constant in both codes, the static or time-dependent seafloor movement is directly translated into an initial water displacement. The following papers (e.g., Madden et al.,

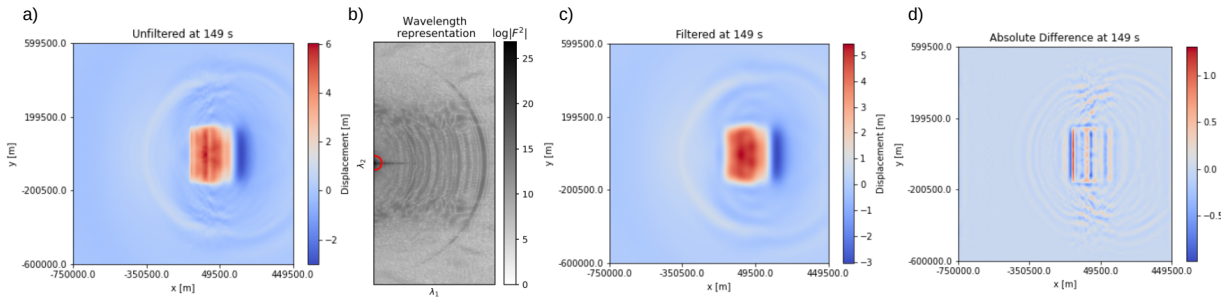



Figure 2.2: **Filtering process for one-way linking of the dynamic rupture to shallow-water tsunami modeling.** The figure is adapted from Wirp et al. (2021). a) Unfiltered seafloor displacement at 149 s simulation time. b) Wavenumber representation of the displacement field. The red line represents the smooth filter kernel that is applied to the data. c) Filtered signal after applying the Fourier filter. d) Difference between the unfiltered (a) and filtered (c) wavefield.

2020; Wirp et al., 2021, 2025) adopt the method by (Tanioka and Satake, 1996) to integrate vertical bathymetry perturbations into the tsunami models. The time-dependent bathymetry uplift or subsidence (Madden et al., 2020), denoted as $\Delta b$, can be described as:

$$\Delta b = \Delta z - \Delta x \frac{\delta b}{\delta x} - \Delta y \frac{\delta b}{\delta y} \, . \tag{2.3}$$

Here, the bathymetry increasing in upward direction is $b = b(x, y)$.

The SeisSol free surface output not only includes the primary tsunami source but also the seismic wavefield. The primary seafloor perturbation stays constant after the rupture propagation, as SeisSol does not model post-seismic relaxation. However, once rupture propagation stops, trapped seismic waves may continue to propagate between the fault interface and the free surface. These waves influence tsunami generation, but the far-field solution remains unchanged (Saito et al., 2019). In the shallow-water tsunami model, seismic waves may generate spurious gravity waves or artifacts that could complicate the simulation results. To distinguish the frequency-wavenumber coefficients of the main perturbation from those of the seismic waves, a space-time Fourier filter can be employed (Madden et al., 2020; Wirp et al., 2021). The fast-propagating seismic waves ($\sim$2500 m/s) and short wavelengths are damped, while the overall uplift remains unaffected (Fig. 2.2).

Usually, the aim of simulating tsunamis is not only to capture the tsunami generation and propagation process, but in particular to model inundation or runup at the coast. If the DR model is kept very simple as in (Wirp et al., 2021), an artificial coast might be included in the tsunami model to illustrate possible runup and inundation. The more complex the coastal bathymetry, the more complex the expected wave height (Wirp et al., 2025) on the coast.

## 2.4 Fully-coupled dynamic rupture-tsunami simulations

Fully-coupled dynamic rupture-tsunami simulations simultaneously model earthquake rupture propagation along with the resulting tsunami and seismic wave propagation in elastic and acoustic media, capturing the complete physics of tsunami generation (Lotto and Dunham, 2015; Lotto et al., 2018; Wilson and Ma, 2021; Ma, 2022). On top of the bathymetry of the 3-dimensional DR modeling domain (elastic), it contains a water layer (acoustic) of variable depth. The interface between both media is implemented in SeisSol through an exact solution of the Riemann problem (Wilcox et al., 2010) for acoustic and elastic properties, assuming the acoustic wave equation to be a special case of the elastic wave equation (Krenz et al., 2021). Therefore, a fully-coupled model can simulate the interaction of 3D elastic, acoustic, and tsunami waves. Unlike the one-way linking from DR to tsunami models, it captures the entire tsunami generation and propagation process. The model includes a modified surface boundary condition on the equilibrium ocean surface that accounts for gravitational effects, such as dispersion, during the tsunami generation phase (Krenz et al., 2021). A disadvantage of the fully-coupled models is the high computational cost, which increases significantly when including the water layer because it must be discretized at a fine scale to capture these processes. Especially for large areas, such as subduction zones (e.g., Hellenic Arc region, Chapter 5), the simulations become costly, making access to supercomputers essential.

### 2.4.1 Meshing workflow

The meshing workflow typically causes the most issues when running fully-coupled dynamic rupture tsunami simulations in SeisSol. The main problem here is the intersection between the plane water layer surface and the topobathymetry.

To generate high-quality, unstructured tetrahedral meshes for the DR scenarios in this thesis, I utilize SimModeler (Simmetrix, `http://www.simmetrix.com/index.php`), which is well-suited for approximating complex 3D model geometries, like subducting megathrusts, and facilitating rapid model generation. The workflow for mesh generation in SeisSol is detailed at `https://seissol.readthedocs.io/en/latest/simmodelerCAD-workflow.html`. For a fully-coupled model, this workflow has to be adapted accordingly. Here, a water layer must be additionally created with Gmsh (`https://gmsh.info/`) and intersected with the topography before proceeding with the standard meshing workflow. The mesh surfaces generated for the water layer and topography must possess comparable mesh sizes to facilitate seamless intersection without complications. Otherwise, the software may be unable to accurately intersect and combine them. Furthermore, the mesh space between two nodes should be minimized to adequately resolve the topography and intersecting regions. Conversely, employing a finer mesh on individual model components can substantially decrease the responsiveness of the SimModeler graphical user interface (GUI).

Challenges at the intersection of topography and water layer are especially common in small features near the water layer, such as sharp coastal regions, small islands, and topography that lies slightly above or below sea level. During the intersection process, these

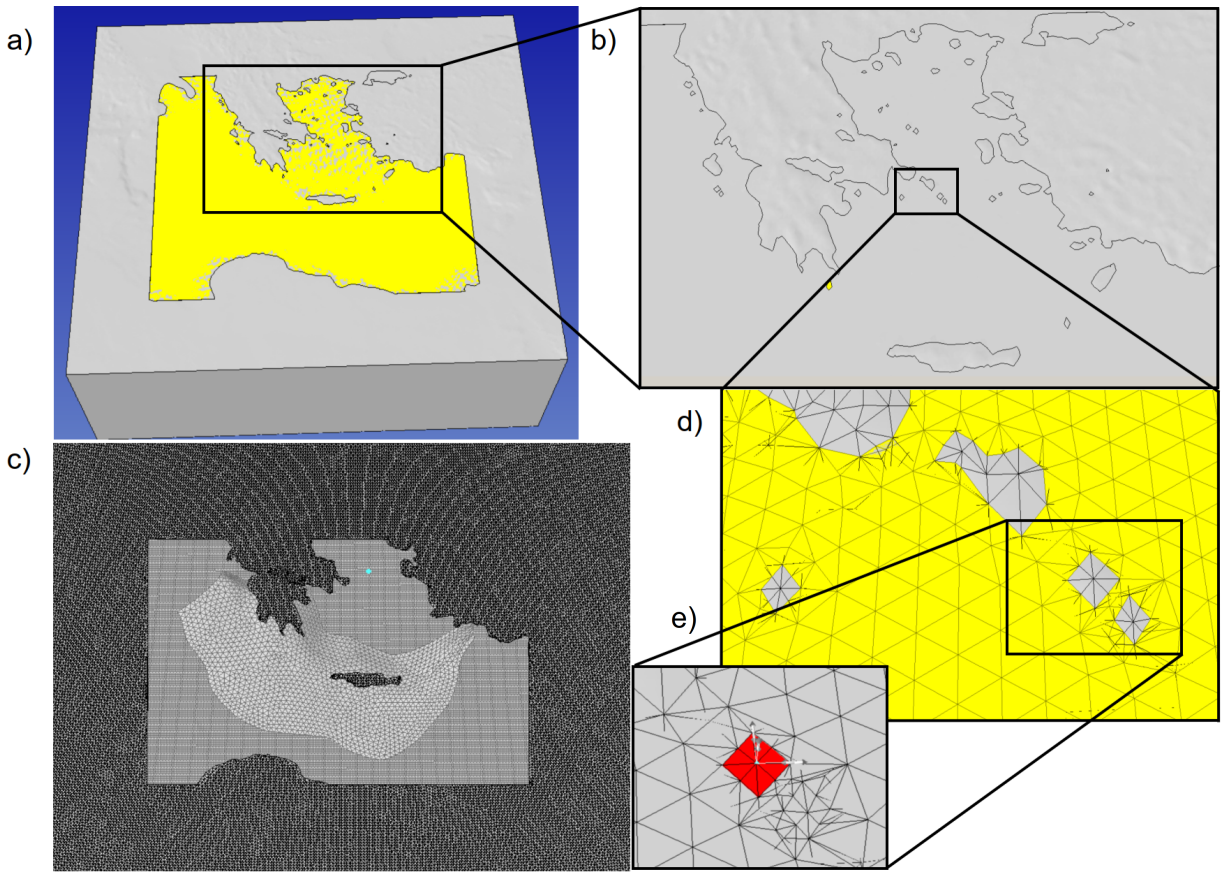



Figure 2.3: **Meshing process:** Snapshots of the meshing process in the SimModeler GUI (`http://www.simmetrix.com/index.php`). a) Intersection of the water layer with the topobathymetry for the Hellenic Arc region. b) and d) Zoom into the region where the intersection causes an error. c) Successful union of the water layer and topography, showing the small mesh space of both regions and the megathrust below. e) Meshing face that requires manual correction. For a) and d), the water layer is colored yellow, the topobathymetry grey.

features cannot be combined in the GUI if they are too small, due to the limited 2D mesh size of each surface. To prevent these issues, I perform a preprocessing step that smooths the topography around 0 km depth before applying the intersection (Chapter 5, Wirp et al. (2025)). This will decrease the accuracy and resolution, but may help when intersecting complex features. Nonetheless, an extensive and complex region like the Hellenic Arc (Fig. 2.3 a,b) contains many of these small-scale features: tiny islands and shallow areas, making it challenging to intersect the water layer with the topography. Figure 2.3 c shows a successful intersection for this region. If the intersection succeeds, the water layer may still not be meshable. In some small-scale elevations and islands (Fig. 2.3 d), the seafloor topobathymetry is too close and/or parallel to the sea surface. That is why, even with very small mesh sizes of a few hundred meters, errors can still occur. The latest versions of SimModeler (from version 11 on) address this problem by providing the exact location where the union fails, allowing it to be fixed manually (Fig. 2.3 e). SimModeler will now be able to mesh the water layer with a 1 km resolution. The shallower the seafloor depth, the smaller the mesh spacing has to be inside the water layer volume, which increases the final mesh size and computational costs.

# Chapter 3

# 3D linked subduction, dynamic rupture, tsunami and inundation modeling: dynamic effects of supershear and tsunami earthquakes, hypocenter location and shallow fault slip


## Abstract

Physics-based dynamic rupture models capture the variability of earthquake slip in space and time and can account for the structural complexity inherent to subduction zones. Here we link tsunami generation, propagation, and coastal inundation with 3D earthquake dynamic rupture (DR) models initialized using a 2D seismo-thermo-mechanical geodynamic (SC) model simulating both subduction dynamics and seismic cycles. We analyze a total of 15 subduction-initialized 3D dynamic rupture-tsunami scenarios in which the tsunami source arises from the time-dependent co-seismic seafloor displacements with flat bathymetry and inundation on a linearly sloping beach. We first vary the location of the hypocenter to generate 12 distinct unilateral and bilateral propagating earthquake scenarios. Large-scale fault topography leads to localized up- or downdip propagating supershear rupture depending on hypocentral depth. Albeit dynamic earthquakes differ (rupture speed, peak slip-rate, fault slip, bimaterial effects), the effects of hypocentral depth (25 to 40 km) on tsunami dynamics are negligible. Lateral hypocenter variations lead to small effects such as delayed wave arrival of up to 100 s and differences in tsunami amplitude of up to 0.4 m at the coast. We next analyse inundation on a coastline with complex topo-bathymetry which increases tsunami wave amplitudes up to ≈1.5 m compared to a linearly sloping beach. Motivated by structural heterogeneity in subduction zones, we analyse a scenario with increased Poisson's ratio of $\nu = 0.3$ which results in close to double the amount of shallow fault slip, ≈1.5 m higher vertical seafloor displacement, and a

difference of up to ≈1.5 m in coastal tsunami amplitudes. Lastly, we model a dynamic rupture "tsunami earthquake" (Kanamori, 1972) with low rupture velocity and peak slip rates and twice as high tsunami potential energy. We triple fracture energy which again doubles the amount of shallow fault slip, but also causes a 2 m higher vertical seafloor uplift and the highest coastal tsunami amplitude (≈7.5 m) and inundation area compared to all other scenarios. Our mechanically consistent analysis for a generic megathrust setting can provide building blocks towards using physics-based dynamic rupture modeling in Probabilistic Tsunami Hazard Analysis.

## 3.1 Introduction

Earthquake sources are governed by highly non-linear multi-physics and multi-scale processes leading to large variability in dynamic and kinematic properties such as rupture speed, slip rate, energy radiation and slip distribution (e.g. Oglesby et al., 2000; Kaneko et al., 2008; Gabriel et al., 2012; Bao et al., 2019; Ulrich et al., 2019a; Gabriel et al., 2020). Such variability may impact the generation, propagation, and inundation of earthquake-generated tsunami or secondary tsunami generation mechanisms such as triggered landslides (e.g., Sepúlveda et al., 2020). For example, unexpectedly large slip at shallow depths may generate large tsunami (Lay et al., 2011; Romano et al., 2014; Lorito et al., 2016).

To model earthquake-generated tsunami, sources can be approximated from earthquake generated uplift (Behrens and Dias, 2015, and references therein). Analytical solutions (e.g., Okada, 1985) describe seafloor displacements sourced by uniform rectangular dislocations within a homogeneous elastic half space. Models of tsunami generated by large earthquakes can routinely and quickly use kinematic finite fault models constrained by inversion of seismic, geodetic and other geophysical data (Geist and Yoshioka, 1996; Ji et al., 2002; Babeyko et al., 2010; Maeda et al., 2013; Allgeyer and Cummins, 2014; Mai and Thingbaijam, 2014; Bletery et al., 2016; Jamelot et al., 2019), but are challenged by the inherent non-uniqueness of kinematic source models (Mai et al., 2016).

Probabilistic Tsunami Hazard Analysis (PTHA) requires the computation of thousands or millions of tsunami scenarios for each specific area of interest (González et al., 2009; Geist and Oglesby, 2014; Horspool et al., 2014; Geist and Lynett, 2014; Lorito et al., 2015; Selva et al., 2016; Grezio et al., 2017; Mori et al., 2018; Sepulveda et al., 2019; Glimsdal et al., 2019). Stochastic source models (McCloskey et al., 2008; Davies and Griffin, 2019) statistically vary slip distributions (Andrews, 1980) and are specifically suited for PTHA in combination with efficient tsunami solvers (e.g., Berger et al., 2011; Nakano et al., 2020). For instance, Goda et al. (2014) highlights strong sensitivities of tsunami height to slip distribution and variations in fault geometry in stochastic random-field slip models for the 2011 Tohoku-Oki earthquake and tsunami. Recently, Scala et al. (2019) use stochastic slip distributions for PTHA in the Mediterranean area.

3D Dynamic earthquake rupture modeling can provide mechanically viable tsunami source descriptions on complex faults or fault systems on the scale of megathrust events (Galvez et al., 2014; Murphy et al., 2016; Uphoff et al., 2017; Murphy et al., 2018; Ma and Nie, 2019; Saito et al., 2019; Ulrich et al., 2022). Such simulations can exploit modern numerical methods and high-performance computing (HPC) to shed light on the dynamics and severity of earthquake behaviour and potentially complement PTHA. For example, in dynamic rupture models shallow slip amplification can spontaneously emerge due to up-dip rupture facilitated by along-depth bi-material effects (Rubin and Ampuero, 2007; Ma and Beroza, 2008; Scala et al., 2017) and free-surface reflected waves within the accretionary wedge (Nielsen, 1998; Lotto et al., 2017a; van Zelst et al., 2019). Dynamic rupture earthquake models can yield stochastic slip distributions, too, under the assumption of stochastic loading stresses (Geist and Oglesby, 2014). Such physics-based models can be directly linked to tsunami models by using the time-independent or time-dependent seafloor dis-

placements (and potentially velocities) as the tsunami source (Kozdon and Dunham, 2013; Ryan et al., 2015; Lotto et al., 2017b; Saito et al., 2019; Madden et al., 2020). For instance, time-dependent 3D displacements from observational constrained dynamic rupture scenarios of the 2018 Palu, Sulawesi earthquake and the 2004 Sumatra-Andaman earthquake are linked to a hydrostatic shallow water tsunami model by Ulrich et al. (2019b). Bathymetry induced amplification of horizontal displacements are thereby accounted for by following Tanioka and Satake (1996).

Observational and numerical studies show that megathrust geometry and hypocenter location influence earthquake rupture characteristics. Ye et al. (2016) state that megathrust earthquakes across faults that are longer horizontally than they are deep vertically (with an aspect ratio of 3 or larger) tend to exhibit primarily unilateral behavior. Also, events with an asymmetric hypocenter location on the fault favor rupture propagation along strike to its far end (Harris et al., 1991; McGuire et al., 2002; Hirano, 2019). Weng and Ampuero (2019) show the energetics of elongated ruptures is radically different from that of conventional circular crack models. Bilek and Lay (2018) find that the complexity of slip as well as bi- or unilateral rupture preferences of large earthquakes highly depend on the depth location of the hypocenter.

Subduction zones worldwide are associated with tectonic, frictional and structural heterogeneity along depth and along-arc impacting megathrust earthquake and tsunami dynamics (Kirkpatrick et al., 2020, e.g.,). Kanamori and Brodsky (2004) show that fracture energy varies between subduction zone earthquakes. A special case are so called tsunami earthquakes (Kanamori, 1972) that may require a large amount of fracture energy, low rupture velocity and low radiation efficiency. Structural heterogeneity in subduction zones includes variations in Poisson's ratio ($V_p/V_s$) (e.g., Liu and Zhao, 2014; Niu et al., 2020)), while dynamic rupture and seismic wave propagation models often adopt an idealized Poisson's ratio of $\nu$ =0.25 governing seismic wave propagation (e.g. Kozdon and Dunham, 2013).

The initial conditions of dynamic rupture simulations that control earthquake rupture nucleation, propagation and arrest include fault loading stresses, frictional strength, fault geometry, and subsurface material properties (e.g. Kame et al., 2003; Gabriel et al., 2013; Galis et al., 2015; Bai and Ampuero, 2017). These initial conditions may be observationally and empirically informed (e.g. Aochi and Fukuyama, 2002; Aagaard et al., 2004; Murphy et al., 2018; Ulrich et al., 2022) but remain difficult to constrain. Particularly in subduction zones where observational data are sparse, space and time scales vary over many orders of magnitude and both geometric and rheological megathrust complexities are likely to control rupture characteristics. Recently, initial conditions for 2D and 3D megathrust dynamic rupture earthquake models have been informed from 2D geodynamic long term subduction and seismic cycle models (van Zelst et al., 2019; Madden et al., 2020; van Zelst et al., 2022). This approach provides self-consistent initial fault loading stresses and frictional strength, fault geometry and material properties on and surrounding the megathrust, as well as consistency with crustal, lithospheric and mantle deformation and deformation in the subduction channel over geological time scales. Such subduction-initialized heterogeneous dynamic rupture models lead to complex earthquakes with multiple rupture styles

(Gabriel et al., 2012), shallow slip accumulation and fault reactivation.

We apply the 2D geodynamical subduction and seismic cycle (SC) model from van Zelst et al. (2019) to inform realistic 3D dynamic rupture (DR) megathrust earthquake models within a complex, self-consistent subduction setup along with their consequent tsunami, following the subduction to tsunami run-up linking approach described in Madden et al. (2020). In this study we introduce a number of important differences to previous work. 2D linking including approximations to match SC and DR fracture energy during slip events leads to differences in slip magnitude between the SC and DR modeling and large magnitudes and high rupture speed in dynamic rupture scenarios (van Zelst et al., 2019). In contrast, we here constrain fracture energy independently from the long-term model. In Madden et al. (2020), a different long-term geodynamic and seismic cycle simulation was used, specifically, assuming different shear moduli. We here change the geometrical 3D extrapolation of the 2D fault geometry compared to the large blind dynamic earthquake scenario of $M_W$9.0 of Madden et al. (2020), to be consistent with empirical earthquake source scaling relations for $M_W$8.5 megathrust events (Strasser et al., 2010).

We use complex 3D dynamic rupture modeling to first study trade-offs and effects of along-strike unilateral versus bilateral rupture and variations in hypocentral depth in subduction zone earthquakes (McGuire et al., 2002). By varying the hypocentral location along arc and along depth, we generate 12 distinct unilateral and bilateral earthquakes with depth-variable slip distribution, rupture direction, bimaterial and geometrical effects in the dynamic slip evolution. We analyse the consequent time-dependent variations in seafloor uplift affecting tsunami propagation and inundation patterns. We define as reference model a bilateral, deeply nucleating earthquake. To this reference model we add a complex and more realistic coastline in the tsunami simulation and study the effects on tsunami arrival time and wave height at the coast.

The linkage from long-term geodynamic to co-seismic dynamic rupture modeling requires assumptions with respect to the incompressibility and visco-elasto-plastic, plane-strain conditions of the subduction model versus the compressible, elastic conditions of the earthquake model. In two additional scenarios we analyse variations in the energy balance of the subduction-initialized dynamic rupture scenarios. We increase fracture energy in the reference model by changing the frictional critical slip distance within the dynamic rupture model and adapting nucleating energy accordingly. The increase in fracture energy leads to large uplift, low radiation efficiency and low rupture velocities, characterising a tsunami earthquake (Kanamori, 1972). Lastly, we analyze the effect of a higher Poisson's ratio throughout the dynamic rupture reference model and the effect on tsunami genesis and inundation.

This leads to a total of 15 subduction-initialized 3D dynamic rupture-tsunami scenarios: 12 dynamic rupture models with varying hypocenters. For one "reference model" (model 3B) of these 12 we vary fracture energy or Poisson's ratio, or coastline bathymetry.

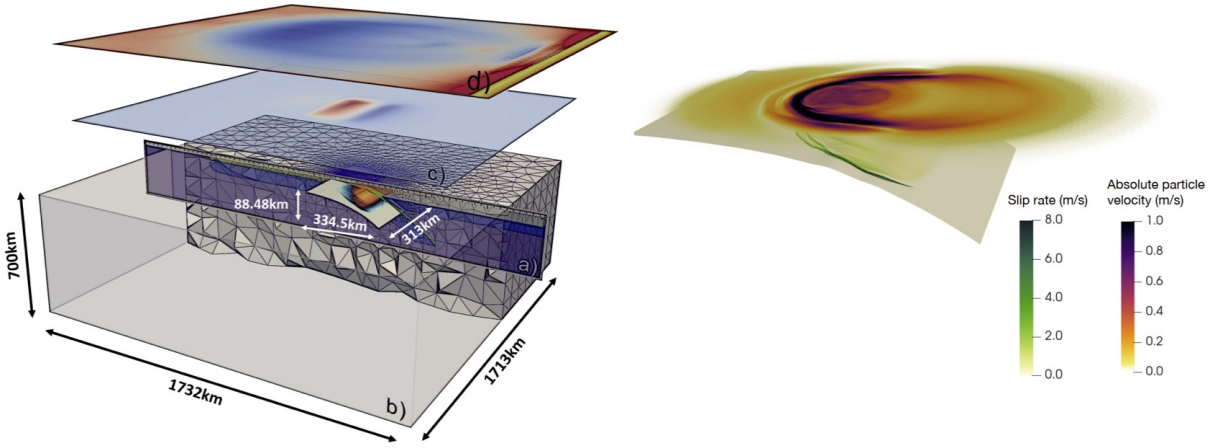



Figure 3.1: **Left:** adapted from Madden et al., 2020 (a) sketch and dimensions of the one-way linked 2D geodynamic subduction model, (b) the 3D dynamic rupture earthquake model, (c) the dynamic rupture seafloor displacement and (d) the 2D tsunami model, modified from Madden et al. (2020). The 3D unstructured tetrahedral mesh of the dynamic rupture model (b) is shown in grey. **Right:** Snapshot of slip rate across the 3D subducting interface (greenish colors) and the seismic wavefield recorded at the free surface in terms of absolute velocity (warm colors). This snapshot is extracted from model 3B after 40 s simulation time.

## 3.2 Methods

Here, we summarize the computational methods used for simulating subduction-initialized dynamic earthquake rupture linked to tsunami generation, propagation and inundation (Fig. 3.1). For an in-depth description of the virtual laboratory for modeling tsunami sources arising from 3D co-seismic seafloor displacements generated by dynamic earthquake rupture models, we refer to Madden et al. (2020). We compute 3D dynamic earthquake rupture and seismic wave propagation with SeisSol (`https:/seissol.org`). Tsunami propagation and inundation uses sam(oa)$^2$-flash, which is part of the open source software sam(oa)$^2$ (`https://gitlab.lrz.de/samoa/samoa`). Both codes use highly optimized and parallel implementations of discontinuous Galerkin (DG) schemes. All simulations were performed on SuperMUC-NG at the Leibniz Supercomputing Centre Garching, Germany.

To link input and output data in massively parallel simulations, we use ASAGI (pArallel Server for Adaptive GeoInformation), an open source library with a simple interface to access Cartesian material and geographic datasets (Rettenberger et al. (2016), `www.github.com/TUM-I5/ASAGI`). ASAGI translates a snapshot of the 2D subduction model into 3D initial conditions for the earthquake model and bathymetry data and seafloor displacements from the earthquake model into initial conditions for the tsunami model. ASAGI organises Cartesian data sets for dynamically adaptive simulations by automatically migrating the corresponding data tiles across compute nodes as required for efficient access.

### 3.2.1 3D earthquake dynamic rupture modeling with SeisSol

Physics-based 3D earthquake modeling captures how faults yield, slide and interact (e.g. Ulrich et al., 2019a; Palgunadi et al., 2020) and can provide mechanically viable tsunami-source descriptions (Ryan et al., 2015; Ma and Nie, 2019; Ulrich et al., 2019b, 2022). We use SeisSol (de la Puente et al., 2009; Pelties et al., 2012, 2014) to solve simultaneously for frictional failure across prescribed fault surfaces and high-order accurate seismic wave propagation in space and time (illustrated in Fig. 3.1, right). SeisSol uses a discontinuous Galerkin (DG) scheme with Arbitrary high-order DERivative (ADER) time stepping on unstructured tetrahedral grids with static mesh adaptivity (Dumbser and Käser, 2006; Käser and Dumbser, 2006) . It is thereby particularly suited for modeling complex geometries such as those in the vicinity of subducting slabs. SeisSol is optimized for current petascale supercomputers (Breuer et al., 2014; Heinecke et al., 2014; Rettenberger et al., 2016; Uphoff and Bader, 2020; Dorozhinskii and Bader, 2021) and uses an efficient local time-stepping algorithm (Breuer et al., 2016; Uphoff et al., 2017; Wolf et al., 2020). Its accuracy is verified against a wide range of community benchmarks (Harris et al., 2011, 2018), including dipping and branching faults with heterogeneous off-fault material and initial on-fault stresses (Pelties et al., 2014; Wollherr et al., 2018; Gabriel et al., 2020). We note that on-fault initial conditions such as frictional parameters or initial fault stresses are assigned with sub-elemental resolution (at each DG Gaussian integration point). However, within each off-fault element, all material properties are constant. We create a 3D

complex structural model in GoCad (Holding, 2018) and discretize it with the meshing software Simmodeler by Simmetrix (Simmetrix Inc., 2017).

Within SeisSol, frictional failure is treated as an internal boundary condition for which the numerical solution of the elastodynamic wave equation is modified. In the dynamic rupture scenarios of our study, fault strength, i.e. its yielding and subsequent frictional weakening, is governed by the widely adopted linear slip weakening (LSW) friction law (Ida, 1972). Over a critical slip weakening distance $D_c$ the effective friction coefficient $\mu$ decreases linearly from static $\mu_s$ until reaching dynamic $\mu_d$. We note that this is different to the rate-weakening friction used in the long-term geodynamic SC model. The process zone width is the inherent length scale defining the minimum resolution required on-fault, and is defined as the area behind the rupture tip in which shear stress decreases from its static to its dynamic value (Day et al., 2005).

### 3.2.2 Subduction seismic cycle modeling for earthquake initial conditions

Figure 3.2 depicts the inferred 3D initial conditions from the subduction seismic cycle model for all dynamic rupture scenarios. These include highly heterogeneous initial shear stress and strength as well as fault geometry and material structure that together govern earthquake nucleation, propagation and arrest. The underlying 2D seismo-thermo-mechanical geodynamic seismic cycle (SC) model simulates subduction dynamics over millions of years and earthquake cycles over several hundreds of years (e.g., Van Dinther et al., 2013, 2014) (Fig. 3.2, a). The long-term phase of the simulation builds up stress as well as self-consistent strength and fault geometries across the subduction interface and fore-arc. The geodynamic SC model includes 70 megathrust events that rupture almost the entire fault and nucleate near the downdip seismogenic zone limit. The same representative event as in van Zelst et al. (2019) is here chosen and linked to the newly designed dynamic rupture model applying the techniques described in Madden et al. (2020). We note, that at the chosen SC time step, the dominant deformation mechanism in the seismogenic zone is elastic behavior, which is consistent with the deformation mechanism in the dynamic rupture model. All material properties, stresses and fault geometries are exported from the SC model at that timestep. Material density and fault strength can be adapted to be used in the DR model. Cohesion varies between 2.5 MPa and 20 MPa and increases with deeper lithologies. At nucleation depth, cohesion is set to 5 MPa. The curved, blind megathrust interface evolves during this slip event and is characterized by large-scale fault roughness including characteristic topographic highs ("bumps") in terms of a distinct change in local gradients of the curved non-planar interface related to sediment intrusion on geodynamic time scales (zoom-in box of Fig. 3.2, a).

In contrast to van Zelst et al. (2019) and Madden et al. (2020), the critical slip weakening distance $D_c$ is here not inferred from the geodynamic SC model directly but is assigned to be a constant value ($D_c$=0.1 m for 13 out of 14 dynamic rupture models) along the entire fault. Increasing the critical slip weakening distance $D_c$, over which effective fric-

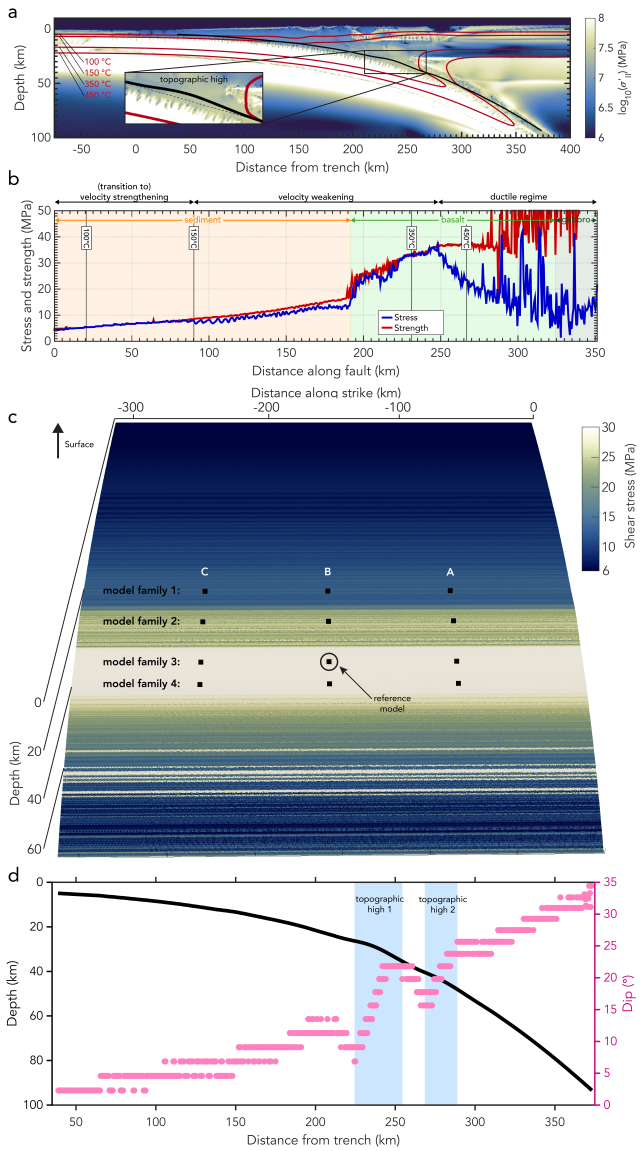



Figure 3.2: Subduction model initial conditions for the dynamic rupture earthquake simulations. **a)** Snapshot of stresses evolving during the 2D long-term geodynamic subduction and seismic cycle simulation at the time-step right before a slip event occurs (adapted from (van Zelst et al., 2019)). The stresses are expanded to the third dimension assuming plane strain conditions. **b)** On-fault shear stress and fault strength in the SC model at the coupling time-step. The fault yields and failure occurs when both align. **c)** Pre-processed (see text) initial shear stress in the three-dimensional dynamic rupture model at timestep t=0 s in the DR model. The black squares indicate nucleation locations that are used for model families 1–4. The hypocenter of the reference model 3B is marked. **d)** Fault geometry in 2D and dip angle of the fault. Regions of increasing dip are highlighted in blue and indicate local topographic highs (1 and 2) in the fault plane.

tion is reduced to its dynamic value, results in a higher fracture energy $G_c$ according to $G_c = 1/2\mu_s P_n - \mu_d P_n D_c$ with $P_n$ being the initial fault normal stress (Venkataraman and Kanamori, 2004). The fracture energy consumed within the frictional process zone indicates how much energy is necessary to initiate and sustain rupture propagation. A high fracture energy results in higher fault slip, higher stress drop and a higher moment magnitude for comparable dynamic rupture scenarios (given the nucleation energy is adopted accordingly). In one model, model 5, we triple the model-wide constant $D_c$ from 0.1 m to 0.3 m while keeping all other parameters constant, thus, tripling fracture energy.

All material properties are extrapolated into the third dimension as constant along arc, for simplicity. We use a plane strain assumption, as in the 2D subduction model, to determine the out-of-plane normal and shear stress components in 3D. This implies that we omit eventual oblique subduction components by setting the out-of-plane shear stresses to zero and the out-of-plane normal stress component to be a function of the two in-plane normal stresses and Poisson's ratio $\nu$. In the SC subduction model a Poisson's ratio of $\nu = 0.5$ is used, which is an appropriate assumption for large time scales. This Poisson's ratio needs to be reassigned within the DR model to represent compressible rocks and to solve the linear elastic wave equations. The choice of $\nu$ affects the material properties as they are transferred from the subduction model to the earthquake model since Lame's parameter is calculated from the re-assigned $\nu$ and the shear modulus $G$ is taken from the subduction model. In all besides one dynamic rupture models we assume $\nu = 0.25$ (Poisson solid, $\lambda = G$). In one 3D dynamic rupture (model 6, modified from reference model 3B), we use a larger Poisson's ratio of $\nu = 0.3$, which is in the range observations of basaltic rocks (Gercek, 2007).

Using the imported on-fault conditions from the geodynamic SC model directly would lead to multiple locations of instantaneous failure on the fault (Fig. 3.2b). We thus use a pre-processing static relaxation step in which we relax the initial fault loading stresses to be just below fault strength before applying them to the DR model following Wollherr (2018). Spontaneous earthquake rupture is commonly initialized by assigning an overstressed or frictionally weaker predefined hypocentral "nucleation" area. We here assign a locally lower static friction coefficient within a circular patch of an empirically determined minimum required size to initiate spontaneous rupture. We choose frictional coefficients $\mu_s$ and $\mu_d$ within this patch constrained from the geodynamic SC model. We prescribe all but the shallowest (model family 1) hypocentral nucleation depths at locations which are close to failure (low strength excess, Fig. 3.2 b) in the SC model. The reference geodynamic SC slip event nucleates at 40 km depth, corresponding to model family 3 in this study.

### 3.2.3 Tsunami and inundation modeling with Samoa

Tsunami are modeled with a limited second order Runge-Kutta discontinuous Galerkin solver (Cockburn and Shu, 1998; Giraldo and Warburton, 2008) for the two dimensional depth-integrated hydrostatic non-linear Shallow Water Equations (SWE, LeVeque et al. (2011)) in the sam(oa)$^2$-flash framework Madden et al. (2020). The SWE are a simplification of the incompressible Navier-Stokes equations, under the assumption that vertical

scales are negligible compared to horizontal scales. As a result, hydro-static pressure and the conservation of mass and momentum are part of the equations, while vertical velocity and turbulence are neglected. Manning friction is included in the model with an additional source term (Liang and Marche, 2009). To allow accurate and robust wetting and drying, the model uses a Barth-Jaspersen type limiter that guarantees the conservation of steady states (well-balancedness), mass conservation and positivity preservation of the water-depth (Vater and Behrens, 2014; Vater et al., 2015, 2019).

The framework sam(oa)$^2$-flash simulates hyperbolic PDEs on dynamically adaptive triangular meshes (Meister et al., 2016). It is based on the Sierpinsky Space filling curve, which allows cache efficient traversals of mesh-cells and -edges with a stack and stream approach. Cell-level adaptive mesh refinement in every time step and a water-depth based refinement criterion, allow for multiple levels of refinement for the tracking of wave fronts and other areas of interest (i.e. coasts). While tsunami are usually sourced by setting a perturbation to the seafloor and water surface as initial condition, sam(oa)$^2$-flash can include the full spatio-temporal evolution of the seafloor displacement in the simulation. sam(oa)$^2$-flash has been validated against a suite of benchmarks (Synolakis et al., 2008).

### 3.2.4 Dynamic rupture modeling for tsunami initial conditions

The time-dependent seafloor displacement generated in the dynamic rupture model is used as input for the tsunami model. Since these displacements are written in form of a triangular unstructured grid by SeisSol, rasterization is required to obtain a regular grid that can be read by sam(oa)$^2$-flash . The resulting grid is comprised of rectangular cells of size $\Delta x \times \Delta y = 500$ m $\times$ 500 m. The geometric center of each cell is used to sample the triangular grid using a nearest-neighbor approach. Since all our examples share a relatively large source area and a short process-time, compared to the ocean depth (2 km), we here omit corrections required for landslide-induced tsunami (Kajiura, 1963) and neglect the effects of water flow from seafloor to seasurface (Saito and Furumura, 2009; Wendt et al., 2009). We directly use the seafloor deformation as time-dependent (or static, for comparison) initial seasurface perturbation.

The seafloor deformation data contains the seismic wavefield and the dominant static displacement, which remains unchanged after dynamic rupture propagation ceased since we do not account for post-seismic relaxation. Saito et al. (2019) shows that seismic waves have an effect on tsunami generation, but do not affect the solution in the far field. However, our earthquake scenarios also include reverberating seismic waves, e.g., trapped within the accretionary wedge. Simulating long enough for such complex seismic waves to stop imprinting on the time-dependent near-source seafloor deformation requires significantly longer simulation times. We here limit computational costs by stopping the DR earthquake simulation after the fault stopped slipping and the dominant static displacement remains constant. We apply the time-dependent seafloor deformation to source the tsunami model during that period and keep the seafloor elevation constant afterwards. In the presence of transient seismic waves, however, this approach may lead to artifacts such as spurious gravity-waves in the tsunami simulation. Thus, we here remove reverberating seismic waves

using a filter-based approach on the seafloor perturbation.

We apply a Fourier filter approach that we base on an analytical test-bed in which we can separate the significant frequency-wavenumber coefficients of the permanent displacement from the ones of seismic waves (Madden et al., 2020). In the wavenumber representation for the displacement field we can identify the coefficients belonging to seismic waves clearly as radial symmetric lines in the wavenumber space.Our analytical test-bed confirms that these lines propagate in the frequency-wavenumber domain with the inverse velocity with which seismic waves propagate in time and space. Coefficients of the permanent displacement on the other hand are dominant close to the origin. To erase seismic waves from the seafloor perturbation we design a kernel to zero-out the radial symmetric waves in the frequency-wavenumber representation depending on their velocity. Close to the origin we leave the representation as it is, to keep the dominant coefficients of permanent displacement. To avoid rolling effects, the kernel is smoothed. As a result, seismic waves of chosen frequencies are effectively damped in the time-dependent displacement field. The effects of seismic wave damping on the permanent displacement are negligible.

## 3.3 Earthquake and tsunami model setup

### 3.3.1 3D heterogeneous megathrust dynamic rupture models

In DR modeling, rupture can only propagate across predefined fault interfaces. In distinction, fault geometry spontaneously arises during slip events in the SC model. The fault geometry for the chosen slip event at the coupling time step is shown in Fig. 3.2a. The locations of the highest visco-plastic strain rate represent the fault. A moving average scheme is used to smooth this 2D fault geometry, which is then uniformly extruded along-arc to construct the 3D DR fault plane (van Zelst et al., 2019; Madden et al., 2020). The 3D dynamic rupture fault (Fig. 3.2c) does not intersect the surface but ends ≈5 km below the seafloor and extends to 93.5 km depth. The fault length in the along-arc y-direction is chosen to agree with the average scaling of the source dimensions of interface and intraslab subduction-zone earthquakes with moment magnitude (Strasser et al., 2010). We here aim to model typical-size tsunamigenic earthquakes of magnitudes close to $M_W$=8.5, and thus choose a fault width of ≈313 km. The curved fault is characterized by large scale roughness. Noticeable are two topographic highs shown in terms of sharp increases of fault dip in Fig. 3.2d. We use a constant element edge length of 1 km along the fault. We ensure that this element size along the fault is sufficient to capture the median process zone width following all error criteria of (Day et al., 2005) in a series of models with different size elements following the analysis in (Wollherr et al., 2018). We measure the median process zone width as 1,386 m for the reference model 3B and 1,224 m for model 1B. For a polynomial basis function of order $p = 5$ (Wollherr et al., 2018) estimate the minimum required resolution to be 1.65 elements per median process zone width. A polynomial basis function of $p = 5$ leads to 6th order numerical accuracy in space and time in the seismic wave propagation solution. We note that each tetrahedral element fault interface is dis-

cretized by $(p+2)^2$ Gaussian points. In we detail two exemplary higher resolution versions (h=500 m, p=5) of the reference model 3B and of model 1B which has the shortest median process zone width. Compared to the coarser resolution of h=1 km, we quantify the error to be <1% for the maximum vertical seafloor displacement, <6% for the rupture velocity, <5% for the average peak slip rate and <2.5% for the average fault slip which agree with the criteria for well-resolved models by Day et al. (2005). We note that in contrast to the simple depth-dependent setup in Wollherr et al. (2018), the peak slip rate and not the average fault slip is most sensitive here.

The 3D model domain extends from x=-657 km to x=1075 km and y=-1023 km to y=700 km and to a depth of z=-700 km. The large model size prevents that waves reflected from non-perfect absorbing boundary conditions interfere with the rupture itself. To limit computational cost, the unstructured tetrahderal mesh is statically coarsened. The sea floor is flat in the DR model (but not in the tsunami simulations) and assigned a free surface boundary condition. The mesh size is 7.8 million elements. Each simulation took 1:10 hours on 75 nodes, with 48 Intel Xeon Skylake cores each, of Supermuc-NG.

To analyze the effects of material directivity and complex initial conditions, as well as uni- and bilateral rupture behaviour in the DR models, and the resulting tsunami, we vary the hypocenter location along arc and depth. We choose fault locations which are close to failure in the 2D SC model, at 30 km, 40 km and 45 km depth (Fig. 3.2 b). To analyze shallower earthquake nucleation locations, we additionally nucleate 3D DR scenarios at 25 km depth (Fig. 3.2 c). The reference dynamic rupture model (Model 3B) is nucleated at the origin location of the slip event in the SC model, that is, at a depth of 40 km and at the centre of the fault along strike (x=267.25 km, y=-156.5 km). The static friction coefficient is reduced to $\mu_s = 0.019$ within a patch of radius 2 km, which represents the minimum value in the SC model within the nucleation area (Tab. 3.1). For all earthquake model families, the assigned nucleation parameters, that is locally reduced static friction coefficients $\mu_s$ and patch radii $r$, are listed in Table 3.1. To evaluate effects in lateral direction, we move the hypocenter from y=-156.5 km (fault width center) to y=-78.25 km (25% of the fault width) and y=-234.75 km (75% of the fault width), exploring observational and statistical inferences of large ruptures being predominantly unilateral or bilateral (McGuire et al., 2002; Mai et al., 2005) (see Fig. 3.2 c). We note that larger nucleation energy (larger radii, lower local strength) are required in fault regions further from failure than the reference model (hypocentral depth of 40 km).

### 3.3.2 Tsunami model setup

The tsunami modeling area extends from x=-600 km to x=600 km and from y=-750 km to y=450 km, the ocean depth being at a constant 2 km. A linearly sloping beach is placed with its toe at x=500 km with an inclination of 5%, which results in the coastline being located at x=540 km in most models (see Fig. 3.3, left). We additionally analyze the inundation behaviour along a more realistic coastline in one model (model 4D). To this end a non-linear coastline is included in model 3B (Fig. 3.3, right). We adapt the coastal topo-bathymetry of the Okushiri benchmark (Yeh et al., 1996; Honal and Rannabauer,

2020) and stretch it along the full y-direction model length. Every tsunami is generated using the time-dependent (dynamic) seafloor displacements generated in the 3D DR models from 0 s to 200 s.

Depending on the used DR model setups, different tsunami modeling refinement levels and output configurations are required. The minimum spatial resolution in sam(oa)$^2$-flash is defined as $\Delta x = \textit{domain-width} \cdot (1/2)^{d/2}$. We use a minimum refinement level of d=18 for all tsunami simulation runs, yielding a minimum spatial resolution of $\Delta$x=2.34 km. To obtain detailed inundation patterns, we use a refinement of d=30 ($\Delta$x=36.62 m) near the coast and a maximum refinement of d=26 ($\Delta$x=146.5 m) in the remainder of the domain. On SuperMUC-NG, these simulations took 2:43 hours on 100 nodes sourced by dynamic displacement. This corresponds to roughly 13,000 CPUh, respectively. Simulation outputs are in general written every 10 s of simulation time. If only sea surface height tracing measurements along a few axes are needed, a run with a maximum refinement of $d = 24$ ($\Delta x = 293.0m$) takes approximately 27 minutes across 100 nodes (2187 CPUh) with dynamic displacement. Output of the full wavefield with a maximum of $d = 24$ took 1:21 hours across 32 nodes (2074 CPUh) for dynamic displacements, writing outputs every 100 s of simulation time between t=0 and t=3000. We note that in all our tsunami models, including a slow "tsunami earthquake", the ratio of tsunami source width / (source time $\times$ tsunami wave speed), in water depth of 2 km is >>1, indicating that the tsunami does not propagate over the source duration (Abrahams et al., 2023). We find differences of up to 10% in the tsunami system energy balance of kinetic and potential energy when comparing static with dynamic sources and source all tsunami in the following from the dynamic seafloor displacement.

## 3.4 Results

### 3.4.1 Dynamic rupture models

We first investigate the effects of varying earthquake hypocenter locations in complex subduction initialized dynamic rupture models. We vary the hypocentral depth between 25 km, 30 km, 40 km and 45 km, which resembles one shallow earthquake and three low strength excess regions in the geodynamic subduction and seismic cycle model. It has been inferred that hypocenters of large earthquakes are not arbitrarily distributed across fault planes, but located closeby regions of large slip (Mai et al., 2005). Additionally, large subduction zone events may propagate preferably unilateral (McGuire et al., 2002) or bilateral (Mai et al., 2005) and rupture dynamics of subduction earthquakes may be significantly affected by bimaterial contrasts (Ma and Beroza, 2008). In our 12 scenarios listed in Table 3.1, different hypocenter depths lead to pronounced differences in dynamic rupture propagation. The models differ in their propagation direction, slip rates and rupture velocities, and include localized supershear rupture at different simulation times and fault locations.

Figs. 3.4, 3.5 and 3.6 compare snapshots of slip rate and rupture velocity as well as

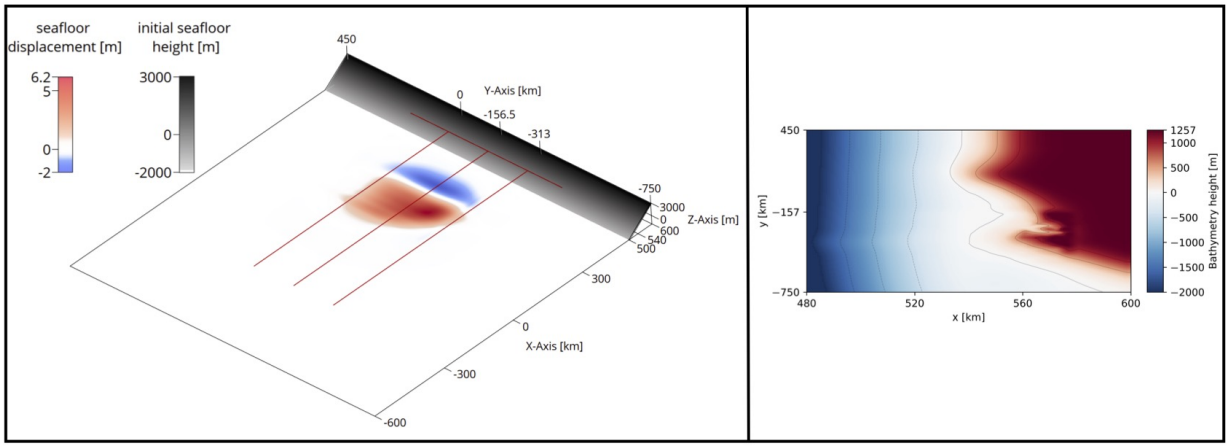



Figure 3.3: **Left:** Sketch of the tsunami model setup for most scenarios for sam(oa)$^2$-flash with a linearly sloping beach starting at x = 500 km. Red and blue colors are an exemplary snapshot of seafloor uplift and subsidence resulting from a DR model that are used to source the tsunami model. **Right:** Zoom-in of the non-linear height profile of the complex beach used in one tsunami scenario (model 4.D) adapted from the Okushiri benchmark. The position and slope are designed to be comparable to the linear beach (left). The depth profile is illustrated by blue and red colors. Contour lines are shown every 500m.

the accumulated fault slip of all 12 models. Animations of slip rate are provided in the electronic supplement. Table 3.2 summarizes all rupture characteristics.

In model family 1 (shallowest hypocenter) nucleation is initiated at a depth of 25 km which is located above topographic high 1 on the megathrust. We observe complex dynamic rupture behaviour, including supershear transition at topographic high 2, localized high slip rates within the fault depression and reactivation of fault slip at a late stage. Rupture propagates at low slip rates before reaching the edge of the first topographic high, where the slip rate increases. As the main rupture front hits the second topographic high (10 s), supershear rupture initiates in downdip direction (Fig. 3.4).

For model family 2, we observe complex downdip propagating dynamic rupture behaviour with supershear rupture being triggered at the second topographic high. The hypocenter is located at the edge of topographic high 1 (Fig. 3.2). As the rupture front passes topographic high 1, slip rate increases, similar to model family 1. Supershear rupture is triggered in downdip direction at 15 s simulation time (Fig. 3.4 and 3.5 ).

The nucleation location in model family 3 corresponds to spontaneous failure in the 2D SC model. It is located on the lowermost point of the geometric depression of the fault, at 40km depth. Slip evolves circularly and propagates away from the hypocenter. After 8 s simulation time, supershear rupture initiates in updip direction at topographic high 1 (see Fig. 3.4 and 3.5).

For model family 4, the hypocenter was placed at a depth of 45 km, which lies at the edge of the second topographic high. A circular rupture front evolves during 9 s simulation

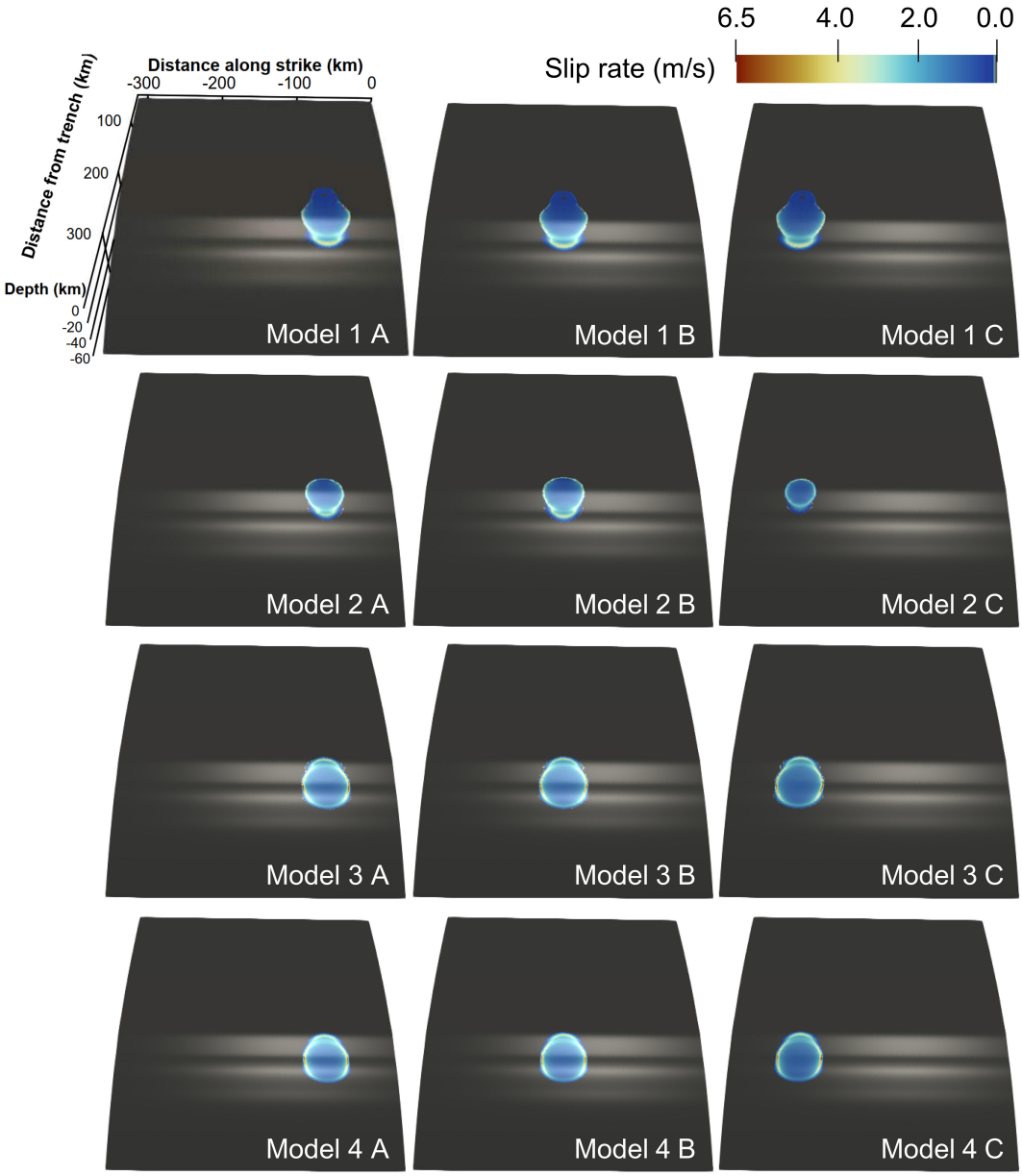



Figure 3.4: Slip rate at the timestep t=12 s (model 1), t=16 s (model 2), t=10 s (model 3) and t=14 s (model 4), capuring down-dip and up-dip propagating supershear rupture being triggered by one of the two topographic highs in the fault geometry depending on hypocentral depth. The white reflections highlight the uneven geometry of the fault. The hypocentral locations vary with depth (25 km, 30 km, 40km and 45km) and laterally on the fault (y=-78.25 km, y=-156.5 km, y=-234.75 km). For model 1 and 2 supershear rupture evolves in downdip direction, whereas for model 3 and 4 in updip direction.

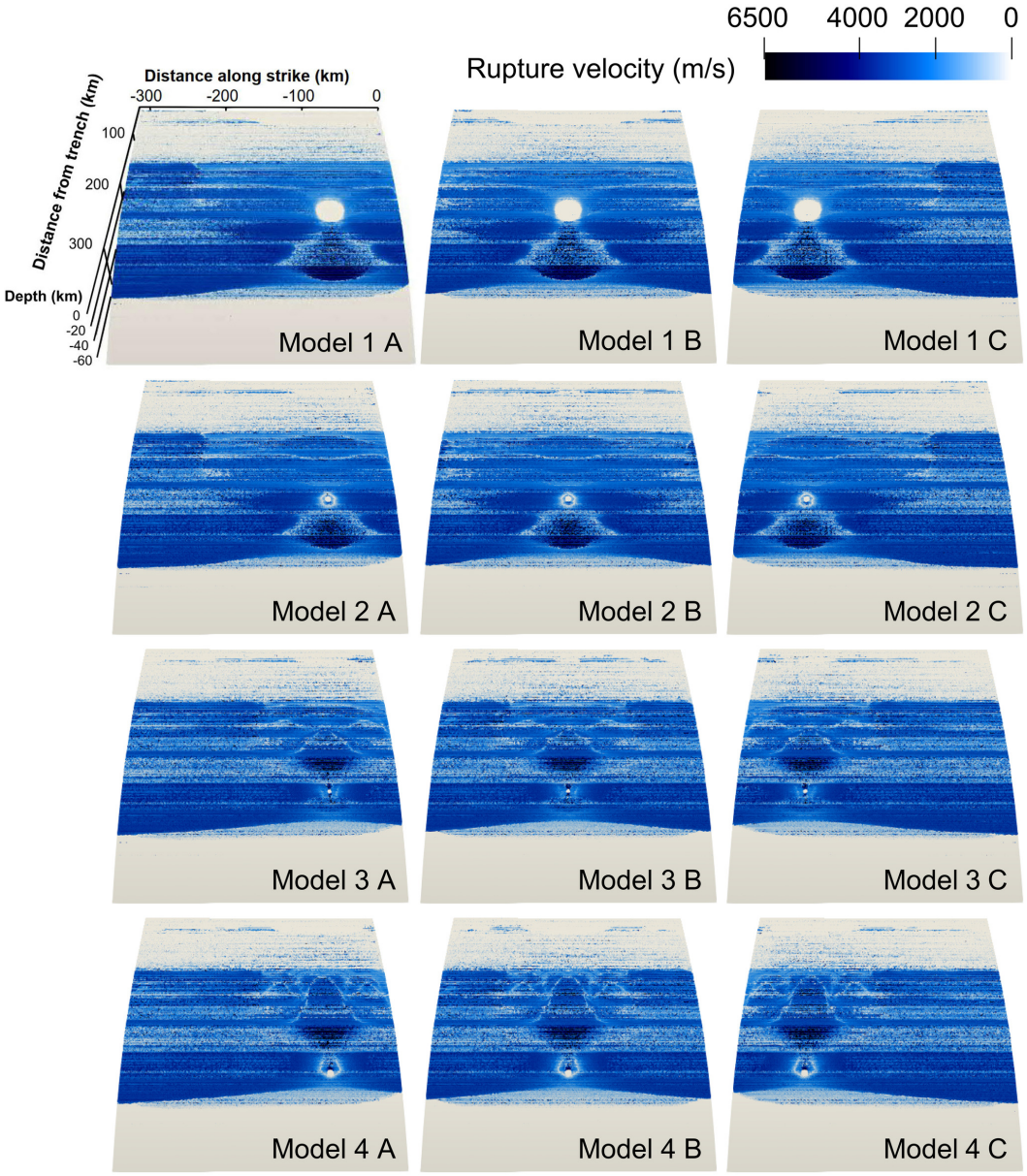



Figure 3.5: Rupture velocity for 12 dynamic rupture simulations with varying hypocenter locations. Note the difference in nucleation radii according to Table 3.1. Most parts of the fault rupture at speeds around 3000m/s. Much lower velocities are visible in the shallower fault part. Supershear rupture is visible as dark blue areas in downdip direction for nucleation locations at a depth of 25 km and 30 km and in updip direction for nucleation depths of 40 km and 45 km. The rupture velocity is very inhomogeneous due to the complex and heterogeneous material properties on the fault.

Table 3.1: Model families 1 - 4 defined by hypocentral location. Each model family includes three dynamic rupture scenarios with varying lateral hypocenter location (A - C). Nucleation characteristics vary between the dynamic rupture model families. The material properties that are imported from the seismic cycle model and used as initial conditions vary with depth. Thus, different static friction coefficients and radii have to be chosen to enable nucleation at different depths. Model 5 is adapted from the reference model 3B friction law with higher fracture energy. Model 6 is the reference model 3B with a higher Poisson's ratio of 0.3.

| **Model family** | **Hypocenter Depth [km]** | **Radius nucleation zone [km]** | **Static Friction Coeff.** |
|---|---|---|---|
| Model 1 | 25 | 15.0 | 0.013 |
| Model 2 | 30 | 3.3 | 0.019 |
| Model 3 | 40 | 2.0 | 0.019 |
| Model 4 | 45 | 3.5 | 0.019 |
| Model 5 | 40 | 10.0 | 0.019 |
| Model 6 | 40 | 1.8 | 0.019 |

time. Supershear rupture arises in updip direction after 13 s, when the rupture front hits the first topographic high (Fig. 3.4 and 3.5).

In all 12 models, rupture fronts reach the lower limit of the seismogenic zone at x=282.25 km after passing the second topographic high. In the SC model, ductile behaviour begins to dominate here which is expressed as strength increase in the DR model. Rupture propagation is spontaneously arrested at this depth. Thus in all 12 models, slip stops at the same depth. At the lateral edges of the prescribed megathrust fault, rupture is geometrically stopped, and no tapering of initial stress or strength is applied. Close to the surface, in the shallowest part of the fault, the sedimentary region allows for small slip while smoothly stopping rupture.

Bilateral rupture evolution appears to be symmetrical for centered hypocenters, despite bimaterial contrasts above and beneath the fault potentially affecting strike-slip faulting contributions (Harris and Day, 2005). For asymmetric hypocenter locations (models A and C of each model family), unilateral dynamic rupture propagation is identical to bilateral models within the first seconds until stopping phases from the closer fault edge affect rupture dynamics. In both cases (A and C), rupture dynamics appear minor symmetric with slight bimaterial effects (see rupture characteristics summarized in Table 3.2). Larger slip is accumulated at the respective far side of the fault (Fig. 3.6). The highest absolute slip is observed in the models with hypocenter locations at y=-234.75 km (C models) and the lowest absolute fault slip is observed for models with hypocenters placed in the center of the fault (B models).

In all 12 models we observe localized weak reactivation of slip after approximately 100 s simulation time due to dynamic triggering caused by trapped waves. Waves are trapped within the accretionary wedge between the uppermost part of the fault and the surface

| | **Model 1** | | | **Model 2** | | |
|---|---|---|---|---|---|---|
| | 1.A | 1.B | 1.C | 2.A | 2.B | 2.C |
| Lateral hypocenter location [km] | −78.25 | −156.5 | −234.75 | −78.25 | −156.5 | −234.75 |
| Max. absolute fault slip [m] | 33.13 | 32.40 | 33.31 | 33.21 | 32.43 | 33.39 |
| Mean absolute fault slip [m] | 15.29 | 15.27 | 15.31 | 15.20 | 15.16 | 15.24 |
| Max. peak slip rate [m/s] | 26.61 | 26.75 | 26.71 | 27.29 | 27.18 | 27.19 |
| Mean peak slip rate [m/s] | 4.11 | 4.24 | 4.08 | 4.11 | 4.21 | 4.09 |
| Magnitude [1] | 8.88 | 8.88 | 8.88 | 8.88 | 8.88 | 8.88 |
| Mean rupture velocity [m/s] | 2083 | 2042 | 2086 | 2134 | 2095 | 2137 |
| Mean stress drop [MPa] | 5.19 | 5.23 | 5.16 | 5.10 | 5.12 | 5.08 |
| Seafloor displacement [m] | 4.58 | 4.54 | 4.58 | 4.59 | 4.58 | 4.61 |
| Tsunami potential [TJ] | 3018.81 | 3078.00 | 3026.03 | 2995.31 | 3062.01 | 3003.95 |
| | **Model 3** | | | **Model 4** | | |
| | 3.A | 3.B | 3.C | 4.A | 4.B | 4.C |
| Lateral Hypocenter Location [km] | −78.25 | −156.5 | −234.75 | −78.25 | −156.5 | −234.75 |
| Max. absolute fault slip [m] | 33.80 | 32.82 | 34.23 | 33.82 | 32.91 | 34.31 |
| Mean absolute fault slip [m] | 15.51 | 15.63 | 15.54 | 15.73 | 15.92 | 15.75 |
| Max. peak slip rate [m/s] | 23.69 | 24.12 | 24.36 | 23.06 | 23.27 | 23.41 |
| Mean peak slip rate [m/s] | 4.08 | 4.15 | 4.07 | 4.04 | 4.12 | 4.02 |
| Magnitude [1] | 8.88 | 8.87 | 8.88 | 8.88 | 8.89 | 8.88 |
| Mean rupture velocity [m/s] | 2119 | 2124 | 2118 | 2116 | 2120 | 2115 |
| Mean stress drop [MPa] | 5.13 | 5.16 | 5.12 | 5.23 | 5.28 | 5.27 |
| Seafloor displacement [m] | 4.66 | 4.60 | 4.64 | 4.66 | 4.62 | 4.67 |
| Tsunami potential [TJ] | 3045.13 | 3133.15 | 3052.87 | 3067.32 | 3149.63 | 3074.53 |

Table 3.2: Dynamic rupture and tsunami characteristics for model 1 to 4 with centered and lateral varying hypocenter locations.

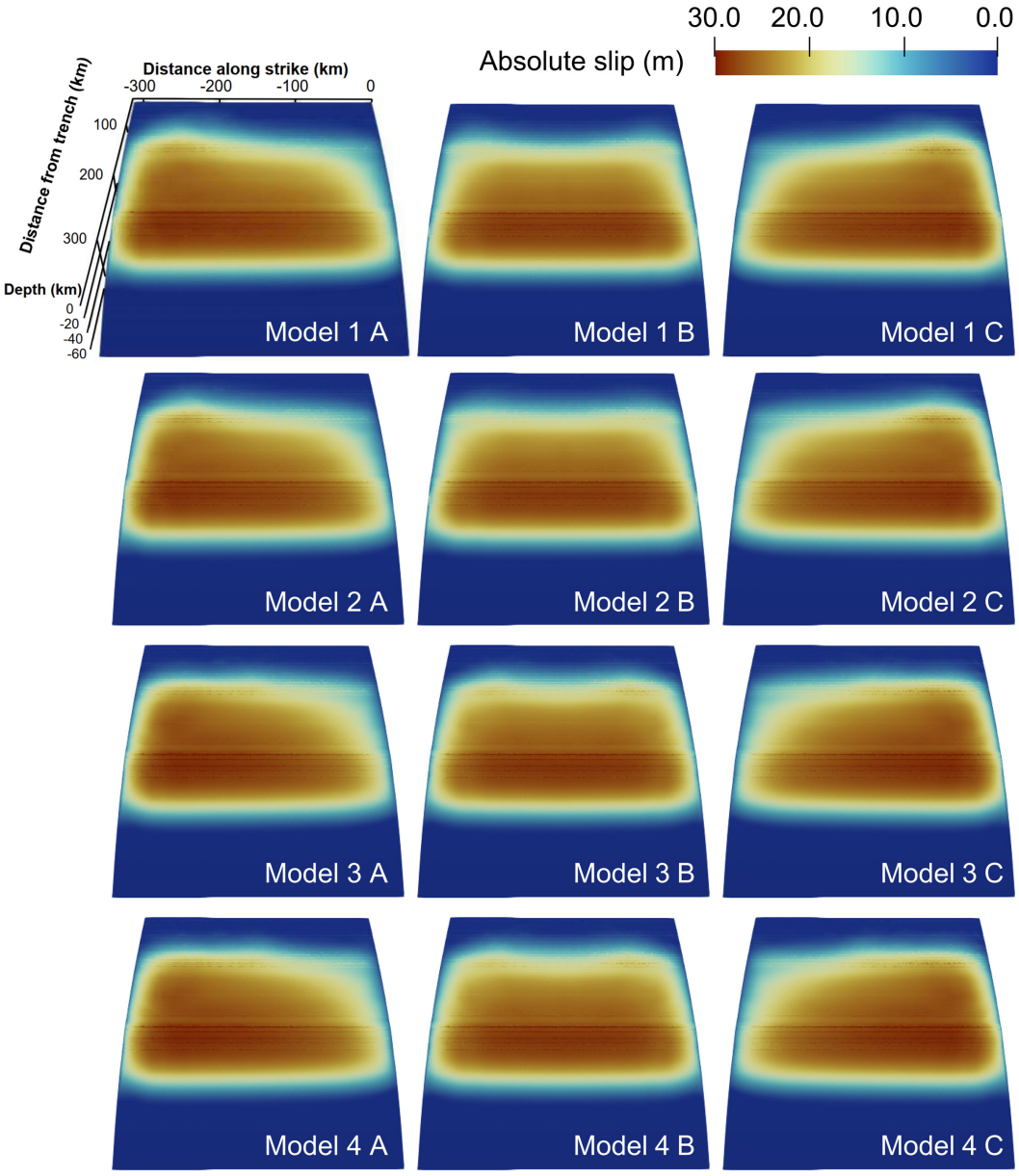



Figure 3.6: Accumulated fault slip at the end of the simulation, after 200s for 12 dynamic rupture models. The hypocenter locations vary with depth (25 km, 30 km, 40 km and 45 km) and laterally on the fault (y=-78.25 km, y=-156.5 km, y=-234.75 km).

until the end of the simulation (200 s). They are reflected at the free surface boundary and propagate back to the fault, which leads to very small amounts of shallow slip in the order of centimeters. As noted before, in the tsunami linking step any artificial contributiion of these waves to seafloor displacements will be filtered.

Across all 12 models, the highest peak slip rate (PSR) occurs on the lower part of the fault, inside the geometric depression at ≈40 km depth, and spread out in along-strike direction (Table 3.2). Model family 2 produces the highest PSR (model 2A, 27.29 m/s). Deeper earthquakes produce lower peak slip rates, such that the earthquakes with the deepest hypocenter (model family 4) exhibits the lowest PSR (model 4A, 23.06 m/s). Along-arc, PSR first increases while rupture propagates away from the hypocenter. Then it decreases due to dynamic interaction with the free surface and other fault edges. At the hypocenter, the PSR is low.

The overall highest absolute slip of 34.31 m is observed for model 4C (see Table 3.2) and the lowest absolute fault slip is observed for model 1B (32.40 m). For models with the same hypocentral depth, the maximum accumulated fault slip is consistently observed when the hypocenter location is located laterally at y=-234.75 km. At the same time, these earthquakes show relatively low peak slip rates. The lowest maximum absolute fault slip for models with the same hypocenter depth is observed for a laterally centered hypocenter. Moment magnitudes vary from $M_W$=8.87 (model 3B) to $M_W$=8.89 (model 4B, Table 3.2).

### 3.4.2 Tsunami simulations

At 200 s simulation time, the filtered vertical seasurface uplift has a maximum of ≈4 m which is located above the buried dynamic rupture fault plane for all 12 models. The sea surface uplift and subsidence reflect the patterns of accumulated slip in Fig. 3.6. Thus, despite the stark dynamic differences in rupture dynamics between the 12 models, including supershear rupture evolution in up- or downdip direction, the static sea surface disturbance is nearly the same. For models of one family, we see lateral differences in the spatial extend of the sea surface uplift which are related to laterally varying hypocenter locations. For models with asymmetric on-fault slip distributions, we observe the same pattern in the sea surface uplift.

After 2300 s simulation time, the tsunami arrive at the coast with wave heights of up to ≈5.5 m. At the coast, we observe differences in the tsunami arrival times for laterally varying hypocenter locations of up to 100 s (Fig. 3.7). The time delay between the tsunami waves caused by an earthquake with a centered hypocenter (B) and an earthquake with a hypocenter located at y=-78.25 km (A) are always some tens of seconds higher than the time delay between events with a centered hypocenter (B) and a hypocenter location of y=-234.75 km (C). We observe only insignificant differences in the tsunami arrival time at the coast with varying hypocentral depths . Tsunami that were generated by deeper earthquakes arrive few seconds later than those being generated by shallower ones.

Figure 3.7 shows the sea surface height (ssh) of the tsunami when arriving at the coast. We observe non-symmetric differences in coastal ssh in dependence of earthquake along-strike hypocentral location. A maximum wave height of ≈5.5 m can be observed in all

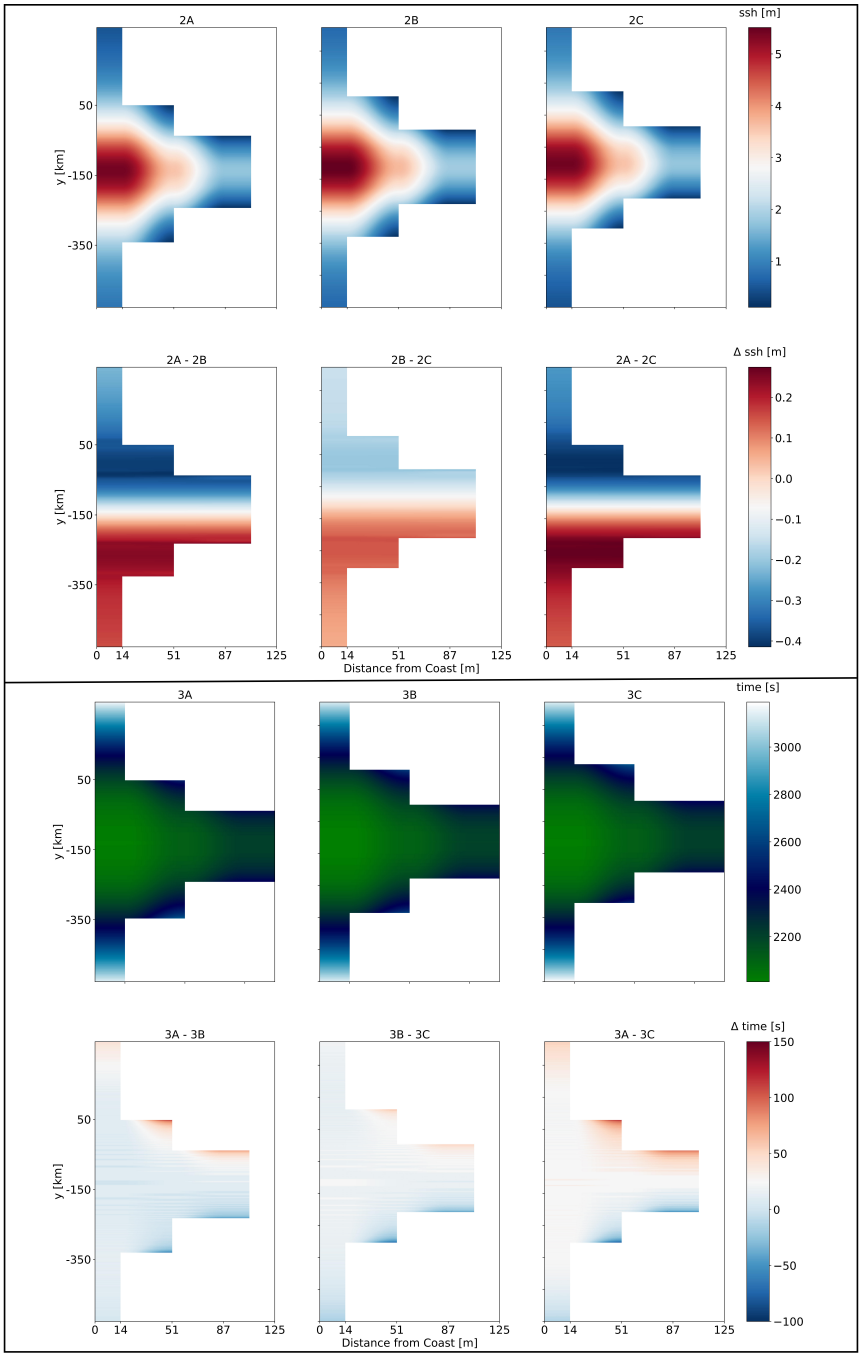



Figure 3.7: **Top:** Comparison of sea surface height (ssh) for tsunami fronts arriving at the coast for the models 2A-2C (upper row). The difference in arrival times between the models is shown as Δssh (lower row). **Bottom:** Inundation comparison for models 3A-3C. The green to white colour scale shows the time delay for the tsunami fronts arriving at the coast (upper row). The difference in inundation between respective models is plotted as Δt (lower row).

12 simulations. The difference in the tsunami height (Δssh) of models with a centered hypocentral location (B) and a hypocenter located at y=-78.25 km (A) present higher values of approximately 0.25-0.4 m than the Δssh of earthquakes with a centered hypocenter location (B) and earthquakes located at y=-234.75 km (C) (Δssh is ≈ 0.1 m). This agrees with the differences in tsunami arrival at the coast. For larger time delays we observe larger differences in the tsunami height accordingly. In summary, comparing all model families 1A-C, 2A-C, 3A-C and 4A-C, the largest difference of 6 cm in coastal seasurface heights can be observed between the shallowest earthquakes (models 1A-C) and earthquakes nucleating at 40 km depth (models 3A-C).

We calculate the potential energy transferred by the earthquake rupture to the sea surface (the "tsunami potential energy")(Melgar et al., 2019; Crempien et al., 2020):

$$E_T = \frac{1}{2}\rho g \int\int_A \eta^2 dA, \tag{3.1}$$

where $\eta$ is the vertical, static sea-floor deformation of the DR model (corresponding to the sea surface heights after 200 s shown in Tab. 3.2 and 3.3), with a water density of $\rho$=1000$kg/m^3$ and the gravitational acceleration being $g$=10$m/s$. The deepest earthquake (model 4B) produces the highest tsunami potential with ≈3150 TJ which marginally differs from the tsunami potential of model 3B (Tab. 3.2). The tsunami resulting from shallower hypocenter depths (models 1B and 2B) have slightly smaller tsunami potentials of 3078 TJ and 3062 TJ. Within model families 1 and 2, a centered hypocenter location leads to the highest tsunami potential, while for model family 3 and 4, the centered hypocenter causes the smallest tsunami potential. Within each model family, tsunami simulations with a hypocenter location at y=-78.25 km (A) always present lower tsunami potentials than models with hypocenter locations at y=-234.75 km (C).

### 3.4.3 Tsunami simulation with complex coastal topo-bathymetry

We perform an additional tsunami simulation, model 3D, which is adapting model 3B by replacing the linearly sloping beach with a complex coastline (see Fig. 3.3, right). We adapt the coastal topo-bathymetry of the Okushiri benchmark (Honal and Rannabauer, 2020) and stretch it along the full y-direction model length (Sec. 3.3.2). The resulting seasurface height and inundation area are displayed in Figure 3.8. Tsunami inundation is observed along the entire length of the coast. While the coastal parts at the far-ends of the domain are hit by a shallow wave of approximately one or two meters, its central part is hit by high wave amplitudes of up to 8 m. In this model, the tsunami amplitudes are ≈2.5 m higher, compared to absolute seasurface heights of ≈5.5 m for the linearly sloping beach.

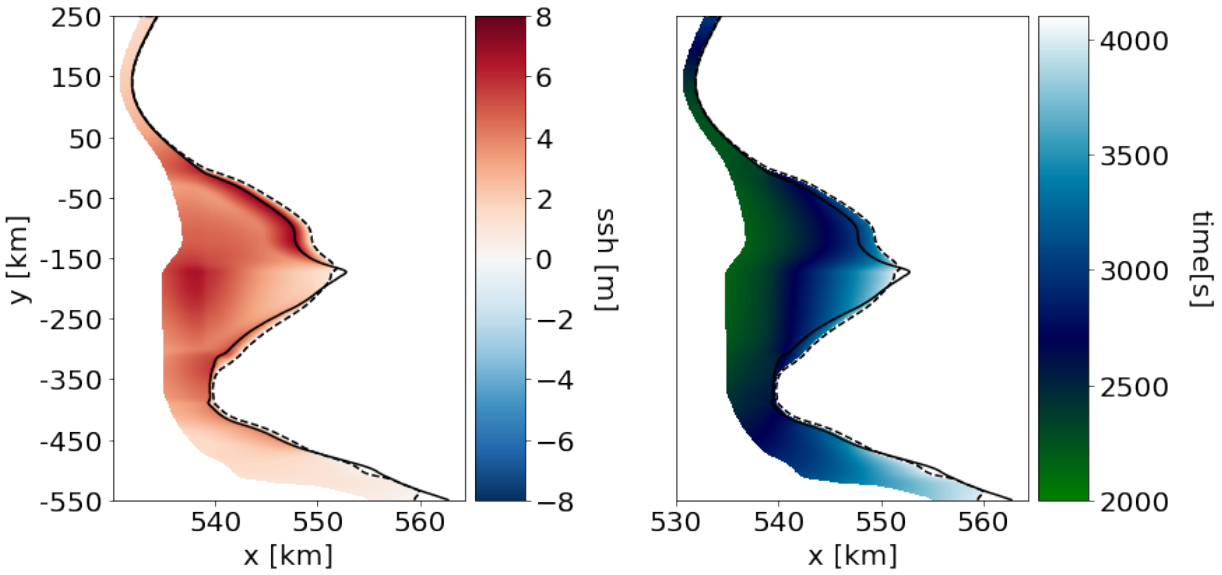



Figure 3.8: Seasurface height of the waves at the coast (**left**) and inundation area and time (**right**) for the tsunami scenario with a complex coast (Fig. 3.3, right). Note the different x-axis scale compared to Fig. 3.7 which is necessary to resolve the complex coastline at the beginning of the simulation (solid black line) accurately. The dotted line illustrates how far in-land the tsunami inundates.

### 3.4.4 Simulations with increased fracture energy and Poisson's ratio

We here analyse two additional dynamic rupture models based on reference model 3B varying on-fault or off-fault rheology. Firstly, we triple the critical slip weakening distance $D_c$ from 0.1 m to 0.3 m (model 5) which triples fracture energy and generates a "tsunami earthquake". Secondly, Poisson's ratio is increased from $\nu$=0.25 to $\nu$=0.3 (model 6) everywhere in the domain. Both models result in shallow slip about twice as high as the reference model 3B (see Table 3.3). Table 3.1 shows the adapted nucleation characteristics that were necessary to initiate rupture on the fault. We do not further decrease the static friction coefficient, but increase the nucleation radius from 3.5 km to 10.0 km (model 5). In model 6 a smaller nucleation area of only 1.8 km is sufficient. For the high fracture energy model 5, rupture dynamics evolve very differently to model 3B, specifically at much lower rupture velocities of max. 1352 m/s. There is no supershear rupture triggered during the entire simulation time. In model 6 the dynamic rupture evolution is similar to model 3B and supershear rupture evolves in updip direction after 9 s. For both models, 5 and 6,

Table 3.3: Dynamic rupture and tsunami characteristics for model 3B, 5 and 6 with centered hypocenter locations.

| | **Model 3B** | **Model 5** | **Model 6** |
|---|---|---|---|
| Max. absolute fault slip [m] | 32.82 | 67.76 | 65.72 |
| Mean absolute fault slip [m] | 15.63 | 33.51 | 32.23 |
| Max. peak slip rate [m/s] | 24.12 | 12.59 | 24.80 |
| Mean peak slip rate [m/s] | 4.15 | 2.73 | 4.48 |
| Magnitude [1] | 8.87 | 9.03 | 9.04 |
| Mean rupture velocity [m/s] | 2124.0 | 1352.0 | 1936.0 |
| Mean stress drop [MPa] | 5.16 | 6.10 | 6.24 |
| Max. seafloor displacement [m] | 4.60 | 6.55 | 6.09 |
| Tsunami potential energy [TJ] | 3133.15 | 6949.16 | 6182.48 |

trapped waves are observed until the end of the simulation (200 s) dynamically interacting with the shallow part of the fault.

Figure 3.9 displays the rupture characteristics of model 3B, model 5 and model 6. Compared to the reference model 3B, both adapted models accumulate large shallow slip. The maximum and average fault slip of models 5 and 6 are about twice as high as in the reference model 3B (see Table 3.3), which reflects in increased earthquake magnitudes of $M_W$=9.03 (model 5) and $M_W$=9.04 (model 6). Also, their dynamic stress drops are higher and the maximum vertical dynamic seafloor displacement is increased by up to ≈2 m. Model 5 shows a much smaller PSR (12.59 m/s) and rupture velocity (1352 m/s) then model 3B (24.12 m/s and 2124 m/s), while the PSR (24.80 m/s) and rupture velocity (1936 m/s) of model 6 are similar to the reference model. The maximum PSR for all 3

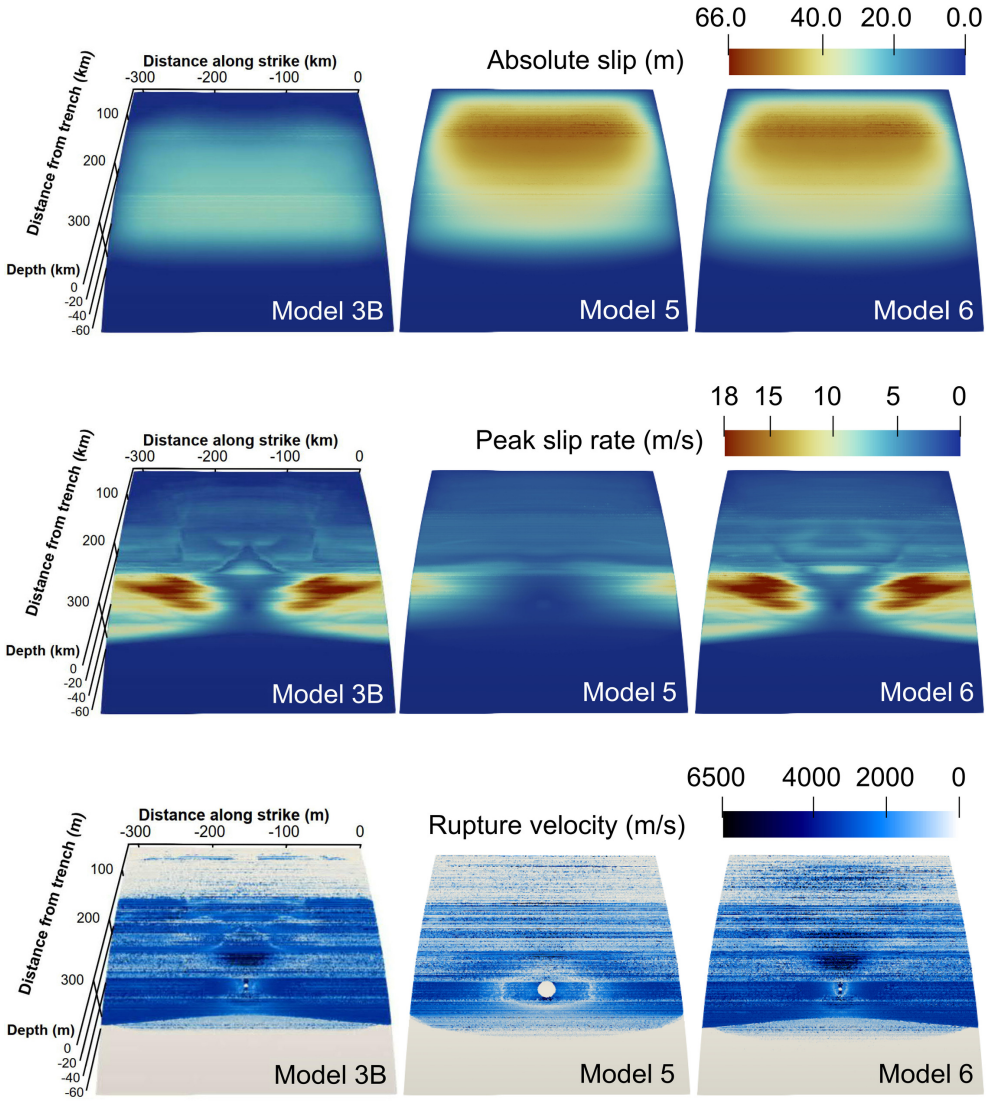



Figure 3.9: Fault slip, peak slip rate and rupture velocity for the dynamic rupture models 3, 5 (increased fracture energy) and 6 (higher Poisson's ratio) after 200 s at the end of the DR simulation.

models is always observed at the same depth which is located within the fault depression at ≈ 40 km depth.

Figure 3.10, top, compares the seasurface height of models 5 and 6 after 200 s, corresponding to the end time of the DR simulation. The overall tsunami waveforms in models 5 and 6 appear to be broader than in model 3B and the trajectories in Figure 3.10, bottom, show much higher tsunami amplitudes. After 1400 s simulation time, the wave amplitudes of model 3B reache extrema of +2 m and -3 m, whereas the tsunami in models 5 and 6 reach values of +2 m and -5 m. After 2300 s simulation time, the wavefronts hit the coast and result in maximum tsunami heights of over 7.5 m. This is ≈2.0 m higher than in the reference model 3B. An important difference between models 5 and 6 is the difference in rupture speed. While model 6 produces supershear rupture, the overall rupture velocity of model 5 is ≈1352 m/s. Thus, although the model 5 earthquake scenario has a slightly smaller stress drop and magnitude than model 6, it produces the highest tsunami amplitudes.

As the waves hit the coast there is a time delay of 100s and a difference in tsunami height of ≈0.5 m between models 6 and 5 (see Fig. 3.11). Due to the overall higher tsunami waves of models 5 and 6, the water inundates further on-shore and reaches higher distances from the coast than for model 3B. Model 5 has the highest tsunami potential with roughly 6950 TJ and model 6 has a tsunami potential of 6182.48 TJ (Table 3.3). The tsunami potential of model 5 is twice as high as the one of reference model 3B.

### 3.4.5 Dynamic effects during tsunami generation by supershear and tsunami earthquakes

Figure 3.12, top, shows snapshots of the unfiltered DR seafloor displacements of models 1B (supershear rupture in downdip direction), 3B (supershear rupture in updip direction) and 5 (tsunami earthquake, no supershear rupture) after 100 s simulation time. Localized, sharp upliftig fronts are visible in the dynamic displacement off-set from the centrally located hypocenter overprinting the static deformation signal. The ocean response recorded within the source region during the tsunami generation process of all 3 models (Fig. 3.12, bottom) reflect the acoustic, seismic and near-field displacements around a rupture front at 100 s simulation time. The time series shown is recorded at x=-100 km and y=-150 km, which is well inside the DR modeling domain.

In our models, co-seismic ocean response phases appear for supershear earthquakes as well as for the "tsunami earthquake" propagating at sub-Rayleigh speed during the duration of earthquake slip and within the DR model, i.e., for the dynamic tsunami generation process. We here do not observe a faster, instananeous supershear mach cone ocean response signature (e.g., identified in Elbanna et al. (2021) for strike-slip events). Due to our filtering approach, seismic waves as well as coseismic ocean response are effectively damped, once rupture stops, inside the DR source and at all times outside of this region. We then do not observe dynamic phases propagating.

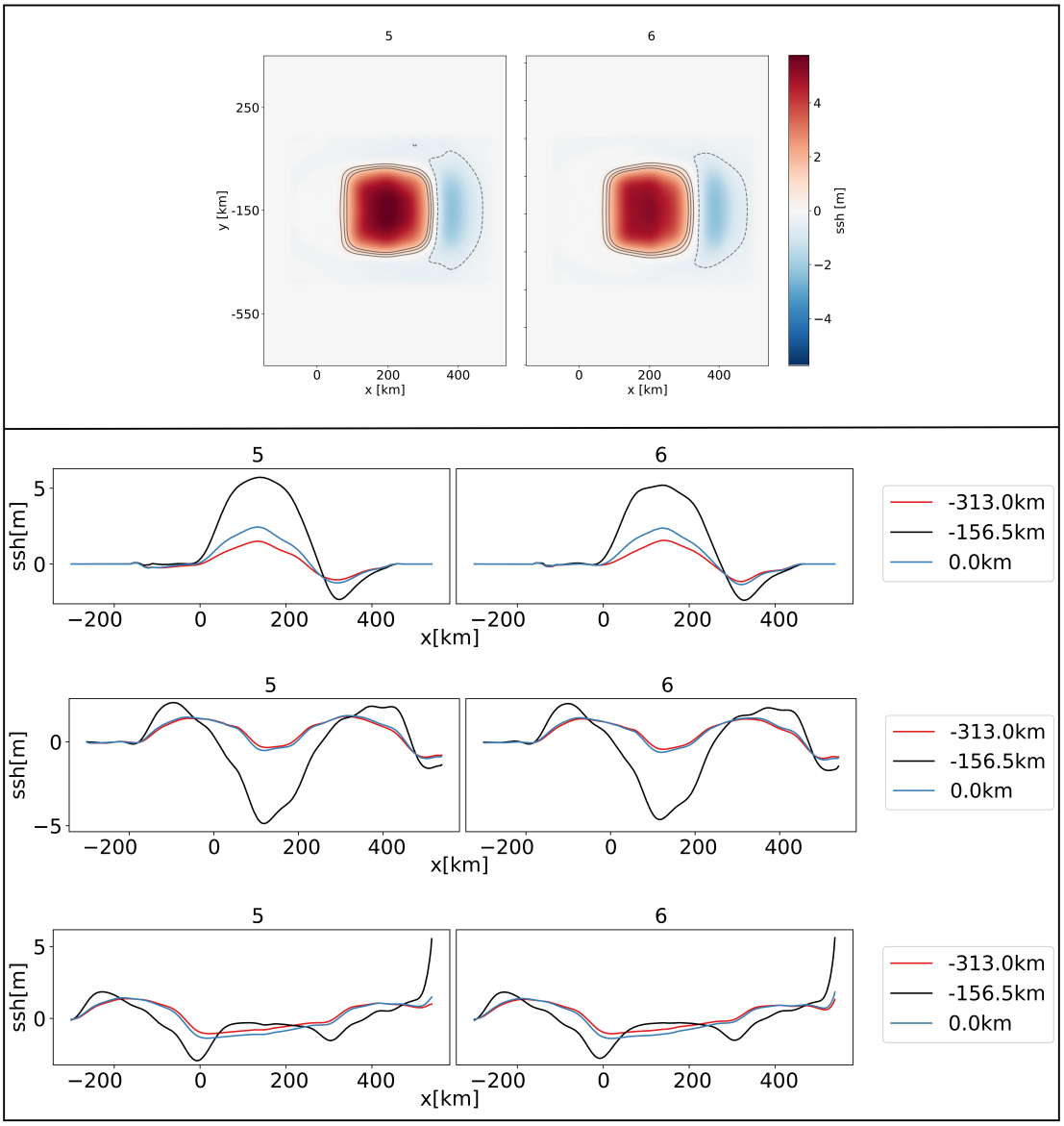



Figure 3.10: **Top** Sea surface height (ssh) for models 5 and 6 at t=200 s with contours at -0.5, 0.5 1.0 and 1.5 m, at the end of the DR earthquake simulations. **Bottom:** Trajectories of the sea surface height for dynamically sourced tsunami (model 5 and 6) measured at y=0.0 km, -156.5 km and -313.0 km. Directly after the earthquake at t=200 s (top), during the wave propagation at 1400 s (middle) and at the time of coastal inundation at t=2,220 s (bottom).

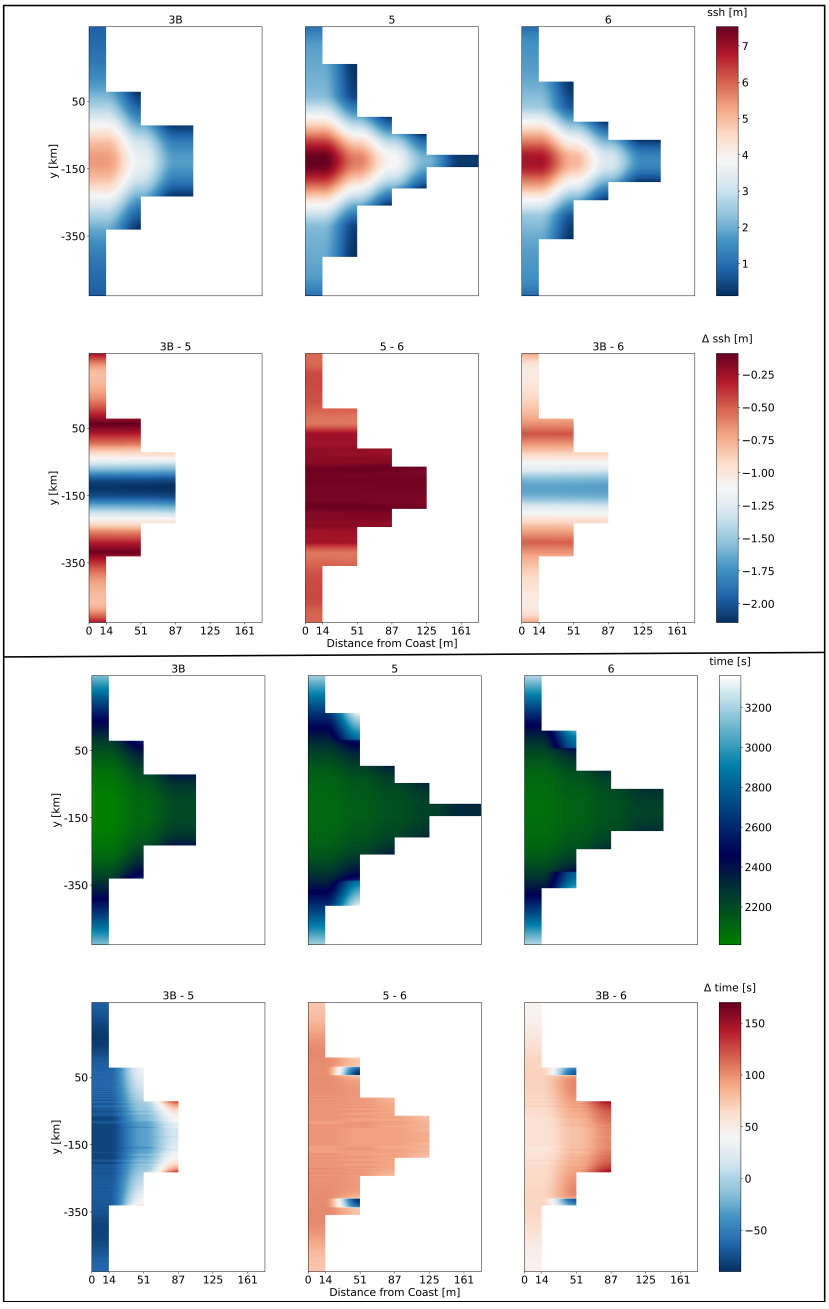



Figure 3.11: **Top:** Comparison of sea surface height for tsunami fronts arriving at the coast for the models 3B, 5 and 6. The difference between the models is shown as Δssh. In contrast to Fig. 3.7 the x-axis (distance from coast) indicates higher values. This is due to the greater inundation area of model 5 which exceeds 161m distance. **Bottom:** Inundation comparison for models 3B, 5 and 6. The green to white colour scale shows the time delay for the wave fronts arriving at the coast. The difference between the models is plotted as Δt with a blue (negative values) to red (p color-scale respectively.

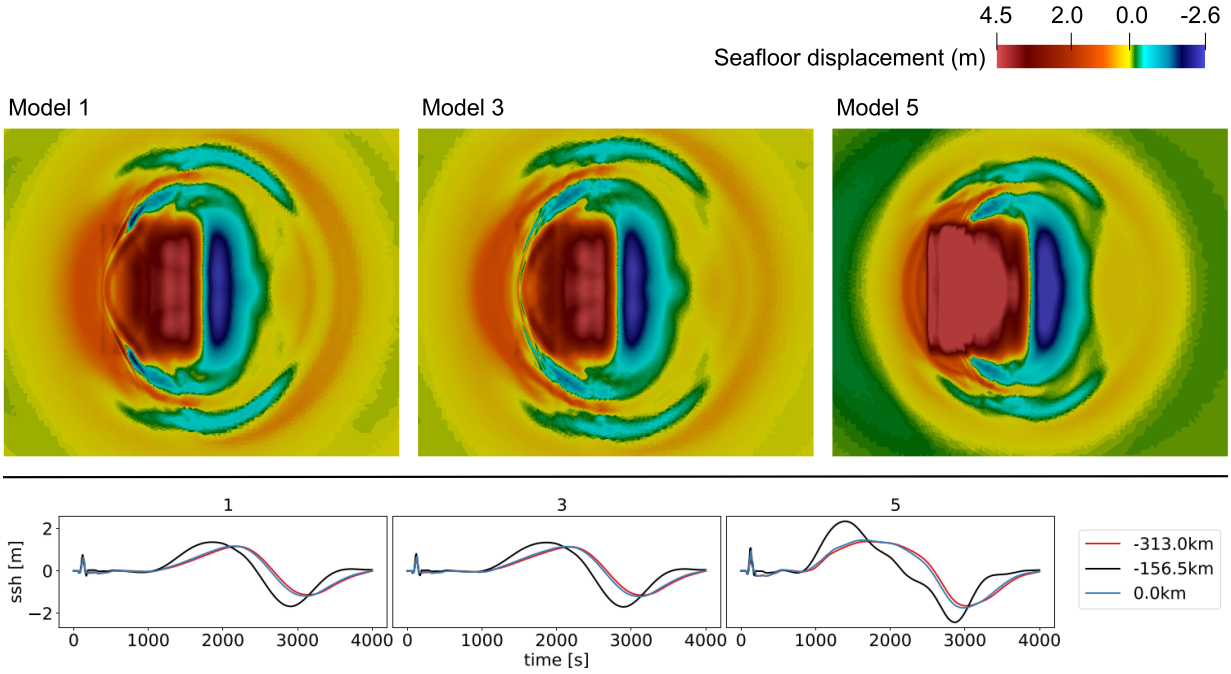



Figure 3.12: **Top:** Unfiltered seafloor displacements from dynamic rupture model 1B (supershear rupture in downdip direction), 3B (supershear rupture in updip direction) and 5 (tsunami earthquake) at a simulation time of 100 s. **Bottom:** Tsunami generation sea surface height timeseries for model 1B, 3B and 5 at x=-100 km, y=-150 km.

## 3.5 Discussion

### 3.5.1 Simplifying model assumptions

In this study, we link 3D dynamic rupture initial conditions to a chosen slip event in a 2D long-term geodynamic subduction and seismic cycle. The linked initial conditions include a curved, blind fault geometry, spatially heterogeneous fault stresses, strength and material properties. The SC 2D material properties, fault geometry, as well as stresses and strength are extruded into the third dimension without adding additional along-strike variability. While limiting complexity, we can in this manner isolate sensitivities, e.g. of hypocentral location, and their effects on rupture dynamics and tsunami generation, propagation and inundation.

In linking from the SC to the DR model, we adopt several simplifying assumptions to bridge the incompressibility and visco-elasto-plastic, plane-strain conditions of the subduction model to the compressible, elastic conditions of the earthquake model. The resulting 3D dynamic rupture is linked with the tsunami model through the time-dependent seafloor displacements, following the same methods as detailed in Madden et al. (2020). All resulting rupture models are characterized by uniformity along strike, rendering the dynamic

earthquake source differences to be associated with along-dip variability in rupture dynamics controlled by the nucleation position relative to the two bands of topography on the megathrust. Future work may extend our analysis to include along-arc variations in stress, strength, rheology and geometry across the megathrust as suggested by detailed imaging of fault geometry and shown to impact earthquake and tsunami dynamics (e.g., Galvez et al., 2019; Ulrich et al., 2022). The adopted "bumpy" fault geometry develops self-consistently with stress, strength and rheology in the SC model. Its along-depth dimensions aligns with conceptual asperity models governing megathrust fault slip. Future work may study the dynamic effects of subducted seamounts (e.g., Cloos, 1992) ensuring to adapt initial stresses consistently.

We use fully elastic material response in combination with linear slip weakening friction. The complexity of the DR model could be increased by including more complex physics, such as rapid velocity weakening rate-and state friction (Ulrich et al., 2019a), thermal pressurization of pore fluids (Gabriel et al., 2020) or off-fault plasticity (Wollherr et al., 2018; Ma and Nie, 2019).

In the linking step from the DR model to the tsunami model, we filter the seafloor displacements using a spatial-temporal Fourier-transform (Sec. 3.4.5). Detailed analysis of the effects of relatively small coseismic phases on tsunami genesis, propagation and inundation is here challanging due to the filter we apply. Future studies may use the unfiltered seafloor displacement as input to the tsunami model to analyse the fully dynamic interaction of the seafloor movements with the tsunami and inundation dynamics. sam(oa)$^2$-flash 's hydrostatic shallow water tsunami model enables the simulation of tsunami genesis, propagation and inundation at the coast. The approach is limited by the assumption of long wavelengths. Additionally, it does not take the interaction of wind with the water interface into account. Overall, the usage of the shallow water equations might overestimate wave amplitudes.

Our DR models do not account for seafloor bathymetry. A more realistic bathymetry would translate the horizontal earthquake motion into vertical displacements, such that the tsunami amplitude might be amplified (Tanioka and Satake, 1996; Lotto et al., 2019; Saito et al., 2019; Ulrich et al., 2019a). Recent work in van Zelst et al. (2022) complement this paper by using the exact subduction bathymetry and topography arising from the 2D seismic cycle model and include it in 2D DR simulation. The resulting seafloor displacement is linked to a one-dimensional shallow water tsunami model. The resulting maximum tsunami amplitude is 6.5 m, larger than our comparable 3D reference model 3B. It is here left for future work to combine their findings with our 3D sensitivity analysis.

The computational costs of each of the presented 15 linked scenarios (see Sec. 3.3.1 and 3.3.2) is well within the scope of the allocation typically available to users of supercomputing centres. While hundreds of such simulations are readily possible, fully physics-based dynamic rupture models rather complement than replace cheaper (e.g., kinematic) source descriptions used for millions of PTHA forward models. Specifically, for narrowing down the high-dimensional and often non-unique source parameter space in conjunction with observational or long-term modeling constraints and for sensitivity analysis of other parameters influencing rupture behaviour and tsunami generation and propagation.

### 3.5.2 Hypocentral depth and up-dip versus down-dip supershear rupture propagation

We vary the hypocenter location across 4 depths (25 km, 30 km, 40 km, 45 km) to study the effects on rupture dynamics and tsunami evolution, propagation and coastal inundation. Earthquakes with shallower hypocentral depths (25 km and 30 km depth) generally generate lower slip than earthquakes with deeper hypocenters (40 km and 45 km depth). The lower accumulated on-fault slip for events with shallower hypocenters leads to comparably lower vertical seafloor displacement. In our SC initialized models, however, these differences are relatively minor and have small impact on tsunami generation, propagation and inundation, in contrast to what is typically observed from observational data (Bilek and Lay, 2018).

For simulations with shallower hypocenter locations, we observe supershear rupture propagating in the downdip direction, while hypocenters located at 40 km and 45 km depth lead to supershear rupture in the updip direction. In either case, the slab geometry (topographic highs) and rheology influences the nucleation and direction of supershear rupture propagation significantly. In all our simulations, supershear rupture initiates when the rupture front hits a topographic high on the fault plane. The first topographic high (1) is related to a pile up of subducted sediments. The weaker material at the depth of the topographic high 1 might facilitate supershear rupture. Supershear rupture is also triggered by the second topographic high highlighting the complex dynamic effects of the long-term self-consistently developing fault roughness, stress and rheology heterogeneities. The direction of supershear rupture propagation is determined by whether the updip or downdip rupture front interacts with the rough fault geometry (Bruhat et al., 2016; Bao et al., 2019; Tadapansawut et al., 2021). Megathrust supershear rupture is challenging to identify observationally but has been suggested in back-projection analysis of the Tohoku-Oki megathrust earthquake (Meng et al., 2011) and was analysed in Cascadia 2D dynamic rupture models by Ramos and Huang (2019) who observe down-dip supershear rupture propagation near the ETS region caused by normal stress gradients (similar to the conditions governing our topographic highs).

Independent of where the earthquakes nucleate, the highest peak slip rate is consistently observed at the same location on the fault: inside the depression that separates the two local fault topographic highs, although the intensity of the slip rate decreases with increasing hypocentral depth. The calculated tsunami potential energy varies in the range of $\Delta E_T \approx$78 TJ for earthquakes nucleating at different depths. This is caused by a difference in the maximum seafloor displacement of approx. $\Delta$ =0.13 m.

### 3.5.3 Bilateral versus unilateral rupture on a complex bimaterial megathrust

To study unilateral versus bilateral rupture effects on rupture dynamics (Hirano, 2019; McGuire et al., 2002) and tsunami generation, we shifted rupture nucleation from a centered hypocenter to 25% (A) and 75% (C) of the fault width (y=-78,25 km and y= -

234,75 km). Overall, differences are small. However, we note that earthquakes with a centered hypocentral location (B) consistently produce the highest stress drops and lowest accumulated slip on the fault, which lead to the lowest vertical seafloor displacement. The simulations with a nucleation patch at 75% (C) of the fault width show the highest accumulated slip for earthquakes at the same depth, but relatively low PSR. Due to the high amount of accumulated slip, we would expect the seafloor displacement to be the highest as well, but this is not the case for all model families, due to bimaterial effects (Brietzke et al., 2009). These effects lead to (minor) differences in amplitudes of the resulting tsunami at the coast and the (short) time delay between the arriving wave fronts. The higher sea surface uplift is also seen in the trajectories of the different models.

We note again, that in difference to Madden et al. (2020), we here use the 2D geodynamic SC model developed in van Zelst et al. (2019) which has twice larger shear moduli. All our earthquakes show a higher stress drop of roughly 5 MPa compared to 2.2 MPa in Madden et al. (2020), whereas the rupture velocity remains the same ($\approx 2100\ m/s$). They also show a comparably lower maximum slip of 32.8 m (Madden et al. (2020) observe a slip of 42.2 m) on the fault plane, which is visible in the lower seafloor displacement as well (4.60 m compared to 28.1 m). Overall, our earthquake and tsunami scenario agree with observational scaling, resulting in a typical tsunami generating earthquake magnitude of $M_W = 8.8$ and a tsunami wave height of roughly 5.5 m at the coast. For all 12 models with hypocenter variations, we find that high earthquake magnitudes (or high fault slip) correspond to the highest seafloor displacements and result in greater tsunami heights, as expected.

### 3.5.4 Comparison of tsunami behaviour for linear and complex coastline

To analyze the effect of coastal complexity on inundation, we included a non-linear coastline in model 3B (see Fig. 3.3). The results show that the complex and more realistic setup yields higher tsunami amplitudes (up to 8 m, Fig.3.8) than the model with a linear beach (seasurface height of up to 5 m, Figs. 3.7 and 3.11). The overall distribution of seasurface heights along a non-linear coast is much more complex. Between y=50 km and y=-160 km, the distance between fault and coast increases. Beyond y=-160 km until y=-350 km this distance decreases. While the part between y=50 km and y=-160 km is hit by tsunami heights of up to 8 m, the seasurface heights at the coast between y=-160 km and y=-350 km are ≈2 m lower. This effect may be enhanced when combining a complex coastline with lateral varying earthquake source characteristics. Even though the waves of both, model 3B and the scenario with the complex beach arrive nearly simultaneously at the coast, they need ca. 1000 seconds longer to reach the farthest on-shore point in the non-linear case.

### 3.5.5 Large shallow slip

Most earthquakes of high magnitudes tend to have a large stress drop, accompanied with a high radiation energy (Festa et al., 2008). Venkataraman and Kanamori (2004) state that

this is different for a special class of megathrust events, "tsunami earthquakes", which have a comparably small radiation efficiency. We here model this dynamically by increasing the critical slip distance, the amount of slip over which the static friction coefficient in the dynamic rupture model decreases to the dynamic friction coefficient. Polet and Kanamori (2000) state that tsunami earthquakes tend to rupture the shallow portions of a fault, which results in a large amount of shallow slip. The increased $D_c$ value in model 5 leads to a lower rupture velocity of 1352 m/s compared to the rupture speed in the initial model 3B of 2124 m/s. The mean velocity of 1352 m/s is lower than 80% of the S-wave speed (van Zelst et al., 2019), which specifies this earthquake by definition as a tsunami earthquake (Kanamori, 1972; Bilek and Lay, 1999). As the rupture propagates updip, we observe high slip on the shallow fault. The slip is twice as high as in the initial model 3B, which leads to a higher max. vertical seafloor displacement (1.5 times the displacement of 3B) and a higher tsunami height (see Fig. 3.11). This behavior is reflected in the tsunami potential of model 5, which is double the tsunami potential in model 3B.

In model 6, we increase the Poisson's ratio from $\nu = 0.25$ to $\nu = 0.3$. The increase in Poisson's ratio results in a reduction of the critical maximal shear stress on the fault (Xie et al., 2009). This means that rupture initiation is facilitated. Whereas van Zelst et al. (2019) observe a decrease in slip with increasing Poisson's ratio, we find higher slip on the fault, together with a higher stress drop; model 6 has also double the amount of slip of model 3B, just as the "tsunami earthquake" model 5. This causes a higher vertical seafloor displacement and thus a higher tsunami. At the same time the rupture velocity remains nearly the same as in model 3B. Due to the high magnitude and accumulated shallow slip, the tsunami potential of model 6 is nearly twice as high as in model 3B. The differences in rupture dynamics between van Zelst et al. (2019) and our model 6 from varying the Poisson's ratio is due to the different choices in linking frictional parameters (we here assume constant $D_c$) which leads to differences in stress drop. While the stress drop in van Zelst et al. (2019) remains the same with increasing $\nu$, we observe an increase of 1.08 MPa.

The main difference between model 5 and 6 are summarized in Tables 3.2 and 3.3. In model 6, the peak slip rate and stress drop get amplified, leading to a similar rupture behaviour than in model 3B with a higher magnitude and absolute slip, resulting in higher tsunami amplitudes. In model 5, the rupture velocity gets reduced and the rupture characteristics change. Although model 5 produces an earthquake with a slightly lower magnitude and stress drop, it produces a seafloor displacement that is 46 cm higher than for model 6. The tsunami earthquake (model 5) generates the highest tsunami amplitude of all of these models and consequently the greatest inundation area at the coast, while the waves arrive significantly later due to the lower rupture velocity. The effect of a Poisson's ratio increase in model 6 is not quite as large as the change of the rupture dynamics and tsunami generation in model 5. While in model 5 rupture propagates at sub-shear speeds, supershear rupture still evolves in model 6. Nevertheless, an increasing critical slip weakening distance $D_c$ just as a change in the material properties in the earthquake rupture model can drastically change the rupture dynamics and influence tsunami generation and propagation (see Fig. 3.11). We note that for future analysis of the effects of enhanced

shallow slip such as occurring in both models 5 and 6, it will be crucial to combine our analysis with 3D non-constant water depth in the source region, since a realistic subduction zone geometry (van Zelst et al., 2022) will place shallow slip in deeper water and cause additional effects due to horizontal motions and steep topography contrasts.

## 3.6 Conclusion

We investigate the influence of hypocentral depth, rupture propagation direction and bimaterial effects, as well as the influence of fracture energy and Poisson's ratio on rupture behaviour and tsunami generation and propagation. We analyse 15 subduction-initialized 3D dynamic earthquake rupture tsunami propagation and tsunami run-up scenarios. We vary the hypocentral depth between 25 km, 30 km, 40 km and 45 km, which resembles four low strength excess regions in the geodynamic subduction and seismic cycle model. In all models, supershear rupture is triggered once the earthquake rupture front crosses one of two distinct topographic highs in the megathrust geometry, which are related to sediment subduction on geodynamic time scales. Earthquakes from shallow hypocenters exhibit supershear rupture in the downdip direction, whereas supershear rupture propagates updip for earthquakes that nucleate deeper. Albeit dynamic earthquakes differ (rupture speed, peak slip-rate, fault slip, bimaterial effects), the effects of hypocentral depth on tsunami dynamics are negligible. Earthquakes with deeper hypocenters accumulate higher slip during up-dip rupture compared to shallow hypocenters, in which rupture mainly propagates downdip. Larger fault slip correlates with larger vertical seafloor displacement by up to 13 cm, which is reflected in the tsunami potentials. These tendencies barely affect the tsunami run-up behaviour at the coast, where the maximum difference in tsunami height is only a few centimeters and the wave arrival times vary by few seconds.

Lateral hypocenter variations lead to small effects such as delayed wave arrival of up to 100 s and differences in tsunami amplitude of up to 0.4 m at the coast. To study unilaterial versus bilateral directivity effects on dynamic megathrust rupture, tsunami generation, propagation and inundation, we varied the hypocenter location along-strike at all of above depth locations. We find that the highest fault slip is always observed for unilateral rupture with hypocenters located at 75% of the fault width (at y=-234.75 km), whereas a centered rupture initiation leads to purely bilateral rupture including the lowest dynamically accumulated slip. In between models of one model family, fault slip varies up to approx. 1.5 meters. We find only minor bimaterial effects; models with hypocenters located at 25% of the fault width mostly mirror those with hypocenters at 75% of the fault width.

We dynamically generate a "tsunami earthquake" by increasing the critical slip distance, and thus increasing the amount of fracture energy and decreasing radiation efficiency of the bilateral, 40 km deep dynamic earthquake rupture model. This results in lower rupture velocities (average rupture velocities in model 5 are 64% of those in model 3B) and doubles the amount of on-fault slip which is then, in contrast to the initial model, concentrated on the shallow part of the fault. This leads to a ≈2 m higher vertical seafloor displacement and a ≈2m higher tsunami amplitude at the coast. Increasing Poisson's ratio has a similarly large effect on shallow fault slip, but less on tsunami height and run-up. Increasing $\nu$ from 0.25 to 0.3 doubles the amount of fault slip and favours shallow slip, leading to a vertical seafloor uplift of ≈6 m, which is an increase of 1.5 m and a difference of up to ≈1.5 m in coastal tsunami amplitudes.

Our sensitivity analysis based on 15 physics-based linked earthquake and tsunami and inundation models for a generic megathrust setting can provide building blocks towards dy-

namic rupture modeling complementing Probabilistic Tsunami Hazard Analysis (PTHA). Virtual laboratories, such as we use here, using computationally efficient and open source earthquake and tsunami computational models enable hypothesis testing and physics-based plausibility assessment of linked tsunami and earthquake models of varying complexity.

# Appendix

## 3.A Supplementary Tables and Figures

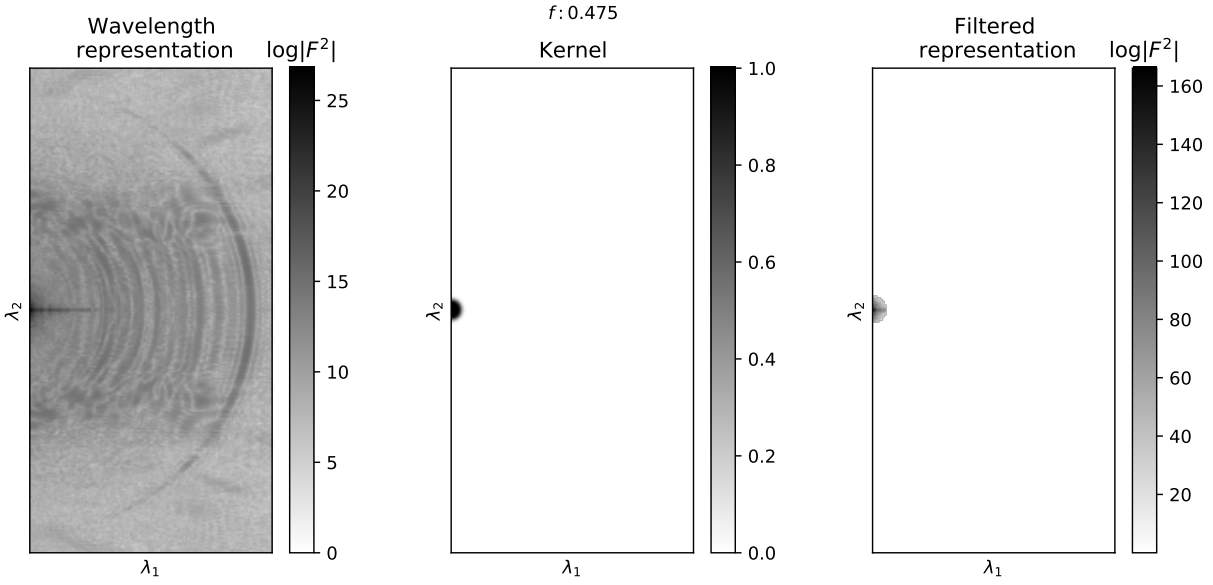



Figure 3.A.1: Fourier-filtering process to remove seismic waves: Exemplary wavenumber representation (left) of the displacement field of model 5: Seismic waves are represented by radial symmetric lines. The coefficients are removed by the developed smooth filter kernel (middle), which results in a filtered wavenumber representation (right).

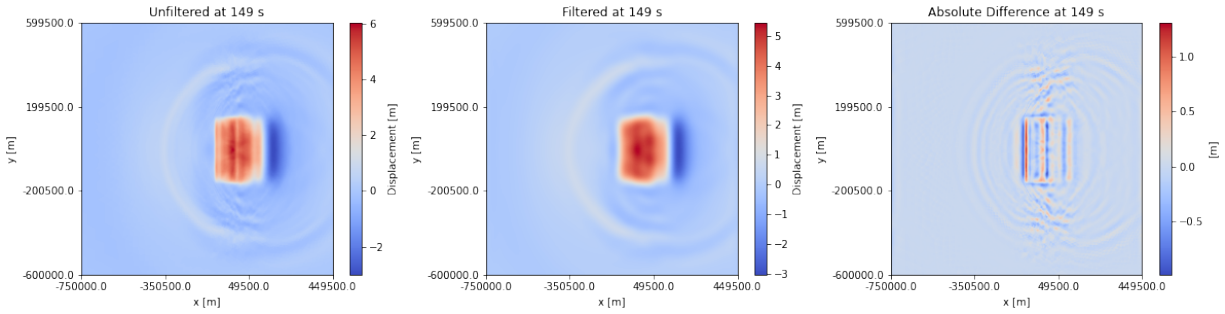



Figure 3.A.2: The earthquake model seafloor displacement of model 5 at t=149 s (left). The filtered displacement (middle) and the difference between both (right).

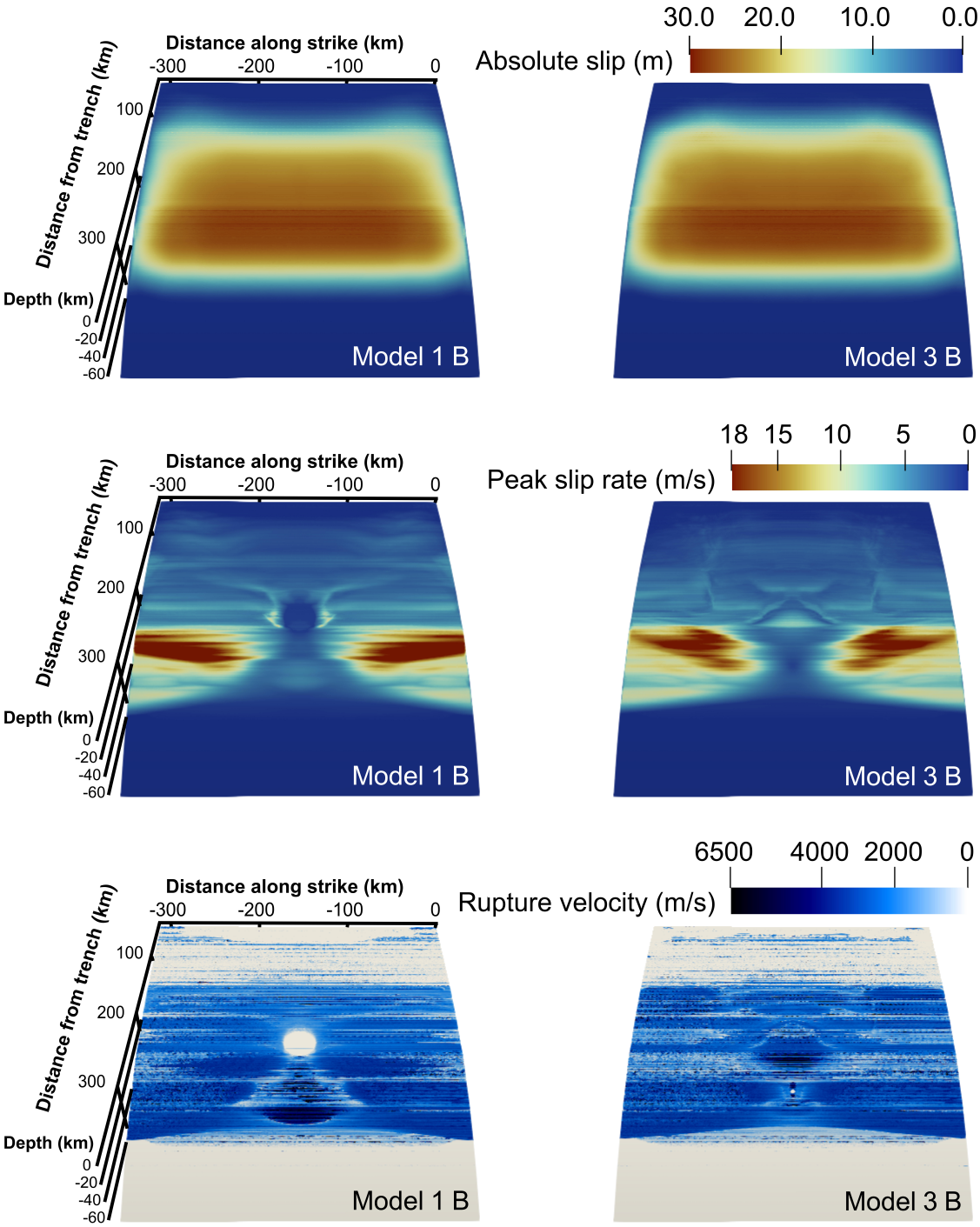



Figure 3.A.3: Final slip, peak slip rate, and rupture velocity for higher resolution (h=500m, p=5) dynamic rupture models 1B and model 3B (reference model) after 200 s at the end of the DR simulation.

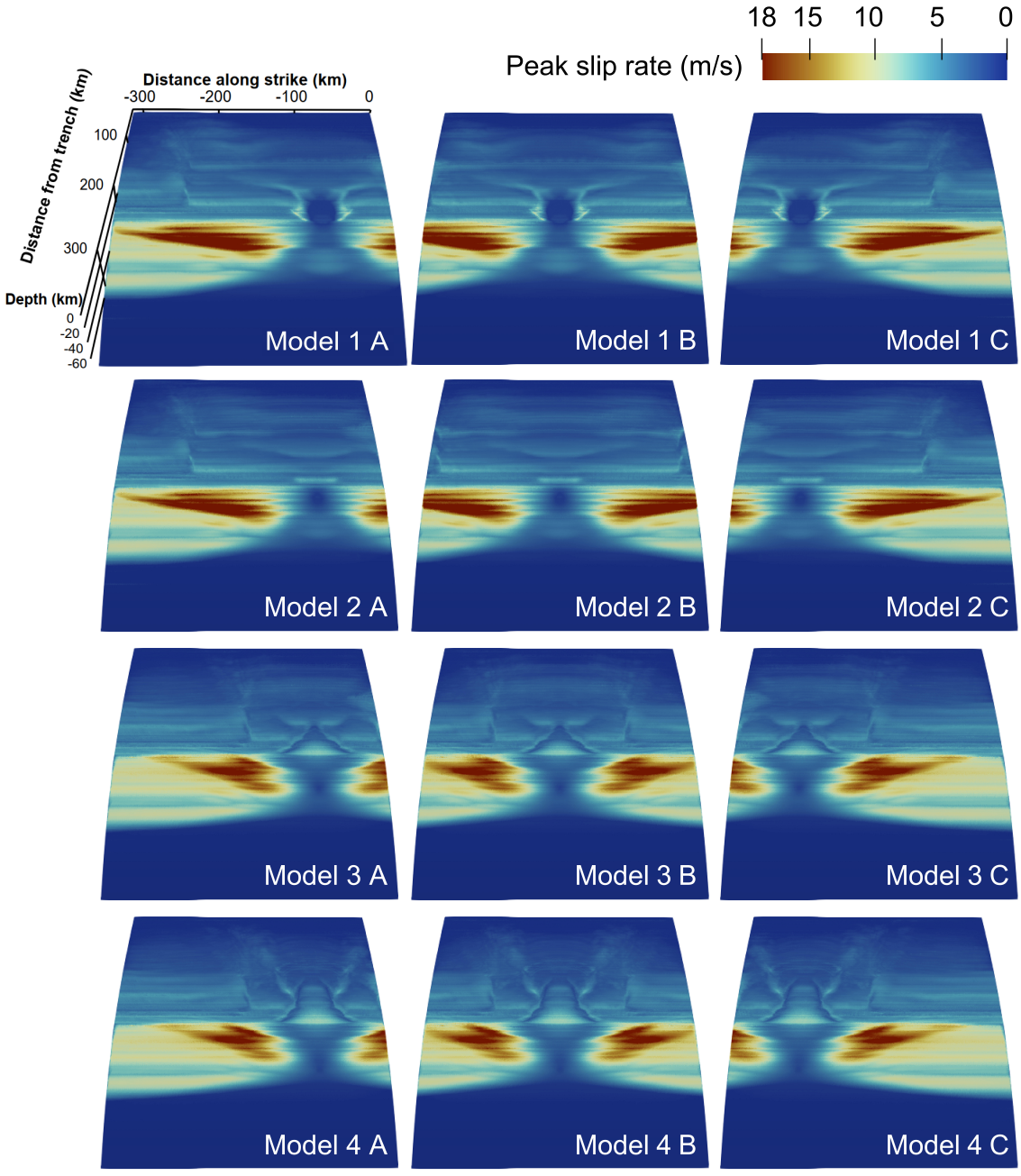



Figure 3.A.4: Peak slip rate (PSR) in m/s on the fault plane at the end of all dynamic rupture models. The highest PSR is located at the same depth for all earthquakes and the overall pattern of the PSR is similar. Lateral extending bands are visible due to lateral extending material properties on the fault. The shallower the hypocenter location, the higher the PSR. Even though the material properties and stresses along strike are the same, we see along arc differences of the PSR distribution at same depths.

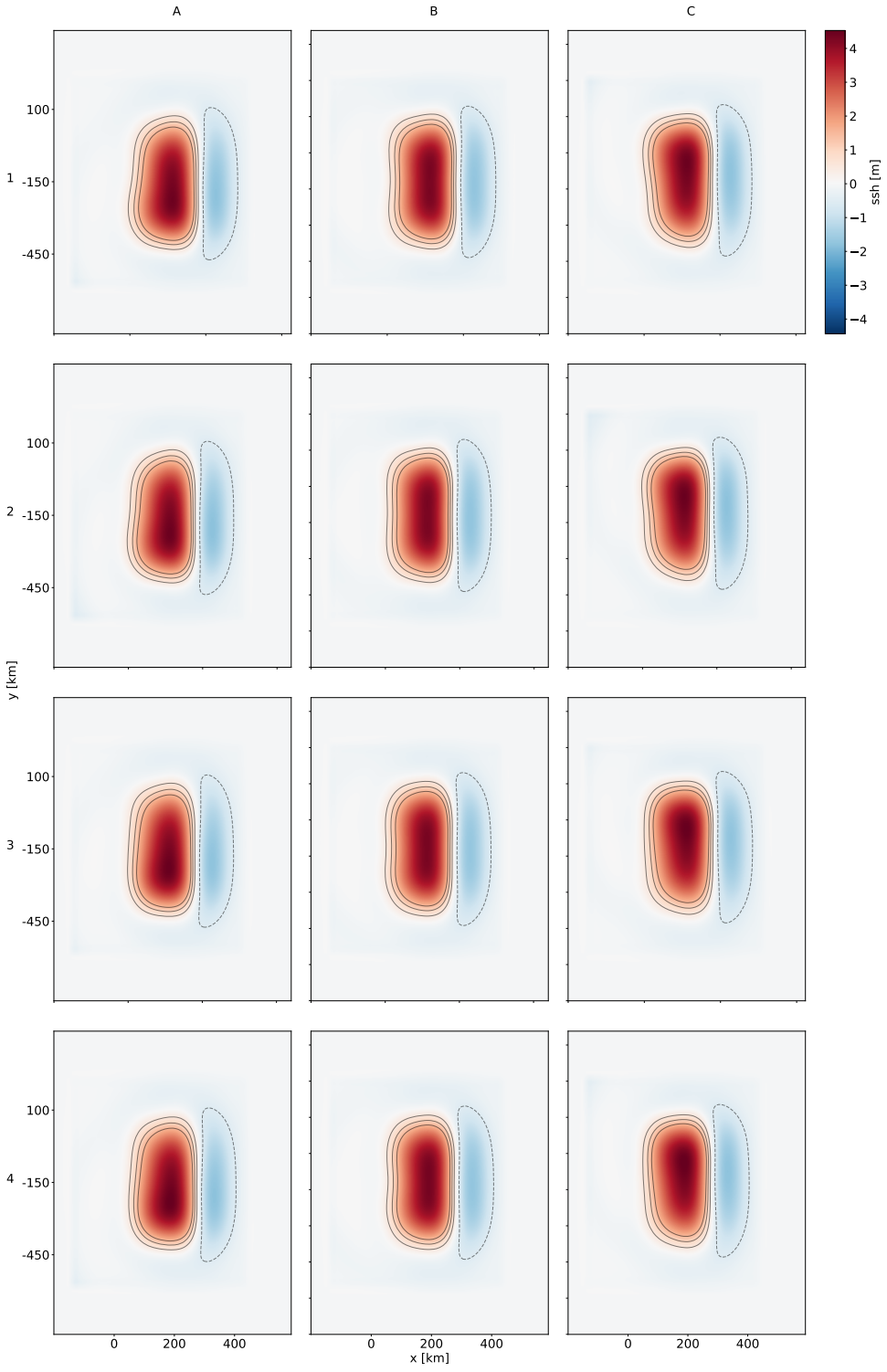



Figure 3.A.5: Seasurface height at t=200 s with contours at -0.5 0.5 1.0 and 1.5 m, at the end of the earthquake simulation.

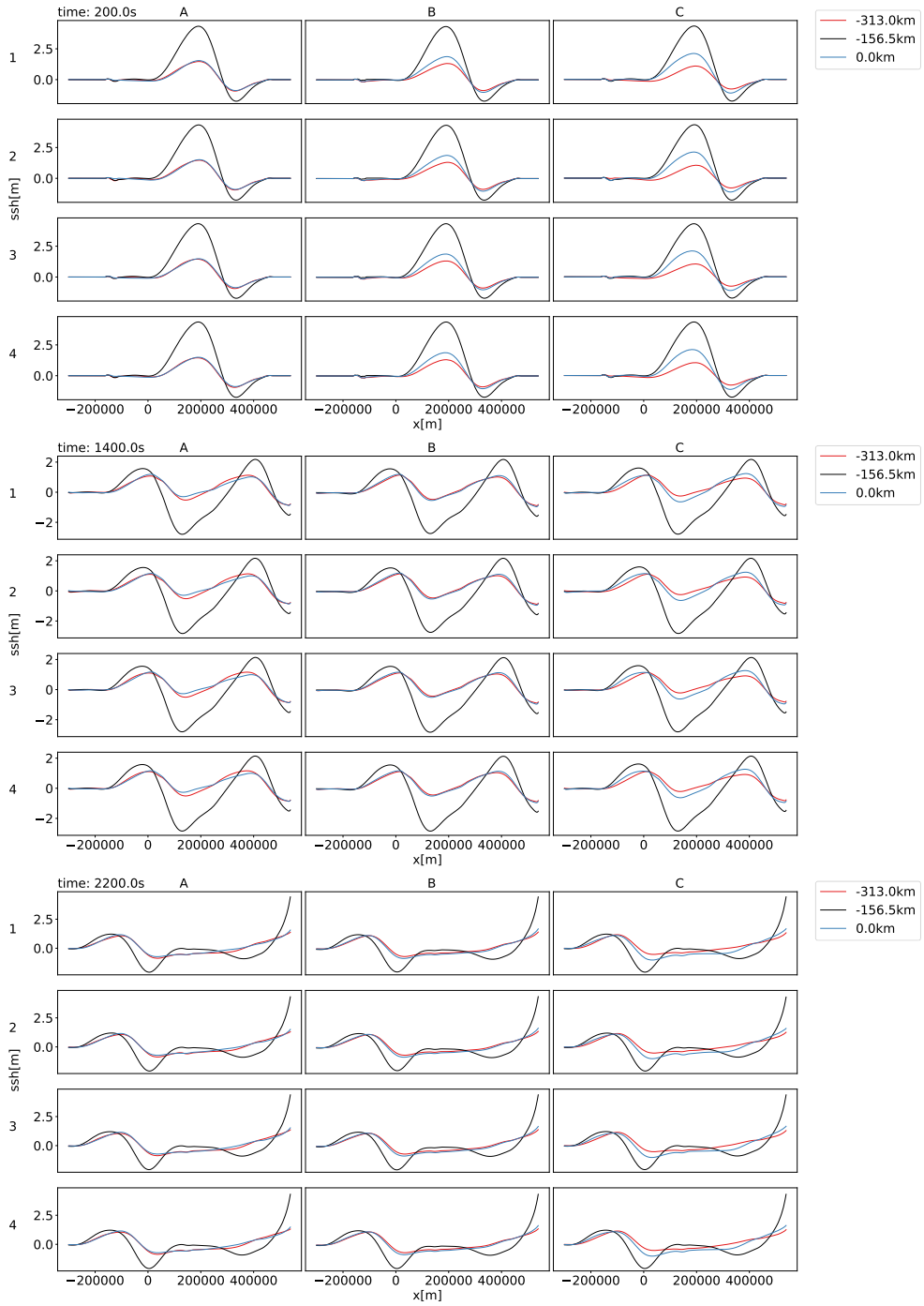



Figure 3.A.6: Trajectories of the sea surface height for dynamically sourced tsunamis at y=-313.o,-156.0 and 0 km. Directly after the earthquake at t=200 s, during the wave propagation at t=1400 s and at the time of inundation at t=2200 s.

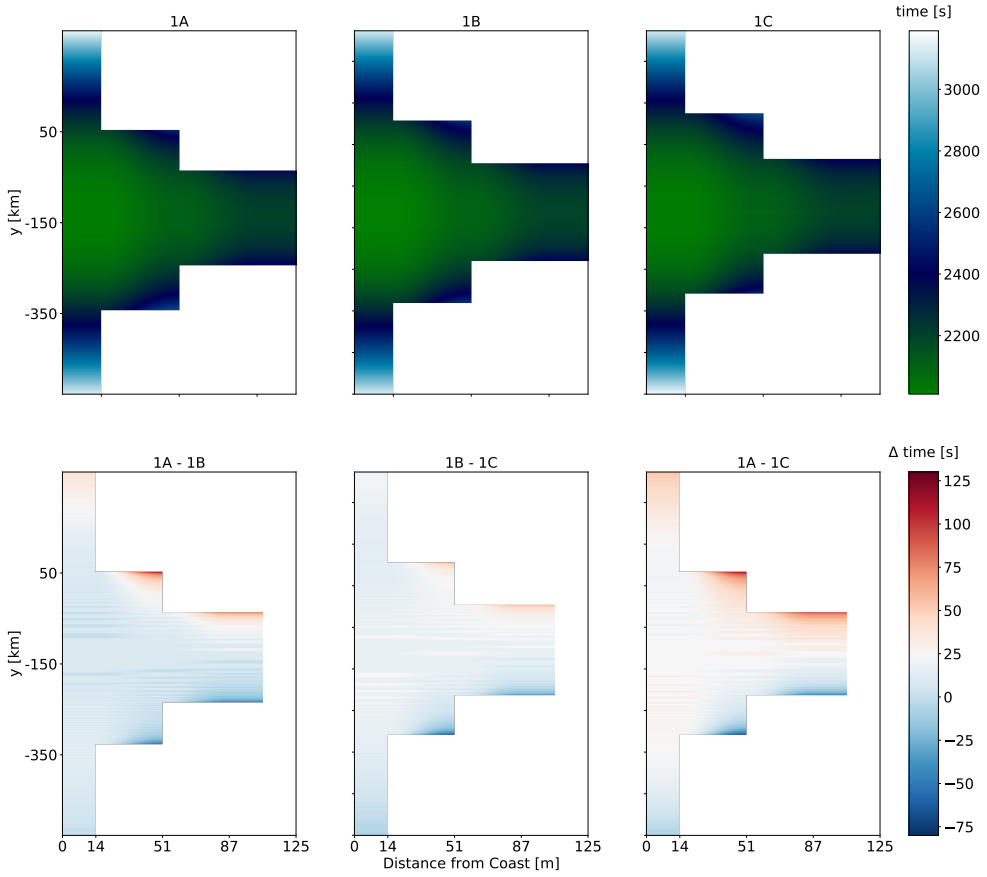



Figure 3.A.7: Inundation comparison for model 1.A-1.C. The hypocenter locations for the dynamic rupture simulations vary along strike.

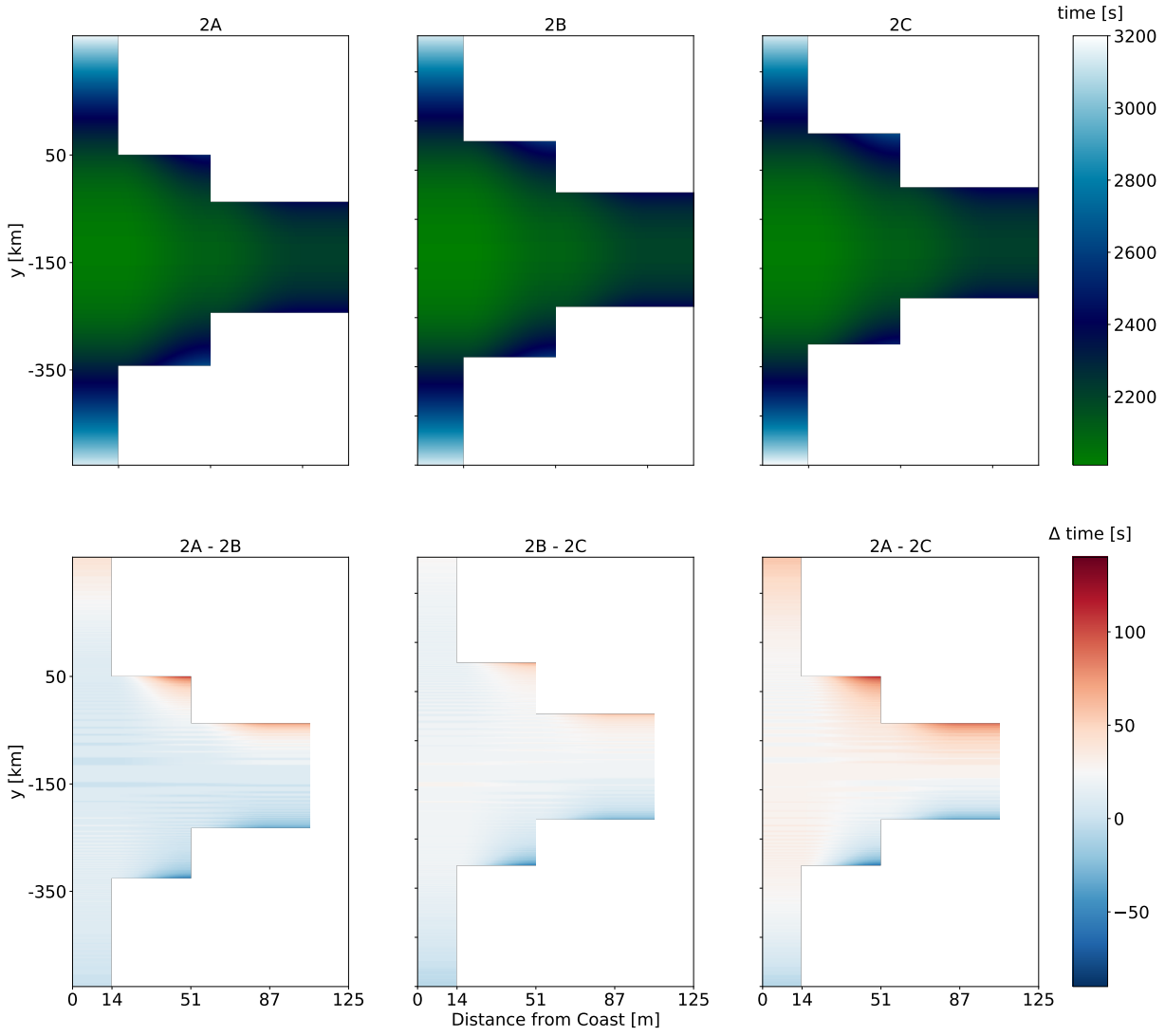



Figure 3.A.8: Inundation comparison for model 2.A-2.C. The hypocenter locations for the dynamic rupture simulations vary along strike.

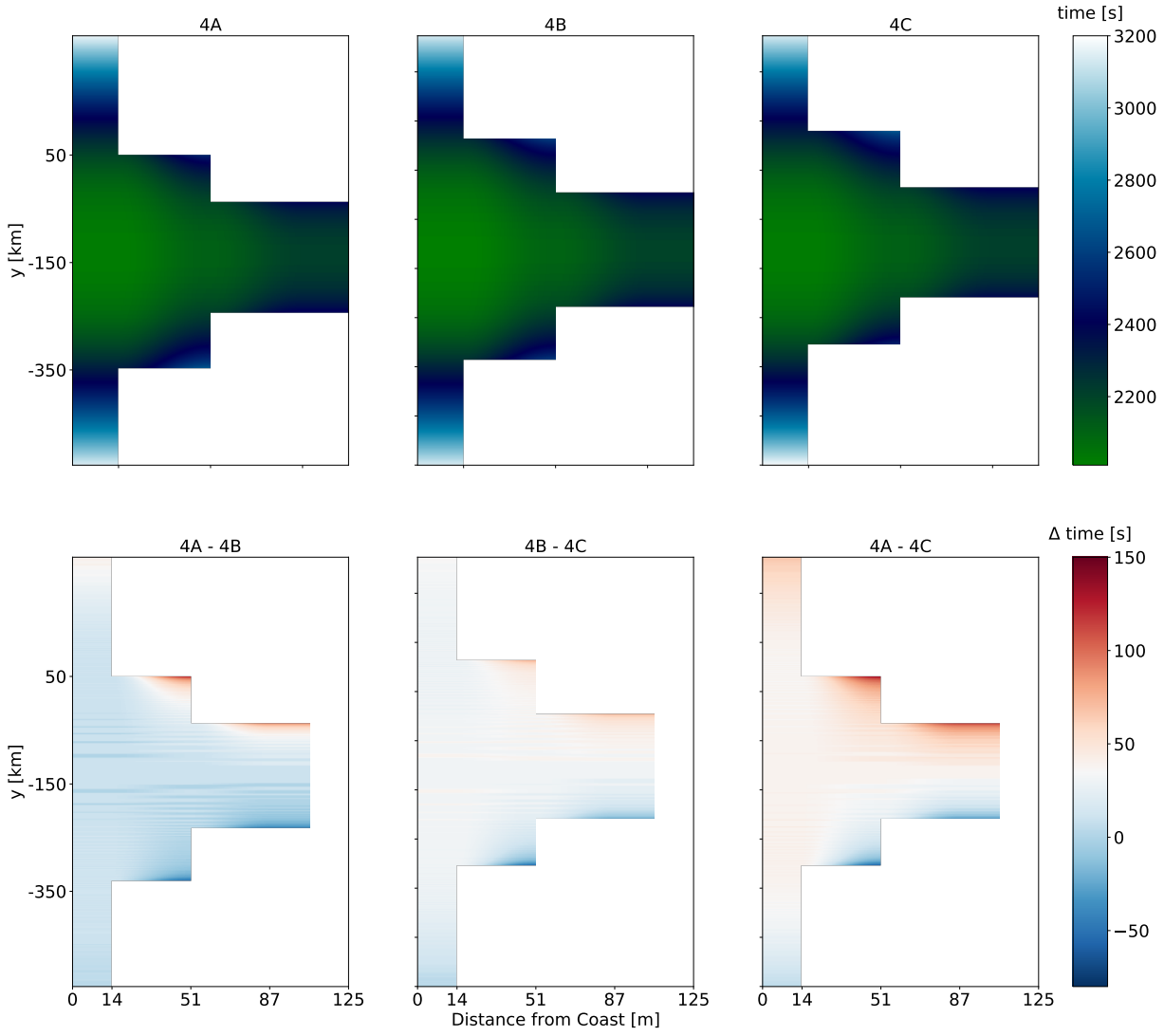



Figure 3.A.9: Inundation comparison for model 4.A-4.C. The hypocenter locations for the dynamic rupture simulations vary along strike.

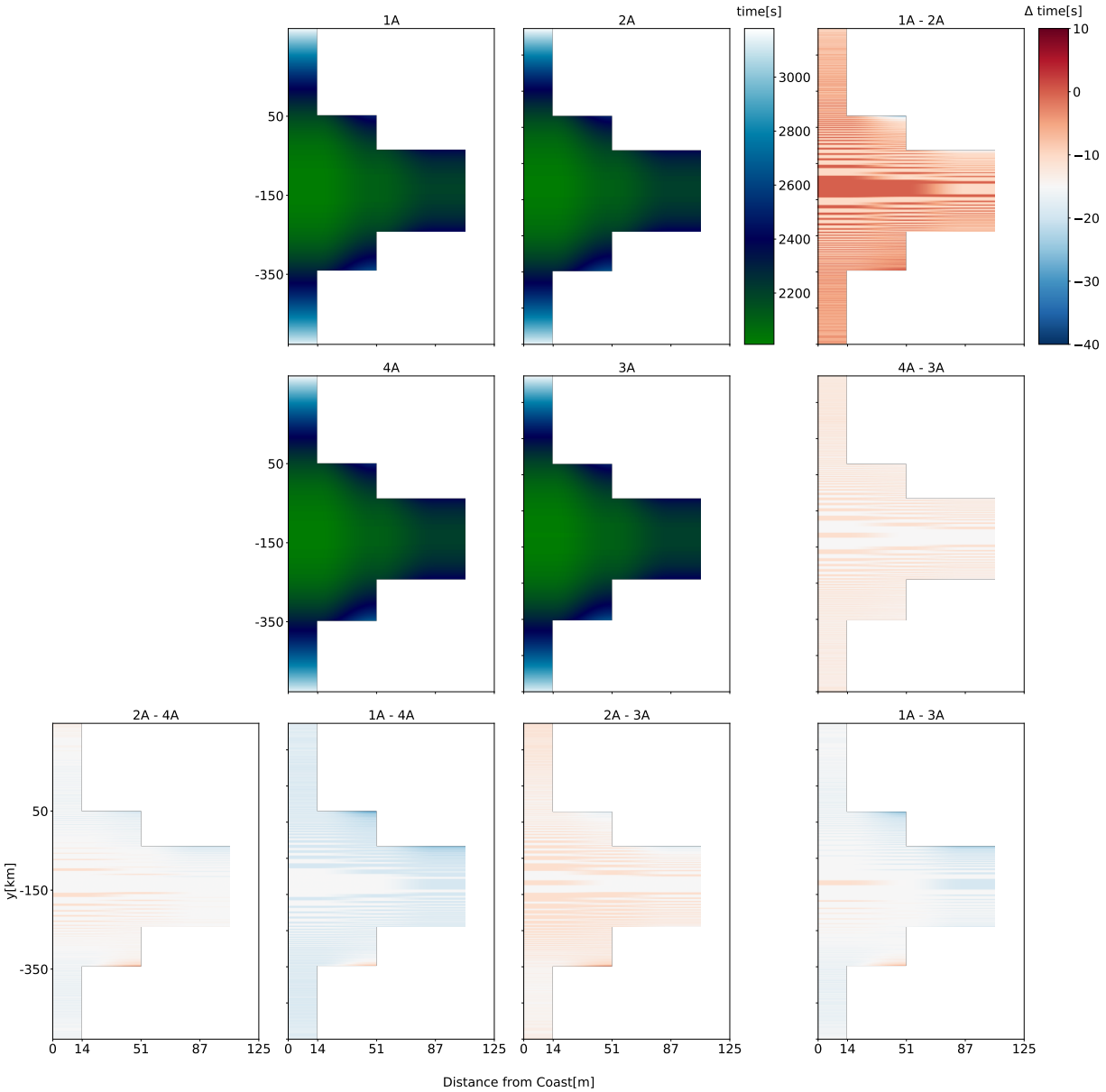



Figure 3.A.10: Inundation comparison for model 1.A-4.A. The hypocenter locations for the dynamic rupture simulations vary with depth.

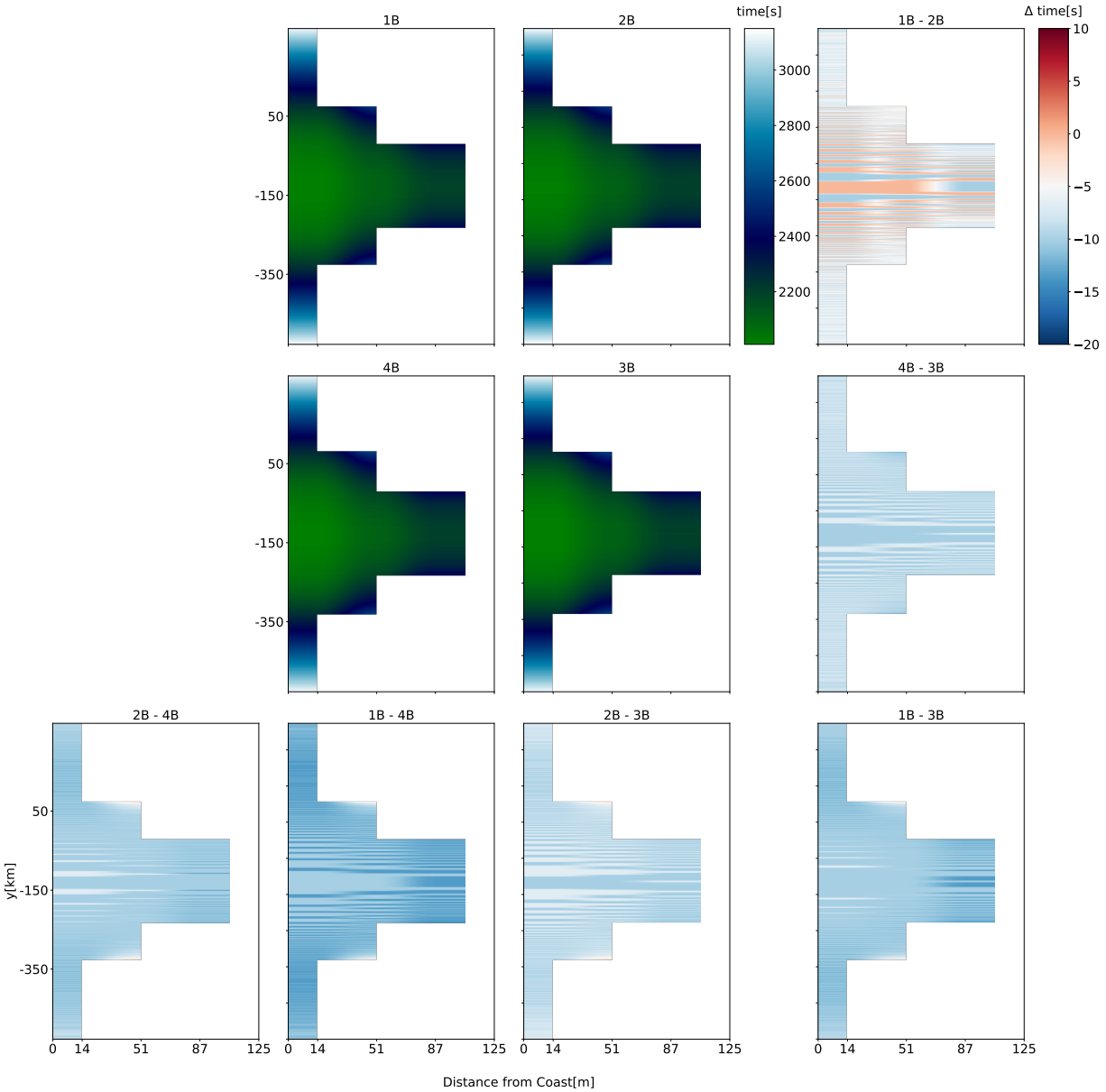



Figure 3.A.11: Inundation comparison for model 1.B-4.B. The hypocenter locations for the dynamic rupture simulations vary with depth.

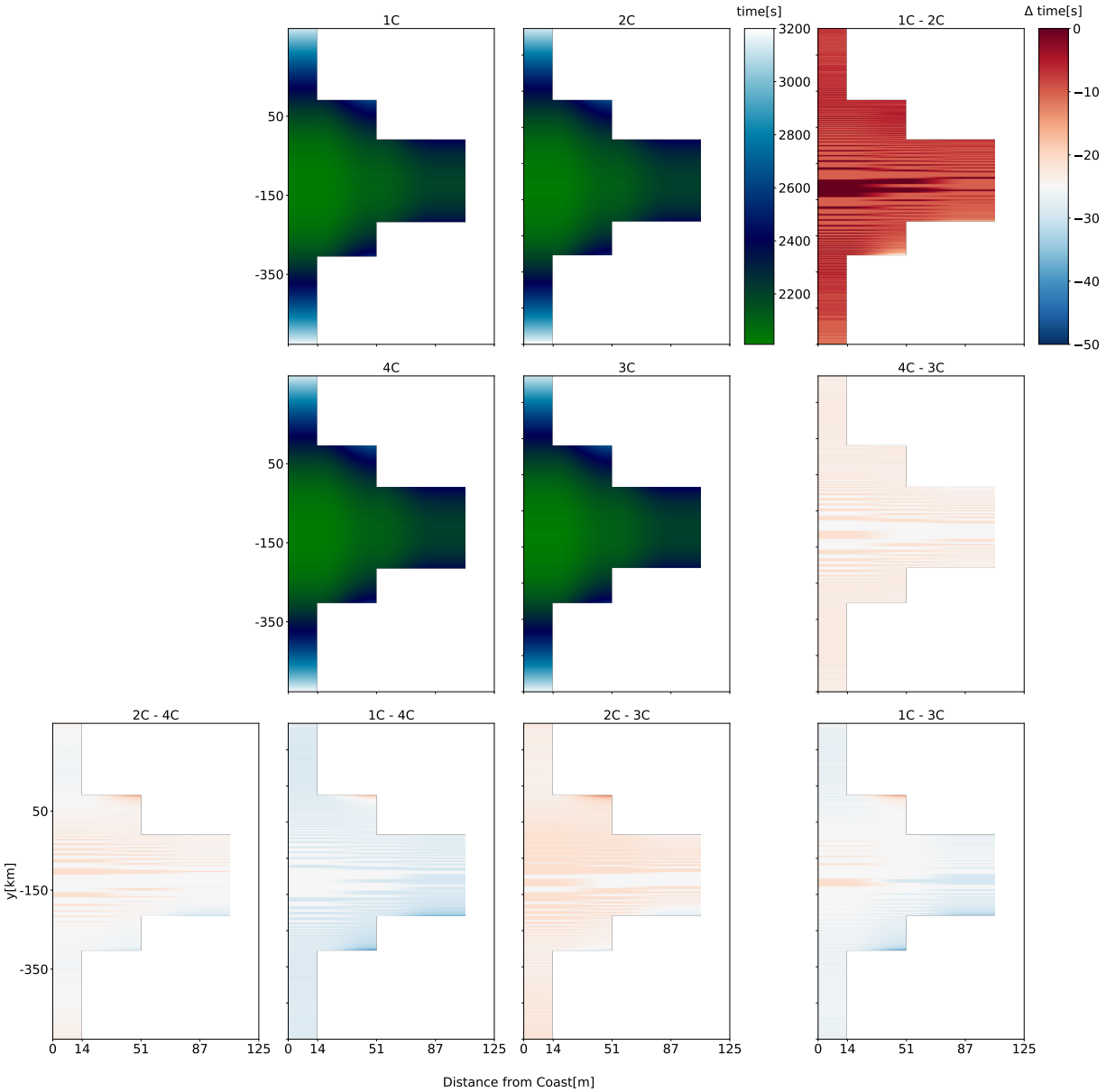



Figure 3.A.12: Inundation comparison for model 1.C-4.C. The hypocenter locations for the dynamic rupture simulations vary with depth.

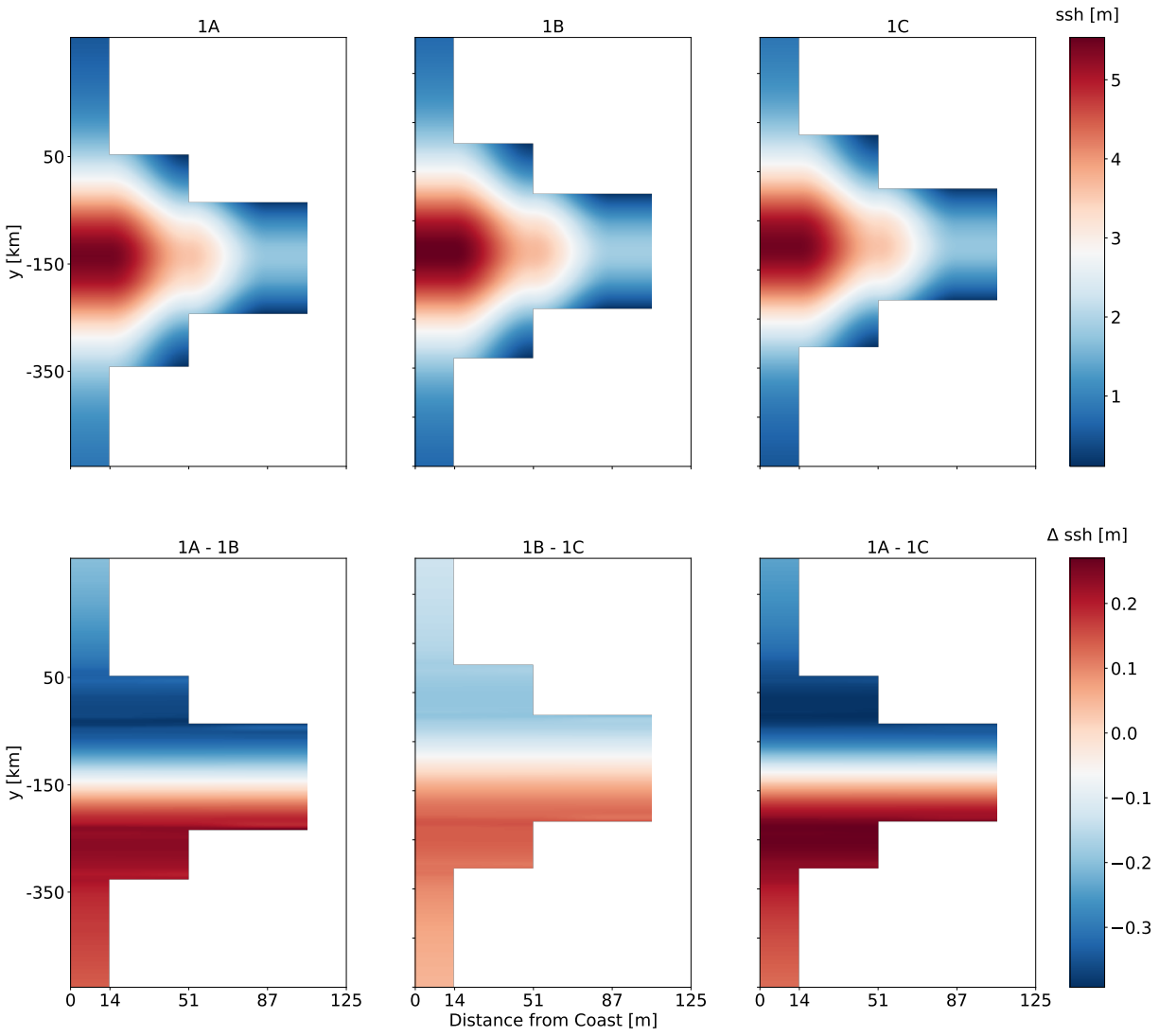



Figure 3.A.13: Comparison of the seasurface height at the moment when the tsunami arrives the coast for model 1A-C. The hypocenter locations for the dynamic rupture simulations vary along strike.

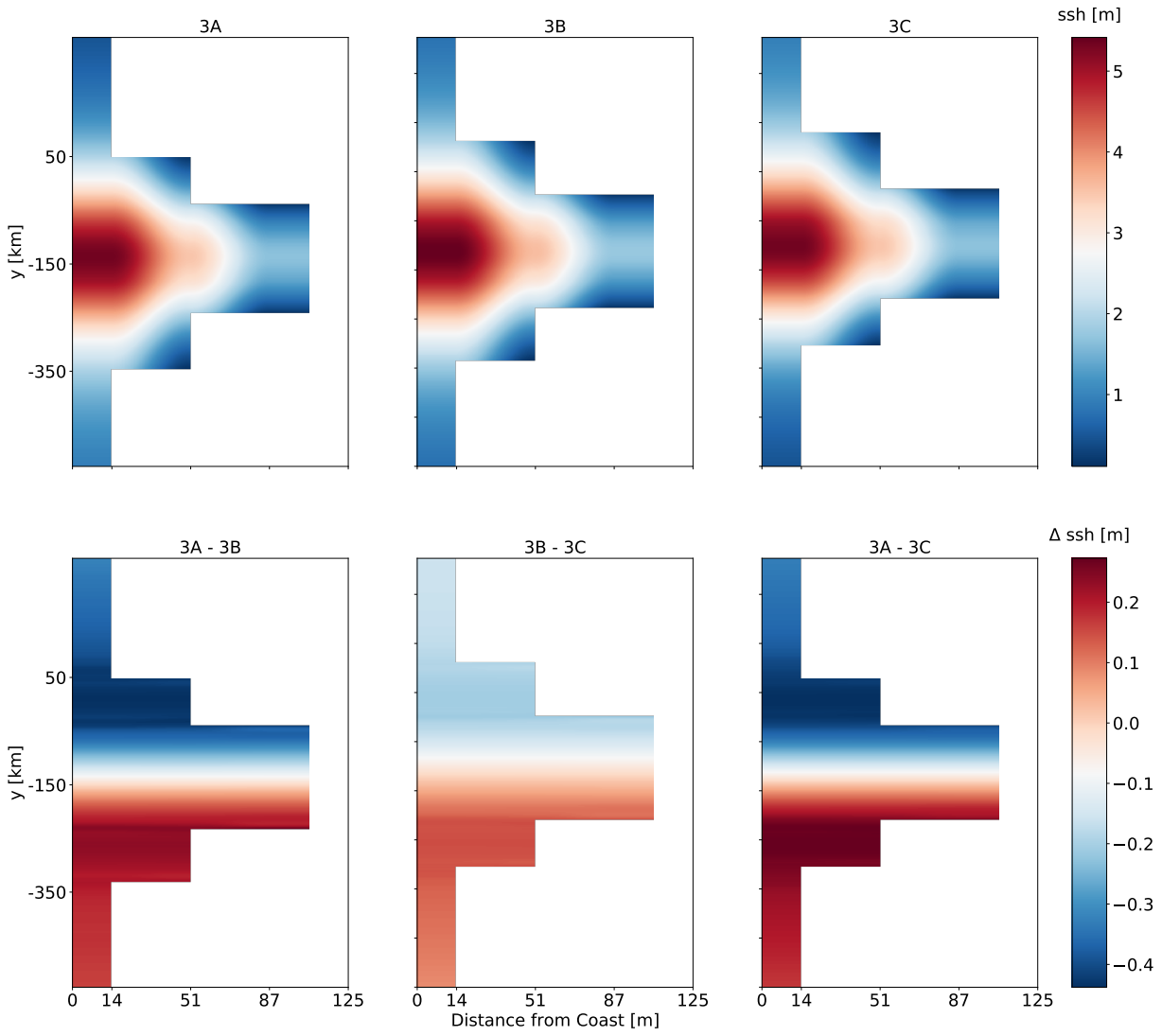



Figure 3.A.14: Comparison of the seasurface height at the moment when the tsunami arrives the coast for model 3A-C. The hypocenter locations for the dynamic rupture simulations vary along strike.

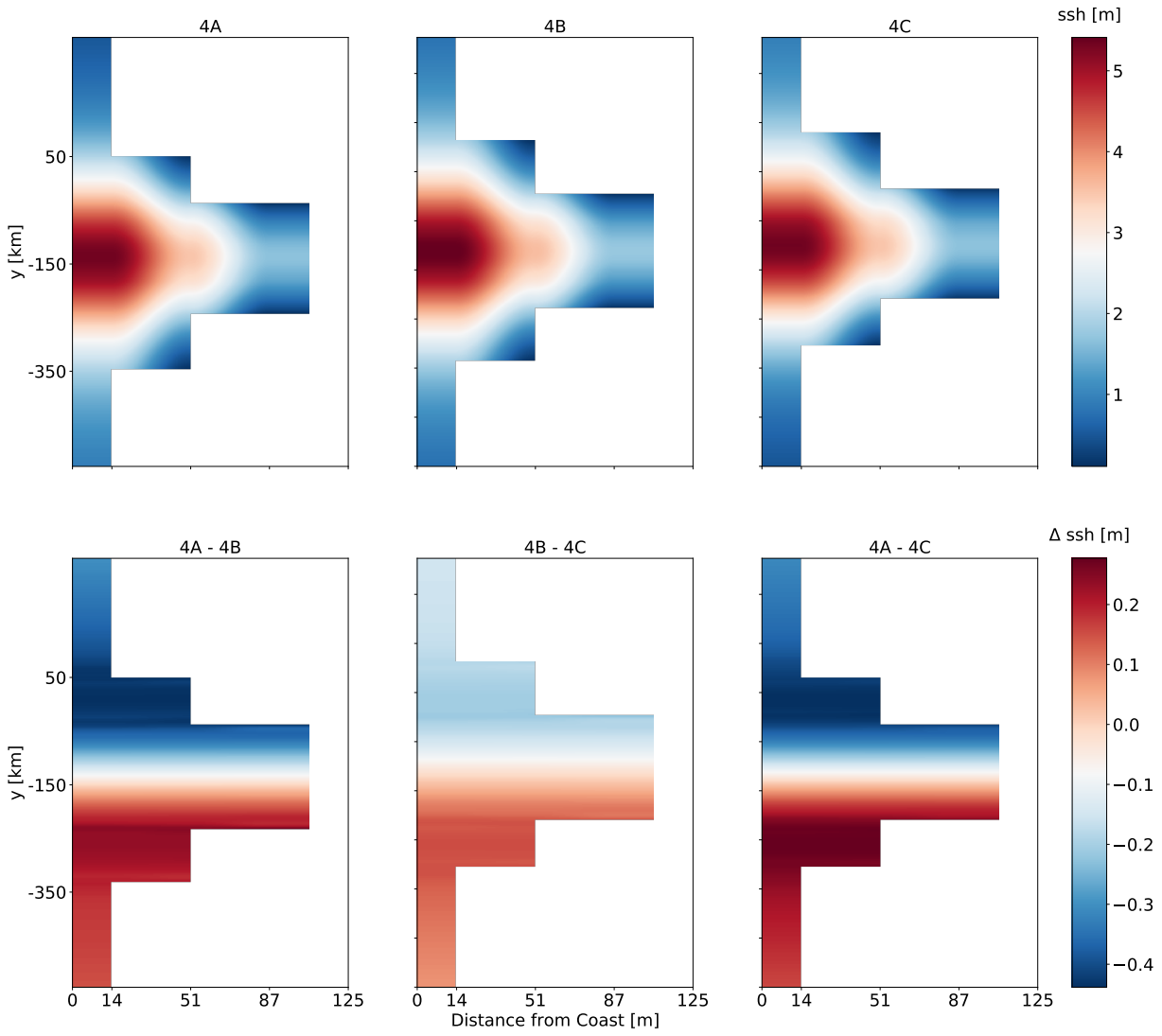



Figure 3.A.15: Comparison of the seasurface height at the moment when the tsunami arrives the coast for model 4A-C. The hypocenter locations for the dynamic rupture simulations vary along strike.

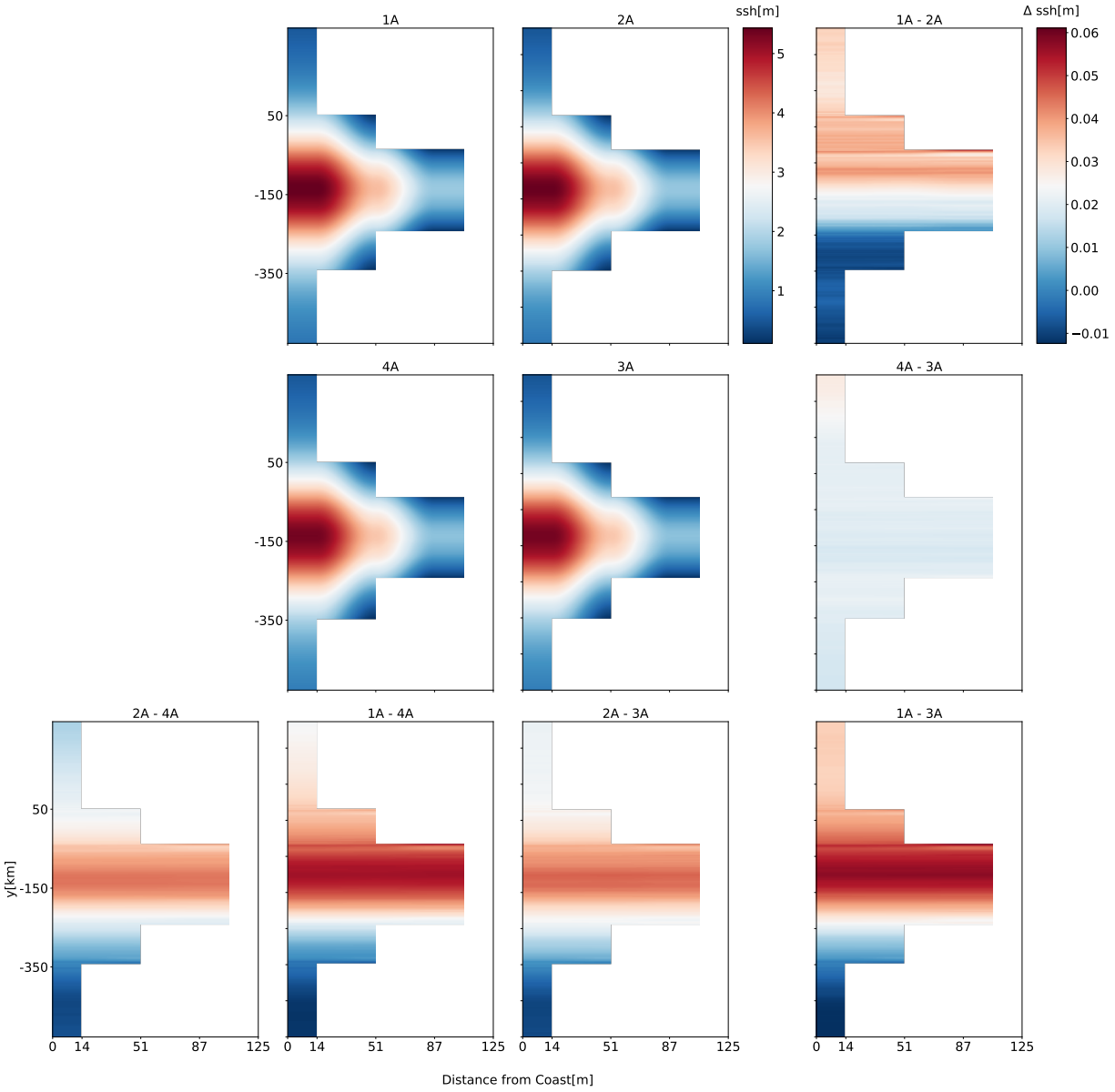



Figure 3.A.16: Comparison of sea surface height for wave fronts arriving at the coast for the models 1.A-4.A. The difference between the models is shown as Δssh.

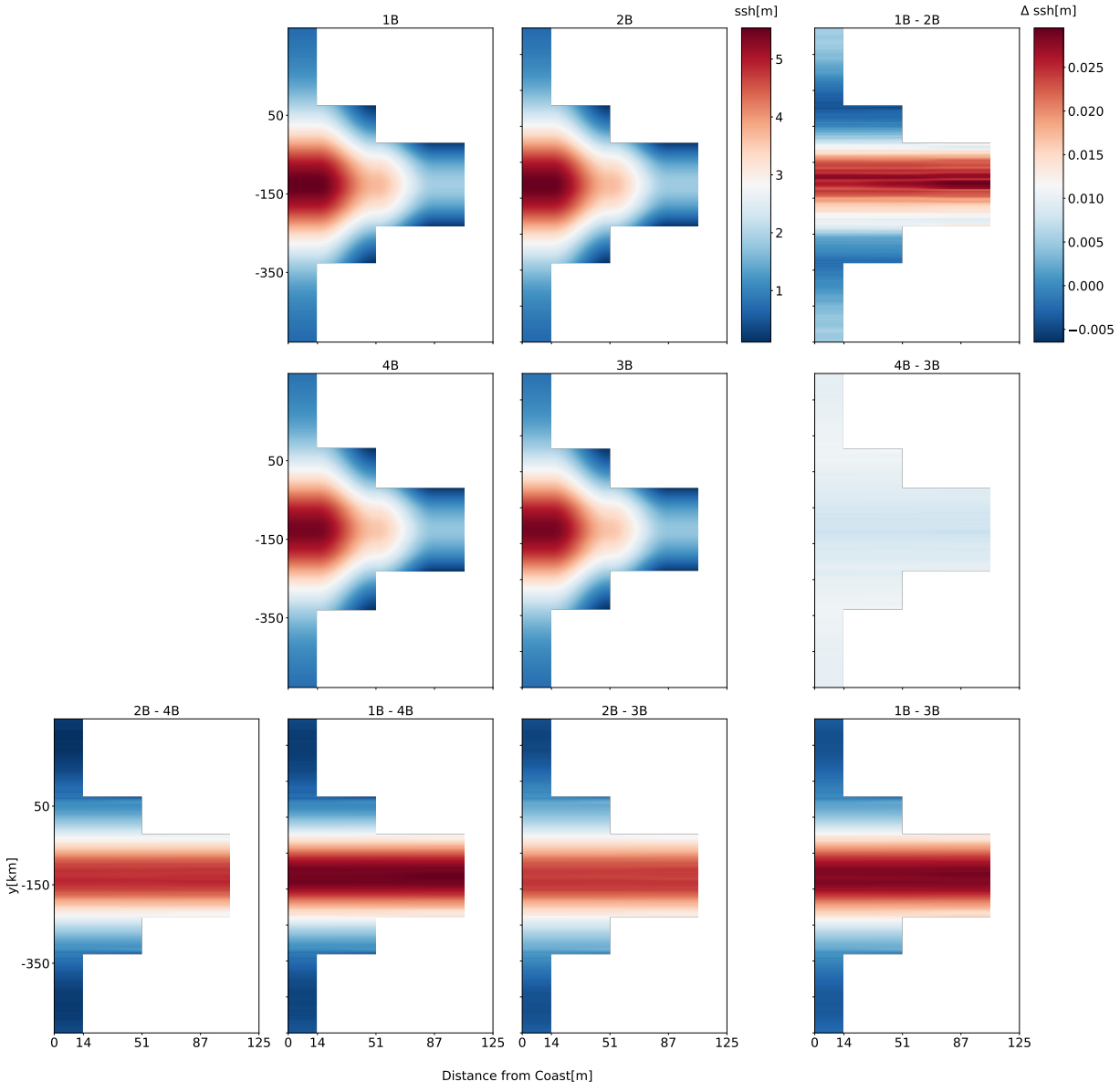



Figure 3.A.17: Comparison of the seasurface height at the moment when the tsunami arrives the coast for model 1.B-4.B. The hypocenter locations for the dynamic rupture simulations vary with depth .

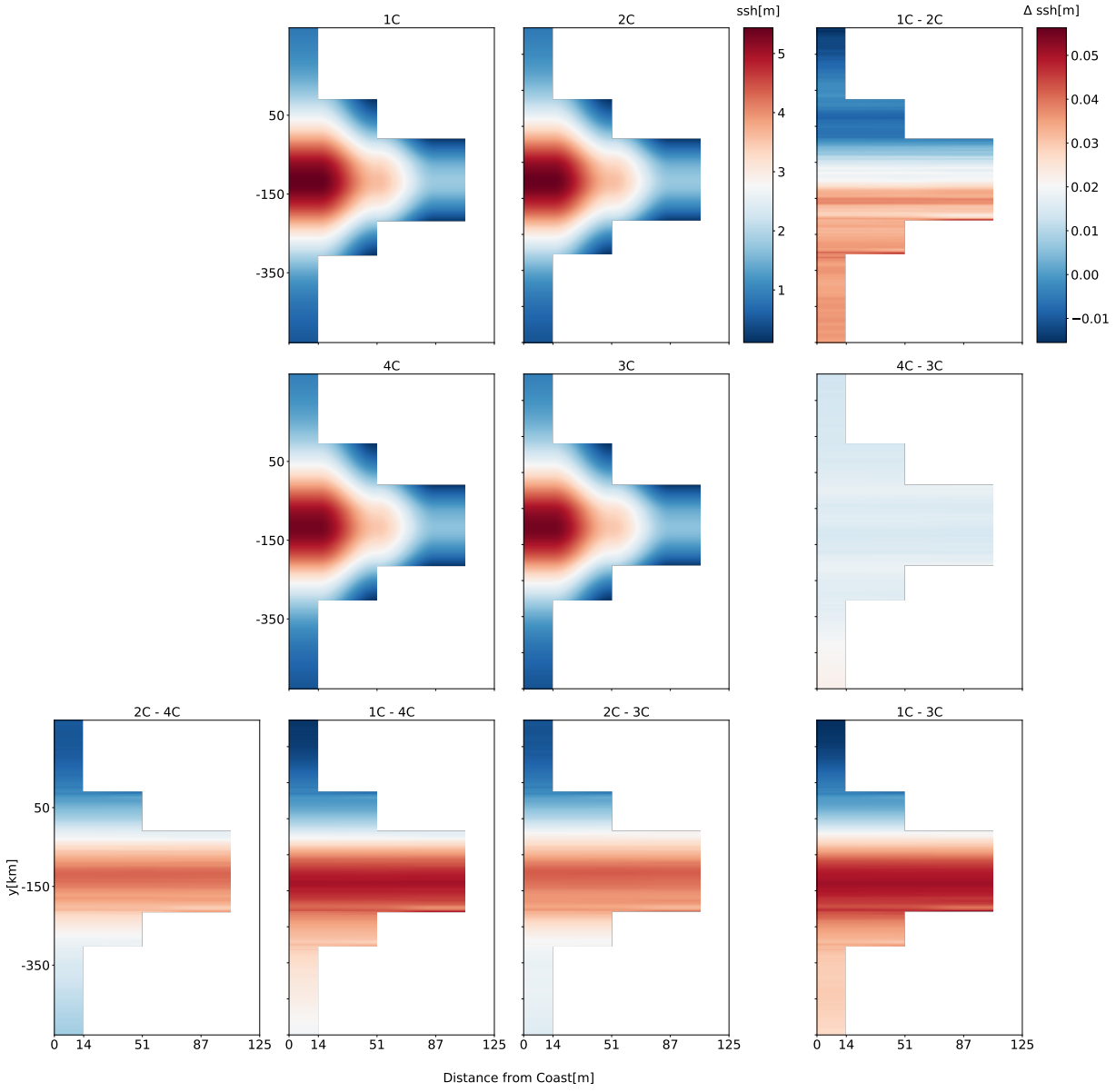



Figure 3.A.18: Comparison of the seasurface height at the moment when the tsunami arrives the coast for model 1.C-4.C. The hypocenter locations for the dynamic rupture simulations vary with depth.

# Chapter 4

# Dynamic rupture modeling of large earthquake scenarios at the Hellenic Arc towards physics-based seismic and tsunami hazard assessment


## Abstract

The Mediterranean Hellenic Arc subduction zone (HASZ) has generated several $M_W \geq 8$ earthquakes and tsunamis. Seismic-probabilistic tsunami hazard assessment typically utilizes uniform or stochastic earthquake models, which may not represent dynamic rupture and tsunami generation complexity. We present an ensemble of ten 3D dynamic rupture earthquake scenarios for the HASZ, utilizing a realistic slab geometry. Our simplest models use uniform along-arc pre-stresses or a single circular initial stress asperity. We then introduce progressively more complex models varying initial shear stress along-arc, multiple asperities based on scale-dependent critical slip weakening distance, and a most complex model blending all aforementioned heterogeneities. Thereby, regional initial conditions are constrained without relying on detailed geodetic locking models. Varying epicentral locations in the simplest, homogeneous model leads to different rupture speeds and moment magnitudes. We observe dynamic fault slip penetrating the shallow slip-strengthening region and affecting seafloor uplift. Off-fault plastic deformation can double vertical seafloor uplift. A single-asperity model generates a $M_W \sim 8$ scenario resembling the 1303 Crete earthquake. Using along-strike varying initial stresses results in $M_W \sim 8.0$-$8.5$ dynamic rupture scenarios with diverse slip rates and uplift patterns. The model with the most heterogeneous initial conditions yields a $M_W \sim 7.5$ scenario. Dynamic rupture complexity in prestress and fracture energy tends to lower earthquake magnitude but enhances tsunamigenic displacements. Our results offer insights into the dynamics of potential large Hellenic Arc megathrust earthquakes and may inform future physics-based joint seismic and tsunami hazard assessments.

# Plain Language Summary

The Mediterranean region around Greece and Crete is a hotspot for earthquakes and tsunamis. Here, the tectonic plates of Africa and Europe collide. History shows that this region has experienced damaging earthquakes. These earthquakes can cause tsunamis, sea waves that may lead to widespread destruction along coastlines. Our study aims to understand better how future earthquakes can be modeled. We use computer models to simulate different earthquake scenarios. Initially, we use simple conditions in our models, showing that if an earthquake propagated across the entire region, it could reach a moment magnitude of 9. When we move the earthquake's location within our model, the size and impact of the resulting earthquake change; some locations lead to larger seafloor displacements, which may cause more dangerous tsunamis. When introducing more complicated loading and fault strength conditions, the resulting earthquakes become smaller, consistent with historical observations. We also simulate how the fault-surrounding rocks can deform during an earthquake. Such deformations can increase the uplift of the seafloor, increasing the potential for tsunamis. Our work shows that computer modeling can be a powerful tool for understanding earthquakes and tsunamis and better prepare for future events.

## 4.1 Introduction

The Hellenic Arc is the most seismically active structure of the Mediterranean Sea (Vannucci et al., 2004; Ganas and Parsons, 2009). It is formed by the subduction of the African plate beneath the Aegean microplate and extends from Lefkada (western Peloponnese) in the west to east of Rhodes Island (Papazachos and Nolet, 1997; Papazachos et al., 2000; Piromallo and Morelli, 2003).

The northward movement of the African plate at 5 mm/yr (Ganas and Parsons, 2009; Vernant et al., 2014) and the fast southwest movement of the Aegean plate at 30.5 mm/yr (Reilinger et al., 2006) lead to relatively high convergence rates. Across the Hellenic Arc, GNSS inferred velocities are the fastest detected in the entire Mediterranean Sea (Kahle et al., 2000; McClusky et al., 2000). However, convergence is slower than in seismically very active subduction zones such as in Chile, Alaska, and Java (DeMets et al., 1990, 1994; Tregoning et al., 1994; Bourgois et al., 1996; McCaffrey, 1997a; Elliott and Freymueller, 2020) challenging observations of complete seismic cycles.

The slab rollback of the Hellenic Arc subduction forms the megathrust into an oval shape (Bohnhoff et al., 2005; Jolivet et al., 2013). Based on stress inversion using observed earthquake faulting mechanisms, Kkallas et al. (2021) identify five seismotectonic domains (Fig. 4.1.1). First, the outer Hellenic Arc, characterized by low-angle NW-SE thrust-faulting interface events with typical focal depths between 30 km and 40 km, is formed by NE-SW compression. Second, the sedimentary arc, including the islands (e.g., Peloponnese, Crete, and Karpathos), which is dominated by north-south oriented normal faults and earthquakes shallower than 30 km depth. Third, the Volcanic arc formed due to extension in the N-S direction, including normal faults that follow the observed volcanic arc strike. Furthermore, the southeastern Aegean region exhibits a combination of subduction-related faulting and southwest-northeast trending arc-parallel strike-slip faulting (Nyst and Thatcher, 2004), forming the Strabo and Pliny trenches and hosting seismicity with focal depths reaching up to 60 km. In the eastern section of the Hellenic Arc, there is a transition from subduction to different tectonic styles, characterized by a progressive rake rotation from a reverse to a strike-slip dominant mechanism as the convergence becomes more oblique. Finally, deeper (50-160 km) in-slab events are observed along strike-slip faults off the subducted slab and often include a notable thrust component.

When portions of a megathrust are considered to be significantly "coupled", they can accumulate pronounced long-term slip deficits, which may be released in earthquakes. Which portions of the Hellenic Arc are seismically coupled is debated. While Ganas and Parsons (2009) argue that the Hellenic Arc is frictionally fully locked, other authors infer that because of the high convergence rate and relatively low seismicity, a large part of the regional plate convergence must be accommodated aseismically (Jackson and Mckenzie, 1988; Becker and Meier, 2010; Shaw and Jackson, 2010; Vernant et al., 2014), or determine along-strike variations in coupling (Laigle et al., 2004). Becker and Meier (2010) assume periods of seismic locking followed by intermediate moment magnitude events and aseismic slip. Vernant et al. (2014) develop a block model of the Aegean to explore the degree of seismic coupling of the megathrust interface and restrict the seismogenic and fully coupled

portion of the Hellenic Arc to 15-45 km depth. They conclude that the absence of crustal shortening and the slip deficit rate of the Hellenic Arc are related to poorly consolidated and saturated sediments and characterize the upper 15 km as aseismic. Shaw and Jackson (2010) state that the plate interface never reaches the surface, and the plate motion discharges in sediment thickening and folding, forming an 8-10 km accretionary prism of thick seafloor sediments that are seismically decoupled from the oceanic crust.

Off-shore areas such as the Hellenic Arc subduction zone are difficult to study due to limited accessibility, specifically for satellite-based geodetic techniques. Additionally, a lack of quantitative data spanning complete seismic cycles of the Hellenic Arc significantly increases the uncertainty regarding the occurrence rate of large earthquakes. Even for recent events that are relatively well-recorded, the detailed rupture process often remains challenging to unravel (e.g., Chousianitis and Konca, 2021; Kiratzi et al., 2022; Ren et al., 2022). The conditions that may enhance or impede future large subduction zone earthquakes in the Hellenic Arc are poorly understood. Important aspects may be, among others, present-day near-trench and depth-extension of the seismic locking, frictional properties, regional stress state, and sediment strength (Lay et al., 2012; Sallarès and Ranero, 2019; Du et al., 2021; Wilson and Ma, 2021; Ulrich et al., 2022; Jeandet Ribes et al., 2023). Specifically, the potential near-surface rupture processes that may control large, vertical seafloor displacements and tsunami hazards are challenging to assess.

Geodetic coupling can help to inform the initial stress conditions of dynamic rupture models (Hok et al., 2011; Ramos and Huang, 2019; Yang et al., 2019; Noda et al., 2021; Gu et al., 2023). The product of slip rate deficit (inferred from seismic coupling studies) and assessed strain accumulation times allows inferring slip deficit distribution and associated static stress change (Ramos and Huang, 2019). Lindsey et al. (2021) show that frictionally unlocked regions above the locked portion of the megathrust can yet exhibit a slip rate deficit of over 80% of the plate convergence rate, which is stress-shadowed by the deeper locked megathrust. However, detailed geodetic constraints are yet unavailable for the Hellenic Arc region.

Dynamic earthquake rupture simulations (e.g., Harris et al., 2018) combine the frictional failure of rocks and seismic wave propagation in a non-linear and multi-physics manner to produce physics-based forecasts and provide insight into the poorly understood fundamental processes of earthquake faulting. As input, dynamic rupture simulations require, among other parameters, fault geometry, on-fault prestresses, and frictional fault strength descriptions (Ramos et al., 2022). This input is generally challenging to constrain observationally, especially in off-shore subduction regions, like the Aegean Sea, with sparse near-trench observations (Ulrich et al., 2022).

We present an ensemble of ten 3D dynamic rupture scenarios of megathrust earthquakes across the Hellenic Arc, including realistic slab geometry, topography, and off-fault plastic deformation, to help address the lack of quantitative observations of historical large earthquakes and a heterogeneous plate coupling model. Our models help better understand how large ruptures may start, propagate, and arrest and which seafloor deformation might result. We develop four large counterfactual scenarios (Woo, 2018) and models that resemble historic tsunamigenic events. Our findings may offer constraints for dynamically plausi-

ble slip distributions, tsunami generation mechanisms, and surface deformation, informing future physics-based probabilistic seismic hazard analysis (PSHA), seismic-probabilistic tsunami hazard assessment (S-PTHA), and joint evaluation of seismic and tsunami hazards in subduction zones.

We explore various approaches for realizing 3D dynamic rupture scenarios on the shallowly dipping Hellenic Arc subduction interface. Assuming homogeneous along-arc stresses and varying hypocenter locations result in counterfactual margin-wide rupture scenarios (models HE, HM, and HW). Dynamic rupture scenarios can penetrate velocity-strengthening fault regions and drastically vary in their amount of shallow slip, depending on the hypocenter location. We also assess the effects of off-fault deformation (model HEP) on seafloor displacement. We then analyze an asperity model (HEA) that may resemble the 1303 Crete earthquake, constrained by subduction earthquake scaling relations (Strasser et al., 2010). Next, we explore heterogeneous initial stress conditions constrained by stress inversions (Kkallas et al., 2021) (models HES and HMS) with epicenters located in the east and center of the Hellenic Arc megathrust. When we incorporate prestress variations, the dynamic rupture extent is limited. We explore how increasing initial stress complexity affects rupture propagation, shallow slip, and seafloor displacement. We then implement fractally distributed frictional asperities (model DCA), with size-dependent critical slip-weakening distance ($D_c$), following Ide and Aochi (2005) and Gallovič and Valentová (2023). Finally, we investigate a model incorporating segmented fault loading and multi-scale asperities (model DCAS). We compare results to existing uplift data in the Hellenic region and discuss implications on tsunami hazards for all dynamic rupture models.

### 4.1.1 Historic tsunamigenic earthquakes: the AD 365 & 1303 events

Historically, the Aegean region hosted at least two $M_W \geq 8$ events, both of which generated regional tsunamis: the AD 365 Crete event, located offshore west of Crete, and the 1303 Crete event, located offshore further east between Crete and Karpathos.

The AD 365 earthquake likely occurred due to thrust faulting beneath Crete (Shaw et al., 2008). The exact location and whether or not it was located on the Hellenic Arc subduction interface itself or on a branching splay fault remains unclear (Papazachos and Nolet, 1997; Bohnhoff et al., 2001; Stiros and Drakos, 2006; Shaw et al., 2008; Ambraseys, 2009). Due to the earthquake and the associated tsunami, thousands of people were killed (Kelly, 2004; Stiros, 2020). Archaeological observations confirm seismic destruction in Crete (DiVita, 1979; Markoulaki, 1987; DiVita, 1995). This earthquake may have produced up to ∼9 m coseismic uplift (Flemming, 1978; Pirazzoli et al., 1982, 1992; Stiros and Drakos, 2006; Shaw et al., 2008). Sedimentology, radiocarbon data, field observations, and seamarks around the shore of Crete evidence a tsunami (Spratt, 1865; Scheffers and Scheffers, 2007; Shaw et al., 2008).

Several studies attempted to reproduce the tsunami generated by the historical AD 365 Crete event using different static or kinematic earthquake models (Tinti et al., 2005;

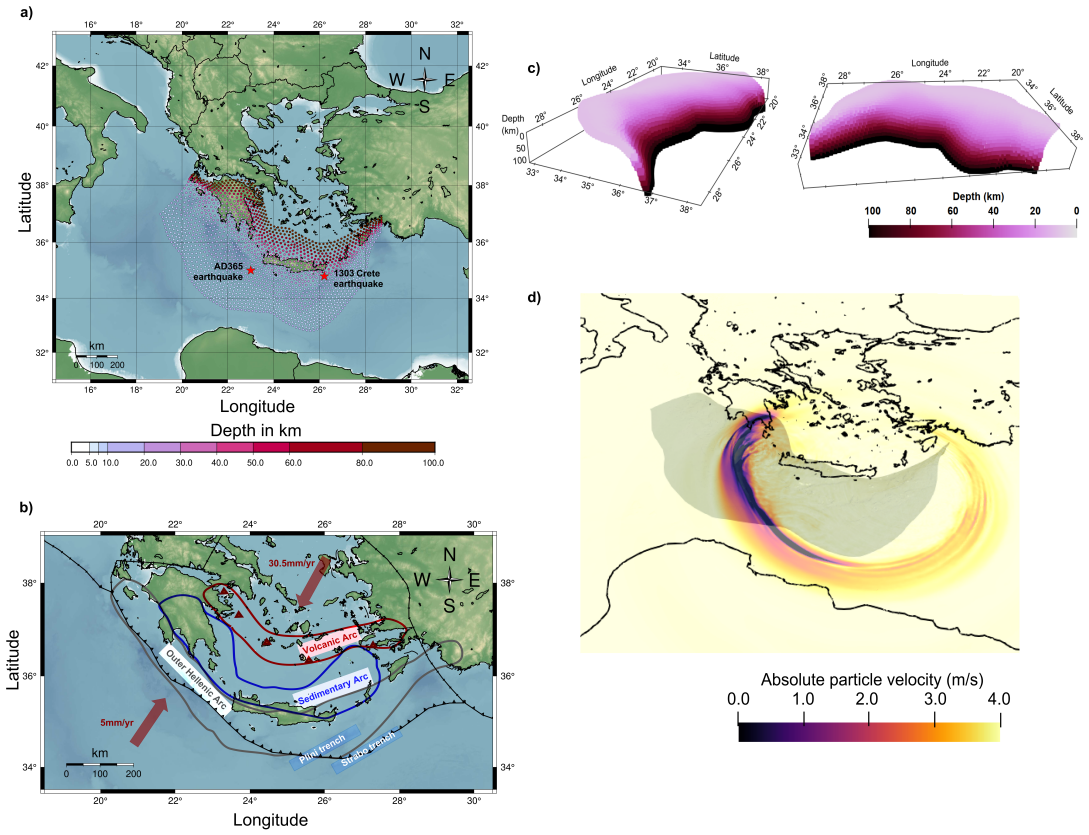



Figure 4.1.1: **Tectonic constraints for 3D dynamic rupture scenarios in the Hellenic Arc area: a)** Hellenic Arc megathrust geometry (Basili et al., 2013) and modeled domain extent. Depth is colored from shallow (white) to deep (purple). The red stars mark the hypocenters of the historical $M_W \sim 8$ AD 365 and 1303 Crete earthquakes that generated destructive tsunamis. **b)** Zoomed-in view of **a)** focusing on the northern trench as the main tectonic feature including plate boundaries and motions of the African and Eurasian Plates, and subduction zone domains. The main plate boundaries (Bird, 2003) are marked with black lines. Subduction zones are also labeled with black triangles, pointing toward subduction. Red arrows indicate the Aegean (30.5 mm/yr Reilinger et al. (2006)) and the African (5 mm/yr Ganas and Parsons (2009); Vernant et al. (2014)) plate motions resulting in a convergence rate of ∼35 mm/yr. A grey line frames the outer Hellenic Arc, a blue line frames the Sedimentary Arc, and the Volcanic Arc is framed by a red line (Kkallas et al., 2021). In-slab events lay below the transition from Sedimentary to Volcanic Arc. **c)** 3D views of the modeled Hellenic arc megathrust. **d)** Modeled absolute particle velocity [m/s] across the Earth's surface with topo-bathymetry in the reference scenario at simulation time 100 s. High-amplitude surface waves extend from Greece and Turkey until the coast of Lybia and Egypt, suggesting that the ground shaking from a margin-wide megathrust event on the Hellenic Arc could directly affect large parts of the eastern Mediterranean.

Papadimitriou and Karakostas, 2008; Shaw et al., 2008; England et al., 2015) with fault lengths ranging from 100 km to more than 200 km, dipping at 20-45 °. The earthquake may have occurred on a splay fault branching the main megathrust (Shaw et al., 2008; Shaw and Jackson, 2010; Stiros, 2010; Saltogianni et al., 2020) or on an antithetic normal fault (Ott et al., 2021), which can explain the high amount of uplift observed on Crete. Papadimitriou and Karakostas (2008) model the AD 365 earthquake on a thrust fault parallel to the megathrust. With a maximum slip of 25 m, a moment magnitude of $M_W$8.4, and a seafloor uplift of up to ∼9 m near southwest Crete, they can fit observations of co-seismically uplifted coastal material from Pirazzoli et al. (1996). England et al. (2015) use the rupture models of Shaw et al. (2008) and Papadimitriou and Karakostas (2008) as sources for a tsunami simulation. While the source of Shaw et al. (2008) produces a smaller tsunami with wave heights of up to ∼7 m, the model from Papadimitriou and Karakostas (2008) generates wave heights of ∼10 m, which fit observations better.

The 1303 Eastern Crete event is among the best-documented historical events in the Mediterranean Area (Yolsal et al., 2007). It probably occurred on a thrust fault (Yolsal-Çevikbilen and Taymaz, 2012), which might be the Hellenic Arc itself or a smaller fault parallel to the megathrust. The earthquake caused a tsunami that affected a large area and was recorded in Crete, Peloponnese, Rhodes, Cyprus, Antalya in south-west Turkey, Acre in Israel, the Adriatic Sea and the Alexandria-Nile delta in Egypt (Ambraseys, 1962, 1994, 2009; Antonopoulos, 1980; Guidoboni and Comastri, 1997; Guidoboni et al., 2005; Altinok and Ş. Ersoy, 2000; Soloviev et al., 2000; Yolsal et al., 2007).

### 4.1.2 Seismic-tsunami hazard assessment in the Hellenic Arc region

Both historic, devastating, tsunamigenic $M_W \geq 8$ events and more recent, smaller earthquakes in the Hellenic Arc region have motivated local and regional earthquake-tsunami hazard studies (Tinti et al., 2005; Lorito et al., 2008; Papoulia et al., 2010; Lorito et al., 2015; Tonini et al., 2011; Grezio et al., 2012; Sørensen et al., 2012; Selva et al., 2016; Davies et al., 2018; Volpe et al., 2019; Scala et al., 2020; Basili et al., 2021; Selva et al., 2021). Tinti et al. (2005) simulated tsunamis initiated by sources related to the AD 365 and 1303 Crete earthquakes, which they assumed to be running parallel to the Hellenic megathrust. Lorito et al. (2008) determined the geometry, kinematics, and size of generally feasible maximum moment magnitude events in the Hellenic Arc region and simulated the related tsunamis. They find that these events produce tsunami waves of up to 5 m in height. Sørensen et al. (2012) developed the first S-PTHA model in the Mediterranean area. They find that the tsunami hazard in the eastern Mediterranean is governed by earthquakes along the Hellenic arc and estimate a near 100% probability of tsunami waves exceeding 1 m in the next 30 years. Recent studies (Selva et al., 2016; Scala et al., 2020; Basili et al., 2021) focus on a formal aleatory and epistemic uncertainty quantification in S-PTHA, while including more

detailed information on the fault structure and account for the effects on the hazard model of potential shallow slip amplification.

3D dynamic rupture models, simulating spontaneously evolving rupture propagation along the megathrust geometry, have not been explored for the Hellenic arc. Yet, physically consistent earthquake scenarios from 3D dynamic rupture modeling and associated time-dependent surface displacements could complement stochastic earthquake source models typically used in S-PTHA. Stochastic earthquake slip models in combination with efficient tsunami solvers are convenient for S-PTHA (e.g., McCloskey et al., 2008; Davies et al., 2018; Scala et al., 2020), as they are computationally cheap, and therefore allow exploring the expected natural - assumed aleatory - variability of earthquake slip distributions to a great extent. Alternatively, plausible source models may be obtained from kinematic source models of past earthquakes based on seismic inversion data (Lorito et al., 2008; Song and Somerville, 2010; Scala et al., 2020). However, questions regarding their use to constrain potential future events remain; specifically, it remains debated whether information based on past earthquakes is sufficient to constrain the source characteristics of future events. Kinematic source models can be designed to match empirical earthquake scaling laws and to produce a range of magnitudes to aid hazard assessment (e.g., Marafi et al., 2019), but are not necessarily compatible with the physical laws of earthquake faulting (e.g., Tinti et al., 2021). Static source models, however, neglect the tsunami-earthquake interaction during the co-seismic seafloor uplift and tsunami generation process. A tsunami can evolve and propagate during its generation phase, especially for long-duration, large, and/or slow earthquakes. This effect is only captured when sourcing the tsunami model using the complete time-dependent co-seismic uplift phase (Madden et al., 2020; Wirp et al., 2021; Abrahams et al., 2023).

3D physics-based earthquake modeling may contribute to a better understanding of earthquake and tsunami source effects, benefiting S-PTHA studies. In particular, it can help to decipher the effects of off-fault damage and heterogeneous on-fault material properties on near-surface slip amplifications and associated seafloor uplift towards a complete understanding of tsunami generation and hazard assessment (Behrens et al., 2021). Dynamic rupture simulations model how earthquakes nucleate, propagate, and arrest in a mechanically self-consistent manner. Due to computational advances, 3D dynamic rupture simulations on the scale of subduction zones are now feasible(Hok et al., 2011; Galvez et al., 2016; Uphoff et al., 2017; Ramos and Huang, 2019; Krenz et al., 2021).

Recent studies (Galvez et al., 2016; Murphy et al., 2016, 2018; Uphoff et al., 2017; Ma and Nie, 2019; Ramos and Huang, 2019; Saito et al., 2019; van Zelst et al., 2022; Li et al., 2023) show that physics-based dynamic rupture models of complex fault systems and megathrusts offer feasible source descriptions for tsunami modeling. These models can provide a time-dependent tsunami source by linking the seafloor displacements and velocities to the tsunami model (Ryan et al., 2015; Lotto et al., 2017b; Amlani et al., 2022; Ulrich et al., 2019b, 2022; Madden et al., 2020; Kutschera et al., 2024a). In this way, the effects of reflected waves at the free-surface in the accretionary wedge (Nielsen, 1998; Lotto et al., 2017b; van Zelst et al., 2019), spontaneously evolving shallow slip amplification (Rubin and Ampuero, 2007; Ma and Beroza, 2008; Scala et al., 2017) caused by bi-material

effects or up-dip rupture propagation, and the impact of off-fault plastic yielding on seismic ground motions (Roten et al., 2014; Xu et al., 2015; Roten et al., 2017) and seafloor displacements (Ma and Hirakawa, 2013; Ma and Nie, 2019; Wilson and Ma, 2021; Ulrich et al., 2022) can be taken into account.

## 4.2 Reference 3D dynamic rupture model setup

We here describe the reference dynamic rupture modeling parameters and model setup forming the base of all ten scenarios. We use the open-source software package SeisSol (`https:/seissol.org`) (e.g., de la Puente et al., 2009; Pelties et al., 2012, 2014) on high-performance computing infrastructure. Our SeisSol simulations simultaneously solve for seismic wave propagation, frictional failure on prescribed fault interfaces, and (visco-)plastic Drucker-Prager off-fault plastic deformation (Andrews, 2005; Wollherr et al., 2018). SeisSol is based on an Arbitrary high-order accurate DERivative Discontinuous Galerkin method (ADER-DG) (Dumbser and Käser, 2006; Käser and Dumbser, 2006)). It uses unstructured tetrahedral meshes enabling models incorporating geometrical complexities (e.g., Ulrich et al., 2019a; Wolf et al., 2020; Li et al., 2023; Taufiqurrahman et al., 2023), such as the shallowly dipping megathrust interface geometry of the Hellenic Arc. In all models, frictional failure and fault slip are governed by a linear slip weakening friction law (Ida, 1972). We adopt the isotropic version of the 1D velocity model PREM (Preliminary Reference Earth Model) (Dziewonski and Anderson, 1981; Bormann, 2009).

### 4.2.1 Geometric model, mesh, and resolution

We build a geometric model of the eastern Mediterranean region, including the Hellenic subduction zone, the Greece and Turkey coastlines, and parts of northern Africa, as well as Italy (Fig. 4.1.1), incorporating topography and bathymetry (Group, 2019) at 15 arc seconds or ∼380 m resolution. We use the Hellenic Arc subduction interface geometry from the European Database of Seismogenic Faults (EDSF, Basili et al. (2013)) at $\sim 0.2\,^{\circ}$ resolution, which is inferred from seismicity distributions, receiver functions, seismic imaging, velocity-gravity models, GPS velocities, geological observations, and topographic analyses. The same fault model was used in recent tsunami hazard studies (Selva et al., 2016; Scala et al., 2020). The modeled slab is 800 km wide, 600 km long, and reaches 90 km depth. Our model domain spans ∼4400 by ∼2800 by ∼500 km.

We use an adaptive unstructured tetrahedral mesh, refined towards the fault and the free surface. Our resulting mesh consists of 38.89 million elements. The smallest elements are used to discretize the megathrust fault interface and have a 650 m edge length. We use high-order accuracy in space and time using polynomial basis functions of order $p$ =5. Thus, each triangular element face, which is assigned a dynamic rupture internal boundary condition, is discretized by $(p+2)^2$ Gauss points.This allows adequately resolving the minimum process zone width at the rupture tip, which we measure as ∼1500 m following Wollherr et al. (2018). We calculate the resolution of the seismic wavefield characterized

by the maximum frequency resolved according to

$$f \approx V_s/\Delta x/elements\,per\,wavelength \tag{4.1}$$

with $\Delta x$ defining the local element size, $V_s$ the s-wave speed, and the minimum required $elements\,per\,wavelength = 2$ for order 6 accuracy in space and time (Käser et al., 2008; Pelties et al., 2014). This mesh resolution allows us to resolve the seismic wavefield up to 2.7 Hz close to the slab. Resolution gradually decreases with static coarsening of the mesh away from the slab interface. However, owing to the relative proximity of the slab to the free-surface, we still achieve a resolution of 1.75 Hz at the free surface above the slab (Fig. 4.A.1).

### 4.2.2 Ambient prestress and relative fault strength

In all our models, we constrain the tectonic background prestress state and megathrust strength at the subduction scale using a regional stress tensor approach (Ulrich et al., 2022) and seismo-tectonic observations, the Mohr-Coulomb theory of frictional failure, and assumptions on depth-dependent pore fluid pressure. We fully constrain a Cartesian prestress tensor representing a regional ambient loading by constraining the orientation of the maximum compressive principal stress $\sigma_1$ (3 angles), the stress shape ratio $\Phi$ (eq. 4.2), the maximum relative prestress ratio $\mathcal{R}_0$ (eq. 4.3), and the effective vertical stress gradient.

We follow Angelier (1990) and Lund and Townend (2007) to define the stress shape ratio, balancing the principal stress magnitudes, $\sigma_i$, as

$$\Phi = \frac{\sigma_2 - \sigma_3}{\sigma_1 - \sigma_3}, \tag{4.2}$$

Constraining $\Phi$ from stress inversions (Kkallas et al., 2021) is challenging. In the following, we assume $\Phi$ =0.4, which is consistent with stress inversion results of interplate events around Crete (Bohnhoff et al., 2005).

Closeness to the onset of frictional failure can be quantified by the relative prestress ratio $\mathcal{R}$ (e.g., Aochi and Madariaga, 2003) defined as:

$$\mathcal{R} = \frac{\Delta\tau}{\Delta\tau_b} = \frac{\tau - \mu_\mathrm{d}\sigma_n'}{c + (\mu_\mathrm{s} - \mu_\mathrm{d})\sigma_n}. \tag{4.3}$$

$\mathcal{R}$ relates the potential stress-drop $\Delta\tau$ to the frictional breakdown strength-drop $\Delta\tau_b$. $c$ is the frictional cohesion, and $\mu_\mathrm{d}$ and $\mu_\mathrm{s}$ are the dynamic and static friction coefficients, respectively. The strength parameter $S$ is directly related to $\mathcal{R}$, as $S = \frac{1}{R} - 1$. We define $\mathcal{R}_0 \geq \mathcal{R}$ as the maximum possible value of $\mathcal{R}$. $\mathcal{R} = \mathcal{R}_0$ for faults optimally orientated towards the regional stress tensor. $\mathcal{R}_0 = \mathcal{R} = 1$ would characterize a critically prestressed optimally oriented fault. For all models, we define their relative fault strength with respect to the frictional strength drop. We use $\mathcal{R}_0 = 0.7$ (S=0.43), implying that fault stress drop can reach a maximum of 70% of the breakdown strength drop. This is large enough to

propagate earthquake rupture on a significant portion of the megathrust but small enough to ensure realistic rupture characteristics such as rupture speed and stress drop.

Many megathrusts are characterized by non-Andersonian prestress conditions, particularly in regions with complex tectonics (Hardebeck, 2015). The crust in the Mediterranean Sea is comparably old and cold (Müller et al., 2008; Speranza et al., 2012; Granot, 2016; Bocchini et al., 2020) potentially implying a low-stress environment. We constrain the stress shape ratio from stress inversion results of Bohnhoff et al. (2005). In all our models, we assume a non-Andersonian prestress state, where none of the principal stresses is purely vertically oriented (Fig. 4.2.1). In the reference prestress model, used in scenarios HE, HM, HW, HEP, and DCA (as defined in Figure 4.2.1 and Sections 4.1 and 4.3), the maximum compressive stress, $\sigma_1$, is assumed shallowly plunging, $\sigma_2$ is horizontal, and $\sigma_3$, normal to the $\sigma_1$-$\sigma_2$ plane, is steeply plunging. Through static analysis and trial-and-error dynamic rupture simulation, we selected this pre-stress condition to optimally pre-stress the slab in the hypocentral region of the reference prestress model setup.

The components of the stress tensor are defined as follows:

$$\sigma'_{zz}(z) = \rho g z - P_f(z) \tag{4.4}$$

$$\sigma'_{xx}(x,y,z) = \Omega(b_{xx}(\sigma'_{zz}(z) + P_f(z)) - P_f(z)) + (1+\Omega)\sigma'_{zz}(z)\,, \tag{4.5}$$

$$\sigma'_{yy}(x,y,z) = \Omega(b_{yy}(\sigma'_{zz} + P_f(z)) - P_f(z)) + (1+\Omega)\sigma'_{zz}(z)\,, \tag{4.6}$$

$$\sigma'_{xy}(x,y,z) = \Omega(b_{xy}(\sigma'_{zz}(z) + P_f(z)) - P_f(z))\,, \tag{4.7}$$

$$\sigma'_{xz}(x,y,z) = \Omega(b_{xz}(\sigma'_{zz}(z) + P_f(z)) - P_f(z))\,, \tag{4.8}$$

$$\sigma'_{yz}(x,y,z) = \Omega(b_{yz}(\sigma'_{zz}(z) + P_f(z)) - P_f(z))\,, \tag{4.9}$$

Where $(b_{ij})$ is a normalized tensor constrained by the orientation of $\sigma_1$, and by $\phi$ and $\mathcal{R}_0$, and where $\Omega$ is a depth-dependent analytical function used to taper deviatoric stresses at the brittle-ductile transition below 50 km as:

$$\Omega = \max(0, \min(1, 1 + (z + 50{,}000\ m)/150{,}000\ m)\,. \tag{4.10}$$

We perform a slip tendency analysis for dynamic rupture simulations following Palgunadi et al. (2020), for which no dynamic rupture simulations are required. We vary the three angles constraining the orientation of $\sigma_1$ and compute the variable on-fault prestress and the closeness to failure, which are both modulated by the complex slab geometry. We find that a prestress, optimally oriented for a fault of azimuth 280 ° and dip 20 ° for pure thrust (rake 90 °) faulting (i.e. $\sigma_1$ plunging 10 ° trenchwards) results in a close to critical prestress on the modeled megathrust around the hypocenter depth when assuming

$\mu_s = 0.6$. We apply these variables to all ten dynamic rupture scenarios (Table 4.2.1 and Fig. 4.2.1).

Finally, we assume a high pore-fluid pressure of 97% of the lithostatic load, which results in low effective normal stress $\sigma'_n$, and realistic slip amplitudes, in line with dynamic rupture simulations of the 2004 Sumatra-Andaman earthquake (Madden et al., 2022).

### 4.2.3 Depth-dependent fault friction and rupture nucleation

All fault-friction parameters are summarized in Table 4.2.1. We account for variations in frictional behavior with depth by using a depth-dependent $\mu_d$ and constant $\mu_s = 0.6$ leading to a depth-dependent frictional strength drop and realistic static frictional strength (Byerlee and Summers, 1976; Tinti et al., 2021). We follow Shaw and Jackson (2010); Vernant et al. (2014); Scala et al. (2020) and consider the seismogenic zone to range from ∼15 km depth to ∼40-50 km depth. Deformation of the uppermost 15 km is assumed to be dominantly aseismic aligned with the HASZ's relatively high convergence rate and low seismicity. We incorporate these constraints in our dynamic rupture models by assuming a slip-strengthening frictional behavior in the uppermost 15 km ($\mu_s = 0.6$ and $\mu_d = 1.2$, Fig. 4.2.2). Slip-strengthening is a linear-slip weakening friction proxy (e.g., Ramos et al., 2021) for shallow velocity-strengthening behavior characterizing aseismic behavior (Shaw and Jackson, 2010; Vernant et al., 2014; Scala et al., 2020). Between 15–40 km depth, we use a lower $\mu_d = 0.3$, resulting in linear slip-weakening behavior. Between 40 km and 50 km depth, we linearly increase $\mu_d$ from 0.3 to 1.2 resulting in slip-strengthening frictional behavior at depths deeper than 43.3 km. We assume constant $\mu_d = 1.2$ below 50 km depth.

We smoothly initiate all dynamic rupture scenarios within a spherical region surrounding the respectively assumed hypocenter location (Figure 4.2.1) by locally reducing the effective friction coefficient from its static to its dynamic value over 0.5 s at smoothly varying speeds with a maximum speed of 2660 m/s, following Harris et al. (2018).

### 4.2.4 Off-fault plasticity

In model HEP, we analyze the effects of weak off-slab sediments co-seismically deforming. To this end, we consider a non-associative (visco-)plastic Drucker-Prager rheology (Andrews, 2005; Wollherr et al., 2018). The Hellenic Arc is characterized by relatively weak and unconsolidated sediments in the upper 15 km (Jongsma, 1977; Pichon and Angelier, 1979; Le Pichon and Angelier, 1981; Taymaz et al., 1990; Bohnhoff et al., 2001; Casten and Snopek, 2006; Shaw and Jackson, 2010).

The bulk material's friction coefficient $\nu$ is set to 0.6 and the bulk cohesion $C(z)$ varies with depth (Fig. 4.2.2a):

$$C(z) = C_0 + C_1(z)\sigma'_{zz}. \tag{4.11}$$

$C_0 = 0.3$ MPa is a constant term that controls the amplitude and location of the off-fault yielding at shallow depth, while $C_1(z)$ is a depth-dependent term defining rock hardening,

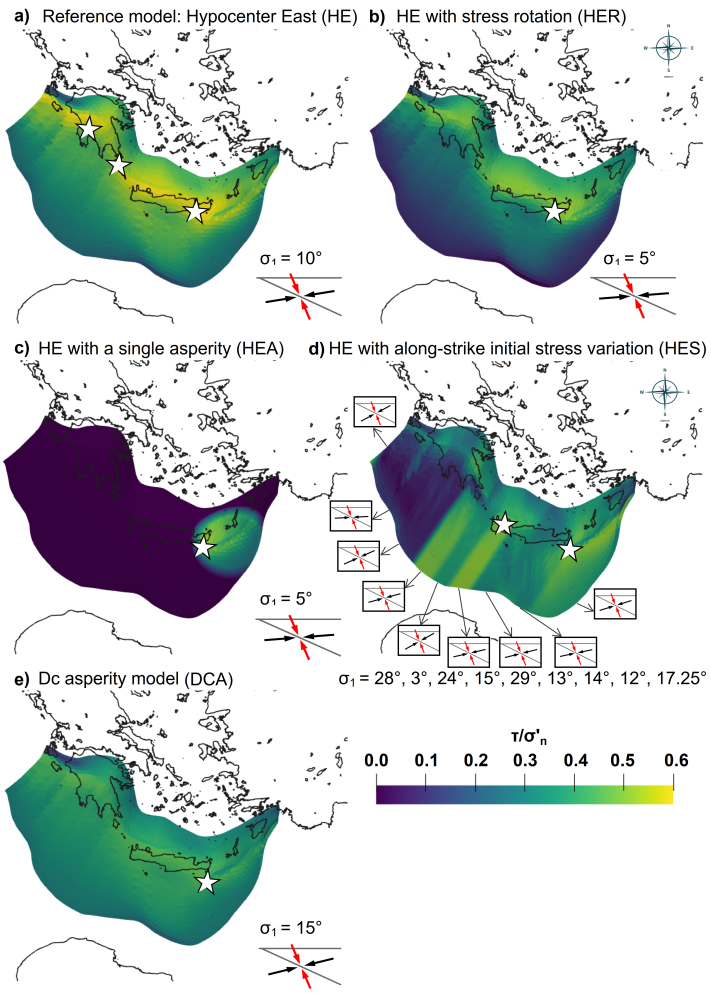



Figure 4.2.1: Ratio of initial shear stress ($\tau$) to effective normal stress ($\sigma'_n$) illustrating closeness to failure prior dynamic rupture onset. In our linear slip-weakening friction framework, frictional failure occurs when $\frac{\tau}{\sigma'_n} = 0.6 = \mu_S$. We here show $\frac{\tau}{\sigma'_n}$ for: **a)** the reference model setup with Eastern (HE), Central (HM), and Western (HW) hypocenters, and the model allowing for off-fault plasticity (HEP). In all of these models, the fault is close to optimally prestressed, which can lead to margin-wide earthquake scenarios of $M_W$~9.0. The bottom-right inset illustrates the plunge of the maximum ($\sigma_1$, black, 10 °) and minimum ($\sigma_3$, red) principal stresses; **b)** the rotated stress model (HER), characterized by a slightly shallower $\sigma_1$ plunge (5 °). Here, the shallower fault portion is less optimally prestressed, which prevents shallow rupture, resulting in a dynamic rupture scenario of $M_W$~8.9; **c)** the single-asperity model (HEA) for a dynamic rupture earthquake scenario resembling the 1303 Crete earthquake, described in Sec. 4.3.2; **d)** the segmented prestress model (HES, DCAS) informed by the regional stress inversion of Kkallas et al. (2021) described in Sec.4.3.3. **e)** the $D_c$-asperity model (DCA), characterized by a slightly steeper $\sigma_1$ plunge (15 °). Here, the deeper fault portion is less optimally prestressed. **(*):** The names of the models are defined in detail in Section 4.3.

Table 4.2.1: Dynamic rupture parameters common to all ten models. The names of the models are defined in Figure 4.2.1 and in Sections 4.1 and 4.3.

| Parameter | Value |
|---|---|
| Static friction coefficient ($\mu_s$) | 0.6 |
| Dynamic friction coefficient ($\mu_d$) | depth-dependent, 1.2–0.3 |
| Critical slip distance ($D_c$) [m] | 1.0 |
| Maximum relative prestress ratio ($\mathcal{R}_0$) | 0.7 |
| Pore fluid pressure ratio ($\gamma$) | 0.97 |
| Stress shape ratio ($\Phi$) | 0.4 |
| Dip of optimally oriented fault segments in Reference prestress model [°] | 20 |
| Plunge of $\sigma_1$ in Reference prestress model [°] | 10 |
| Plunge of $\sigma_1$ in model HER [°] | 5 |
| Plunge of $\sigma_1$ in models HES & DCAS [°] | 3–29 |
| $\sigma_2$ in Reference prestress model | horizontal in along-strike direction |
| Plunge of $\sigma_3$ in Reference prestress model [°] | -80 |
| Seismogenic depth [km] | $\sim$ 15–43.3 [a] |

[a] see Fig. 4.2.2

$\sigma'_{zz}$ is the effective lithostatic stress. We use a viscoelastic relaxation time of $T_v$=0.03 s. The off-fault plastic strain (Ma, 2008) is quantified as

$$\eta(t) = \int_0^t \sqrt{\frac{1}{2}\dot{\epsilon}^p_{i,j}\dot{\epsilon}^p_{i,j}}. \tag{4.12}$$

A fully elastic rheology is considered in all other 9 models besides HEP.

## 4.3 Increasingly complex initial conditions

In the following, we describe dynamic rupture model setups, which successively increase complexity based on the reference prestress and fault strength parameterization to account for smaller-scale megathrust heterogeneity.

All prestress initial conditions in our models are based on available seismic observations and a few trial-and-error dynamic rupture simulations. We use stress inversion results to generate our regionally varying initial stress setup. This enables constraining realistic initial conditions for dynamic rupture simulations without relying on geodetic locking models, which have been successfully used to initialize dynamic rupture scenarios (Chan et al., 2023; Ramos and Huang, 2019; Yang et al., 2019) but are difficult to obtain for offshore regions.

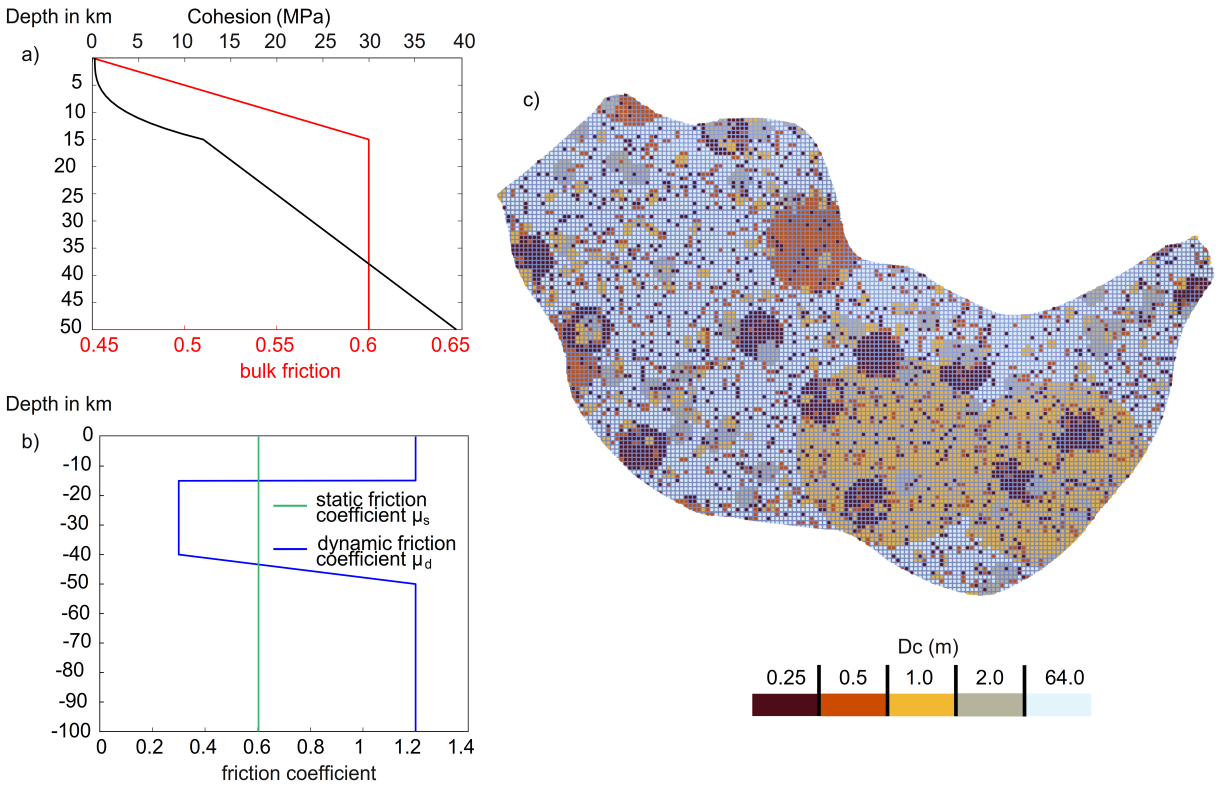



Figure 4.2.2: **a)** Depth-dependent plastic cohesion and bulk friction for model HEP with off-fault plasticity. **b)** Depth-dependence of friction coefficients in all models. We assume a constant static friction coefficient $\mu_s$, while the dynamic friction coefficient $\mu_d$ varies with depth. Slip-strengthening ($\mu_d > \mu_s$) is assumed in the upper 15 km and at depths lower than 43.3 km, and slip-weakening ($\mu_d < \mu_s$) is assumed within the seismogenic zone. **c)** Multiscale asperity models, with scale-dependent critical slip-weakening distance ($D_c$), following Ide and Aochi (2005) and described in Sec. 4.3.4.

However, this reference prestress state remains relatively homogeneous. Various additional ingredients may be invoked to capture additional smaller scale heterogeneities, including prescribed stress asperities and barriers (Miyatake, 1992; Shibazaki and Matsu'ura, 1992; Dalguer et al., 2008; Cocco et al., 2016), (computationally challenging) fault roughness (Bartolomeo et al., 2010; Taufiqurrahman et al., 2022), or velocity-strengthening regions (Kaneko et al., 2010).

In this study, we explore the role of large stress asperities, along-strike segmented prestress, multi-scale frictional strength asperities

### 4.3.1 Reference laterally homogeneous prestress and friction parameters

Our reference model setup (HE) is based on a laterally homogeneous prestress setup with $\sigma_1$ dipping at 10 ° (Fig. 4.2.1a and Table 4.2.1). All other parameters are set as described in Sec. 4.2. The model's rheology is purely elastic. In this reference model setup, we vary the epicentral location along the Hellenic Arc to investigate the influence of epicentral location on shallow slip, keeping the initial conditions constant and homogeneous. In the next step, we add off-fault plastic yielding to the reference model, maintaining the same homogeneous initial on-fault stress conditions.

### 4.3.2 Single-asperity prestress model (HEA)

Our single-asperity model (HEA) earthquake scenario resembles the 1303 Crete tsunamigenic earthquake. We limit the potential rupture size by reducing the initial loading outside a circular predefined region, a prestress asperity. A laterally homogeneous stress setup is applied within this asperity, with a constant prestress ratio of $\mathcal{R}_0 = 0.7$. Outside, the shear stress is smoothly tapered over 35 km away from the asperity by linearly decreasing the shear stress until it reaches a value that equals the lithostatic stress.

Aiming to dynamically model a $M_W \sim 8$ earthquake, we choose an asperity size of radius 180 km based on the subduction-specific earthquake scaling relationship of Strasser et al. (2010), and consistent with earlier studies of the 1303 event (e.g., Tinti et al., 2005) (Fig. 4.2.1c). We use $\sigma_1$ plunging 5 ° (an optimally prestressed fault would be oriented with a strike of 290 ° and dipping at 25 °). We consider four possible epicenter locations, constrained from Papazachos et al. (1999); Papadopoulos et al. (2012); Yolsal-Çevikbilen and Taymaz (2012); Necmioğlu and Özel (2014), respectively, and three different prestress settings, based on Papadopoulos et al. (2012); Yolsal-Çevikbilen and Taymaz (2012); Necmioğlu and Özel (2014) by changing $Sh_{max}$ accordingly. The laterally-homogeneous stress is defined as in a), but we vary the orientation of principal stresses.

Of these 12 epicenter-prestress combinations, only three lead to spontaneous dynamic rupture propagation: (i) the epicenter and stress setup by Necmioğlu and Özel (2014); (ii) the epicenter location proposed by Papadopoulos et al. (2012) in combination with the stress orientations inferred by Necmioğlu and Özel (2014); and (iii) the epicenter location

from Necmioğlu and Özel (2014) together with the initial stress setup from Papazachos and Nolet (1997). Our preferred scenario is (iii) since it best reproduces the 1303 Crete earthquake in terms of dynamic rupture extent and moment magnitude.

### 4.3.3 Segmented stress models (HMS and HES)

In models HMS and HES, we assign along-arc varying initial stresses based on the stress inversion of Kkallas et al. (2021). We include only the stress values inferred from focal mechanisms (Kkallas et al., 2021) that contain a dominant thrust component. This leads to principal stress variations of $\sigma_1$ between 3° and 29° across the here assumed segments. The change of $\sigma_1$ influences how well the shallow or deep fault is prestressed and how close the segments are to failure.

We divide our HASZ modeling domain into nine seismotectonically homogeneous regions along an NW to SE axis and constrain the principal stress orientations for each area based on the stress inversion results. We smooth out sharp prestress discontinuities at the boundaries between sub-regions by applying a 2-D Gaussian smoothing kernel with standard deviation $\sigma = 3$ across the ∼2-4 km sampled 2D rectilinear grid storing the stress parameters.

The resulting segmented prestress is shown in Fig. 4.2.1d. The azimuth and plunge of the maximum principal stress $\sigma_1$ vary segment-wise along the margin. The north-western portion of the slab, being non-optimally oriented, resolves little shear stress, while the south-eastern part is closer to failure. Higher shear over effective normal stress ratio at shallow depths compared with the stress model of a) relates with locally steeper $\sigma_1$ plunges.

### 4.3.4 Multi-scale asperity models (DCA and DCAS)

$D_c$ asperities that act as barriers can evolve due to differences in the fluid content of the subducted slab material, or coincide with fault roughness, or subducted seamounts (Bassett and Watts, 2015; Molina-Ormazabal et al., 2023). In models DCA and DCAS, we apply randomly distributed circular asperities with scale-dependent critical slip weakening distance ($D_c$) and fractal size-distribution, resulting in fewer larger than smaller-sized asperities (Fig. 4.2.2). This multi-asperity model is adopted from Ide and Aochi (2005). To allow for sustained, realistic rupture propagation under our prestress assumptions, we adopt the following parameterization for the HASZ: $D_c$ varies between 0.25 m, 0.5 m, 1 m, and 2 m. We chose $D_c$ =1.0 m within the largest asperity, which is consistent with the $D_c$ value of all other scenarios with constant $D_c$. Smaller asperities may superimpose the larger ones. Consistent with Ide and Aochi (2005), we chose a background value of $D_c$=64 m outside the asperities to limit rupture propagation. We note that other forms of heterogeneity may act as barriers, such as smaller-scale heterogeneity in prestress, static or dynamic friction coefficients, scale-dependent fracture energy, or geometric complexity (e.g., Wesnousky, 2006; Ke et al., 2018; Weng and Ampuero, 2019; Ke et al., 2022; Gabriel et al., 2024; Wei et al., 2024).

Our DCA model combines these multi-scale asperities with a steeper dipping $\sigma_1$ compared to the reference laterally homogeneous stress setup (Fig. 4.2.1 and Sec. 4.3.1). The steeper plunge of $\sigma_1$ is necessary to facilitate sustained dynamic rupture propagation, given the locally increased fracture energy due to the heterogeneous Dc. Our model DCAS combines the multi-scale asperities with the segmented stress loading (Sec. 4.3.3), leading to the most heterogeneous initial conditions of all models studied in this work.

## 4.4 Results

### 4.4.1 Margin-wide 3D dynamic rupture scenarios

We present five models loaded by a laterally homogeneous Cartesian prestress tensor (Fig. 4.2.1a,b and Fig. 4.4.1). Four of these models explore "counterfactual" scenarios based on margin-wide dynamic rupture earthquake simulations and their sensitivity to epicenter location, prestress orientation, and off-fault plasticity.

All margin-wide counterfactual rupture scenarios are based on laterally homogeneous initial stress conditions and reach $M_W$∼9 moment magnitude (Table 4.4.1). The fifth scenario illustrates the sensitivity of the potential for margin-wide dynamic rupture on prestress configuration. While rupture dynamics of margin-wide scenarios with different epicenter locations are comparable, including localized supershear transition at the exact same deep slab location beneath Western Greece, the further west the epicenter location, the higher the amount of shallow slip and the more pronounced the modeled localized near-trench uplift. Adding off-fault plastic yielding limits shallow on-fault slip by preventing slip from penetrating into the velocity-strengthening region. A five-degree more shallowly plunging $\sigma_1$ leads to spontaneous rupture arrest before crossing the complete margin and prevents shallow slip.

#### Reference model with laterally homogeneous prestress and friction parameters and eastern hypocenter (HE)

We prescribe the hypocenter of our reference model (HE) below southeast Crete at a depth of 30 km (Fig. 4.4.1a). Little slip penetrates to the west and into the shallow slip-strengthening region. Dynamic rupture initiates as a circular crack, turning pulse-like and propagating unilaterally towards the west after ∼60 s simulation time (Fig. 4.4.2a and Animation S1). Localized, deep supershear rupture is observed at the deep and steeply dipping portion of the slab, at ∼40 km depth around western Crete, and coincides with the area of the largest peak slip rate up to 6.9 m/s (Table 4.4.1). At the same depth (∼40-45 km), the highest stress drop is observed (Fig. 4.4.3). The slab interface changes from a relatively flat dipping portion of the slab to a much steeper dipping segment of the megathrust at this depth. This geometry change coincides with higher initial stresses (Fig. 4.2.1). Large-scale megathrust geometry changes leading to deep, localized propagating

supershear rupture have been reported previously in geodynamically constrained 2D and 3D megathrust dynamic rupture models (van Zelst et al., 2019; Wirp et al., 2021).

Dynamic rupture propagates west until reaching the prescribed north-western edge of the Hellenic Arc slab model, i.e., yielding a margin-wide rupture scenario, after 150 s simulation time. The highest accumulated slip of ∼11 m is modeled below southwest Crete. The resulting vertical seafloor displacement distribution reflects the distribution of fault slip. Uplift of up to 1.6 m is modeled south of Crete and southwest of Peloponnese. Subsidence of ∼1 m can be observed north of Crete, on Peloponnese, and across the islands of Zakynthos and Kefalonia (Fig. 4.4.1a).

### Models with different hypocenter locations (HM and HW)

We vary epicentral locations to investigate the effect of rupture propagation direction on rupture dynamics, slip distribution and extent, and seafloor displacements. We present two models, one with its epicenter located between Crete and Peloponnese (middle hypocenter model, HM), and one with an epicenter located further west, below northwest Greece (western hypocenter model, HW). Both have the same epicentral depth of ∼30 km as model HE.

In the scenario with a middle hypocenter (HM), we observe initial circular crack-like rupture followed by bilateral pulse-like rupture propagation towards the east and the west after the up-dip rupture front reached the shallow velocity-strengthening region (Fig. 4.4.2b and Animation S2). Supershear transition occurs at around 50 s simulation time at the same deeper, steeply dipping portion of the slab close to western Crete as in model HE. However, supershear rupture is, in this scenario, initiated by a SE propagating rupture front. The location of supershear rupture onset again coincides with the maximum PSR in this model, reaching ∼6.1 m/s, and high local stress drop.

In the western hypocenter scenario (HW), we observe similar but mirrored rupture dynamics compared to model HE, resulting in unilateral eastward pulse-like rupture propagation. Localized supershear transition occurs at a later stage of the simulation, at around ∼100 s simulation time (Fig. 4.4.2c and Animation S3) when rupture reaches the deep slab beneath western Crete at ∼45-50 km depth. Supershear transition coincides with the model's maximum PSR of ∼8.2 m. Despite the overall similar earthquake characteristics, in model HW we observe a wide, localized area of shallow slip to the trench, reaching up to 10 m in amplitude and driven by shallow peak slip rates of ∼3-4 m/s.

Cases HE, HM, and HW all result in margin-wide rupture. In all of these models with varying epicentral locations, the rupture front penetrates into the shallow slip-strengthening fault region after ∼100 s simulation time, respectively. Importantly, the further west the epicentral location, the higher the amount of shallow slip. Rupture propagation into the shallow slip-strengthening region of the fault is more pronounced for models HM and HW, evidenced by the high slip rate in the shallow part, and results in an additional localized near trench seafloor uplift (Fig. 4.4.1). Variations between the models are solely due to dynamic rupture evolution and rupture directivity.

For all three scenarios, the maximum slip is resulting at the center of the megathrust,

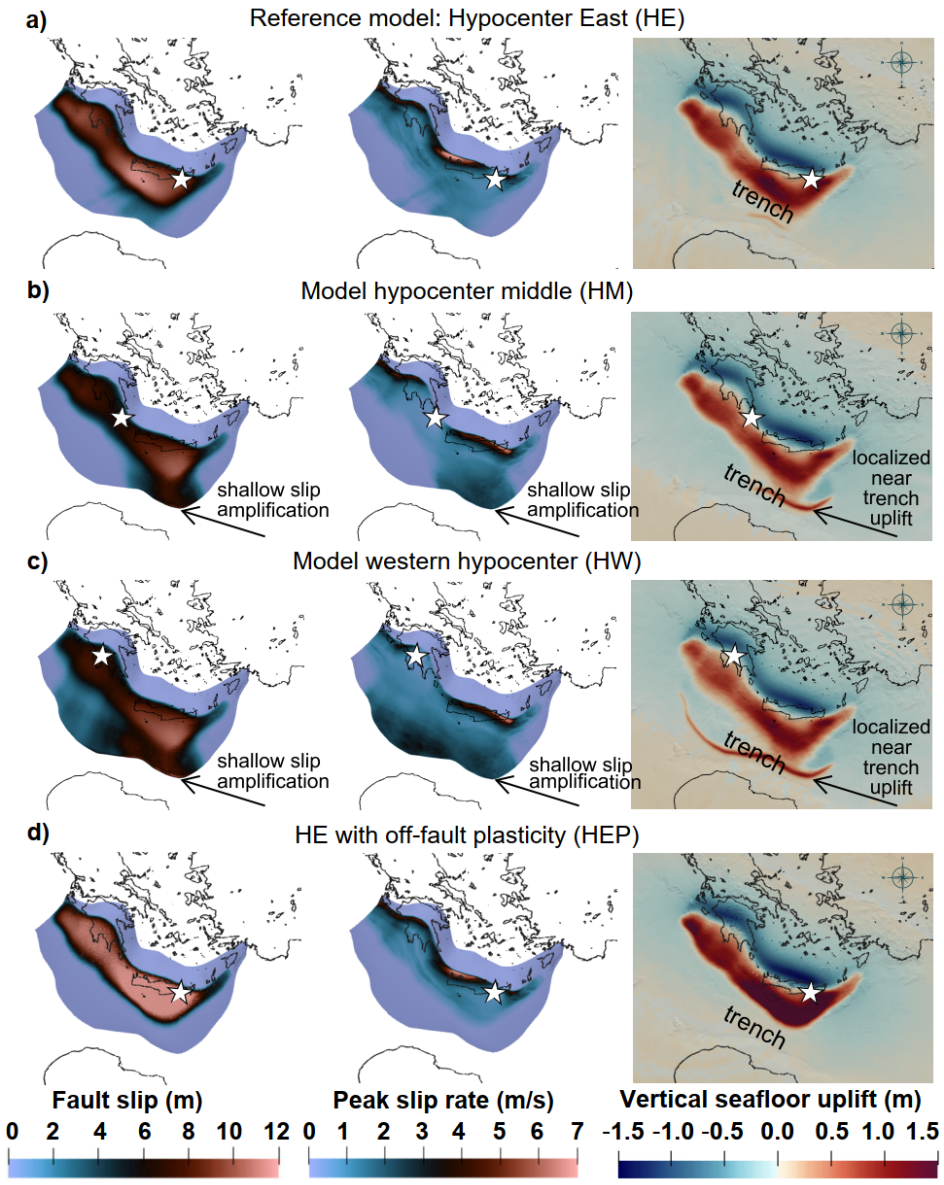



Figure 4.4.1: **Rupture characteristics of modeled counterfactual margin-wide 3D dynamic rupture scenarios HE, HM, HW, and HEP:** Fault slip ([m], left), peak slip rate ([m/s], middle), and vertical seafloor uplift ([m], right) distributions. Changing the hypocenter location (white star) in **a), b)** and **c)** impacts shallow fault slip, generating localized near-trench uplift visible in the vertical seafloor displacements (right). We account for the possibility of off-fault plasticity in model HEP (**d)**), extending the eastern hypocenter reference (HE) scenario in **a)**. This restricts slip to the deeper fault areas but generates increased slip amplitudes, which, combined with off-fault plastic strain, increases vertical seafloor displacements. The color scales are saturated. See Table 4.4.1 for absolute maximum values. See Animations S1-S4 for illustrations of slip rate evolution across the megathrust.

below Crete, within the deeper slip-weakening region (Fig. 4.4.1). With a high accumulated slip of ∼11.3 m (HE), ∼13.0 m (HM), and ∼15.5 m (HW), the models produce comparable maximum vertical seafloor displacement of 1.64 m (HE), 1.50 m (HM) and 1.48 m (HW), respectively.

The stress drop for models HM and HW resemble the stress drop of the HE model, with some differences at shallow depths, where HM and HW display apparently high stress drop locally. The stress drop is measured as the difference in fault stress before and after the earthquake in the dynamic rupture simulations as

$$\sqrt{T_s^2 - T_d^2}, \tag{4.13}$$

with $T_s$ and $T_d$ being the shear stress changes in strike and dip direktion. Consequently, shallow rupture propagation into the slip-strengthening region of the slab (Fig. 4.4.3), which is associated with locally small or negative stress drops, appears as, apparently elevated stress drops. While shallow stress drop is not high in absolute terms, it contrasts with the absence of stress drop observed in model HE, associated with the absence of shallow rupture propagation. For all three models (HE, HM, and HW), the highest stress drop is observed near the slab's deep, steeper dipping edge, which may explain deep high-frequency radiation as observed for the Tohoku-Oki earthquake (e.g., Meng et al., 2011; Galvez et al., 2014).

The seafloor uplift, i.e., the vertical seafloor displacement distribution, produced by models HM and HW resembles the uplift of the HE scenario (Fig. 4.4.1), except for localized near-trench uplift, produced by shallow slip. The further west the epicenter, the more pronounced and elongated the modeled localized near-trench uplift.

### The role of off-fault plasticity (model HEP)

We add off-fault plastic yielding to the reference scenario (HE) to investigate the role of unconsolidated sediments in the dynamically evolving slip and seafloor displacements. Our dynamic rupture models show that considering 15 kilometers of relatively unconsolidated sediments that deform co-seismically can significantly enhance the amount of uplift. Off-fault plastic yielding is most pronounced at shallow depths and within the hanging wall of the megathrust (Fig. 4.4.4). Off-fault deformation forms a characteristic flower structure at shallow depth. The distribution of the off-fault plastic deformation follows the fault geometry and uplift patterns in Fig. 4.4.1d. Vertical seafloor uplift is now reaching ∼3 m (Fig. 4.4.1d), which is double compared to the elastic scenario HE.

Both the maximum rupture speed, $V_r$, and the peak slip rate, PSR, are expected to be limited in dynamic rupture simulations with off-fault plasticity (e.g., Andrews, 2005; Dunham et al., 2011a; Gabriel et al., 2013). However, we observe that the average rupture velocity is not reduced in model HEP compared to model HE. In distinction, PSR is ∼1.5 m/s, which is lower than in model HE. Thus, while we do observe lower PSR when allowing for off-fault plasticity, the average rupture speed remains comparable. We note that our choice of $\mathcal{R}_0 = 0.7$ implies that the $S$ ratio of initial strength excess to nominal

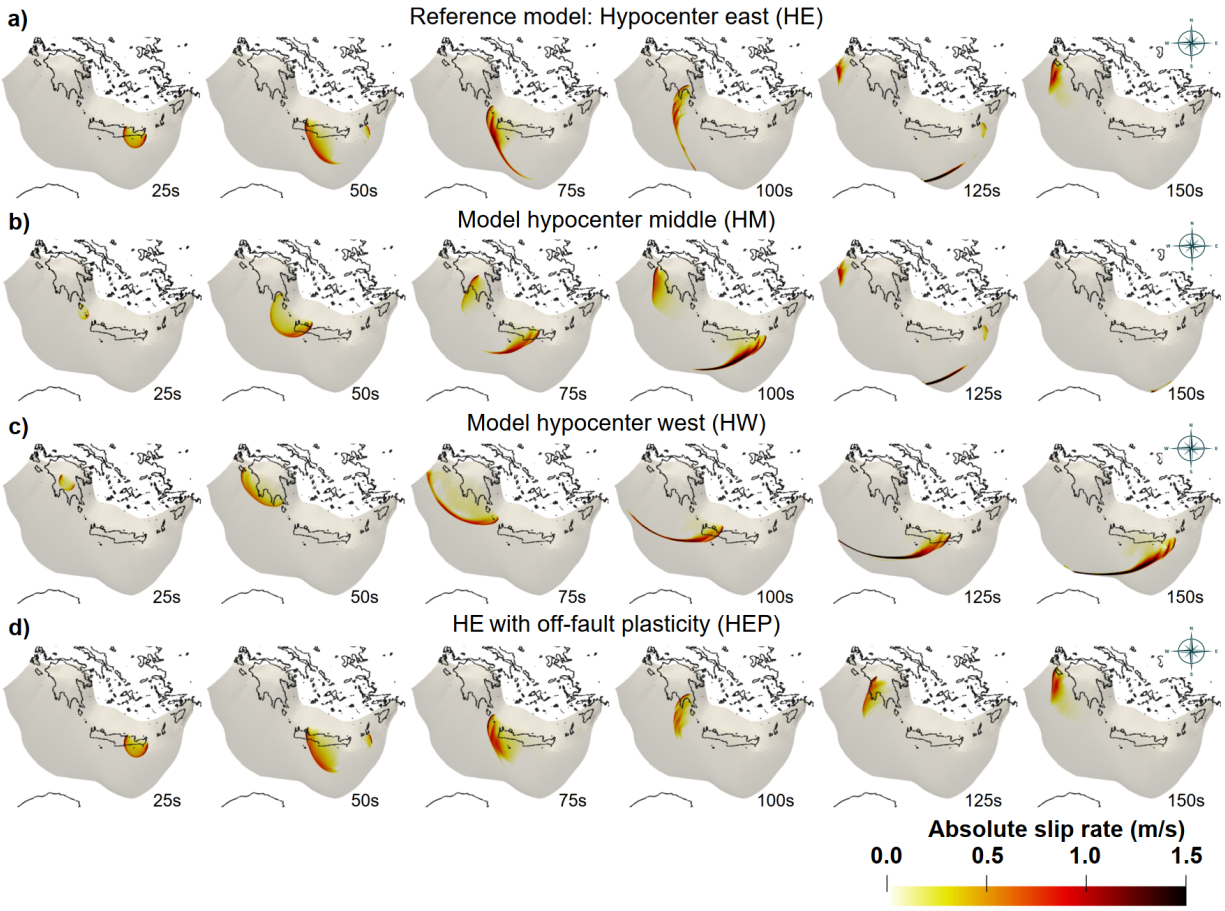



Figure 4.4.2: **Slip rate evolution of four margin-wide rupture scenarios:** Absolute slip rate [m/s] after 25 s, 50 s, 75 s, 100 s, 125 s, and 150 s simulation time (Movies S1-S4): **a)** Reference scenario: Hypocenter East (HE), **b)** Hypocenter Middle (HM), **c)** Hypocenter West (HW), and **d)** Hypocenter East with off-fault Plasticity (HEP) scenarios. The color scale is saturated. For absolute maximum slip rate values see Table 4.4.1.

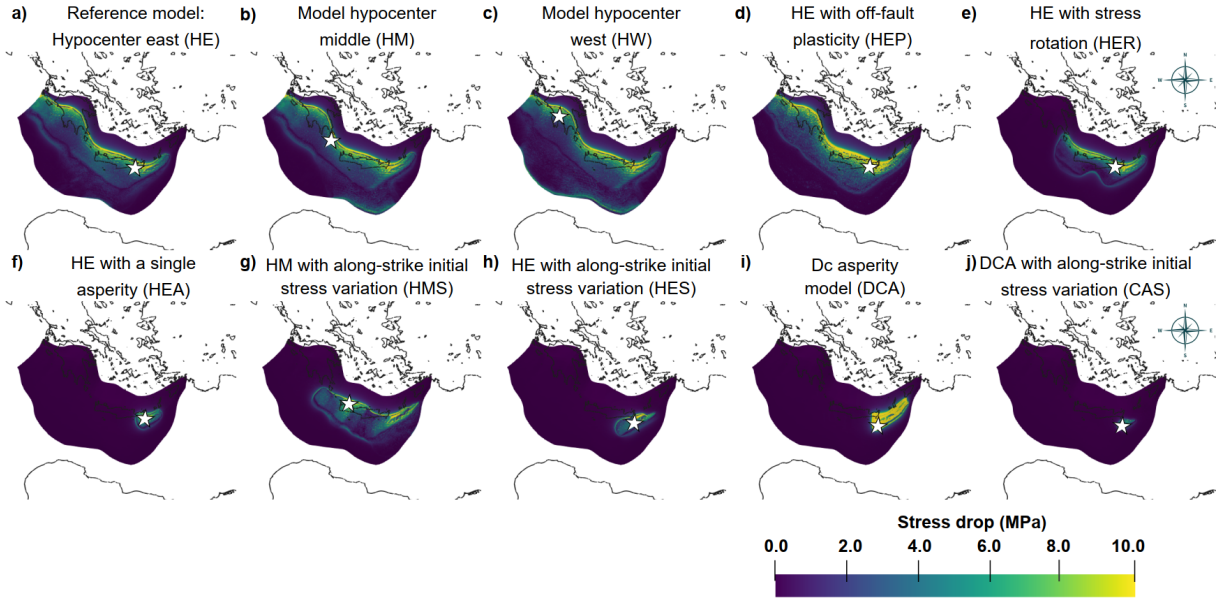



Figure 4.4.3: **Stress drop of the ten dynamic rupture scenarios presented in this study: a) - c)** Margin-wide dynamic rupture scenarios based on laterally-homogeneous initial stress conditions (HE, HM, HW), **d)** HEP dynamic rupture scenario incorporating off-fault plastic yielding, **e)** HER model with a less steeply dipping maximum principal stress $\sigma_1$ than in HE (HER), **f)** single-asperity model (HEA), **g)** and **h)** segmented stress models (HMS and HES), **i)** multiscale asperity model based on the reference laterally-homogeneous stress (DCA), and **j)** multiscale asperity model based on the segmented stress model (DCAS). The highest stress drop for **a) - e)** can be observed near the slab's deep, steeper dipping edge. In **g)**, the stress drop is highly inhomogeneous and follows the heterogeneous initial stress conditions (Fig. 4.2.1). For **i)**, the stress drop is particularly high, compared to the other models. A closeup of **f)**, **h)**, and **j)** can be found in the Appendix Fig. 4.B.2. We measure stress drop as the difference in fault stress before and after dynamic rupture. We caution that shallow rupture propagation into the slip-strengthening region of the slab, which is associated with small or negative stress drops, appears as locally apparently elevated stress drops.

stress drop (Das and Aki, 1977) of models HEP and HE is with $S = 0.43$ lower than values explored in previous studies.

Off-fault plastic yielding limits shallow on-fault slip, as observed in 3D dynamic rupture scenarios of the 2004 Sumatra megathrust event (Ulrich et al., 2022) and for low-angle normal faults (Kim and Sanderson, 2006; Biemiller et al., 2023). Shallow slip within the slip-strengthening region is efficiently prevented (Fig. 4.4.1d).

The maximum on-fault slip is ∼10 m larger than in the purely elastic scenario HE, while the moment magnitudes of both scenarios are comparable (Table 4.4.1). Localized supershear transition after 100 s simulation time is persistent (Animation S4). The highest PSR of ∼7 m/s is modeled on the deep, steeply dipping portion of the slab, where the highest stress drop is observed (Fig. 4.4.3).

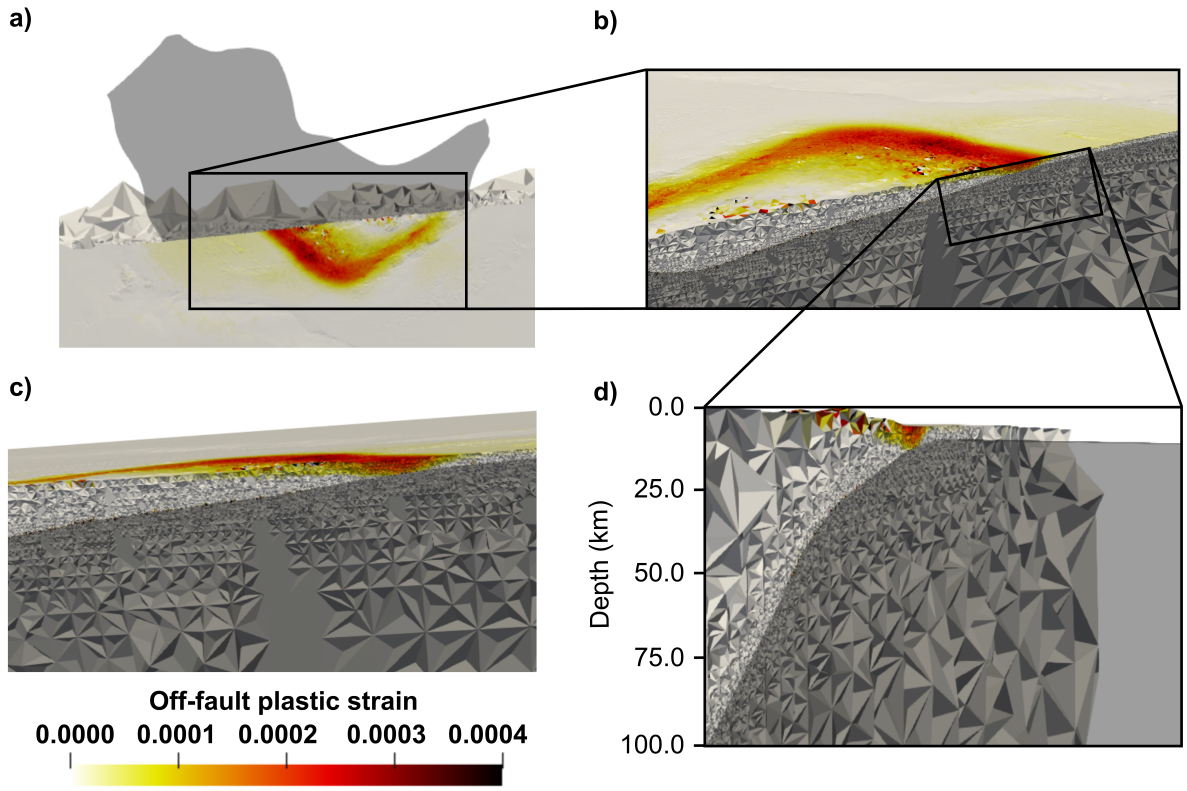



Figure 4.4.4: Accumulated off-fault plastic strain quantified as $\eta$ in scenario HEP (Sec. 4.2.4): **a)** Map view of the fault and free surface showing $\eta$ and the location of the cutting plane used for the vertical slice in **b), c)** and **d)**. **b)** Close-up cut-away view combining a map view and a vertical slice through the damage zone. The megathrust interface is transparent dark grey. $\eta$ is displayed from above and on the cutting plane. **c)** Same as in **b)**, but from another viewing direction. **d)** Cut-away view from NW combining the megathrust interface, displayed as transparent dark grey, and a vertical slice showing $\eta$. The unstructured tetrahedral mesh is refined around the slab and coarsens with distance.

### Shallowly plunging $\sigma_1$ (model HER) prevents margin-wide rupture and shallow slip

In scenario HER, we assume that $\sigma_1$ plunges at 5 °, which is slightly less than in the HE reference scenario, which assumes a $\sigma_1$ plunge of 10 °. Such shallowly plunging $\sigma_1$ leads to an increase in the ratio of initial shear stress $\tau$ over effective normal stress $\sigma_n$ on the deeper portions of the slab (Fig. 4.2.1b) and a decrease at shallower depths. We do not account for a potential depth-dependence of $\sigma_1$. Kkallas et al. (2021) divide the stress regime of the Hellenic arc seismogenic zone into segments of 0-30 km and 30-60 m depth, which could be explored in future models. Similarly to the model allowing for off-fault plasticity (HEP), dynamic rupture propagation in model HER remains limited to the deeper megathrust. The maximum slip is located below Crete and is 5 m–9.3 m lower than in the margin-wide rupture models HE, HM, and HM (Table 4.4.1 and Fig. 4.4.5). This results in a smaller moment magnitude of $M_W$∼8.6. In this model, neither supershear rupture transition nor rupture propagation into the shallow slip-strengthening region is observed (Fig. 4.4.6d). Dynamic rupture spontaneously arrests in the west. The stress drop of model HER is highest at the deep, steeply dipping portion of the fault, similar to models HE, HM, HW, and HEP (Fig. 4.4.3).

The maximum seafloor uplift southeast of Crete is ∼1.6 m, comparable to the reference model (HE). We observe notable differences between models HER and HE in the distribution of seafloor displacements (Fig. 4.4.5 and Fig. 4.4.1). The uplift area in the HER model is much smaller and located solely south of Crete. A subsidence of ∼0.5 m is observed north of Crete.

## 4.4.2 Single prestress asperity model (HEA)

This model illustrates the effectiveness of prestress asperities in limiting the resulting moment magnitude and slip extent of dynamic rupture earthquake scenarios while simultaneously causing a relatively high seafloor displacement. We discuss the applicability of this approach to model the 1303 Crete earthquake in Sec. 4.5.2.

In the single asperity dynamic rupture scenario HEA, we taper shear stress from a laterally homogeneous stress tensor outside a circular region, which size is constrained by the earthquake scaling relationship of Strasser et al. (2010) as explained in Sect. 4.2.

In model HEA, dynamic rupture propagation stops after 50 s at the eastern edge of the asperity (Fig. 4.4.6, and Animation S6) and does not propagate to shallow depths. The resulting fault slip and seafloor displacements are displayed in Figs. 4.4.5b and 4.B.1a. This $M_W$8.0 earthquake scenario causes a maximum fault slip of ∼5 m, which is ∼6 m less than in the reference model HE. It produces a vertical seafloor uplift of up to ∼1.3 m located SE of Crete. Even though the lateral extent of the seafloor displacement is limited to a small area compared to the counterfactual margin-wide rupture scenarios HE, HM, and HW, the local peak uplift is only ∼0.2-0.3 m smaller. The highest PSR of model HEA is observed at the deeper and steeply dipping portion of the slab (Figs. 4.4.3f and 4.B.2a), similar to the margin-wide earthquake scenarios (HE, HM, and HW).

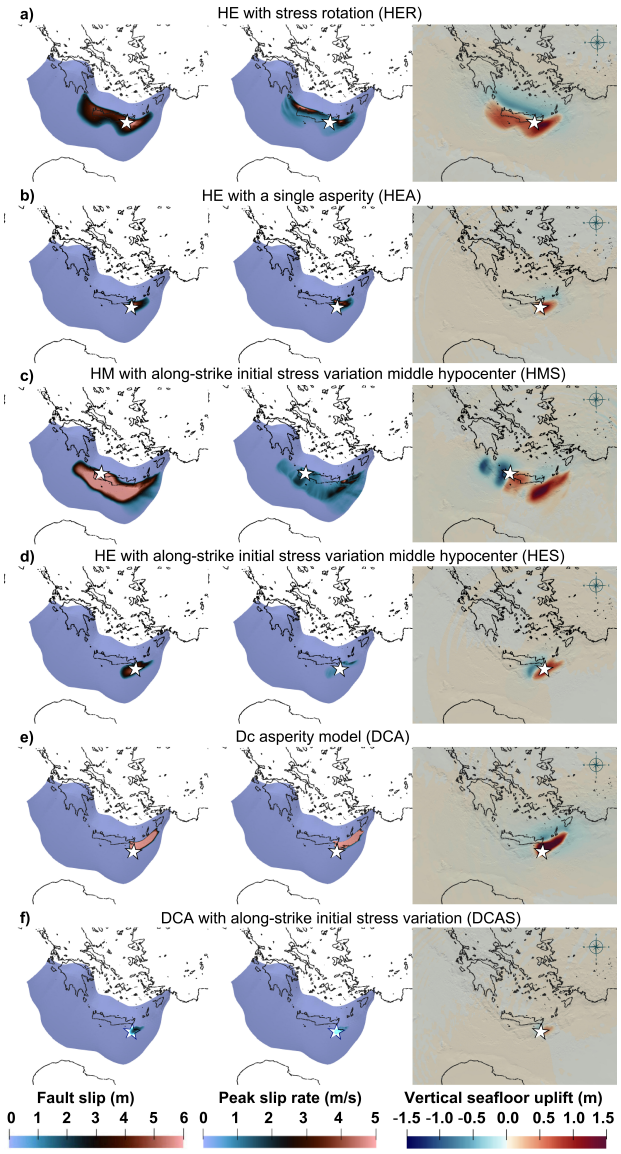



Figure 4.4.5: **Rupture characteristics for the six non-margin-wide spontaneously arresting dynamic scenarios:** Fault slip [m], peak slip rate [m/s], and vertical displacement distribution for **a)** model HER using a less steeply oriented maximum principal stress $\sigma_1$ than in HE,**b)** the single-asperity model (HEA), **c)** and **d)** models HMS and HES based on a segmented stress model with two different epicenter locations, **e)** the multiscale asperity model DCA using the reference laterally-homogeneous stress and **f)** the multiscale asperity model DCAS using the segmented stress. White stars mark the respective hypocenters. Note the significant differences in fault slip across the scenarios and varying seafloor uplift patterns. The color scales are saturated. For absolute maximum values and other characteristics such as moment magnitudes, see Table 4.4.1. A closeup of **b)**, **d)** and **f)** is shown in Appendix Fig. 4.B.1 and 4.B.4.

### 4.4.3 Dynamic rupture models with along-arc segmented prestress (models HMS and HES)

We increase the complexity and realism of our dynamic rupture initial conditions by assuming a heterogeneous, along-arc segmented prestress. Under these conditions, we investigate how different epicentral locations lead to differences in rupture extent, peak slip rate, and absolute slip, resulting in remarkably different moment magnitudes, with higher PSR and $M_W$ for a hypocenter located further west (HMS). Heterogeneities of the initial stress limit the fault slip extent and restrict rupture propagation to the deeper slip-weakening region of the slab. The segmentation in terms of initial stresses is reflected in the uplift pattern (HMS), which is much more complex than for the models with laterally homogeneous initial stress (HM).

Figs. 4.4.5c,d and 4.B.1b present two dynamic rupture earthquake scenarios based on the along-strike highly variable, segmented prestress model constrained from stress inversion by Kkallas et al. (2021) (Fig. 4.2.1 and Sec. 4.2). The HMS scenario (middle hypocenter) uses a hypocenter located below Chania in north-western Crete, while the HES scenario (eastern hypocenter) is based on a hypocenter located southeast of Crete. Both hypocenters are located within regions with a high ratio of initial shear over effective normal stress.

In the HMS scenario, rupture propagates bilaterally to both sides of the Hellenic Arc megathrust (Figs. 4.4.6c, 4.B.3c, and Animation S7). Large parts of the megathrust are ruptured. However, at shallow depths, rupture does not propagate into the slip-strengthening region across the complete margin but only near the shallow eastern edge of the slab (Fig. 4.4.5c). The maximum fault slip is ∼12.2 m, which is comparable to the margin-wide rupture scenarios (HE, HM, and HW). High accumulated fault slip concentrates southwest of the island Kynthera and below western Crete, modulated by the shape of the megathrust. The highest PSR of ∼4.8 m/s is simulated southeast of Crete (Fig. 4.4.5c) and aligns with the stress drop distribution, with areas of high stress drop experiencing high PSR (Fig. 4.4.3).

The HMS scenario results in a maximum vertical seafloor uplift of ∼1.7 m southeast Crete and subsidence of ∼1 m close to western Crete and southwest of Peloponnese and the island Kynthera. This uplift is slightly higher than for the margin-wide rupture models HE, HM, and HW. The uplift pattern of the HMS model is much more complex than that of the other models. The along-arc segmented loading provokes two near trench uplift features east of the hypocenter, and two subsidence features west of the hypocenter. The HMS scenario moment magnitude is $M_W$∼8.81, which is slightly smaller than that of the counterfactual margin-wide scenarios.

The HES scenario ruptures a smaller area than the HMS scenario and leads to a smaller maximum slip of ∼5.2 m, southeast the Crete island (Figs. 4.4.5d, 4.B.1b, and Animation S8). This moment magnitude $M_W$∼8.12 earthquake causes a relatively small vertical seafloor uplift of ∼1.2 m. In this scenario, the rupture propagation stops after 50 s (Fig. 4.4.6d) and does not penetrate into the shallow slip-strengthening region.

The absolute slip in model HMS is comparable to the counterfactual margin-wide rup-

ture scenarios and ∼0.8 m smaller than in model HM. However, the maximum PSR of ∼4.8 m is with ∼2 m/s much smaller than in model HM. In contrast to HM, the highest PSR does not coincide with the deep and steeper dipping portion of the slab but represents the heterogeneous prestress distribution (Fig. 4.2.1). The heterogeneity in the prestress of HMS results in a very different seafloor uplift compared to HM. No localized near trench uplift is observed. While the uplift in model HM follows the fault structure, with subsidence located north of it. In model HMS, the uplift is located east of the hypocenter location, while the subsidence is located west of the hypocenter, following the prestress segmentation.

### 4.4.4 Combining a multi-scale $D_c$-asperity model with laterally homogeneous prestress (model DCA)

Model DCA is characterized by a comparable maximum slip and rupture velocity to the counterfactual margin-wide rupture scenarios HE, HM, and HW, but a smaller $M_W$. With a ∼5-times higher PSR and highly heterogeneous rupture dynamics caused by the randomly distributed $D_c$-asperities on the slab, it results in vertical seafloor displacements of up to ∼3.5 m, which is more than double the amount of that of the $M_W$9 margin-wide rupture models.

In scenario DCA, we use the multi-scale asperity model (Sec. 4.3.4) in combination with laterally homogeneous prestress but a slightly steeper dipping $\sigma_1$ (plunge 15 °) compared to the reference model HE (and in models HM, HW, HEP and HER). $D_c$ can now locally be smaller or higher than in previous scenarios. Dynamic rupture is initiated within a large asperity with $D_c$=1 m on the south-eastern part of the slab and propagates unilaterally towards the east (Fig. 4.4.6e and Animation S9). Dynamic rupture arrests when propagating into slab areas combining low initial shear stresses and high $D_c$ values.

Model DCA results in a $M_W$∼8.42 earthquake, with a maximum slip of ∼13.8 m (Table4.4.1 and Fig. 4.4.5e). The $D_c$-asperities induce strongly heterogeneous and locally high peak slip rates compared to the previously described non-margin-wide rupture scenarios. The stress drop is high throughout the ruptured area (Fig. 4.4.3) and specifically higher than in model HE. Dynamic rupture stress drop variations are controlled mainly by the initial stress and the friction coefficients $\mu_s$ and $\mu_d$ but not by $D_c$, given that slip is locally, in general, exceeding $D_c$. Thus, DCA's higher stress drop is due to the steeper dipping $\sigma_1$ in this model (Fig. 4.2.1).

Model DCA shows more heterogeneous dynamics than the previous models. The rupture front first propagates in the downdip direction towards the east (Figs. 4.4.2e, 4.B.3e), and then, while the rupture propagates along the fault strike, it splits up into two rupture fronts. In agreement with the analysis in Ide and Aochi (2005), dynamic rupture propagation governed by multi-scale $D_c$-asperities is complex, forming a cascade triggering asperities. Thus, forecasting earthquake characteristics solely based on its epicentral location is difficult.

The peak uplift of ∼3.5 m is significantly larger than for the HE scenario with homo-

geneous prestress and eastern hypocenter. The uplift area extends from southeast Crete to southeast of the island of Karpathos. This uplift is consistent with worst-case scenario assumptions made in regional tsunami studies (e.g., Tinti et al., 2005; Lorito et al., 2008).

### 4.4.5 Model combining the multi-scale asperity model and the segmented stress model (DCAS)

Combining heterogeneous prestress and frictional megathrust properties ($D_c$) lowers dynamic rupture fault slip, rupture extent, and moment magnitude due to effective barriers arising from the imposed asperities. The rupture propagation is highly heterogeneous, governed by the rupture front interacting with the $D_c$-asperities and being affected by changing stress conditions.

Our dynamic rupture scenario DCAS combines the multi-scale asperity model and the segmented stress model (see Sect. 4.2) to the most complex initial conditions among the ten models. We use the same south-eastern epicentral location as in the DCA scenario. In model DCAS, rupture propagates eastward (Fig. 4.B.2f) and splits into two rupture fronts, one propagating downdip and the other propagating along the fault strike direction. The rupture area is relatively small compared to model DCA or HES. In model HES, rupture propagates bilateral, while in DCA and DCAS, propagation is primarily unilateral towards the northeast. In both $D_c$-asperity models (DCA and DCAS), the random distribution of $D_c$-patches along the arc governs rupture propagation complexity. As the rupture front propagates, it triggers the $D_c$ patches on the fault, which generates unpredictable and heterogeneous rupture propagation patterns (Ide and Aochi, 2005). The maximum fault slip in DCAS is with $\sim$2.6 m five times smaller than in the DCA model and half the amount of slip of HES (Table 4.4.1 and Figs. 4.4.5f, 4.B.1c). The maximum PSR is a tenth of the PSR in model DCA and four times smaller than in the margin-wide rupture models (HE, HM, and HW). It is slightly higher than in model HES but comparable to the single asperity model (HEA). The small area of rupture propagation (Fig. 4.B.4) and the relatively small amount of slip results in relatively small vertical seafloor displacements of up to $\sim$0.56 m, southeast of Crete. The moment magnitude of $M_W \sim 7.5$ is the smallest among all models.

### 4.4.6 Shake maps

We compare shake maps, spatial distributions of the modeled rotationally-independent geometric mean at 50% of the horizontal peak ground velocities (PGVs), for three margin-wide dynamic rupture models (HE, HW, HEP) and three non-margin-wide rupture models (HEA, DCA, DCAS). By this means, we investigate – to first order – how epicentral location, rupture directivity, off-fault plasticity, and increasing initial condition complexity influence long-period peak ground motions (Fig.4.4.7). We note that our models have a relatively high resolution of up to 2.7 Hz of the seismic wavefield close to the slab but have gradually decreasing resolution away from it (Sec. 4.2.1). This allows us to explore several

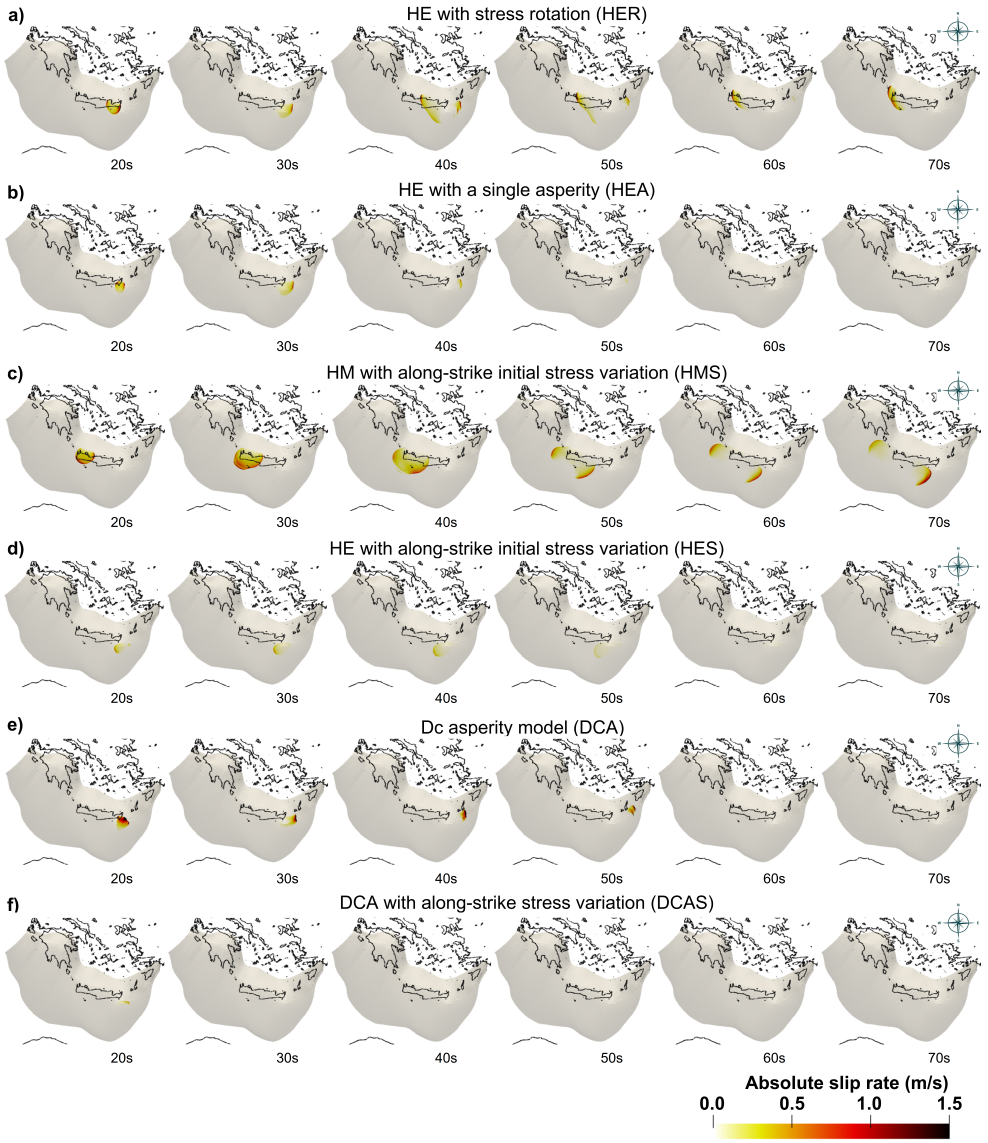



Figure 4.4.6: **Slip rate [m/s] snapshots for the six non-margin-wide spontaneously arresting dynamic rupture scenarios (Movies S5-S10): a)** HER, based on a less steeply oriented maximum principal stress $\sigma_1$ than in HE, **b)** HEA, the single prestress asperity model, **c)** and **d)** HMS and HES, combining along-arc heterogeneous, segmented prestress with two different hypocenter locations, **e)** DCA, the multi-scale $D_c$-asperity model combined with the reference laterally-homogeneous prestress and **f)** DCAS, the multi-scale $D_c$-asperity model combined with along-arc heterogeneous prestress. Slip rates [m/s] are shown at 20 s, 30 s, 40 s, 50 s, 60 s and 70 s simulation time. The rupture evolution model DCAS after 5 s, 10 s, 15 s, 20 s and 25 s can be found in Appendix Fig. 4.B.4. A closeup of the rupture evolution for all models at 20 s simulation time can be found in Appendix Fig. 4.B.3.

dynamic rupture scenarios efficiently. However, dynamic rupture simulations with constant high resolution in a larger region would be required for physics-based ground motion simulations in the frequency band of interest to earthquake engineering (Taufiqurrahman et al., 2022; Uphoff et al., 2017).

We find that the modeled amplitude of PGVs may double between different epicentral locations. Off-fault plastic yielding limits the overall amplitudes of PGVs and the spatial extent of high shaking. The smallest moment magnitude scenario (DCAS) does not produce the smallest PGVs. The high stress drop model DCA is producing relatively high PGVs.

In model HE (eastern hypocenter location), the distribution of high PGV reflects the location and shape of the highest fault slip, located south-west of Crete and Peloponnese, where PGVs reach ∼0.6 m/s (Fig. 4.4.7a). Peloponnese, Crete, and the Southern Aegean Sea islands are affected by PGVs of ∼0.3-0.4 m/s. PGV decreases with distance from the trench. We observe relatively higher ground motion in the direction of rupture propagation on the fault towards Sicily and in the South towards the coast of Libya.

For model HEP, the PGV distribution is similar, with the highest PGVs towards the west, in the rupture directivity direction (Fig. 4.4.7d). Nevertheless, the area of high PGVs is narrower than for model HE. In addition, the effect of directivity, leading to high PGVs towards Sicily, is less than for model HE. HEP generates ∼0.1 m/s smaller peak ground velocity at the Libyan coast (∼0.1-0.2 m/s). The smaller area of high PGVs can be explained by the energy loss within the off-fault plastic material (Andrews, 2005; Dunham et al., 2011a; Gabriel et al., 2013), contributing to the fracture energy. Roten et al. (2018) show that materials of low strength, such as unconsolidated sediments, can reduce PGVs by 15-30% in a continental strike-slip setting. Our results for the HASZ with a local PGV reduction of ∼30-50% agree with these estimates.

For model HW (western hypocenter location), the directivity of rupture propagation leads to a different PGV distribution than model HE. The highest PGVs of ∼1.0 m/s are located further southwest above the shallow Hellenic Arc (Fig. 4.4.7b). The high slip rate on the shallow fault (Sec. 4.3.1 and Fig. 4.4.1) produce PGVs up to ∼0.5 m/s higher than the maximum PGVs in model HE. The Peloponnese is barely affected by ground motions, while we note high PGVs south of Crete that affect the Lybian and Egyptian coasts ranging from ∼0.4-0.9 m/s.

For model DCA, the highest PGVs of ∼1.0 m/s are located northeast of Crete (Fig. 4.4.7e). In this scenario, only the eastern coastal part of Crete Island experiences high PGV. High PGVs are directed towards the northeast due to directivity effects. For this model, the smaller islands northeast of Crete are mostly affected by high PGVs of ∼0.5-0.6 m/s. We observe PGVs of ∼0.4 m/s at Rhodes and PGVs of ∼0.2 m/s affecting the Turkish coast. The maximum PGV amplitudes of ∼1.0 m/s in model DCA are larger than for model HE and HEP, likely reflecting the higher stress drop and higher slip rates, and ultimately the locally shorter critical slip weakening distances (Fig. 4.4.3).

In model DCAS, the highest PGVs of ∼0.06-0.2 m/s appear concentrated to southeast Crete (Fig. 4.4.7c). Directivity effects imprint on PGV distributions. Compared to model DCA, the maximum PGVs are relatively small (∼0.45 m/s smaller), which is in agreement with the model's smaller stress drop (Fig. 4.4.3) and its ∼93% lower peak slip rate

amplitudes (Table 4.4.1).

The single asperity model HEA shows the smallest PGVs among the models located southeast of Crete with a maximum amplitude of ∼0.02 m/. While the moment magnitude of this event is similar to that of model DCA (Table 4.4.1), the peak amplitude of peak slip rate and stress drop of model HEA are ∼93% and ∼50% smaller than for model DCA (Figs. 4.4.5b, 4.4.3f, 4.B.1a, 4.B.2a).

Table 4.4.1: Rupture characteristics for all 10 dynamic rupture simulations.

| **Model description** | **ASl**[a][m] | **PSR**[b][m/s] | $\mathbf{V}_r$[c][m/s] | **Disp.**[d][m] | $\mathbf{M}_W$[e] |
|---|---|---|---|---|---|
| Reference model: hypocenter east (HE) | 11.323 | 8.600 | 3248 | 1.642 | 9.04 |
| Model hypocenter middle (HM) | 12.974 | 6.974 | 3003 | 1.504 | 9.06 |
| Model hypocenter west (HW) | 15.501 | 8.207 | 2900 | 1.477 | 9.12 |
| HE with off-fault plasticity (HEP) | 22.125 | 7.084 | 3297 | 2.913 | 9.13 |
| HE with rotated stress (HER) | 6.239 | 5.108 | 2859 | 1.625 | 8.61 |
| HE with single asperity (HEA) | 4.963 | 2.205 | 2374 | 1.288 | 8.04 |
| HM with along-strike initial stress variations (HMS) | 12.175 | 4.819 | 2585 | 1.708 | 8.81 |
| HE with along-strike initial stress variations (HES) | 5.244 | 1.829 | 1631 | 1.171 | 8.12 |
| $D_c$-asperity model (DCA) | 13.768 | 33.044 | 3138 | 3.492 | 8.42 |
| DCA with along-strike initial stress variations (DCAS) | 2.626 | 2.355 | 2185 | 0.557 | 7.52 |

[a] Fault slip, [b] Peak slip rate, [c] Rupture velocity, [d] Displacement, [e] Moment magnitude

## 4.5 Discussion

### 4.5.1 The AD 365 earthquake and tsunami

Large ground deformation during the AD 365 event is assumed to have caused large tsunami amplitudes (e.g., Stiros and Drakos, 2006). We show that earthquakes similar in magnitude to the historical AD 365 earthquake might not solely be mechanically plausible on splay faults branching the main megathrust but on the Hellenic Arc subduction interface itself. In model HEP, we allow weak off-slab sediments to plastically deform during earthquake rupture. We show that sediments may play an important role in causing locally high

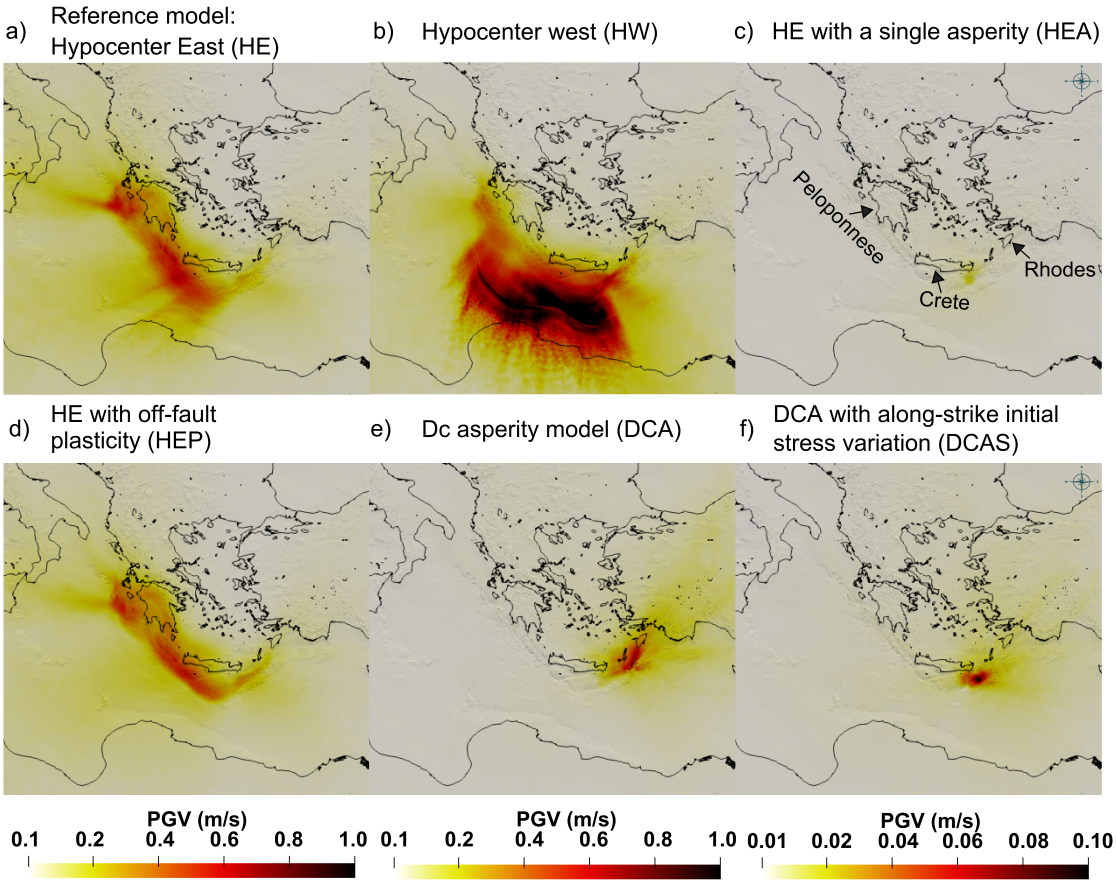



Figure 4.4.7: Horizontal peak ground velocities (PGVs) (resolved up to 2.7 Hz in the vicinity of the slab but with spatially decreasing accuracy away from it) for **a)** Reference model (HE), **b)** model with western hypocenter location (HW), **c)** single stress-asperity model (HEA), **d)** model including off-fault plastic yielding (HEP), **e)** the model based on the multi-scale asperity model and the reference laterally-homogeneous stress (DCA) and **f)** the model based on the multi-scale asperity model and the segmented stress model (DCAS). Note the different scales for **c)** and **f)**. In **a)** (model HE), the highest PGV is located above the western Hellenic Arc. The PGV in **d)** (model HEP) has a similar pattern but high PGVs (e.g., >0.5 m/s) affect a smaller area than in model HE. **b)** (model HW) shows the highest PGVs (∼1.0 m/s) and also the largest spatial extent of high PGV values, with PGVs higher than 0.5 m/s extending up to the northern coast of Africa. Models HEA, DCA, and DCAS are characterized by locally smaller and more localized PGVs due to their smaller rupture extent (Fig. 4.4.5) and moment magnitude (**c)** max. PGVs of model HEA ∼0.02 m/s, which is ∼2% of max. PGVs of model HW, **e)** PGVs of model DCA, restricted to a small area east of Crete, **f)** max. PGVs of model DCAS ∼0.06-0.2 m/s, which is ∼6-20% of max. PGVs of model HW). The color scale is saturated. For absolute maximum values see Table 4.4.1.

seafloor uplift. The high amount of off-fault plastic deformation (Fig. 4.4.4) generates a higher vertical displacement (Fig. 4.4.1d) compared to the purely elastic model, while rupture propagation in the slip-strengthening region remains limited (Fig. 4.4.1d, 4.4.3). In addition, including multi-scale $D_c$-asperities in our model significantly enhances the seafloor uplift. All these effects together may help to explain what caused historical tsunamis, such as the AD 365 earthquake.

The amount of vertical uplift (∼3 m) in the model with off-fault plasticity (HEP) is twice as large as the uplift modeled when considering a purely elastic rheology (HE model). However, it is still not comparable to the coseismic uplift of ∼10 m inferred for the AD 365 earthquake from seamarks, fallen blocks, co-seismic seafloor uplift, and tsunami modeling around western Crete (Spratt, 1865; Flemming, 1978; Pirazzoli et al., 1982; Stiros and Drakos, 2006; Shaw et al., 2008; England et al., 2015), associated with large (∼7 m) tsunami layer deposits (Pirazzoli et al., 1992).

The HEP model generates a maximum accumulated on-fault slip of ∼22 m, which is significantly higher than the slip of all other models: Compared to model HE (1.6 m uplift), the twice larger fault slip leads to twice as high peak vertical seafloor displacements (2.9 m) off-shore of southwestern Crete. The peak accumulated fault slip in model HEP is comparable to the maximum amount of slip from Papadimitriou and Karakostas (2008), although the moment magnitude of our model is higher ($M_W$∼9 compared to $M_W$8.4), which may be due to our simplified subsurface velocity model.

The on-fault $D_c$ heterogeneities in the DCA model lead to high accumulated on-fault slip, which is ∼1.5 m higher in amplitude than in the margin-wide $M_W$9 rupture model HE. Wirp et al. (2021) show that an increase in $D_c$ (i.e., increased fracture energy, Rice (1980); Cocco et al. (2023); Kammer et al. (2024)) can enhance megathrust on-fault slip significantly and lead to larger tsunamis. The DCA model produces a moment magnitude of $M_W$∼8.4, demonstrating that the multi-scale asperity approach, incorporating the expected but hard-to-constrain heterogeneities in subduction zones, offers an efficient way to parameterize earthquake rupture extents on an otherwise smooth and non-segmented subduction interface geometry. The DCA model generates a peak vertical seafloor displacement of ∼3.5 m, which is much larger than in the other $M_W$∼8 models we propose. While the specific characteristics of the DCA rupture model originate from the assumed multi-scale $D_c$ variations, we expect that alternative models with (scale-dependent) heterogeneous fault stress, e.g., constrained by past seismicity, could achieve similar characteristics, such as a limited rupture extent and a more complex rupture process (e.g., Oral et al., 2022).

Combining the segmented stress and the multi-scale asperity models further reduces the modeled moment magnitude to $M_W$7.5, rendering model DCAS as our scenario with the smallest $M_W$. The combination of regions of unfavorably oriented stress and on-fault heterogeneities effectively limit moment magnitude in our dynamic rupture scenarios.

### 4.5.2 Modeling the 1303 earthquake as constrained by a single asperity versus stress segmentation

In the following, we compare two different approaches to modeling dynamic rupture earthquake scenarios yielding magnitudes similar to the 1303 Crete earthquake ($M_W sim 8$) on the Hellenic Arc megathrust itself. Both dynamic rupture examples have hypocenter locations and seafloor uplift that may resemble the 1303 earthquake. First, we discuss that prescribing a single fault stress asperity (model HEA) is an efficient way to limit earthquake dynamic rupture slip and moment magnitude. Second, regionally segmented initial stress based on stress inversions (model HES) also acts as an efficient barrier.

#### The single asperity approach

The moment magnitude of the single asperity model (HEA, $M_W 8.04$) fits the moment magnitude inferred for the 1303 earthquake (Papazachos et al., 1999). However, the modeled maximum vertical seafloor uplift of ∼1.29 m is relatively low compared to Necmioğlu and Özel (2014), who use a displacement of 9 m as a source for their tsunami model representing the 1303 event. The vertical seafloor uplift in our model can be explained by the relatively deep location of the hypocenter and the slipping asperity, in conjunction with the low on-fault slip modeled. We conclude that a fault stress asperity offers a simple way to effectively restrict rupture propagation to a predefined fault area.

#### The segmented stress model

Accounting for along-arc variations of regional stress orientation as constrained by stress inversions allows modeling non-margin-wide ruptures. In several regions, the constrained regional stress does not promote rupture propagation across the megathrust, which can lead to spontaneous rupture arrest. The partial ruptures using the segmented stress model are associated with 6.13% (HMS) and 53.69% (HES) lower on-fault slip than the margin-wide rupture scenarios. With moment magnitudes of $M_W$=8.81 (HMS) and $M_W$=8.12 (HES) and maximum seafloor uplifts of 1.71 m (HMS) and 1.17 m (HES), the two segmented stress models are comparable to maximum events proposed for tsunami studies in the Hellenic arc area (e.g., Tinti et al., 2005; Yolsal et al., 2007; Lorito et al., 2008; Necmioğlu and Özel, 2014).

The moment magnitude, hypocenter location, and distribution of the seafloor deformation of the HES model resemble scenarios of the 1303 Crete earthquake modeled by Necmioğlu and Özel (2014). We, nevertheless, note that the fault slip and associated ground deformation pattern of this event are poorly constrained. As an illustration, Yolsal et al. (2007) model the 1303 Crete earthquake and the associated tsunami using a smaller southeast striking, northeast dipping fault plane. Due to the fault orientation, their assumed initial water displacement caused by the 1303 event is different than what we would expect from the seafloor displacement of the HES model. Their modeled northwest-southeast oriented uplift of the water column, located south of Crete, disagrees

with the rupture propagation direction in our models that causes southwest-northeast oriented seafloor uplift.

### 4.5.3 Shake maps

We find that maximum PGVs vary by epicentral locations among the models, but highly depend on shallow slip into the slip-strengthening region of the fault. Thus, models with a western hypocenter lead to a broader extent of higher PGVs, compared to a hypocenter on the eastern Hellenic Arc. High stress drop of model DCA produces relatively high PGVs, which are localized northeast of Crete island. The models DCA, DCAS, and HEA, which are all M$_\sim$8-8.5 magnitude events, are not able to reproduce a shaking that we believe would be great enough to cause tsunamis compared to the AD365 or 1303 Crete events. Allowing for off-fault plastic yielding doubles the amount of on-fault slip and nearly doubles the maximum vertical seafloor displacement directly above the fault interface while simultaneously limiting the spatial distribution of high PGVs. These compound effects, characterized by increased on-fault slip and larger but more localized uplift in model HEP, align with previous dynamic rupture models in various tectonic contexts (Ma, 2008; Ma and Andrews, 2010; Kaneko and Fialko, 2011; Ma, 2022; Roten et al., 2014, 2017; Ulrich et al., 2022). Off-fault plastic yielding leads to a redistribution of stress and energy that allow for more sustained slip over a larger area, while at the rupture front, the peak slip rate remains limited.

### 4.5.4 Implications for regional earthquake and tsunami hazard assessments

Probabilistic seismic hazard analysis (PSHA), seismic-probabilistic tsunami hazard assessment (S-PTHA) models, as well as tsunami early warning systems, often utilize uniform or stochastic source models; however, these may not fully represent dynamic rupture and tsunami generation complexity. Our study illustrates the key driving factors and ingredients for realistic 3D dynamic rupture models for earthquake scenarios in the Hellenic Arc region. For example, we show that earthquakes comparable in moment magnitude and slip to the AD 365 and 1303 Crete earthquakes can be dynamically viable on the megathrust itself. This finding may support the assumptions underlying the NEAMTHM18 model (Basili et al., 2021), which is the reference regional hazard model for the Tsunami Early Warning and Mitigation System in the North-eastern Atlantic, the Mediterranean and connected sea (NEAMTWS).

For different source locations among our models, the evolving on-fault rupture dynamics and thus, fault slip, peak slip rates, stress drop, and seafloor displacement are highly variable. Specifically, the presented scenarios differ in shallow slip and potentially lead to complex near trench seafloor uplift, which in turn affects PGV distribution (Figs. 4.4.1 and 4.4.7).

Tsunami models based on kinematic or statically derived slip distributions may account for shallow slip amplification (Scala et al., 2020). However, kinematic models are

highly non-unique (Mai et al., 2016; Wong et al., 2023) and may lack the physical self-consistency of dynamic models that can jointly describe spontaneously evolving on-fault slip distribution, seafloor uplift, and peak ground velocities capturing their interplay.

Addressing epistemic uncertainty remains challenging (e.g., Bommer and Scherbaum, 2008; Atkinson et al., 2014; Tarbali et al., 2018; Rodriguez-Marek et al., 2021; Gómez Zapata et al., 2022). Various modeling approaches, such as static, kinematic, and dynamic earthquake models, could be used jointly and differently weighted (Marzocchi et al., 2015). For example, physics-based dynamic rupture models may form differently weighted alternatives within an established PTHA logic tree used in ensemble modeling (Li et al., 2016). The CyberShake model is a prominent example that incorporates physics-based 3D ground motion simulations and wave propagation effects in their seismic hazard calculations for southern California (Maechling et al., 2007; Graves et al., 2011; Meng et al., 2023; Moschetti et al., 2023).

Dynamic rupture models may also be used to directly explore natural earthquake variability (Ripperger et al., 2008; Schmedes et al., 2010; Gallovič and Valentova, 2020) - often treated as aleatory in S-PTHA (e.g., Lorito et al., 2015; Selva et al., 2016; Gibbons et al., 2020; Souty and Gailler, 2021). This would require computational optimization and resources to allow for running sufficiently many scenarios (e.g., Panzera et al., 2016; Li et al., 2023; Folch et al., 2023). To keep computational costs low, dynamic rupture models may help to constrain and to inform less computationally expensive stochastic scenarios (e.g., Murphy et al., 2016; Savran and Olsen, 2020).

### 4.5.5 Limitations of this work

We here do not show models of smaller earthquakes ($M_W$ <7.5), which likely requires including smaller-scale heterogeneity, i.e., smaller size asperities (Murotani et al., 2008; Blaser et al., 2010; Strasser et al., 2010) or fault roughness (Griffith et al., 2010; Candela et al., 2011; Zielke et al., 2017). Instead, we model counterfactual along-arc rupture propagation scenarios (HE, HM, HW, HER) and reproduce magnitudes (HEA, HES) and potential displacements (HEP, DCA) of historic events. Our 3D simulations are computationally challenging, as we include a large part of the megathrust interface, across which the rupture process zone and asperities need to be resolved, and a large portion of the east Mediterranean region to make our simulations applicable to source tsunami simulations.

Smaller magnitude earthquakes ($M_W$ <7) with high tsunamigenic potential (Bocchini et al., 2020) may occur on splay faults, which we do not consider in this study (Wendt et al., 2009; Kiratzi, 2013; Papadimitriou et al., 2016; Ganas et al., 2020). Specifically, high-angle reverse faults in the upper plate above the plate interface may add to the tsunamigenic potential of inter-plate earthquakes (Fukao, 1979; DeDontney and Rice, 2012; Lotto et al., 2019; van Zelst et al., 2022) and should be explored in future studies.

Our ground motion and shake map analysis is meaningful in a relative sense - to compare between scenarios - but is limited by the simplified 1D velocity model we use and by the resolution of 1.75 Hz. For example, Causse et al. (2023) illustrate, based on rupture propagation models, that local basin amplification effects (in thick sediments) can dominate

regional ground motion accelerations in the Mediterranean.

## 4.6 Conclusions

We demonstrate mechanically self-consistent approaches to constrain realistic and heterogeneous initial conditions integrating available observations for Hellenic Arc subduction zone (HASZ) 3D dynamic rupture earthquake scenarios. We analyze an ensemble of ten 3D dynamic rupture earthquake scenarios utilizing a realistic slab geometry in combination with increasing levels of initial condition complexity, from homogeneous to heterogeneous initial stress conditions, and from single-asperity to stochastic multi-scale asperity models.

Our ensemble of 10 dynamic rupture simulations illustrates various aspects of the dynamic variability of fault slip and uplift. Models with different epicentral locations and homogeneous initial conditions represent counterfactual margin-wide scenarios reaching $M_W$∼9. Dynamic rupture propagates into shallow slip-strengthening portions of the slab. The further west the epicenter location, the more shallow slip is dynamically generated and, consequently, the more pronounced the modeled localized near-trench uplift becomes. A slightly more shallowly plunging maximum compressive stress leads to spontaneous rupture arrest before crossing the complete margin, generating a moment magnitude of $M_W$8.61 but a similar maximum vertical displacement of ∼1.6 m compared to the margin-wide rupture scenarios. Off-fault plastic deformation of unconsolidated sediments efficiently prevents shallow fault slip, reduces local PGVs by about ∼30-50%, and doubles the amount of seafloor uplift. A prescribed prestress asperity dynamic rupture earthquake scenario effectively limits fault slip to a moment magnitude similar to the 1303 Crete event. Incorporating regional along-strike variations of the initial stress, constrained by stress inversion, limits dynamic rupture propagation and slip to the deeper slip-weakening region of the slab. The resulting $M_W$∼8.5 earthquakes show complex uplift patterns reflecting the more heterogeneous initial conditions. Adding multi-scale, randomly distributed frictional asperities leads to five times higher peak slip rates than in the other models and causes the largest seafloor displacements of up to ∼3.5 m. In the most complex model, we combine a multi-scale asperity approach with the regional along-arc segmented prestress, resulting in the highly heterogeneous rupture propagation and the smallest rupture area.

This study is a first step towards including dynamic rupture modeling in regional Hellenic Arc seismic and seismic-tsunami hazard assessment. Our approach of constraining dynamic rupture initial conditions with increasing levels of complexity can be valuable for other, mostly 'quiet' subduction zones, such as the Cascadia subduction zone, as it may provide a catalog of physics-based scenarios suitable to inform hazard assessment and disaster risk management planning in the absence of long and complete historical records.

# Acknowledgments

We thank the Editor Satoshi Ide, the Associate Editor, and two anonymous reviewers for their thoughtful and constructive comments. We thank Janina Moser for her initial analysis as part of her Bachelor's thesis. We thank Lukas Krenz and Michael Bader for their technical expertise.

This work was supported by the European Union's Horizon 2020 Research and Innovation Program (TEAR ERC Starting grant agreement No. 852992), Horizon Europe (ChEESE-2P grant No. 101093038, DT-GEO grant No. 101058129 and Geo-INQUIRE grant No. 101058518), the National Science Foundation (grant nos. EAR-2225286, EAR-2121568, OAC-2139536, OAC-2311208), and the National Aeronautics and Space Administration (80NSSC20K0495).

The authors acknowledge the Gauss Centre for Supercomputing e.V. (`www.gauss-centre.eu`, projects pr63qo, pn68fi, pr83no, pn49ha) for funding this project by providing computing time on the GCS Supercomputer SuperMUC-NG at Leibniz Supercomputing Centre (`www.lrz.de`). Computing resources were also provided by the Institute of Geophysics of LMU Munich Oeser et al. (2006).

# Appendix

## 4.A Computational mesh used for all ten dynamic rupture simulations

We show the computational mesh to illustrate the mesh resolution and coarsening away from the fault.

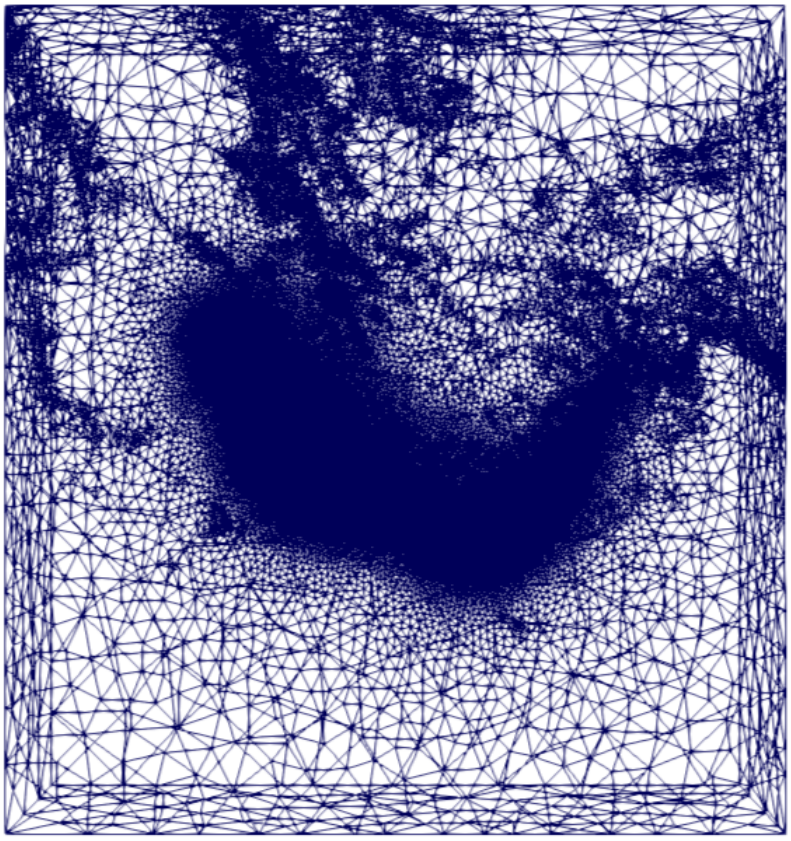


Figure 4.A.1: Top view on the wireframe of the computational mesh used to run the DR models of this study. Note the fine mesh resolution above the fault and the mesh coarsening to the simulation boundaries.

## 4.B Close-up views of dynamic rupture simulation results

We show close-up views of chosen results of dynamic rupture simulations to better visualize small-scale rupture characteristics compared to the spatial extent of the slab. Due to the smaller rupture in models HEA, HES, and DCAS, it is helpful to zoom in on the fault area where rupture propagation occurs and the surface area where we observe uplift. For models HER, HEA, HMS, HES, DCA, and DCAS, we add a closeup after 20 s rupture propagation to better visualize differences in dynamics at this early stage of rupture propagation. All figures relate to figures in the results section (Sec. 4.4).

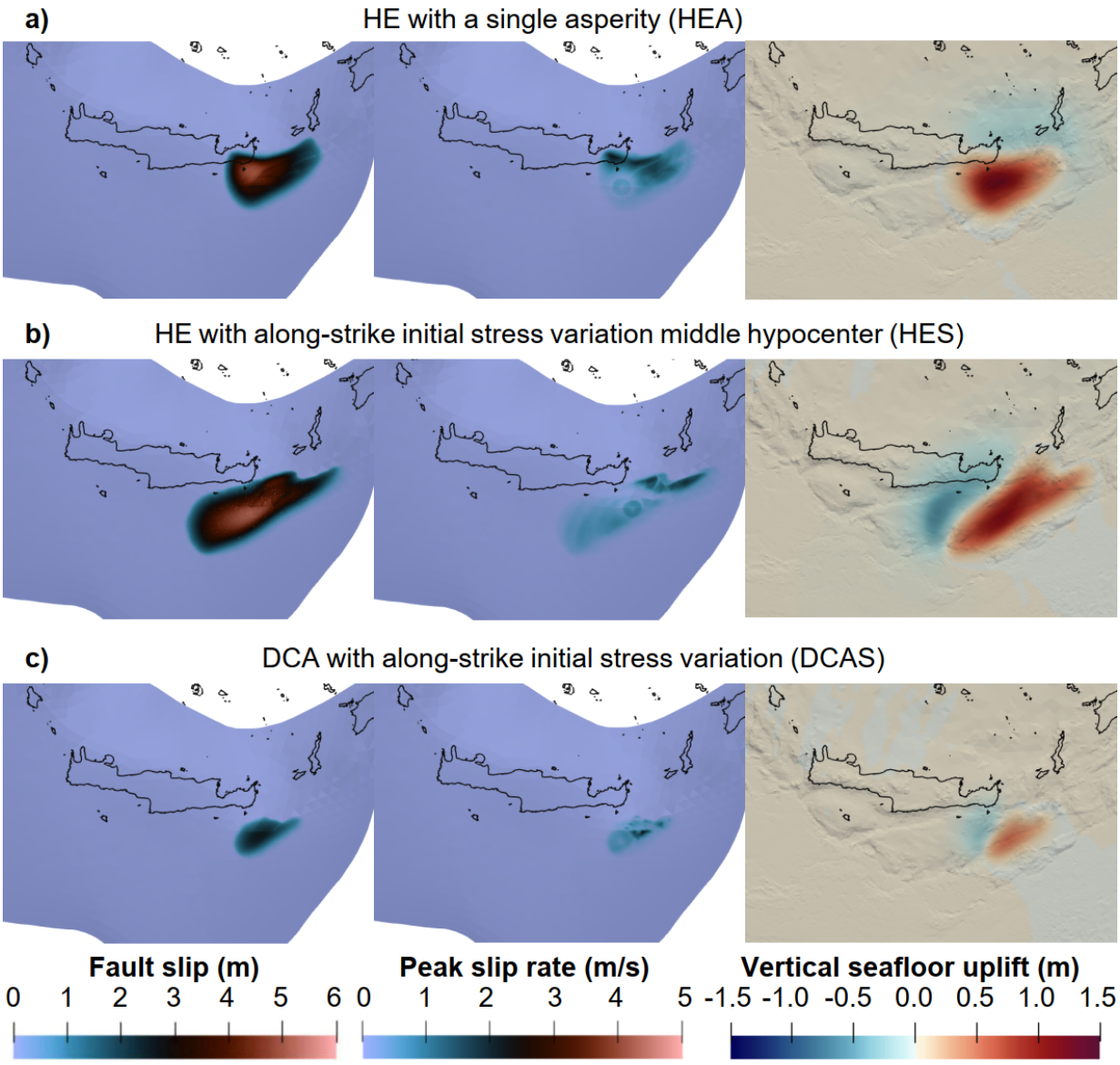



Figure 4.B.1: **Close-up of rupture characteristics of model HEA, HES and DCAS:** Zoom in of Fig. 4.4.5b,d, and e showing the final fault slip, peak slip rate, and vertical seafloor displacement. The color scales are saturated. For absolute maximum values see Table 4.4.1. Areas of high PSR do not coincide with areas of high fault slip. The vertical seafloor displacement mirrors the final on-fault slip. The seafloor subsidence for HES is more pronounced than for HEA and DCAS.

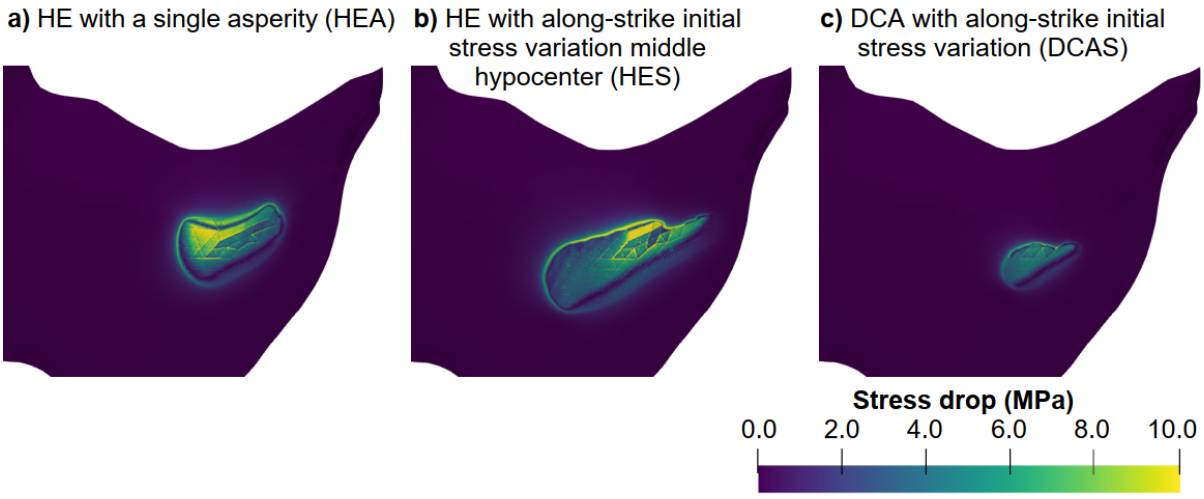



Figure 4.B.2: **Stress drop for model HEA, HES, and DCAS:** Close-up of Fig. 4.4.3f,h and j. For HES, the stress drop is highest at the steeper dipping fault, whereas the stress drop of HEA and DCAS is homogeneously distributed.

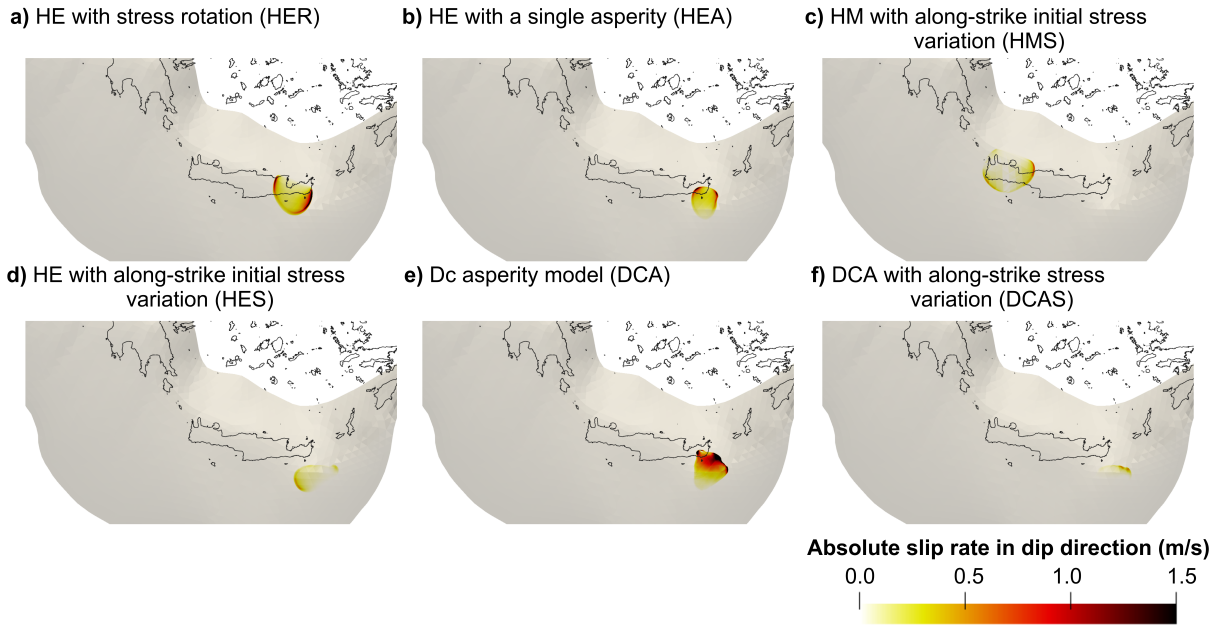



Figure 4.B.3: **Close-up of Fig. 4.4.6:** Slip rate in dip direction for simulations HER **a)**, HEA **b)**, HMS **c)**, HES **d)**, DCA **e)**, and DCAS **f)** at 20 s simulation time. Note the bilateral rupture evolution for models HER, HEA, and HMS. For DCA, the slip rate is highest, whereas the smaller moment magnitude DCAS scenario experiences a lower slip rate than all other models.

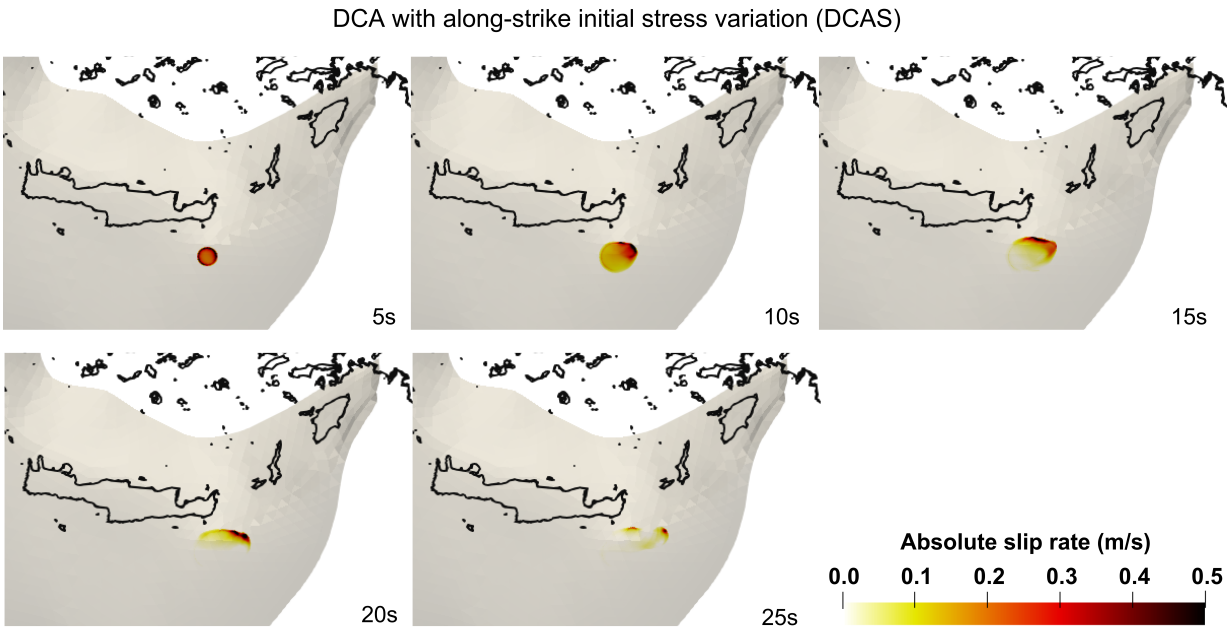



Figure 4.B.4: **Close-up of Fig. 4.4.6f:** Slip rate in dip direction for simulation DCAS at 5 s, 10 s, 15 s, 20 s, and 25 s simulation time. Note the changed color scale compared to Figs. 4.4.6 and 4.B.3.

# Chapter 5

# Hellenic Arc tsunami generation from $M_W$8+ 3D margin-wide dynamic rupture earthquake scenarios

## Abstract

The Hellenic Arc subduction zone is the most seismically active region in the Mediterranean, capable of generating large earthquakes and tsunami. Given the proximity of densely populated coastlines, understanding the characteristics of potential future large tsunamigenic earthquakes is crucial for assessing tsunami hazard. We present non-linear shallow water tsunami simulations sourced from the static seafloor displacements of five $M_W$8–9 dynamic rupture earthquake scenarios along the Hellenic Arc, varying in hypocentral location, rupture extent, and moment magnitude. In three of these 3D rupture models, slip penetrates the shallow slip-strengthening region of the megathrust, generating uplift patterns modulated by the location of the hypocenter. Our results show that shallow slip and off-fault plastic deformation control the vertical near-trench uplift and tsunami height in the near-field. Maximum tsunami amplitudes reach up to ∼6.6 m near central and eastern Mediterranean coastlines, while the northern Aegean and the western Mediterranean remain mostly shielded by landmasses in all scenarios. One scenario is further extended into a large-scale fully-coupled 3D earthquake-tsunami model, capturing dynamic rupture, seismic and acoustic wave propagation, and time-dependent tsunami generation. The fully-coupled simulation reveals complex interactions between acoustic and tsunami waves during the early generation phase, including dispersion and wave conversions between seismic and ocean acoustic waves not captured by static or linked models. These results highlight the value of integrating 3D dynamic rupture modeling with tsunami simulations, enhance our understanding of tsunami generation mechanisms, and can provide physics-based insights to tsunami hazard assessment and early warning strategies.

# Plain Language Summary

The region around the Greek islands is the most earthquake and tsunami-prone area in the Mediterranean. Historically, this region produced powerful earthquakes that triggered tsunami waves, affecting populated coastal areas and devastating towns. Thus, it is important to consider different earthquakes and the tsunamis they generate to better constrain seismic and tsunami hazard. We here use computer models to simulate tsunamis of five possible earthquakes. We vary the earthquake's starting point and get earthquakes of a moment magnitude of 9, which spread across the entire region. The earthquakes produce different vertical deformation patterns, which lead to different ocean wave heights and arrivals on the coasts. The waves reach the coasts around the eastern Mediterranean, but do not extend to France, Spain, or Algeria in the West, as they are protected by land masses. When including plastically deforming rocks in our earthquake models, the tsunami amplitudes get much higher (6.6 m). This study also includes a detailed simulation that combines the earthquake and tsunami in one 3-dimensional model and demonstrates the complexities of tsunami generation. Our results highlight that combined earthquake-tsunami modeling is a powerful tool to improve hazard assessment for this region and elsewhere.

# 5.1 Introduction

## 5.1.1 The tectonic setting of the Hellenic Arc Subduction Zone

At the Hellenic Arc Subduction Zone (HASZ), the African plate subducts beneath the Eurasian plate at a convergence rate of 25–60 mm/yr (Taymaz et al., 1990; McClusky et al., 2000; Reilinger et al., 2006). This leads to thrust faulting along the outer Hellenic Arc (McKenzie, 1972, 1978; Benetatos et al., 2004). The subduction is suggested to be driven by slab roll-back of the subducting Nubian plate, pushing the African plate towards the Aegean Sea plate (Bohnhoff et al., 2005; Sachpazi et al., 2016; Meng et al., 2021). The resulting arc-orthogonal compression in the west and arc-oblique convergence in the east shape the Hellenic Arc into an elliptical structure (see Fig. 5.1.1, a). The interplay of subduction and regional tectonics generates complex deformation patterns, including east-west extension in the inner arc (McClusky et al., 2003; Kreemer and Chamot-Rooke, 2004) and north-south extension in the southern and central Aegean (Kiratzi and Papazachos, 1995; McKenzie, 1978; Pichon and Angelier, 1979). This leads to diverse faulting styles including strike-slip faulting southeast of Crete, associated with the Plini and Strabo trench (Jongsma, 1977), and a transition to more oblique faulting towards the north-west (Goldsworthy et al., 2002; Karakostas and Papadimitriou, 2010; Bie et al., 2017; Chousianitis and Konca, 2019; Cirella et al., 2020), occasionally causing moderate tsunami. Although the HASZ has long been considered to accommodate slip aseismically due to its relatively low seismicity compared to its high convergence rate (e.g., Papazachos and Kiratzi, 1996; Shaw et al., 2008), recent studies indicate that the megathrust may be fully seismically coupled and capable of generating large earthquakes (Laigle et al., 2004; Ganas and Parsons, 2009), motivating an improved understanding of the characteristics of potential future large tsunami, specifically in the proximity of densely populated coastlines.

## 5.1.2 Hellenic Arc tsunamigenic earthquakes

Earthquakes associated with the subducting Hellenic Arc megathrust or surrounding tectonic features, such as splay faults branching off the megathrust, reportedly produced several tsunami (e.g., Galanopoulos, 1960; Ambraseys, 1962; Antonopoulos, 1980; Papadopoulos and Chalkis, 1984; Guidoboni and Comastri, 1997; Papadopoulos et al., 2012). The largest known earthquakes of the HASZ are the AD 365 and the 1303 Crete events, which ruptured the south-western and eastern segment of the Hellenic Arc, generating estimated moment magnitudes of $M_W \approx 8$ (see Fig. 5.1.1, b) (Ambraseys, 1994; Guidoboni et al., 1994; El-Sayed et al., 2000; Hamouda, 2006; Shaw, 2012; Papadimitriou and Karakostas, 2008). Both earthquakes sourced devastating tsunamis that inundated many coastal regions of the eastern Mediterranean, causing destruction and loss of life (Papadopoulos et al., 2014; Cirella et al., 2020).

Several moderate earthquakes with moment magnitudes ranging from $M_W \sim 5.5$–$6.8$ (in 1494, 1612, 1741, 2000, 2009, 2017, 2018, and 2020) produced smaller and more localized tsunami (Papadopoulos et al., 2010; Bocchini et al., 2020; Baglione et al., 2021; Moham-

mad and Riadi, 2021). The 1st July 2009 event, for example, ruptured the offshore margin near the trench of the HASZ south of Crete, probably breaking a reverse fault of the upper plate and causing a tsunami height of 0.3 m. The $M_W$6.8 25th October 2018 event that occurred near Zakynthos island was followed by a moderate tsunami recorded by several tide-gauge stations in the Ionian Sea (Cirella et al., 2020; Papadopoulos et al., 2020a). Two $M_W$6.6 thrust-faulting events occurred in May 2020 near the location of the 2009 $M_W$6.4 earthquake, south of Crete, and both caused tsunami reaching the Crete coast (e.g., Papadopoulos et al., 2020b). Other thrust-faulting interplate events, such as the 1952 $M_W$7.0 and the 1972 $M_W$6.5 earthquakes south of Crete (Papadopoulos and Chatziathanasiou, 2011), or the 2013 $M_W$ ∼6.6 earthquake of the western HASZ (Vallianatos et al., 2014) did not cause any noticeable tsunami.

The earthquake and tsunami history of the HASZ makes it the most seismically active tsunami-prone region of the Mediterranean Sea (Pirazzoli et al., 1996; Vannucci et al., 2004; Ganas and Parsons, 2009; Ozer et al., 2018; Chorozoglou and Papadimitriou, 2019). Several $M_W$ ≥7 earthquakes related to the HASZ (Papazachos and Papazachou, 2003; Guidoboni et al., 2005; Ambraseys, 2009), including 11 earthquakes of moment magnitude ≥7 have been recorded since 1900 (Papadimitriou et al., 2016), motivating the focus of this study on large tsunamigenic earthquake scenarios. Probabilistic seismic and tsunami hazard studies agree on the high hazard posed by the HASZ (e.g., Coban and Sayil, 2020; Papadopoulos and Kijko, 1991), associated with its active tectonics. In particular, Probabilistic tsunami hazard assessment (PTHA) studies (Sørensen et al., 2012) confirm that the eastern Mediterranean is under the highest tsunami hazard within the Mediterranean Sea.

### 5.1.3 Earthquake sources in tsunami models

Tsunami models, particularly for PTHA studies, commonly use simplified static or kinematic earthquake source models. These models may utilize different representations of complexities in their initial conditions, such as depth-dependent structural properties (Scala et al., 2020; Basili et al., 2021) or stochastically distributed heterogeneous slip (Small and Melgar, 2021; Cifuentes-Lobos et al., 2023). Also, different filters can be considered when linking earthquake sources to tsunami (Madden et al., 2020; Sementsov and Nosov, 2023; Abbate et al., 2024; Scala et al., 2024; Sementsov et al., 2024). Testing of stochastic earthquake models against deep ocean observations shows that the tsunami they generate are statistically similar to the observations themselves, at least in the deep sea and in the far-field (Davies and Griffin, 2019). It remains to be further assessed whether these models are equally performing in the near-field and in terms of coastal inundation, as well as if the degree of variability typically imparted to these models can be reduced. Several solutions have been proposed in this respect, either based on statistical or machine-learning approaches (Lorito et al., 2015; Volpe et al., 2019; Davies et al., 2022; Briseid Storrøsten et al., 2024; Abbate et al., 2025).

Stochastic earthquake models may not realistically represent the highly complex physical and time-dependent rupture dynamics of natural earthquakes (Tinti et al., 2021), that

include, for example, rupture complexity, interactions with off-fault plastic deformation, supershear, slow rupture speeds, or near-surface rake rotation (Geist, 2002; Ma and Nie, 2019; Wirp et al., 2021; Elbanna et al., 2021; Ulrich et al., 2022; Kutschera et al., 2024a). The instantaneous uniform slip derived from point-source seismic inversion and/or scaling relations (e.g., Maeda et al., 2013; Melgar and Bock, 2013; Dias et al., 2014; Mori et al., 2017; Davies et al., 2018; Davies and Griffin, 2019; Gibbons et al., 2022), can differ significantly from the complex spatio-temporal varying seafloor displacements generated by dynamic rupture simulations (Wendt et al., 2009; Madden et al., 2020). A time-dependent tsunami source initialization can specifically make a difference for long rupture duration earthquakes, large and/or slow earthquakes (Luo and Liu, 2021; Scala et al., 2024; Sementsov et al., 2024).

Dynamic rupture models may complement simpler tsunami hazard approaches and help better understand the physics underlying the propagation of earthquake rupture, reduce nonphysical variability, and unravel how ground velocities and acceleration depend on complex earthquake dynamics (Dunham and Archuleta, 2005; Ripperger et al., 2008; Shi and Day, 2013; Galvez et al., 2016; Withers et al., 2018; Gallovič and Valentová, 2023). Despite challenges in constraining dynamic input parameters such as the prestress distribution (Lambert et al., 2021; Tang et al., 2021; Chen et al., 2024), dynamic rupture models are physically self-consistent and can be used to directly source a tsunami simulation. Various approaches exist to link dynamic rupture to tsunami modeling. One possibility is to extract the static or time-dependent seafloor displacement from a dynamic rupture simulation and use it as static or time-dependent input for a tsunami simulation (Wendt et al., 2009; Saito et al., 2019; Madden et al., 2020; Wirp et al., 2021; Prada et al., 2021; Wilson and Ma, 2021; Ma, 2022; Ulrich et al., 2022; Kutschera et al., 2024a).

"Fully-coupled" earthquake-tsunami models contain a water layer atop a dynamic rupture earthquake model and can account for the non-hydrostatic ocean response (Lotto and Dunham, 2015; Lotto et al., 2018; Krenz et al., 2021; Wilson and Ma, 2021; Ma, 2022). Such models simultaneously solve for the rupture process, seismic wave propagation in elastic media and acoustic wave propagation in the ocean, and the induced tsunami, while capturing dispersion effects during the tsunami generation phase (Krenz et al., 2021; Abrahams et al., 2023; Kutschera et al., 2024a), where the tsunami is modeled through a gravity-restoring boundary condition at the sea surface (Sec. 5.2.3).

### 5.1.4 Overview of this study

In this study, we investigate the dynamics of large tsunami sourced by $M_W$8–9 megathrust earthquakes across the HASZ using two techniques to model earthquake-tsunami interactions, one-way linked models using the seafloor displacement from 3D dynamic rupture simulations and a fully-coupled simulation (Abrahams et al., 2023).

We use five recently developed physics-based dynamic rupture models, named HE, HM, HW, HEP, and HEA following Wirp et al. (2024), that capture a range of plausible rupture scenarios, detailed hereinafter (Sec. 5.2). The models differ in epicentral locations, rupture extent, and magnitude, resulting in variations of shallow slip amplification and

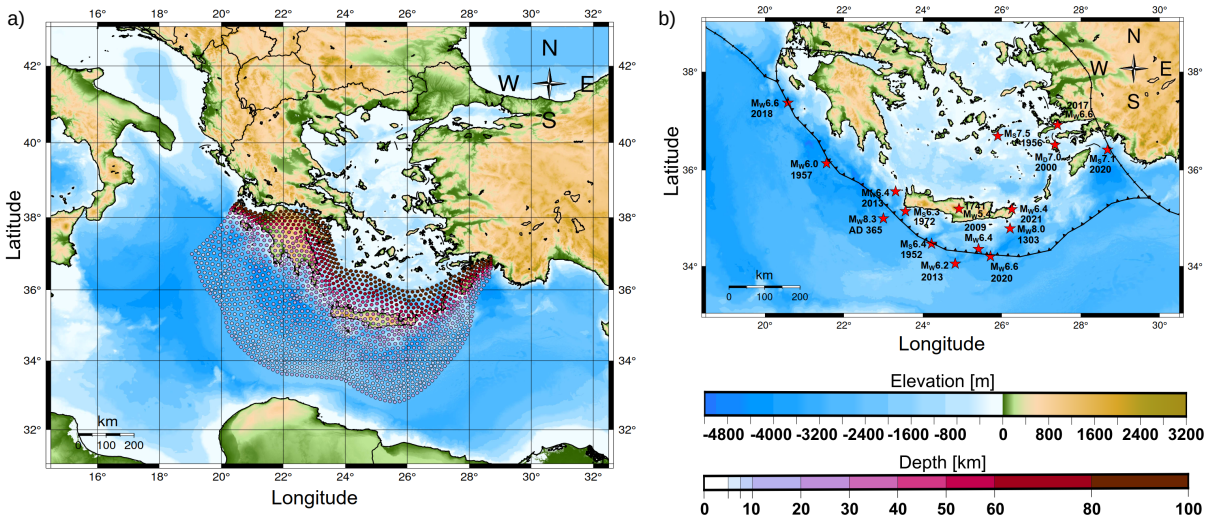



Figure 5.1.1: **Dynamic rupture modeling domain:** a) The Hellenic Arc megathrust by Scala et al. (2020); Basili et al. (2021) used in this study. The dark red color indicates deeper fault depths. Note that the tsunami modeling computational domain extends beyond the dynamic rupture modeling domain (Figs. 5.3.2 and 5.3.3). b) Zoom into the Hellenic Arc region with $M_W$ >5.4 earthquakes (red stars) related to the Hellenic Arc subduction or surrounding tectonics (Papadopoulos et al., 2010; Bocchini et al., 2020; Cirella et al., 2020; Coban and Sayil, 2020). Plate boundaries are indicated by black lines (Bird, 2003), and the convergent subduction margin is marked with triangles.

co-seismic uplift. The hypocenter of model HE is prescribed below southeast Crete at a depth of 30 km (Fig. 5.3.1a,f). We vary the hypocentral location to investigate the effect of rupture propagation direction and slip distribution on co-seismic seafloor displacements and tsunami propagation. In model HM (middle hypocenter, Fig. 5.3.1b,g), the hypocenter is located between Crete and Peloponnese. In model HW (western hypocenter, Fig. 5.3.1c,h), it is located further west, below northwest Greece. Both models have the same hypocentral depth as model HE. Model HEP includes a non-associative (visco-)plastic Drucker-Prager rheology (Andrews, 2005; Wollherr et al., 2018) to analyze the effects of weak sediments on co-seismic seafloor deformation and tsunami amplitudes. In model HEA, we use a single prestress asperity to limit the potential rupture size by reducing the initial loading outside this region, resulting in an $M_W$ ∼8 event.

We remodel the selected scenarios at higher resolution to use the same computational mesh for both the fully-coupled scenario and the linked earthquake-tsunami models. We select three margin-wide rupture models (HE, HM, HW) that vary in hypocentral location, shallow fault slip, and consequent evolving seafloor displacement. Additionally, we use an earthquake rupture scenario that includes off-fault plastic yielding (HEP), leading to a much higher seafloor displacement than the other models. Lastly, we use a single initial stress asperity model (HEA) at the approximate location of the 1303 Crete earthquake (Wirp et al., 2024).

The dynamic rupture and tsunami setups are detailed in Sec. 5.2, while Sec. 5.3.1 summarizes the results of the five earthquake rupture scenarios used for this study. Sec. 5.3.1 highlights the results of the tsunami sourced by the static seafloor displacement of the dynamic rupture simulations. We show "worst-case" scenarios in terms of earthquake magnitude and their earthquake-tsunami interaction simulated in the HASZ. We investigate how adding off-fault plastic yielding or a stress asperity in the dynamic rupture model may influence tsunami generation and propagation in this region. We further extend scenario HE into one of the largest-scale fully-coupled 3D earthquake-tsunami models to date, to better understand tsunami genesis (Sec. 5.3.2). We discuss the limitations and challenges of both approaches and provide guidance on selecting the appropriate method for different research questions.

## 5.2 Methods

This section describes the methods and workflow for performing one-way linked and 3D fully-coupled dynamic rupture earthquake-tsunami models. We first introduce SeisSol, the open-source scientific software for the numerical simulation of seismic wave phenomena and earthquake dynamics (Sec. 5.2.1), before we clarify differences between the one-way linked shallow water tsunami models simulated with GeoClaw (Sec. 5.2.2) and the fully-coupled approach implemented in SeisSol (Sec. 5.2.3). We then detail the model domain (Sec. 5.2.4), followed by the dynamic rupture modeling setup, which includes on-fault friction and initial stresses (Sec. 5.2.5), and off-fault plasticity (Sec. 5.2.6).

### 5.2.1 Dynamic rupture modeling with SeisSol

We use the open-source software package SeisSol (`https://seissol.org`; Uphoff et al. (2024)) on the Munich high-performance supercomputing cluster SuperMUC-NG to simulate five 3D earthquake dynamic rupture scenarios on the HASZ. SeisSol uses the Arbitrary high-order accurate DERivative Discontinuous Galerkin method (ADER-DG) (Käser and Dumbser, 2006; Dumbser and Käser, 2006; de la Puente et al., 2009) and achieves high-order accuracy in both space and time in modeling the seismic wavefield (Breuer et al., 2015; Heinecke et al., 2014; Uphoff et al., 2017; Krenz et al., 2021). Here, we simultaneously simulate non-linear frictional on-fault failure, off-fault plastic deformation, and seismic wave propagation. SeisSol accounts for (visco-)plastic Drucker-Prager off-fault plastic deformation (Andrews, 2005; Wollherr et al., 2018). We use unstructured tetrahedral meshes enabling models incorporating complex three-dimensional model geometries and topography (e.g., Ulrich et al., 2019a; Wolf et al., 2020; Li et al., 2023; Taufiqurrahman et al., 2023; Kutschera et al., 2024a). The software has been verified against community benchmarks for dynamic rupture earthquake simulations (Pelties et al., 2014; Harris et al., 2018; Vyas et al., 2023), including heterogeneous off-fault material and initial on-fault stresses.

### 5.2.2 One-way linked tsunami modeling with GeoClaw

In the one-way linking approach, we use the static displacement at the end of each dynamic rupture simulation (400 s after rupture onset) to source a state-of-the-art tsunami simulation. By this time, the rupture process has terminated, and the ground deformation pattern is permanent, with no transient waves remaining (Madden et al., 2020). We use the software GeoClaw (Berger et al., 2011; LeVeque and George, 2008; LeVeque et al., 2011), which implements the nonlinear 2-dimensional depth-averaged shallow water equations with adaptive mesh refinement (AMR) using high-resolution finite volume methods. Our GeoClaw simulations do not account for inundation. GeoClaw has been extensively validated (e.g., Arcos and LeVeque, 2015; Omira et al., 2022; Kutschera et al., 2024b) and approved by the US National Tsunami Hazard Mitigation Program (Gonzalez et al., 2011).

GeoClaw can handle heterogeneous seafloor displacements to source a tsunami. We closely follow Ulrich et al. (2022) to transform the SeisSol surface output to GeoClaw input. To approximate the contribution to tsunami generation of horizontal coseismic displacements, particularly relevant with strong bathymetric gradients, we apply the Tanioka filter (Tanioka and Satake, 1996). The element-wise unstructured triangular seafloor output from SeisSol is stored in a Cartesian coordinate system. This output is interpolated onto a structured latitude–longitude grid on a spherical surface. We apply a Hanning window to prevent sharp displacement discontinuities at the limits of the region of imposed displacements. We use the GEBCO (Group, 2019) bathymetry dataset with a horizontal resolution of 15 arcsec (approx. 380 m). The tsunami model domain extends beyond the earthquake model domain and captures the source region, as well as most of the Mediterranean Sea (Fig. 5.3.2), from 30° in longitude from 7° to 37° and 16° in latitude from 30° to 46°. We use three AMR levels in our GeoClaw simulations, with the finest grid spanning

48 arcsec. We simulate tsunami propagation for 8 hours, which is sufficient to capture tsunami extrema everywhere in the modeled domain. Each 8-hour GeoClaw simulation required <6 CPU hours, which is considerably less than the 3D fully coupled simulation described in the next sections.

### 5.2.3 3D fully-coupled earthquake-tsunami modeling

We showcase one high-resolution 3D fully-coupled earthquake-tsunami simulation for the HASZ. Fully-coupled earthquake-tsunami models combine earthquake rupture dynamics, wave propagation in elastic and acoustic media, and tsunami propagation in a compressible ocean (Lotto and Dunham, 2015; Lotto et al., 2018; Wilson and Ma, 2021; Ma, 2022) in a self-consistent way. They naturally account for the non-hydrostatic ocean response that leads to dispersion effects during the tsunami generation and propagation phases. At the interface between the acoustic and elastic medium, the physical conditions can be matched numerically, by solving the Riemann problem (Wilcox et al., 2010) exactly and as a combination of both, elastic and acoustic properties. This elastic-acoustic coupling is implemented in SeisSol by treating the acoustic wave equation as a special case of the elastic wave equation (Krenz et al., 2021). In the water layer, the rigidity is set to zero ($\mu = 0$). The acoustic wave speed is set to $\sim$1500 ms$^{-1}$. Our fully-coupled model accounts for gravitational effects using a modified surface boundary condition, which is applied on the equilibrium ocean surface, to correctly capture the onset of tsunami propagation (Krenz et al., 2021). Aiming at capturing the full physics of the tsunami generation process, we build a structural model including a three-dimensional water layer of variable depth on top of a realistic bathymetric surface representation. For the fully-coupled model, we choose the HE earthquake dynamic rupture scenario. The fully-coupled model and the one-way linked earthquake tsunami scenario share the same initial conditions and the same solid Earth mesh.

### 5.2.4 Computational domain and meshing

We use the same HASZ slab geometry as in Wirp et al. (2024), which is based on tsunami hazard studies of the Mediterranean region (Scala et al., 2020; Basili et al., 2021). The modeling domain of the dynamic rupture model spans most of the Eastern Mediterranean, including southern Italy and parts of Sicily in the West, the African coast of Libya and Egypt in the south, extensive parts of Turkey's East Coast, and the whole Greece up to the Black Sea in the North (see Fig. 5.1.1), and reaches the western limit of Cyprus island in the east. The mesh of the dynamic rupture model is generated from the mesh used for the fully-coupled model by excluding the water layer part. It consists of 87.66 million elements. The fault is resolved by a 1000 m mesh. We use basis functions of polynomial order $p = 5$ (i.e., sixth-order accuracy in time and space of the wave propagation kernels), which is sufficiently high to accurately resolve rupture dynamics (Wirp et al., 2024).

In the fully-coupled SeisSol models, to reduce the high computational costs associated with the oceanic acoustic and tsunami wave simulation (see Fig. 5.A.1), the water layer

of the fully-coupled DR-tsunami model spans not the complete domain but a region of 1.100 by 800 km. Thus, the water layer has a smaller horizontal extent than the modeling domain of the dynamic rupture simulations. It includes large parts of the Greek coast and a part of the Libyan coast in northern Africa (see Figs. 5.A.1a,b,c). In the SeisSol mesh, we allow for static coarsening of the mesh elements towards the domain boundaries (Figs. 5.A.1a,d).

A finely sampled bathymetry is primordial for being able to model accurately propagation of shorter tsunami wavelengths in shallower water depth regions. The water layer is meshed with a spatial discretization of 200 m, small enough to model wavelengths of ≈1200 m; resulting in a total mesh size of 243 million elements for the fully-coupled model.

Each dynamic rupture earthquake model required ≈8 h on 700 nodes (each with 48 cores) on the Munich supercomputer SuperMUC-NG, which equals to 268,800 core hours. The fully-coupled model is an order more costly and required ≈30 h on 700 nodes, which equals to 1,008,000 core hours. The dynamic rupture models include 6.6 min simulation time, producing an output size of 2.4 TB, while the fully-coupled earthquake-tsunami model captures 5 min simulation time, producing an output of 2.9 TB.

### 5.2.5 Initial stresses and fault friction

As in Wirp et al. (2024), we prescribe a non-Andersonian prestress state. We define a homogeneous regional stress field as a Cartesian stress tensor constrained by assumptions on the effective normal stress depth gradient, and seismo-tectonic constraints on stress orientation and stress amplitude ratio.

The stress shape ratio $\Phi$ balances the principal stress amplitudes and is defined as (Lund and Townend, 2007):

$$\Phi = \frac{\sigma_2 - \sigma_3}{\sigma_1 - \sigma_3}, \tag{5.1}$$

where $\sigma_i$ are the principal stresses with $\sigma_1$ being the orientation of the maximum compressive principal stress and $\sigma_3$ the orientation of the minimum stress. We assume a stress shape ratio of $\Phi$=0.4, consistent with stress inversion results for interplate events around Crete by Bohnhoff et al. (2005). The assumed maximum principal stress $\sigma_1$ dips shallowly at 10° at an azimuth of 280° (290° for model HEA), $\sigma_2$ is horizontal, and $\sigma_3$ steeply plunges and is normal to the $\sigma_1$-$\sigma_2$ plane.

All five dynamic rupture models use a linear slip-weakening (LSW) friction law (Ida, 1972; Andrews, 1976b) and all fault-friction parameters are summarized in Table 4.2.1. The seismogenic part of the Hellenic Arc subduction interface has been inferred at depths of 15–45 km (Vernant et al., 2014), while unconsolidated sediments in the upper 15 km may influence shallow rupture behavior and tsunami generation. We use a depth-dependent strength drop by applying varying dynamic friction value $\mu_d$ = 1.2–0.2 and a constant Byerlee compatible static friction value $\mu_s$ = 0.6 (Byerlee and Summers, 1976). In all models expect HEA, the uppermost 15 km of the fault are assumed to be slip-strengthening ($\mu_s \geq \mu_d$, and for model HEA in the uppermost 10 km) to capture the aseismic deformation behavior of the upper fault. Slip-weakening frictional behavior is assumed for the depth

of 15–43.3 km (10–43.3 km for HEA, respectively), while depths deeper than 43.3 km are governed by slip-strengthening. The critical slip weakening distance $D_c$ is constant and set to 1.0 m in all models.

The relative prestress ratio $\mathcal{R}$ (e.g., Aochi and Madariaga, 2003) is defined as:

$$\mathcal{R} = \frac{\Delta\tau}{\Delta\tau_b} = \frac{\tau - \mu_\mathrm{d}\sigma_n'}{c + (\mu_\mathrm{s} - \mu_\mathrm{d})\sigma_n}, \tag{5.2}$$

and relates the maximum potential stress-drop during dynamic rupture $\Delta\tau$ to the frictional breakdown strength-drop $\Delta\tau_b$, with $c$ being the frictional cohesion, and $\mu_\mathrm{d}$ and $\mu_\mathrm{s}$ the dynamic and static friction coefficients, respectively. We define $\mathcal{R}_0 \geq \mathcal{R}$ as the maximum possible value of $\mathcal{R}$. $\mathcal{R} = \mathcal{R}_0 = 1$ characterizes critically prestressed faults that are also optimally orientated towards the regional prestress tensor. $\mathcal{R}_0$ is set to 0.7, as in (Wirp et al., 2024).

We define the pore fluid pressure ratio as:

$$\sigma_{zz}'(z) = (1 - \gamma)\rho g z \tag{5.3}$$

with $\sigma_{zz}'$ being the effective lithostatic stress, $\gamma$ the pore fluid pressure ratio defined as $\gamma = \rho_{water}/\rho_{rocks}$ which is set to 0.97, $g$ the gravitational force, $\rho$ the density, and $z$ the depth.

| **Parameter** | **Margin-wide rupture models** |
|---|---|
| Static friction coefficient ($\mu_\mathrm{s}$) | 0.6 |
| Dynamic friction coefficient ($\mu_\mathrm{d}$, depth-dependent) | 1.2-0.3 |
| Critical slip distance ($D_\mathrm{c}$) [m] | 1.0 |
| $SH_\mathrm{max}$ [deg] | 280 [a] |
| slip-weakening depths [km] | 15–43.3 [b] |
| Nucleation depth [km] | ∼30 [c] |
| Maximum relative pre-stress ratio ($R_0$) | 0.7 |
| Pore fluid ratio ($\gamma$) | 0.97 |
| Stress shape ratio ($\Phi$) | 0.4 |

Table 5.2.1: Dynamic rupture parameters for five dynamic rupture models HE, HM, HW, HEP, and HEA, selected from the ensemble in Wirp et al. (2024). [a] The orientation of the maximum horizontal stress is $SH_\mathrm{max}$ =280 ° for models HE (eastern hypocenter), HM (middle hypocenter), HW (western hypocenter), and HEP (model HE including off-fault plasticity) but $SH_\mathrm{max}$ =290 ° for HEA (single-asperity model). [b] The seismogenic depth is 15–43.3 km for models HE, HM, HW, and HEP but 10–43.3 km for HEA. [c] The hypocenter depth is ∼30 km for models HE, HM, HW, and HEP but ∼7 km for model HEA.

### 5.2.6 Off-fault plasticity

In all dynamic rupture models, we use the 1D isotropic version of the PREM (Preliminary Reference Earth Model) velocity model (Dziewonski and Anderson, 1981; Bormann,

2009). The HASZ is characterized by unconsolidated weak sediments in the upper 15 kms (Jongsma, 1977; Pichon and Angelier, 1979; Le Pichon and Angelier, 1981; Taymaz et al., 1990; Bohnhoff et al., 2001; Casten and Snopek, 2006; Shaw and Jackson, 2010). One of the five dynamic rupture models (model HEP) allows for off-fault plastic deformation (Wirp et al., 2024), which provides a more realistic representation of weak off-slab sediments co-seismically deforming. We use a non-associative (visco-)plastic Drucker-Prager rheology (Andrews, 2005; Wollherr et al., 2018). As in Ulrich et al. (2019a); Wirp et al. (2024), the bulk cohesion $C(z)$ varies with depth

$$C(z) = C_0 + C_1(z)\sigma'_{zz}. \tag{5.4}$$

$C_0 = 0.3$ MPa controls the location and amplitude of the off-fault plastic yielding and is constant. $C_1(z)$ defines rock hardening with depth, $\sigma_{zz}$' is the effective lithostatic stress. The bulk material's friction coefficient $\nu$, defined in the elastic solid medium, is assumed to be constant and is set to 0.6, equaling the fault static friction coefficient ($\mu_s = 0.6$). The off-fault plastic strain $\eta(t)$ at the end of the simulation time $t$ (Ma, 2008) is quantified as

$$\eta(t) = \int_0^t \sqrt{\frac{1}{2}\dot{\epsilon}^p_{i,j}\dot{\epsilon}^p_{i,j}}\,, \tag{5.5}$$

with $\dot{\epsilon}_{ij}$ being the time-dependent plastic strain increment.

## 5.3 Results

### 5.3.1 One-way linked dynamic rupture earthquake-tsunami scenarios

#### Rupture dynamics

In the following, we summarize the rupture dynamics in our selected five scenarios. For more details, the reader is referred to Wirp et al. (2024). The three margin-wide earthquake dynamic rupture scenarios HE, HM, and HW are all initialized using the same laterally homogeneous Cartesian prestress tensor (see Sec. 5.2). We consider them as "worst-case" scenarios, since they yield high moment magnitudes of $M_W$ ∼9 (Table 5.3.1). The three selected hypocenters are located on the eastern (below eastern Crete, model HE) and the western (below Peloponnese, model HW) part, as well as in the middle (between Crete and Peloponnese, model HM) of the megathrust interface (see Fig. 5.3.1). Depending on hypocentral location, the main rupture propagation mode varies from unilateral to west (HE) or east (HW) to bilateral to east and west for model HM. Scenario HW produces the largest maximum fault slip (15.93 m, Tab. 5.3.1, Fig. 5.3.1c) localized at intermediate depth (∼20–30 km) on the fault segment below south of Crete, which is ∼3.5 m higher than for scenario HE.

Including off-fault plastic deformation in our fourth dynamic rupture model (model HEP) leads to overall similar rupture characteristics (fault slip, peak slip rate, and rupture

velocity) as for the purely elastic reference model HE (Tab. 5.3.1, Fig. 5.B.1). Nevertheless, rupture propagation is here limited to the deeper fault portion as off-fault plastic deformation efficiently inhibits rupture propagation to the sediments (upper 15 kms). The accumulated plastic strain surrounding the HA megathrust generates a flower-shaped structure with depth (Wirp et al., 2024).

In the fifth scenario, model HEA, the rupture propagation is restricted by the assumed initial stress asperity. Thus, the rupture arrests after ∼60 s simulation time. Model HEA produces the smallest moment magnitude of ∼8 among all five scenarios. The maximum fault slip is 10.92 m, which is ∼5 m smaller than in scenario HW and the maximum peak slip rate of 2.2 m/s is ∼5.7 m/s smaller than in scenario HE (Table 5.3.1, Figs. 5.3.1a-e and 5.B.1).

| **Model** | **HE** | **HM** | **HW** | **HEP** | **HEA** |
|---|---|---|---|---|---|
| $M_W$ | 9.07 | 9.09 | 9.17 | 9.06 | 8.06 |
| Avg. fault slip [m] | 5.09 | 6.03 | 6.56 | 6.17 | 2.32 |
| Max. fault slip [m] | 12.55 | 14.30 | 15.93 | 12.71 | 10.92 |
| Avg. peak slip rate [m/s] | 1.40 | 1.51 | 1.77 | 1.40 | 0.68 |
| Max. peak slip rate [m/s] | 7.87 | 6.76 | 6.69 | 6.90 | 2.20 |
| Avg. rupture velocity [m/s] | 3373 | 3283 | 3341 | 3398 | 2413 |
| Max. rupture velocity [m/s] | 5379 | 5379 | 5375 | 5372 | 4562 |
| Rupture time [s] | 177 | 160 | 198 | 180 | 59 |
| Computational cost [CPUh] for 300 s simulation time | 190,400 | 185,920 | 141,680 | 158,480 | 187,040 |
| Max. seafloor uplift [m] (after Tanioka filter) | 9.46 | 8.02 | 9.34 | 10.22 | 1.91 |
| Max. sea-surface height anomaly [m] | 4.31 | 4.13 | 4.39 | 6.58 | 1.55 |

Table 5.3.1: Key results of our here considered five earthquake dynamic rupture scenarios, see also Wirp et al. (2024).

### Static bathymetry perturbation

Figure 5.3.1f-j shows the bathymetry perturbation used as input in the tsunami models resulting from the accumulated seafloor deformation in the five dynamic rupture simulations. The margin-wide dynamic rupture scenarios with varying hypocentral locations HE, HM, and HW are similar in magnitude but show remarkable differences in the induced seafloor displacement and associated bathymetry perturbation (see Fig. 5.3.1f-h). While all three scenarios develop similar primary uplift and subsidence features collocated with high on-fault slip, we observe additional narrow bands of uplift near the trench that differ in their length and are associated with rupture propagation into the shallow slip-strengthening region of the subduction interface. The direction of rupture propagation controls the amount of shallow slip, resulting in the largest uplift band for a western hypocenter (scenario HW).

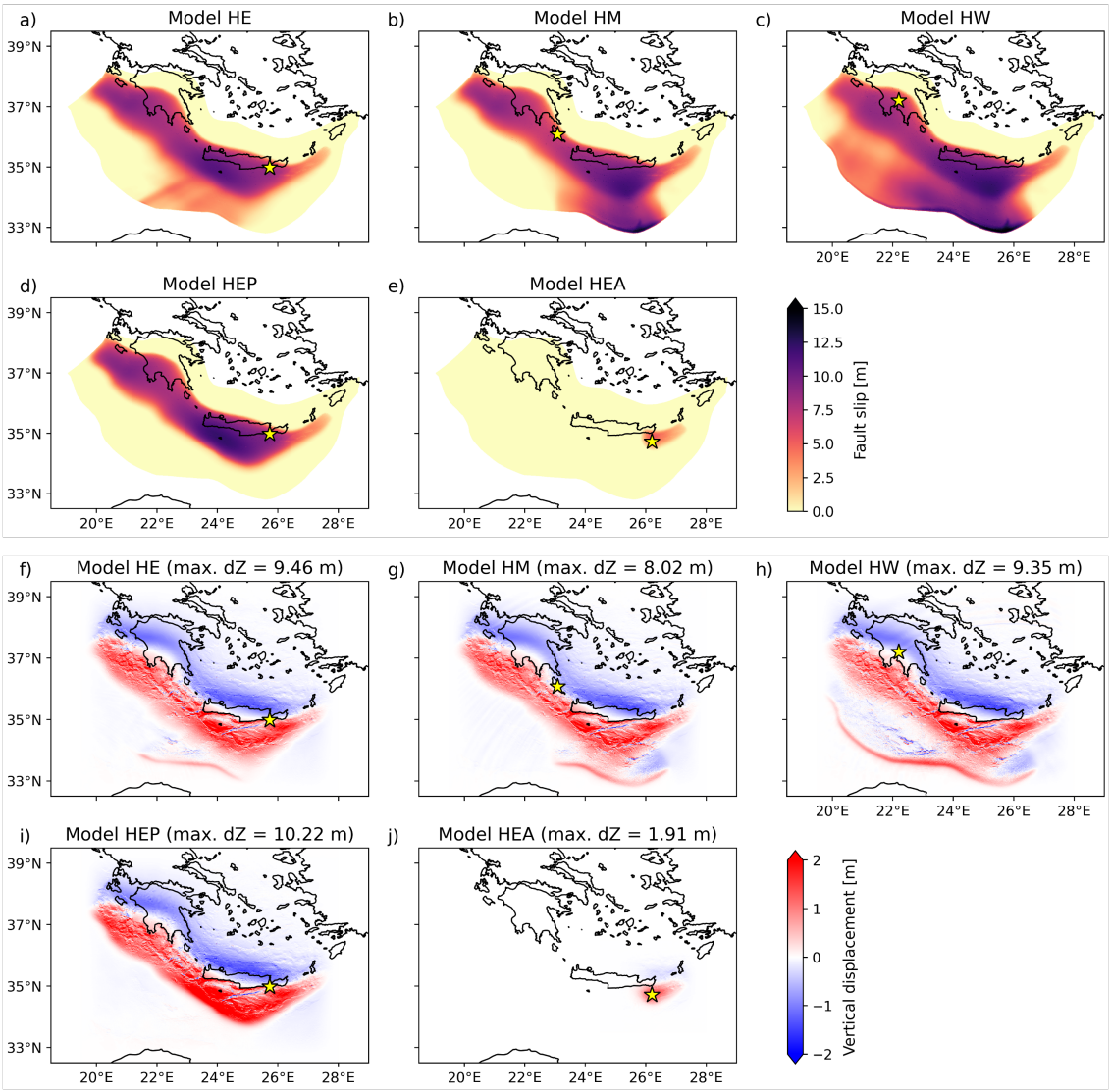



Figure 5.3.1: **Accumulated fault slip at the end of five SeisSol dynamic rupture simulations** for models a) HE, b) HM, c) HW, d) HEP, e) HEA. Depending on the hypocentral location, fault slip penetrates the shallow slip-strengthening fault portion, causing a pronounced band of near-trench uplift. Yellow stars mark the hypocenters. **Computed bathymetry perturbation** used as input in the tsunami models associated with the earthquake dynamic rupture simulations for margin-wide rupture scenarios based on laterally homogeneous initial stress conditions f) HE, g) HM, h) HW, i) HEP including off-fault plastic strain and j) the single initial stress asperity approach (HEA). It combines the vertical surface displacement with the contribution from the horizontal displacement from the Tanioka filter (Tanioka and Satake, 1996). Max. dZ refers to the maximum bathymetry perturbation of each scenario. Note the thin band of near-trench uplift in panels f), g), and h) produced by slip penetrating the shallow slip-strengthening fault region (see a), b), c)).

Enabling off-fault plastic yielding in our model (HEP) inhibits rupture propagation into the shallow slip-strengthening part of the fault interface but leads to a higher amount of vertical seafloor uplift (maximum 10.22 m) south of Crete. Applying a single prestress asperity to the initial loading (model HEA) limits rupture extent and fault slip amplitudes. In this case, a maximum uplift of 1.91 m is located southeast of Crete.

### Nonlinear shallow-water tsunami simulations sourced by static seafloor displacement

The tsunami simulation domain (Figs. 5.3.2, 5.3.3) covers large parts of the Mediterranean, including the islands of Corsica and Sardinia in the west, the eastern Italian and Croatian coasts in the north, the African coasts of Tunisia, Libya, and Egypt in the south, and the whole eastern Mediterranean Sea, covering the Turkish coast, Syria, and Israel.

Fig. 5.3.2 shows snapshots of the tsunami evolution after 0.5 h, 1.5 h, and 2.5 h simulation time. The first column represents the early stage of tsunami generation after 0.5 h. We define the deviation of the sea surface from the ocean at rest as sea surface height anomaly (ssha [m]). In the early stage, the tsunami evolution does not differ much between the four margin-wide rupture scenarios HE, HM, HW, and HEP, despite the differences in max. amplitudes of ssha (Fig. 5.3.3). 0.5 h after all four earthquakes, a tsunami leading front of $\sim$1.25 m height reaches the North African coasts of Libya and Egypt. In all four margin-wide models, the tsunami has reached most parts of the Cyclades, south Aegean, Crete, the Dodecanese, and the Ionian Islands, as well as large parts of the western Greece coasts are affected by the tsunami. After 1 h, a smaller tsunami front propagates in the northwest direction through the Ionian Sea towards southern Italy and the east direction through the Levantine Sea. Smaller wave heights of $\sim$0.2-0.5 m approach Sicily and Cyprus, while the main tsunami front travels towards the east and west direction along the African coast. After 2-2.5 h simulation time, the tsunami reaches the eastern Mediterranean coasts and approaches the northern Aegean islands. We see complex wave interaction with the coasts, superposition, and waves being trapped between the Greek islands (Fig. 5.3.2, third column). For the western Mediterranean coasts, no tsunami waves of significant amplitudes are observed. The tsunami kinematics among models HE, HM, HW, and HEP are overall similar. The main difference when including off-fault plastic deformation in model HEP is that the maximum values of ssha are up to 2.27 m higher, while the wave propagation evolution is similar to the purely elastic model (HE). Later, differences in the tsunami wave propagation are barely visible (Figs. 5.C.1, 5.C.2, 5.C.3, 5.C.4). The tsunamis reach the western boundaries of the model area after $\sim$8 h simulation time.

In the non-margin wide scenario HEA, the ensuing tsunami differs greatly from the four margin-wide rupture scenarios (Figs. 5.3.2e, 5.C.5). The tsunami waves of max. $\sim$0.5 m reach the African coast later than in the other models, after $\sim$0.75 h simulation time, and approach Sicily island after $\sim$2 h with heights of $\sim$0.1 m. The tsunami waves reach the Cyclades after 0.5 h simulation time, but act like a shield for the north Aegean islands. Likewise, in scenarios HE, HM, HW, and HEP, we observe a complex wave interaction with the African coasts and superposition of waves (Fig. 5.3.2e, second and third column).

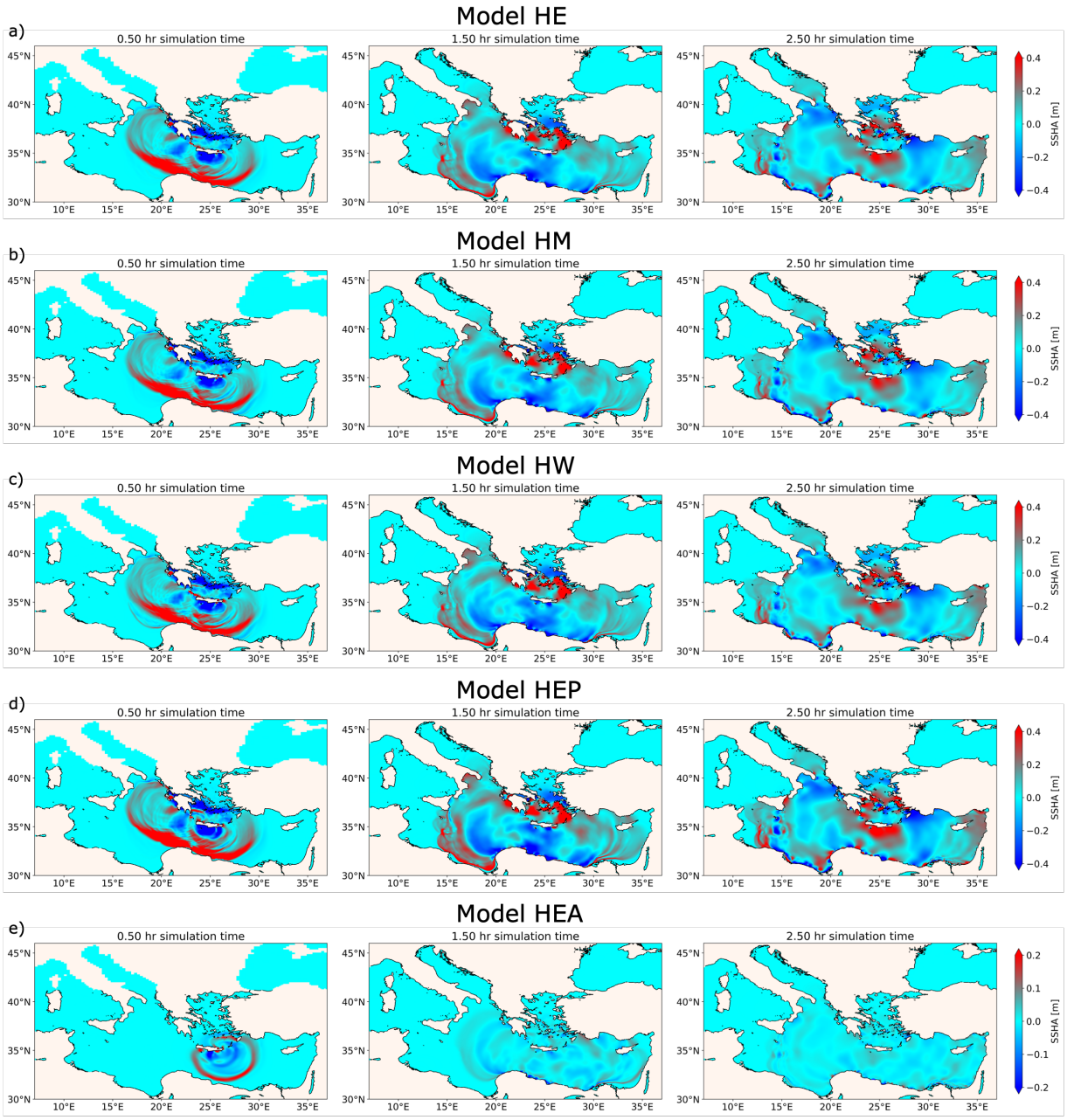



Figure 5.3.2: Sea surface height anomaly (ssha) of all five one-way linked earthquake-tsunami scenarios at 0.5 h (first column), 1.5 h (second column), and 2.5 h (third column) simulation time. The initial coarse grid in the North (see 0.5 h simulation time) is refined with increasing simulation time. Note the different color scale for panel **e)**.

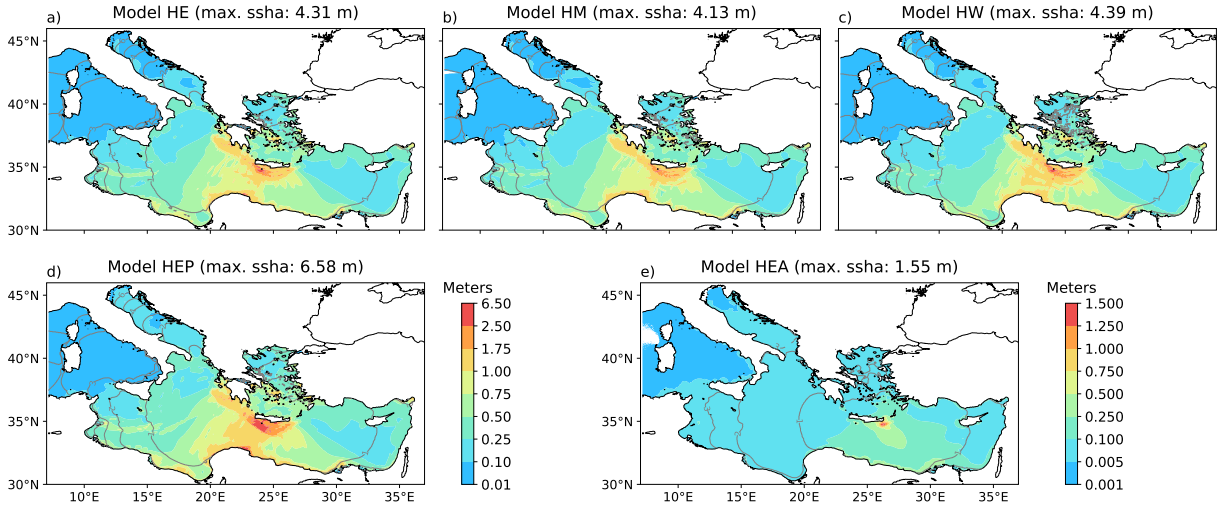



Figure 5.3.3: Maximum sea surface height anomaly (ssha [m]) in the Mediterranean during the simulation time of 8 h for five non-linear shallow water equation tsunami simulations induced by static bathymetry perturbations computed from the coseismic displacement of five dynamic rupture scenarios. The contour lines show the tsunami propagation expansion after 1 h, 2 h, 3 h, 4 h, 5 h, and 6 h, respectively. In **a)** model HE, **b)** model HM, and **c)** model HW, the epicenter location in the dynamic rupture models is varied (Fig. 5.3.1), **d)** model HEP allows for off-fault plastic deformation in the upper 15 km, and **e)** model HEA uses a single initial stress asperity. Note the different color scale for panel **e)**. See Animations S1, S2, S3, S4, and S5 for illustrations of the time-dependent evolution of ssha.

Figure 5.3.3 shows the maximum ssha over 8 h simulation time for all five dynamic rupture scenarios (Animations S1, S2, S3, S4, and S5). Grey lines mark the wave propagation expansion after 1 h, 2 h, 3 h, 4 h, 5 h, and 6 h, respectively. The maximum ssha highlights differences among the tsunami of the margin-wide rupture scenarios. They mainly differ in tsunami heights south of Crete, between the African coasts and Crete island. The contribution from the small band of near-trench seafloor uplift (see Sec. 5.3.1, Fig. 5.3.1) that varies with hypocentral location can be identified in the maximum ssha distribution, south of Crete. This feature is most pronounced for model HW and smallest for model HM among the margin-wide homogeneous initial pre-stress scenarios, and explains why larger tsunami amplitudes of ∼4.4 m are resulting from scenario HW, while in model HM, smaller wave amplitudes of ∼4.1 m are observed.

The differences in ssha associated with the small band of near-trench seafloor uplift are also visible in the tide gauges around Crete (Figs. 5.C.6, 5.C.7, 5.C.8). The gauge stations south and west of Crete report remarkable differences in ssha, while north-east of Crete the ssha is similar for different hypocentral locations (i.e., gauge 5). For example, gauge 12 reports a maximum deviation of the sea surface height of ∼2.2 m for the eastern hypocenter (model HE), while for the western hypocenter (model HW) this height is reduced to ∼2 m and ∼1.7 m for the middle hypocenter (model HM). For larger distances (Figs. 5.C.6, 5.C.7, 5.C.8 gauges 17-23), the differences in tsunami arrival and height between the models are marginal.

In model HEP, unconsolidated sediments in the upper 15 km of the seafloor enhance the seafloor displacement and result in the largest tsunami amplitudes, reaching maximum values of ∼6.6 m south-west Crete (Fig. 5.3.3 d). A tsunami front of more than 2.5 m height reaches the North African coast after ∼1 h simulation time (Fig. 5.C.9, gauge 22).

For model HEA, tsunami amplitudes are the smallest. This $M_W8$ scenario produces maximum wave amplitudes of 1.55 m southeast Crete island (Fig. 5.C.10, gauge 9). The tsunami approaches the North African Coast with a height of ∼0.5 m. The Mediterranean coasts west of Crete island, east of Cyprus island, and north of the Cyclades are barely affected by the tsunami.

### 5.3.2 3D fully-coupled scenario

We extend model HE into a fully-coupled earthquake-tsunami scenario. Due to the high computational cost, simulation time is chosen shorter than the shallow-water models to 300 s, which allows capturing the dynamic tsunami generation phase and the beginning of the tsunami propagation, but does not allow comparing it with the full tsunami evolution simulated by the one-way linked approach. Figure 5.3.4 shows the tsunami evolution of the fully-coupled model after 150 s simulation time. During rupture propagation, seismic waves are generated in the solid, elastodynamic part of the model domain. These waves interact with the acoustic waves being generated in the water layer and with the time-dependent seafloor displacement close to the source. Acoustic and seismic waves superimpose at the early tsunami generation stage in the near-fault region (panels a) and b) of Figs. 5.3.4, 5.D.1, 5.D.2, 5.D.3, and Animation S6) and at a later stage also close to the edges of the

simulation domain (Fig. 5.D.4a). We select three profiles perpendicular to the average strike of the megathrust and plot the ssha across these profiles (Figs. 5.3.4, 5.D.1, 5.D.2, 5.D.3, 5.D.4, 5.D.5 c) to better understand the complex superposition of the different wave types. We observe high-amplitude seismo-acoustic waves in the early tsunami generation stage. The acoustic waves are much faster than the actual tsunami and reach the southern simulation bands after 100 s simulation time. Panels (b) show the sea surface vertical velocity (ssvv) in [m], dominated by the acoustic waves rather than by the tsunami waves (Kutschera et al., 2024a). At 300 s simulation time, 100 s before the timestep that is used to source the tsunami simulations in the one-way linked approach (Sec. 5.3.1), the tsunami has already begun propagating in the fully-coupled model (Fig. 5.D.5 and Animation S7). The narrow near-trench uplift band identified in Fig. 5.3.1f-h is much less obvious in the fully-coupled model, and may have been filtered out by the ocean layer response due to its short wavelengths.

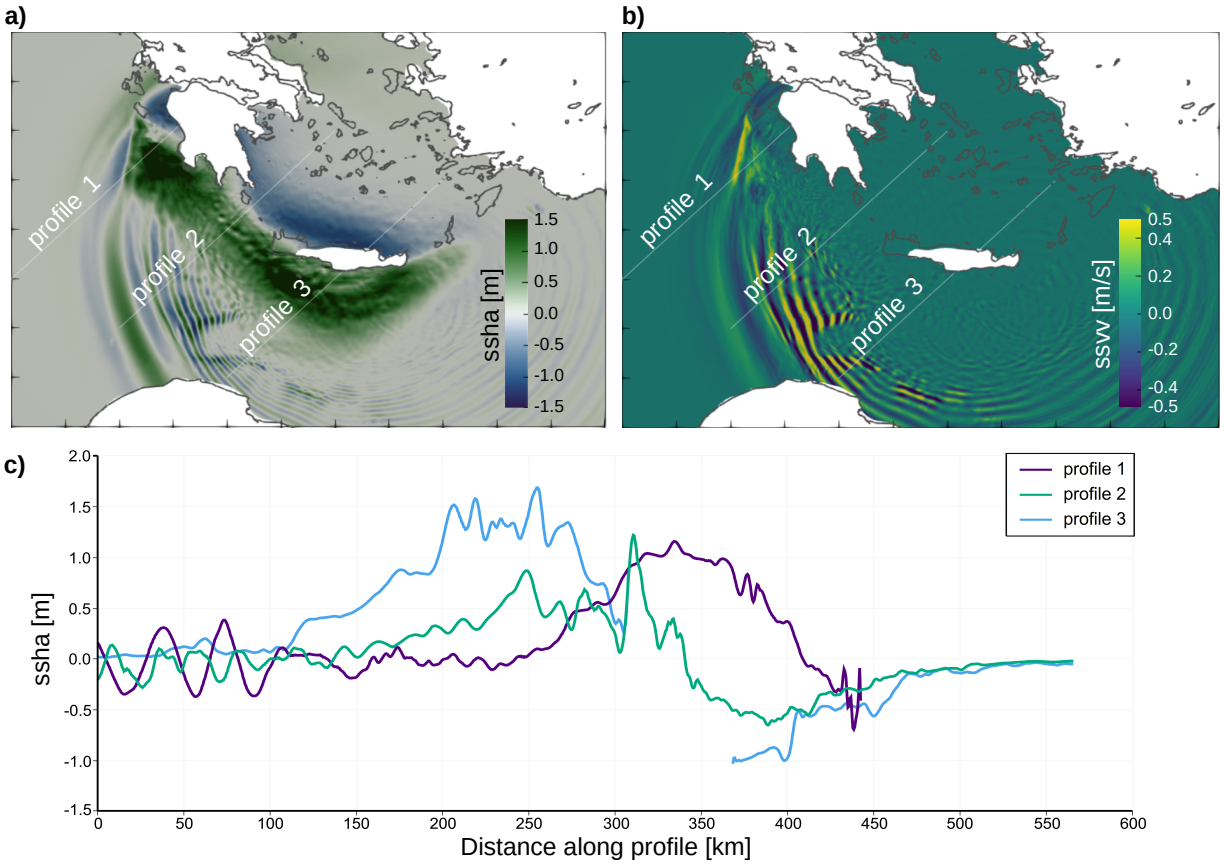



Figure 5.3.4: Large-scale 3D fully-coupled earthquake-tsunami scenario (HE). a) Sea surface height anomaly (ssha) after $t$ =150 s simulation time. b) Sea surface vertical velocity (ssvv) after $t$ =150 s simulation time. c) Sea surface height anomaly (ssha) along three selected cross-sections (profiles 1–3). See Animations S6 and S7 for illustrations of the time-dependent evolution of ssha and ssvv.

#### Tide gauges and Spectrograms

Analysis of synthetic time series at virtual near-coast tide gauges shows directivity effects and locally large amplitudes of acoustic waves generated during tsunami initiation.

Figure 5.D.6 shows the vertical velocity of the water column recorded at 11 synthetic tide gauge stations (red triangles in Figure 5.3.5 b). We observe acoustic waves reaching the stations located on the Crete coast during the early tsunami generation stage, ∼30–60 s after rupture onset. As the on-fault rupture propagates from east to west, they are first recorded at stations 13 and 14 located on eastern Crete, and later at stations 15 and 16 that are situated on western Crete. The maximum ssvv due to the acoustic waves recorded at gauges 13 and 14 is ∼0.03–0.05 m/s. In the records of stations 15 and 16, the first arrival of the acoustic wave is more pronounced, reaching a maximum of 0.4 m/s at gauge 16. Stations 17 and 18 record much smaller acoustic wave velocities of 0.025–0.01 m/s arriving after ∼100 s simulation time. The rupture propagation direction across the Hellenic Arc is from east to west, causing a time-dependent seafloor displacement and tsunami generation also evolving from east to west (Figs. 5.D.1a, 5.D.2a). Thus, higher signals of ∼0.35–0.5 m/s are also recorded at gauges 19 and 22 that are located north- and southeast of Crete. For some stations, we observe the acoustic waves as very narrow peaks (gauges 14, 15, 16, 19), whereas at others they are recorded as broader signals (stations 13, 17, 18, 20, 21, 22, 23).

To analyze the time-dependent frequency content of simulated sea surface signals, we compute spectrograms of the tsunami vertical velocity for all near- and far-field gauge stations (Fig. 5.3.5). The signature of direct acoustic waves can be identified in the high-frequency leading waves. This signal is followed, for example, at receivers 13, 17, and 18, by dispersive waves, which we identify as oceanic Rayleigh waves (Oliver and Major, 1960; Kozdon and Dunham, 2014; Wilson and Ma, 2021), surface waves that propagate at the interface between ocean water and the underlying solid crust.

## 5.4 Discussion

### 5.4.1 Comparison with historic tsunamis

We compare our modeled tsunami scenarios to the historic AD 365 and 1303 Crete tsunamis. The margin-wide rupture models and resulting tsunami may plausibly reproduce historic events, as the modeled coseismic uplift matches observations and the simulated tsunami impacts the entire eastern Mediterranean, with a leading wave reaching the African coast and Nile delta. The AD 365 earthquake and tsunami, key events governing Mediterranean tsunami hazard, have been extensively studied (e.g., Shaw et al., 2008; Yolsal-Çevikbilen and Taymaz, 2012; England et al., 2015; Tinti et al., 2005; Bahrouni et al., 2024). While the event is generally agreed to have ruptured a dip-slip fault rather than the megathrust, dynamic rupture models suggest its resulting seafloor displacement could have been caused by a margin-wide megathrust event (Wirp et al., 2024), specifically by an earthquake resembling model HEP that includes large off-fault plastic deformation. Tsunami deposits

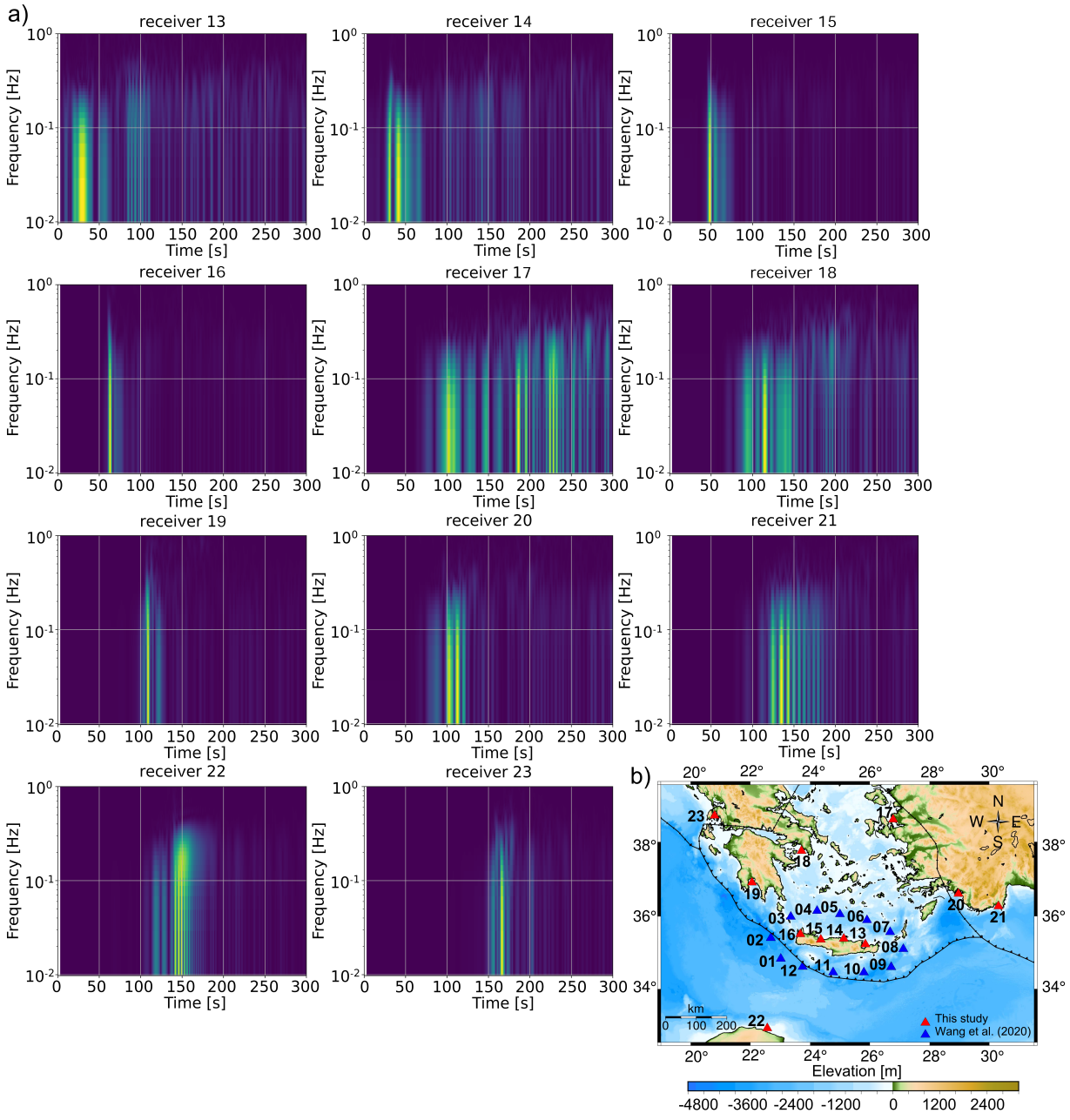



Figure 5.3.5: a) Spectrograms of acoustic signals recorded at the 11 tide gauge stations (b) in the fully-coupled earthquake-tsunami simulation. The signature of direct acoustic waves can be identified in the high-frequency leading waves. This signal is followed at stations 13, 17, and 18 by dispersive waves, which we identify as oceanic Rayleigh waves (Oliver and Major, 1960). b) Map showing the tide gauge locations used in this study. Blue triangles mark the tide gauge stations from Wang et al. (2020), while red triangles are the stations added in this study.

of the AD 365 earthquake were found in western Crete, close to the ancient harbor Phalasarna (Pirazzoli et al., 1992). Paleoshorelines at the eastern Crete island edge suggest a coseismic uplift of up to ∼10 m which reduces towards the north-east (Flemming, 1978; Pirazzoli et al., 1982, 1996; Stiros and Drakos, 2006; Shaw et al., 2008), with tsunami deposits potentially associated to this event reported also in Tunisia (Bahrouni et al., 2024), and in Eastern Sicily (De Martini et al., 2010). The corresponding tsunami destroyed many towns on Crete island and hit most of the eastern Mediterranean coasts, including northern Africa up to the Nile delta (Stiros, 2020). Tinti et al. (2005), Shaw et al. (2008), and Yolsal-Çevikbilen and Taymaz (2012) model the tsunami propagating from the source to the opposite side of the Mediterranean Sea, reaching the African coasts, sweeping west- and eastward towards Tripolis and the Nile Delta.

The tsunamis sourced by our margin-wide rupture scenarios show highest amplitudes around Crete, Rhodes, the southern Aegean, eastern Libya, and Egypt, while the western Mediterranean is barely affected by the tsunami, which is in agreement with Tinti et al. (2005). The margin-wide rupture models predict edge waves along the African coast amplified by shoaling effects (Shaw et al., 2008), which are waves traveling along the shoreline and confined by the sloping seabed. Sardinia is being mainly shielded by Sicily and the land mass of Tunisia, and on a dominant curved band of locally high maximum ssha south of Malta. The initial coseismic uplift of ∼8-10 m induced by the margin-wide models southeast Crete fits the seafoor displacement of 10 m that was inferred from topography changes, seamarks, and fallen blocks (Spratt, 1865; Flemming, 1978; Pirazzoli et al., 1982; Stiros and Drakos, 2006) associated with the AD 365 event. The similarity between models HE, HM, and HW of different hypocentral locations highlights the difficulty in identifying a source location for historical events.

The tsunami caused by the 1303 Crete earthquake has also been the focus of several earlier studies (e.g., Yolsal et al., 2007; Yolsal-Çevikbilen and Taymaz, 2012; England et al., 2015; Tinti et al., 2005). It affected the Greek Islands and Peloponnese, propagating north and directing to southwest Turkey, reaching Cyprus towards the east and the African coast to the south (Yolsal et al., 2007). For this event, Yolsal et al. (2007) model a maximum wave height of 7 m east of Crete. Such a high tsunami is among our models only feasible for an $M_W$ ∼9 event breaking the entire Hellenic Arc megathrust (model HEP). The tsunami evolution modeled by Yolsal et al. (2007) is similar to our margin-wide rupture scenarios (HE, HEP), both in terms of kinematics and wave heights. Wirp et al. (2021) identify the elastic model with eastern hypocenter (HEA) to resemble the location and magnitude of the 1303 tsunamigenic event. However, while our tsunami simulation (Figs. 5.3.2e, 5.3.3e and Animation S5) sourced by model HEA produces a realistic distribution of ssha, it does not reproduce the high tsunami amplitudes inferred for the event, likely due to its too deep slip. This means that a $M_W \leq 8$ megathrust event is unlikely to resemble historical tsunami records.

### 5.4.2 Implications for regional and transnational tsunami hazard assessment

The active margin of the Hellenic Arc with average repeat times of 66 years for $M_W$7.0 earthquakes poses a high seismo- and tsunamigenic potential (Papadopoulos and Kijko, 1991; Papadopoulos et al., 2012). This highlights the need for seismic and tsunami hazard assessment in the region and in distant areas potentially impacted by tsunami caused by earthquakes on the Hellenic Arc megathrust (e.g., Okal et al., 2009; Yolsal et al., 2007; Sørensen et al., 2012; Yolsal-Çevikbilen and Taymaz, 2012; Coban and Sayil, 2020; Basili et al., 2021; Triantafyllou et al., 2024). The NEAM Tsunami Hazard Model 2018 (NEAMTHM18) (Basili et al., 2021), for example, is a probabilistic hazard model covering the Mediterranean, and making use of stochastic models to explore a large tsunami source variability (Scala et al., 2024). They use both, seismicity-based and tectonic models (e.g., Davies et al., 2018), together with depth-dependent subduction and rupture properties, including the potential for shallow slip amplification (e.g., Murphy et al., 2016).

However, the absence of digital records of large tsunamigenic earthquakes on the Hellenic Arc megathrust together with long return periods and uncertainties about fault geometries and properties hinder the understanding and correct assessment of earthquake and tsunami hazard studies in this area (e.g., Shaw et al., 2008; Ganas and Parsons, 2009; Vernant et al., 2014; England et al., 2015). Dynamic rupture simulations of megathrust earthquakes may contribute to reducing the epistemic uncertainty associated with tsunami hazard analysis. The models use physically consistent initial conditions that could help reduce the random variability of stochastic slip models. Dynamic rupture model also provides time-dependent initial seafloor displacements for tsunami simulations, which may remove some biases due to simplifying assumptions of instantaneous and static tsunami initial conditions. Such models can help in refining stochastic and probabilistic tsunami hazard assessments (e.g., Murphy et al., 2016; Savran and Olsen, 2020), with additional physically viable earthquake scenarios (Ripperger et al., 2008; Schmedes et al., 2010), and adding the resulting tsunami adds additional observables to validate dynamic rupture (e.g., Davies and Griffin, 2019; Ulrich et al., 2022).

The dynamic rupture examples presented here focus on (worst-case) $M_W$8+ megathrust earthquakes. Their corresponding tsunami exemplify that the main megathrust should be taken into account when calculating the hazard for surrounding areas and regions that lie further away, for example, the Italian and northern African coasts. Our results show overall higher tsunami amplitudes to the South, exceeding 1 m along the northern coast of Egypt and Libya, which is in agreement with current operational tsunami hazard models using thousands of simpler models (Basili et al., 2021). However, balancing the required source variability, including smaller earthquakes, for probabilistic tsunami simulations with the feasible number of simulations remains a challenge, particularly for dynamic rupture simulations, which are inherently computationally expensive.

**Shallow water and instantaneous sourcing tsunami modeling assumptions**

In Table 5.4.1, we follow Abrahams et al. (2023) and summarize several non-dimensional parameters that allow us to assess the validity of simplifying modeling assumptions for our tsunami model setup. These parameters control the solution behavior for a Gaussian source. Assuming a source width of $\sigma_r$ =100 km, the shallow water approximation

$$H/\sigma_r \ll 1 \tag{5.6}$$

is valid everywhere within our model domain given that the maximum water depth of the Aegean is $H$ =3,544 m close to Crete. We further consider a source duration $\sigma_t$ of 180 s for model HE. For

$$H/(c_0 \cdot \sigma_t) \ll 1 \tag{5.7}$$

the contribution of acoustic waves to the tsunami should theoretically be negligible. Assuming an instantaneous source is appropriate if

$$\sqrt{gH} \cdot \sigma_t/\sigma_r \ll 1\,, \tag{5.8}$$

with $c_0$ =1500 m/s being the acoustic wave speed and $g$ =9.81 m/s$^2$ the gravitational acceleration. In the case of all our scenarios, this condition is not fulfilled. Applying instantaneous sourcing will omit a potentially non-negligible amplitude of acoustic waves during tsunami generation, as illustrated in our fully coupled scenario.

| **Source width** $\sigma_r$ (m) | **Source duration** $\sigma_t$ (s) | **Shallow water limit** $H/\sigma_r \ll 1$ | **Negligible acoustic wave excitation** $H/(c_0 \cdot \sigma_t) \ll 1$ | **Instantaneous source** $\sqrt{gH} \cdot \sigma_t/\sigma_r \ll 1$ |
|---|---|---|---|---|
| 100,000 | 180 | Valid | Valid | 0.33 |

Table 5.4.1: Non-dimensional parameters for our model setup, as introduced by Abrahams et al. (2023). $c_0$ =1500 m/s is the acoustic wave speed $g$ =9.81 m/s$^2$ the gravitational acceleration and $H$ is the maximum water depth of the Aegean east of Crete (∼3,544 m).

### 5.4.3 Source spectrum analysis of oceanic acoustic and tsunami waves

Kozdon and Dunham (2014) identify normally and anomalously dispersed Rayleigh waves in their 2D fully-coupled dynamic rupture-tsunami simulations of the 2011 Tohoku-Oki earthquake in the Japan Trench. They showcase the complex oceanic wavefield, which might be recorded by ocean bottom seismometers, including large-amplitude waves that propagate slower than the ocean sound speed. Similar waveform characteristics have been observed in 2D fully-coupled simulations of Cascadia earthquake and tsunami scenarios by

Wilson and Ma (2021). They find that the excitation of oceanic Rayleigh waves changes with the amount of shallow rupture. Abrahams et al. (2023) analyze the acoustic signals generated in simplified 3D fully-coupled earthquake tsunami simulations. They identify initially arriving normally dispersed long-period oceanic waves that leak oceanic P-wave modes, the "PL" waves (Oliver and Major, 1960; Kozdon and Dunham, 2014; Wilson and Ma, 2021), which are followed by wave packets of Rayleigh waves. They show that the wave spectra vary with direction from the source due to directivity effects.

In our 3D fully-coupled simulation, we observe high-frequency leading acoustic waves, followed by packets of dispersed oceanic Rayleigh waves, similarly to previous work. We observe the maximum ssvv (sea surface vertical velocity) of acoustic waves depending on the location of the gauge stations relative to the rupture direction from the source (Figs. 5.3.5b, 5.D.6). Stations located in the rupture propagation direction (e.g., stations 15, 16, 19, 22) record more pronounced and up to 90% higher acoustic amplitudes than stations located on the opposite side of the megathrust (e.g., stations 20, 21).

We extract the vertical velocity of the sea surface along the three profiles from Fig. 5.3.4b, with their respective spatio-temporal evolution shown in Fig. 5.4.1. We observe a dominant, fast-traveling wavefront at 3000 $\mathrm{ms}^{-1}$ (black dashed line) wave speed in profile 3. Signals with the same wave speed are visible in profiles 1 and 2 as well. Due to the long source duration of 180 s for the margin-wide rupture model HE, the tsunami source is not instantaneous (Eq. 5.8) and acoustic signals could be emitted during the tsunami generation phase. Acoustic signals, propagating at $c_0$ =1500 $\mathrm{ms}^{-1}$ (red dashed line) can be identified in profile 1 and 2. All three profiles show multiple signals (light blue dashed line) propagating at speed of around 80 $\mathrm{ms}^{-1}$, corresponding with the expected speed of a tsunami propagating in a 640 m shallow water layer. The amplitudes of the sea surface vertical velocity of the fast-propagating primary wavefront are $\sim$2.5 m/s larger than the actual tsunami amplitudes. For profiles 1 and 2, the acoustic wave amplitudes are $\sim$0.5 m/s and as large as those corresponding to the tsunami. Since the average depth of the water $H$ is much smaller than $c_0 \cdot \sigma_t$ (Table 5.4.1), we would expect from simplifying analysis that the amplitudes of the acoustic waves should be negligibly small (Abrahams et al., 2023). However, in our realistic 3D model setup, this is only the case for profile 3, where the acoustic wave amplitudes remain smaller than 0.5 m/s. In distinction, profiles 1 and 2 include acoustic waves with ssvv amplitudes comparable to the respective gravity tsunami waves amplitudes, up to $\sim$0.5 m/s in profiles 1 and 2. These unexpectedly high acoustic wave amplitudes may be due to the complex topo-bathymetry in the Mediterranean, since the conversion between seismic and ocean acoustic waves is assumed to occur mainly at slopes of the seafloor (Noguchi et al., 2013). None of our scenarios includes surface breaching ruptures, another common cause of high acoustic amplitudes during the tsunami generation phase (Abrahams et al., 2023), since the Hellenic Arc megathrust does not intersect with the seafloor.

The observed complex superimposition of sizable acoustic waves and tsunami waves in the near-field even in shallow water can challenge the understanding of the tsunami generation phase. However, in the far-field, high-amplitude acoustic waves may be useful as a "rapid indicator" of tsunamigenic earthquake rupture. At near-fault gauge stations,

the amplitude of simulated acoustic waves is large enough to be extracted from tide gauge signals, and may help tsunami early warning before the arrival of the main tsunami wave. While beyond the scope of this work, a better understanding of how acoustic signals are linked to tsunamigenic seafloor motion can improve tsunami early warning, e.g. using ocean bottom pressure sensors or seafloor DAS (e.g., Yamamoto, 1982; Mei and Kadri, 2017; Gomez and Kadri, 2021; Becerril et al., 2025; Henneking et al., 2025).

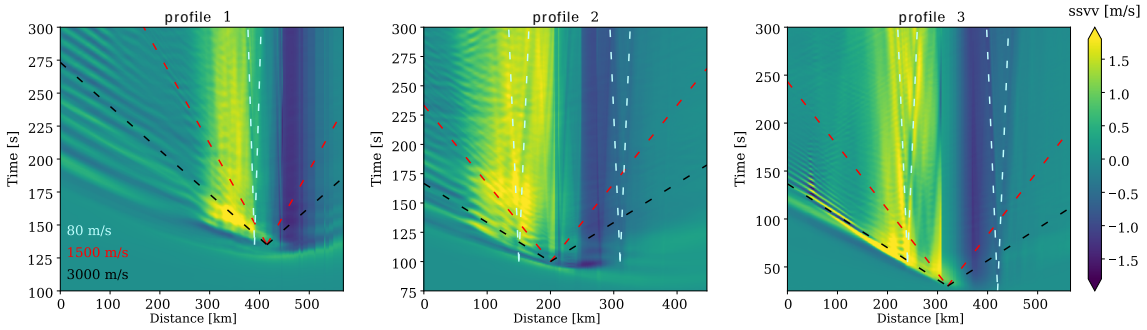



Figure 5.4.1: Space-time evolution of the sea surface vertical velocity (ssvv) for profiles 1, 2, and 3 of Fig. 5.3.4 for the full duration of the fully-coupled simulations. Dashed lines indicate velocities of 3000 m/s (seismic), 1500 m/s (acoustic waves), and 80 m/s (tsunami).

### 5.4.4 Limitations

For the one-way linking approach, we do not account for time-dependent seafloor motions but translate the static seafloor uplift into a displacement of the water column, resulting in a sea surface elevation. As a result, time-dependent dissimilarities in the tsunami generation process are not resolved between margin-wide models of different hypocentral locations (models HE, HM, HW), and are not discussed in this paper. In future work, the time-dependent variations of the 3-dimensional coseismic seafloor displacement could be translated into 2-dimensional vertical bathymetry perturbations for tsunami modeling (e.g., Wendt et al., 2009; Lotto et al., 2017b; Ulrich et al., 2019b; Madden et al., 2020; Wirp et al., 2021; Amlani et al., 2022; Kutschera et al., 2024a), utilizing temporal (Saito et al., 2019) or space-time Fourier filters (Madden et al., 2020).

Madden et al. (2020) show that the usage of a time-independent tsunami input can result in a later tsunami arrival at the coast, compared to a time-dependent source, together with a faster coastal inundation. However, Williamson et al. (2019) find that near-field one-way linked tsunami amplitude estimates are not significantly influenced by the assumption of instantaneous seafloor displacement. At the same time, recent work by Melgar (2025) has shown that tsunami amplitudes can increase by over 30% in the far-field when rupture duration and directivity are taken into account for large events ($M_W > 9.0$). However, the

events studied by Melgar (2025) had primarily homogeneous slip, while the scenarios in this study are highly heterogeneous.

The one-way linked tsunami simulations are performed using the software GeoClaw (Berger et al., 2011; Gonzalez et al., 2011), a non-linear shallow-water tsunami solver. GeoClaw is currently in use for tsunami hazard assessment by several research groups (e.g., MacInnes et al., 2013; Borrero et al., 2015). Non-linear shallow water equations are the standard modeling method for tsunami propagation and run-up and the basis of other well-established tsunami codes, for example HySEA (Macías et al., 2017) and MOST (Titov and Gonzalez, 1997; Titov et al., 2016). These equations are less accurate for short wavelengths as the dispersive terms become more significant. Especially in near-shore regions, the tsunami flow evolves three-dimensionally, and the depth-averaged equations might become inaccurate. Boussinesq solvers, such as Funwave-TVD (Shi et al., 2012) and BoussClaw (Kim et al., 2017), can be used to incorporate wave dispersion. Even more accurate but computationally expensive would be the usage of fully-coupled earthquake-tsunami simulations for more than the one scenario presented here, which are able to capture the full tsunami generation phase and to model normal and anomalous dispersion (Sec. 5.4.3). Our fully-coupled simulation takes the time-dependent rupture propagation into consideration, but does not account for inundation and relies on a modified, simplified bathymetry. Since these models are computationally expensive due to the large simulation domain (Sec. 5.2.4) and the high resolution required to adequately resolve the tsunami, seismic, and acoustic waves. Thus, our fully-coupled simulation ran for a relatively short time (300 seconds), focusing on the generation phase of the tsunami.

Future computational optimization and improvement of computational resources (e.g., Panzera et al., 2016; Li et al., 2023; Folch et al., 2023) might allow running more of these fully-coupled models and running them for a longer simulation time. For now, we would advise using fully-coupled models only for selected extreme-scale scenarios, comparing with and translating the learned into less costly models for tsunami hazard assessment, which could be done with a two-step approach (Saito et al., 2019; Abbate et al., 2024; Abrahams et al., 2023).

## 5.5 Conclusions

We present five $M_W8+$ megathrust earthquake-tsunami scenarios along the Hellenic Arc, including four margin-wide ruptures and one non-margin-wide event, all sourced from 3D dynamic rupture simulations. By sourcing tsunamis from physically consistent rupture scenarios, these models offer a way to reduce nonphysical variability in stochastic models and better constrain source parameters for probabilistic tsunami hazard assessment. While the four margin-wide scenarios share similar moment magnitudes, their induced seafloor displacements vary greatly: three margin-wide scenarios with different hypocentral locations but without off-fault plastic yielding cause slip to the trench, leading to small bands of near-trench uplift that vary in size, causing maximal displacements of 8.02 m–9.46 m. One scenario with plastic deformation inhibits rupture propagation into the shallow

slip-strengthening region of the subduction interface, generating larger seafloor displacement away from the trench exceeding 10 m. These distinct uplift patterns caused by the varying rupture dynamics influence near-field tsunami amplitudes but have limited impact on far-field propagation, assuming instantaneous sources in non-linear shallow water tsunami simulations. Maximum sea surface height anomalies (ssha) reach up to 4.4 m in the margin-wide scenarios, with energy focused along the Libyan and Egyptian coasts due to edge wave trapping, while the northern Aegean and western Mediterranean remain largely unaffected. Incorporating off-fault plastic deformation substantially enhances tsunami generation, increasing maximum ssha by more than 2 m and producing the largest modeled wave amplitudes, up to 6.6 m southwest of Crete. This enhanced tsunami response suggests that unconsolidated sediments and inelastic deformation may have played a critical role in amplifying historical events such as the AD 365 Crete tsunami. In contrast, the non–margin-wide $M_W8$ scenario produces a maximum ssha of only 1.55 m, indicating that such megathrust events alone may be unlikely to account for the extreme wave heights inferred from historical records.

We demonstrate a large-scale 3D fully-coupled earthquake-tsunami simulation that integrates dynamic rupture, seismic and acoustic wave propagation, and tsunami generation. Using large-scale supercomputing and overcoming meshing challenges, we are able to perform this fully coupled model across a large, realistic domain, covering the Greek islands, the western Greek coast and Peloponnese, the Turkish coast to Kumluca, and parts of the Libyan coast. The fully-coupled approach is computationally expensive (∼1 million CPU hours for 5 minutes simulation time), limiting its use here to one selected scenario. However, it can inform and calibrate cheaper models. Tsunami signals recorded at near and far tide gauge stations exhibit complexities not represented in one-way linked tsunami models. Therefore, we confirm that large earthquakes with long-duration ruptures (∼180 s) and depth-dependent dispersion affect tsunami initiation. The fully-coupled simulation captures early-phase complexities of tsunami genesis, including acoustic and seismic waves and their transitions into tsunami motions. This superposition complicates signal attribution and may pose challenges to early warning systems and waveform inversion. However, the fully-coupled model also captures large-amplitude acoustic waves and oceanic Rayleigh waves, which arrive earlier than the main tsunami and are recorded as leading signals in near-field gauges, suggesting potential utility for early warning if detected by Mediterranean ocean-bottom pressure sensors or hydrophones.

# Appendix

## 5.A Meshing challenges

We build a complex structural model, incorporating the Hellenic Arc megathrust, topography, bathymetry, and the sea surface, and we generate high-quality unstructured tetrahedral meshes from this complex structural model using SimModeler (Simmetrix Inc., 2017). Incorporating a sea surface layer intersecting with a finely sampled bathymetry-topography surface is challenging, but is required for fully-coupled models.

This water layer is necessary to include the acoustic medium (Ocean) on top of the elastic (Earth) dynamic rupture model. To facilitate the calculation of the intersection, we resolve both the sea and bathymetry-topography surfaces with roughly similar mesh sizes in the structural model before calculating the intersection in SimModeler. This strategy has proven effective, although the large number of elements on the surface to be intersected can still pose challenges.

To further improve the intersection process, we smooth the topography using a Gaussian kernel with $\sigma = 1$ and adjust bathymetry nodes with $|z| < 200$ m to $\pm 200$ m, reducing the risk of near-coplanar intersections. However, the software can still require manual adjustments when intersecting seafloor and sea surfaces in certain configurations.

An extensive and complex region such as the Hellenic Arc includes many of those challenging configurations: small-scale features in the topography, such as small islands or regions with shallow seafloor that lie close to sea level, did indeed challenge the intersection process and forced us to remove many of them. This simplification results in a more streamlined coastline representation in the 3D fully-coupled model. Moreover, we had to restrict the water layer to a smaller area to reduce the high computational costs associated with the oceanic acoustic and tsunami wave simulation (see Fig. 5.A.1). For the pure dynamic rupture models, we remove the water layer from the unstructured tetrahedral mesh, such that the bathymetry and resolution of the fully-coupled model are the same as for the one-way linked workflow.

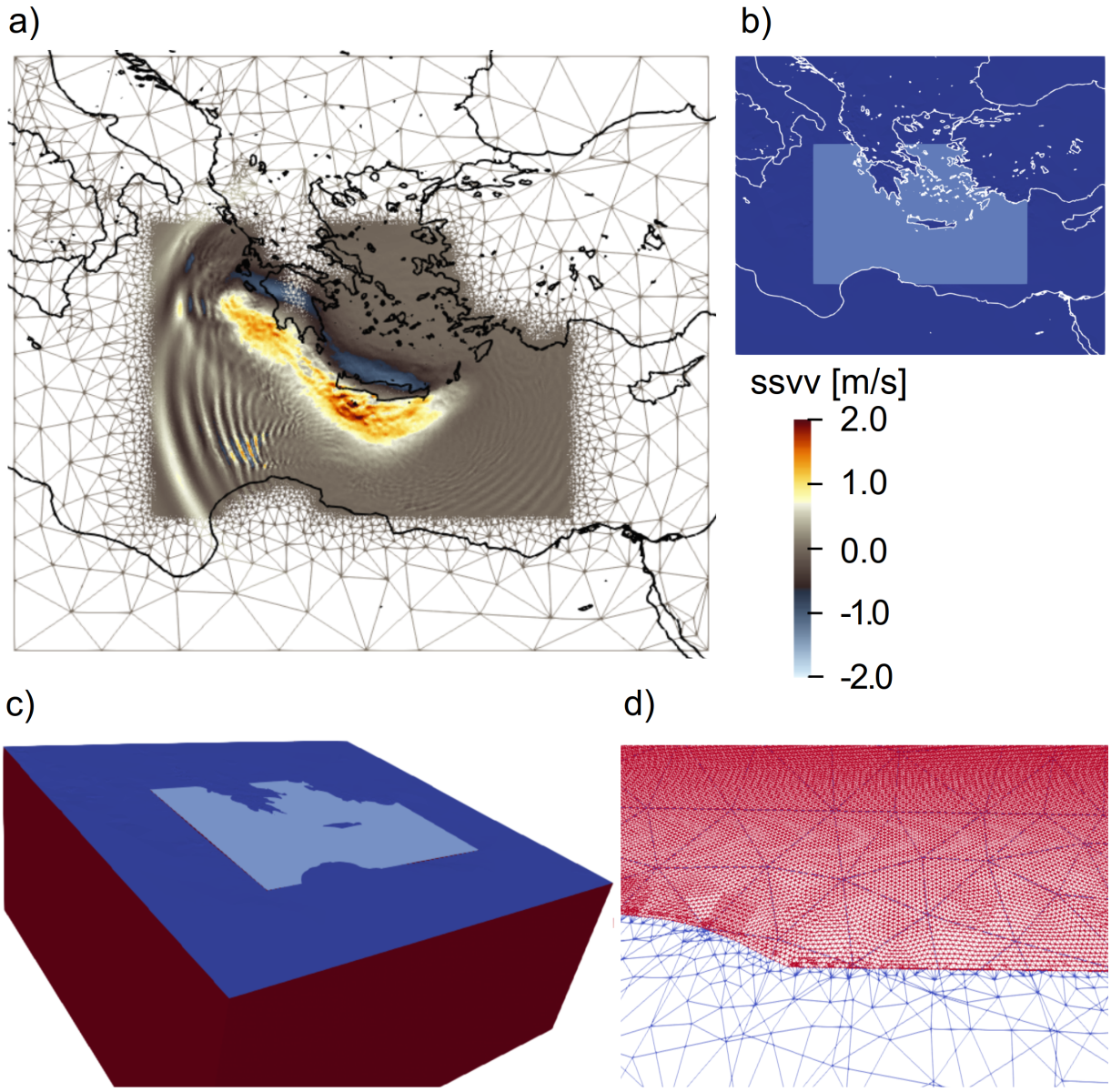



Figure 5.A.1: a) Computational mesh of the fully-coupled earthquake-tsunami model, including the water layer. The sea surface vertical velocity after 200 s simulation time ranges from -2 to 2 m/s to highlight complexities in the early stage of tsunami generation. Note that the modeling domain of the fully-coupled tsunami model is smaller than the one used with GeoClaw (Figs. 5.3.2 and 5.3.3). b) Map view and c) perspective view of the modeling domain of the fully-coupled model. The water layer is colored light blue, the free surface and absorbing boundary conditions are colored dark blue and red, respectively. d) Zoom into the connection of the water layer (red) and surroundings (blue). Note the finer mesh resolution of the water layer and the mesh size coarsening away from the water layer.

# 5.B Dynamic rupture modeling results

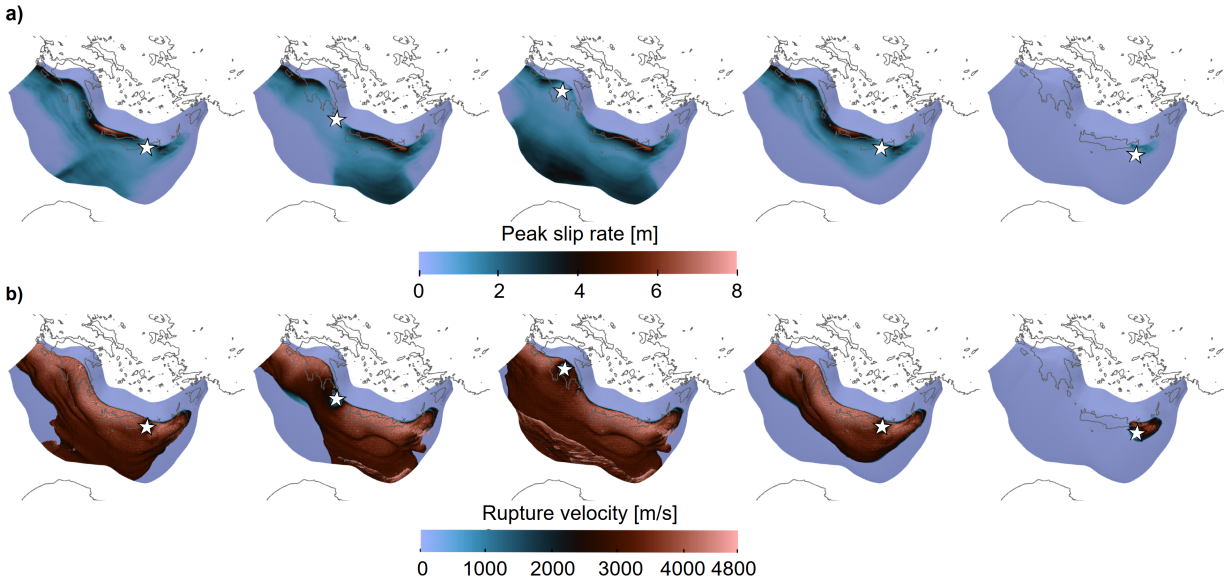



Figure 5.B.1: **SeisSol dynamic rupture results:** a) Peak slip rate and b) rupture velocity for models HE, HM, HW, HEP, and HEA, respectively. Depending on the hypocentral location, fault slip penetrates the shallow slip-strengthening fault portion, causing a pronounced band of near-trench uplift. White stars mark the hypocenter.

## 5.C One-way linked tsunami results

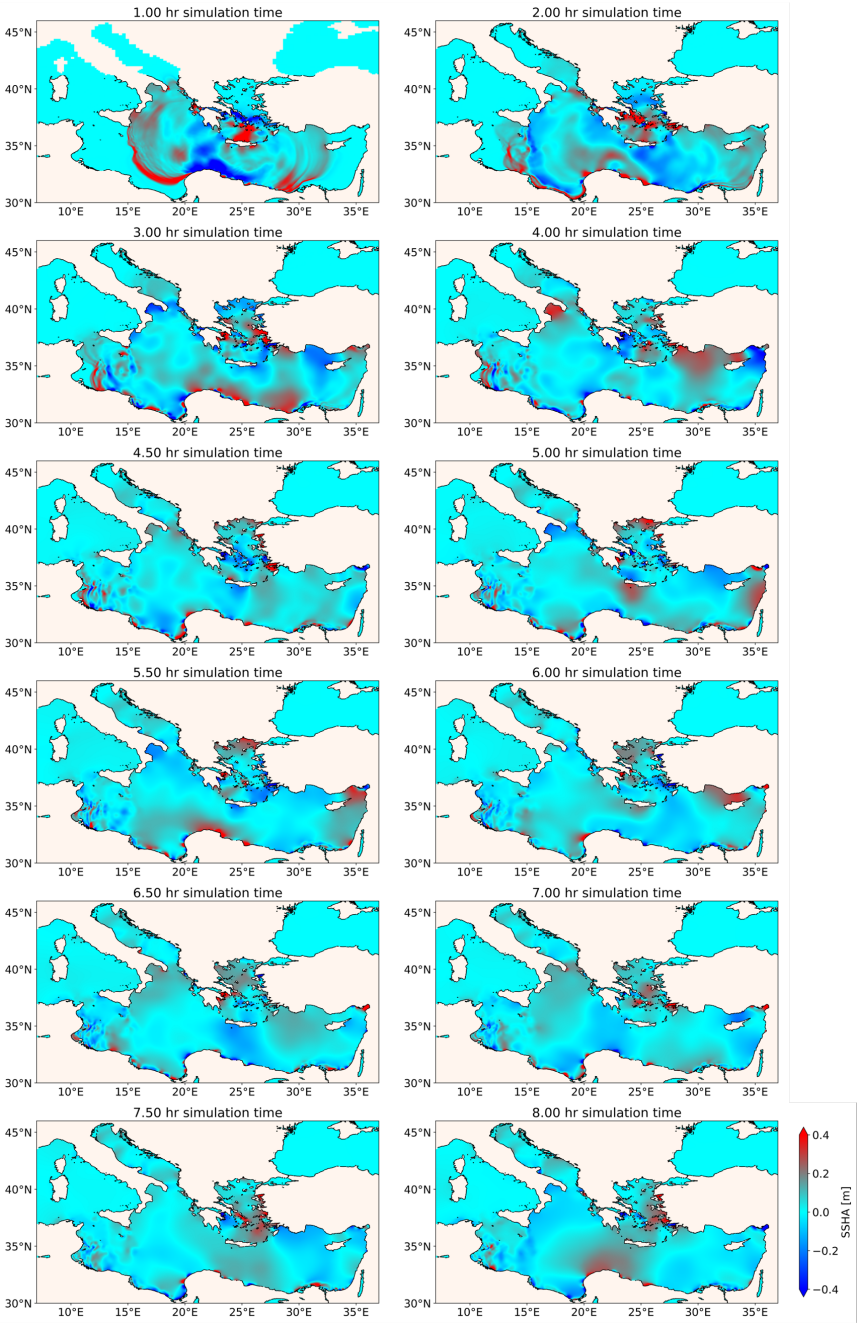



Figure 5.C.1: Tsunami evolution (ssha [m]) for model HE (eastern hypocenter) after 1 h, 2 h, 3 h, 4 h, 4.5 h, 5 h, 5.5 h, 6 h, 6.5 h, 7 h, 7.5 h, 8 h simulation time. Red marks elevation, and blue marks depression from the sea surface at rest.

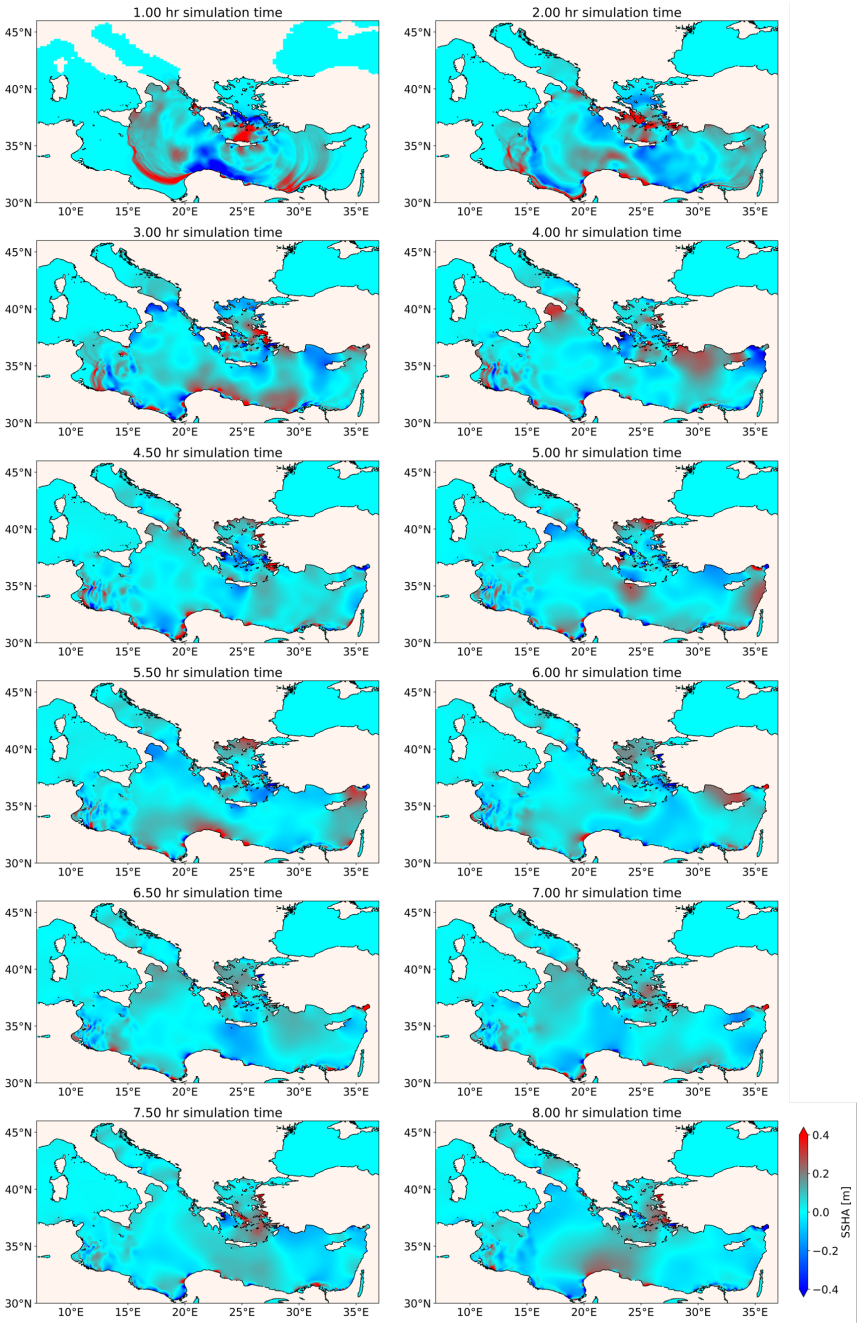



Figure 5.C.2: Tsunami evolution (ssha [m]) for model HM (middle hypocenter) after 1 h, 2 h, 3 h, 4 h, 4.5 h, 5 h, 5.5 h, 6 h, 6.5 h, 7 h, 7.5 h, 8 h simulation time. Red marks elevation, and blue marks depression from the sea surface at rest.

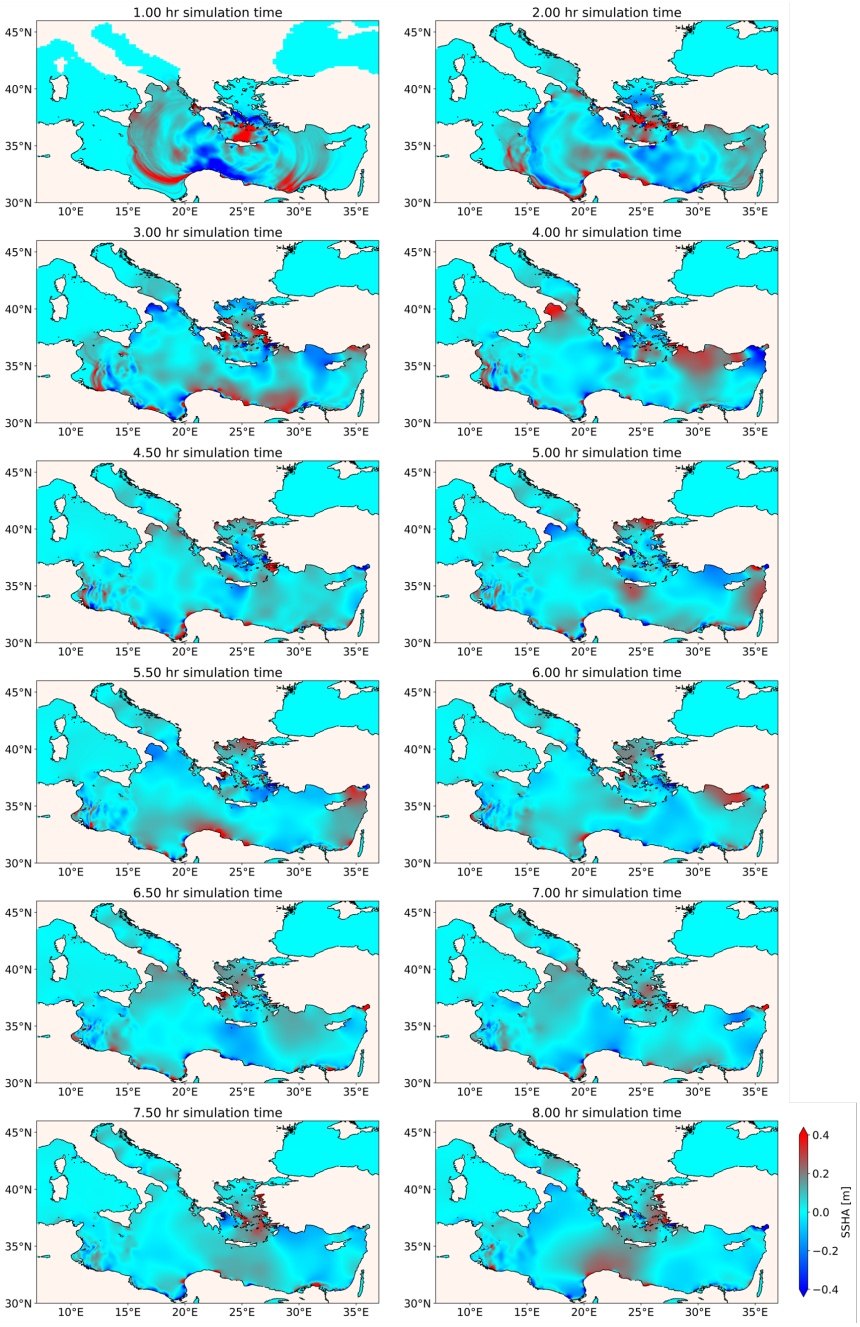



Figure 5.C.3: Tsunami evolution (ssha [m]) for model HW (western hypocenter) after 1 h, 2 h, 3 h, 4 h, 4.5 h, 5 h, 5.5 h, 6 h, 6.5 h, 7 h, 7.5 h, 8 h simulation time. Red marks elevation, and blue marks depression from the sea surface at rest.

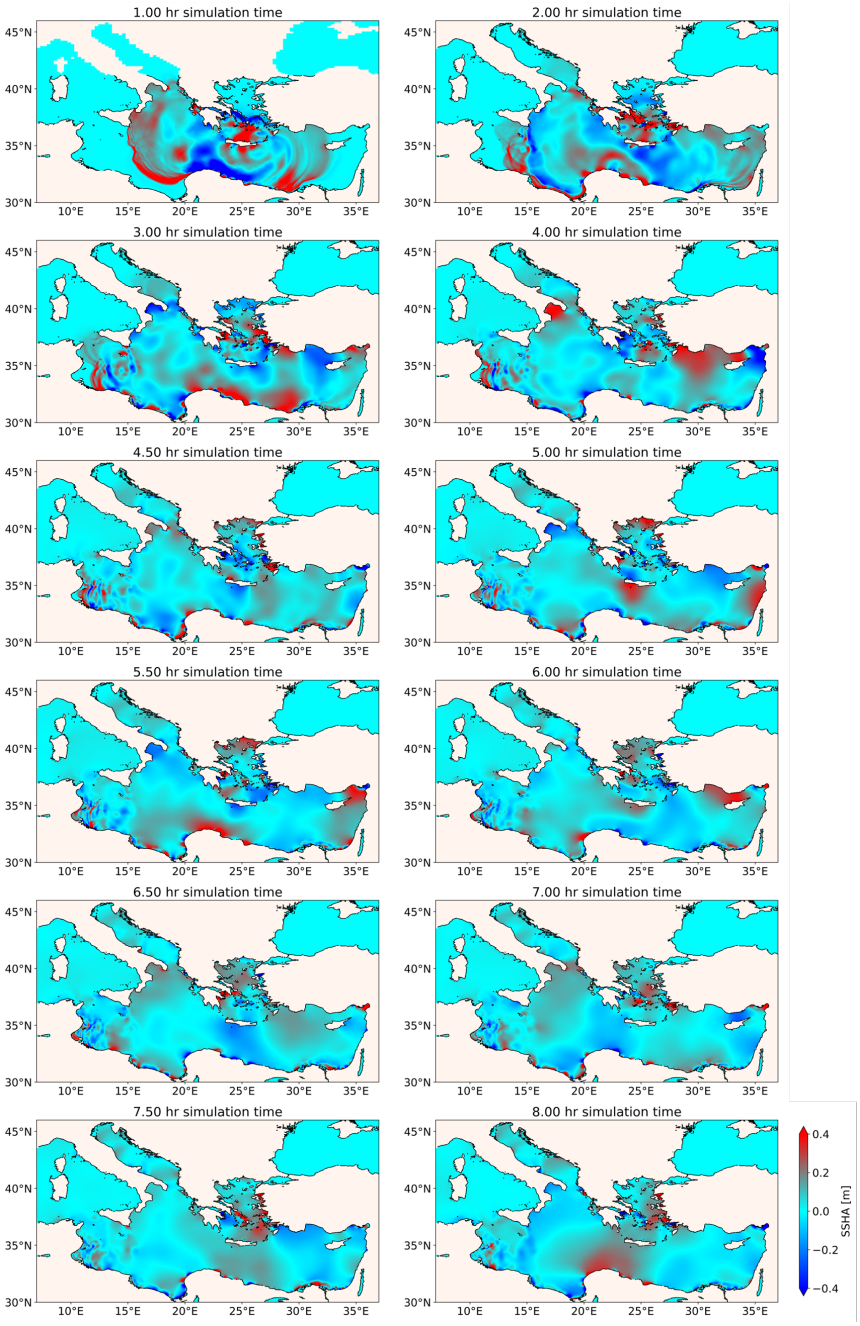



Figure 5.C.4: Tsunami evolution (ssha [m]) for model HEP (eastern hypocenter, including plastic deformation) after 1 h, 2 h, 3 h, 4 h, 4.5 h, 5 h, 5.5 h, 6 h, 6.5 h, 7 h, 7.5 h, 8 h simulation time. Red marks elevation, and blue marks depression from the sea surface at rest.

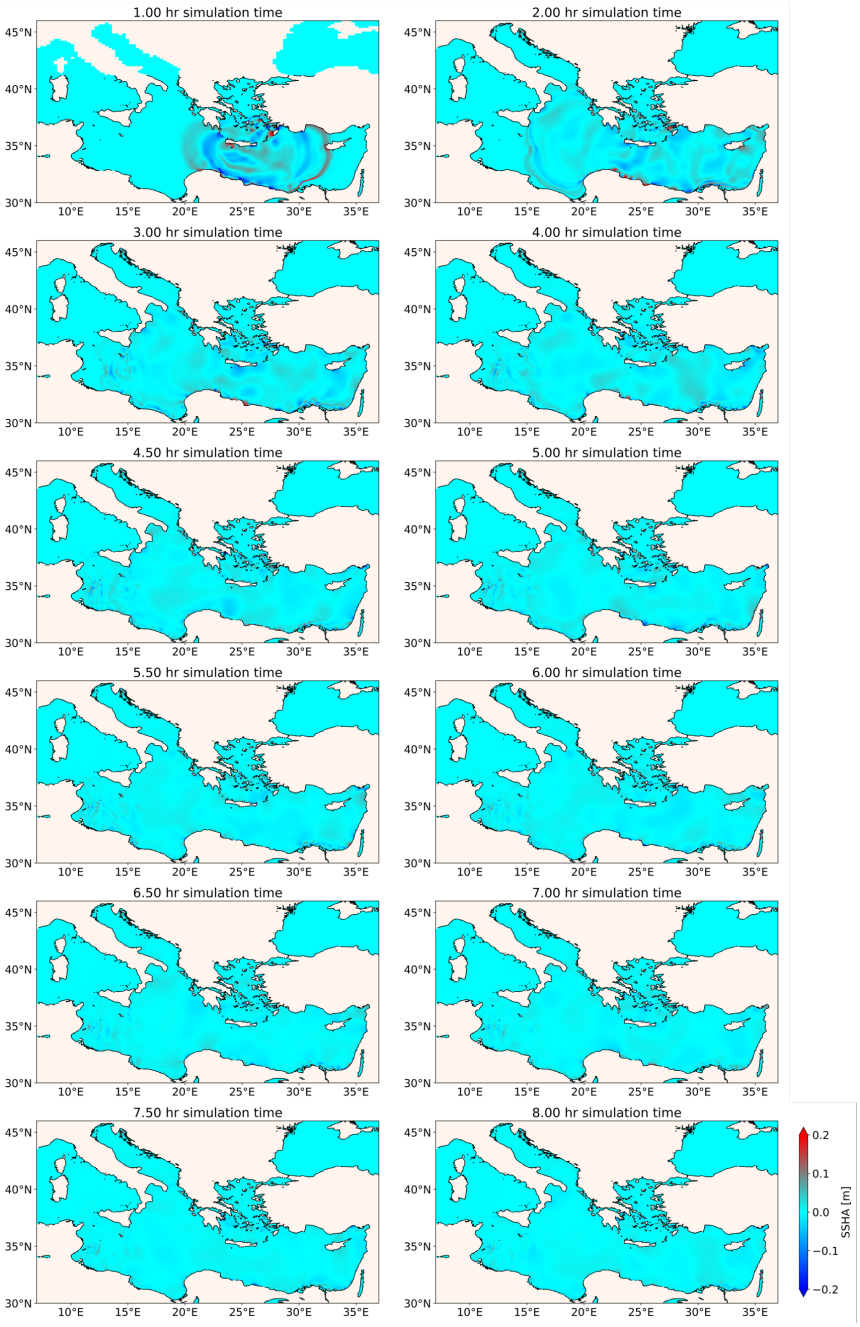



Figure 5.C.5: Tsunami evolution (ssha [m]) for model HEA (eastern hypocenter with initial stress asperity) after 1 h, 2 h, 3 h, 4 h, 4.5 h, 5 h, 5.5 h, 6 h, 6.5 h, 7 h, 7.5 h, 8 h simulation time. Red marks elevation, and blue marks depression from the sea surface at rest.

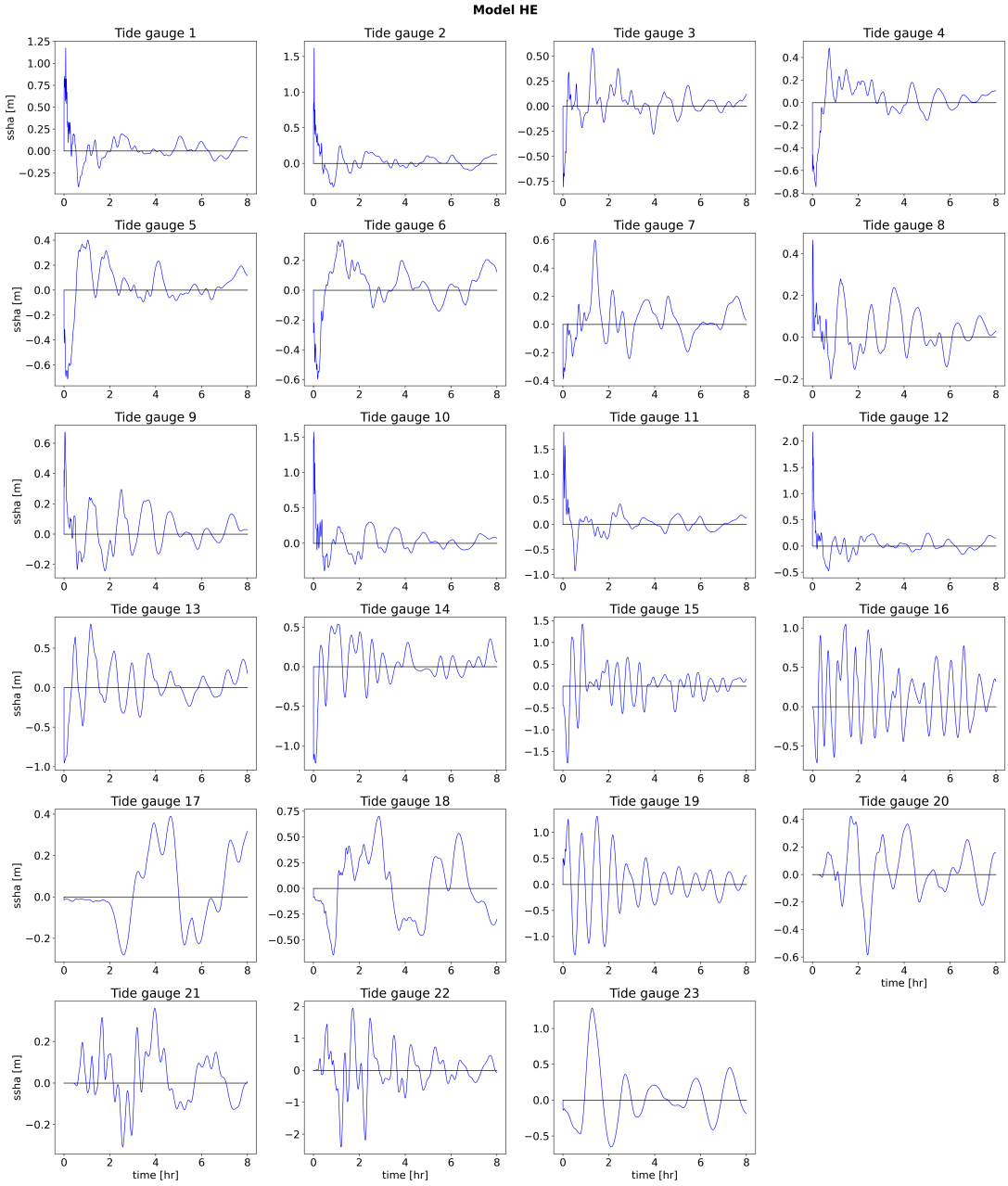



Figure 5.C.6: Synthetic tide gauges showing the sea surface height anomaly (ssha [m]) vs simulation time (8 h) for the one-way-linked model HE (eastern hypocenter) at 23 stations (Fig. 5.3.5 b).

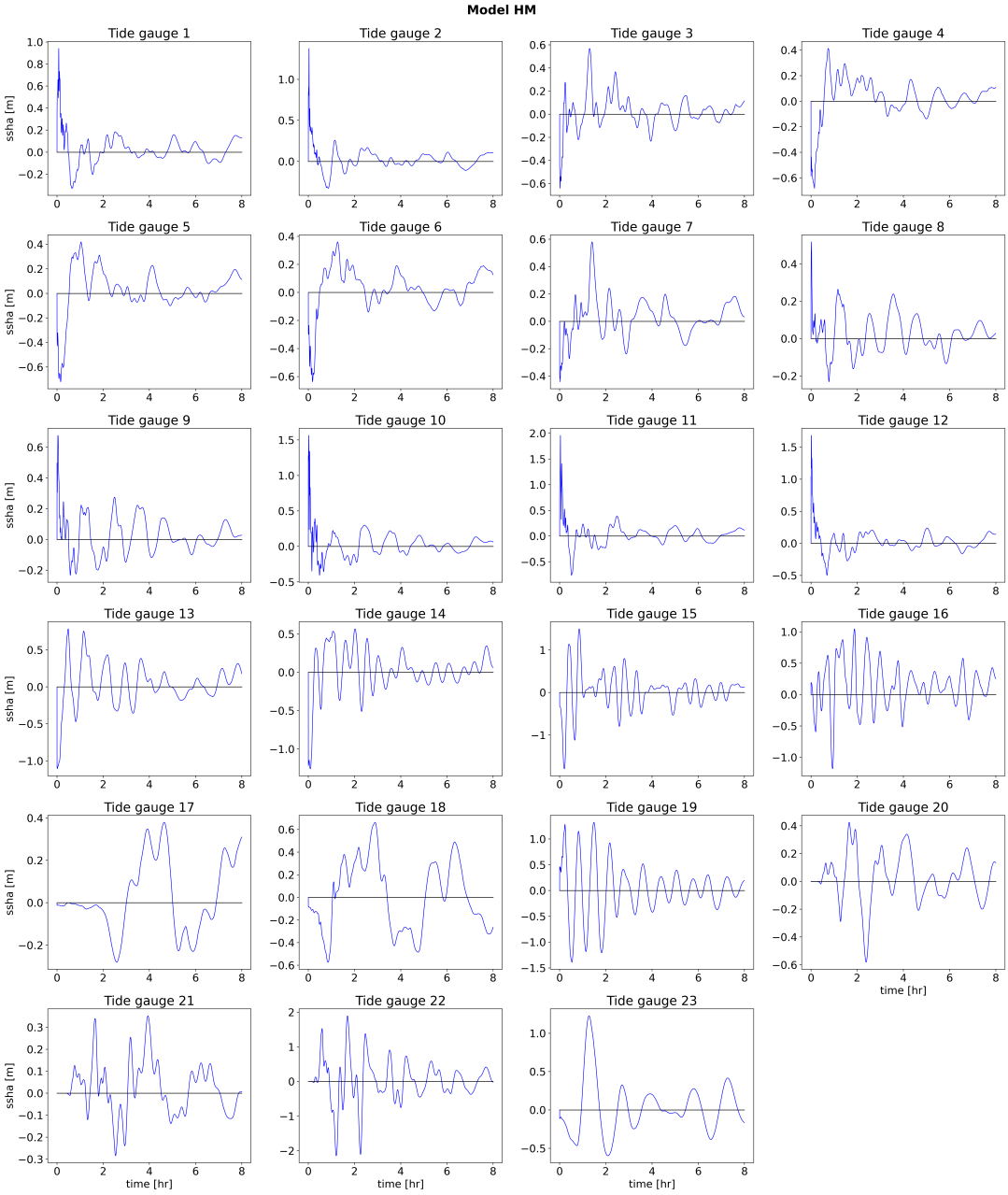



Figure 5.C.7: Synthetic tide gauges showing the sea surface height anomaly (ssha [m]) vs simulation time (8 h) for the one-way-linked model HM (middle hypocenter) at 23 stations (Fig. 5.3.5 b).

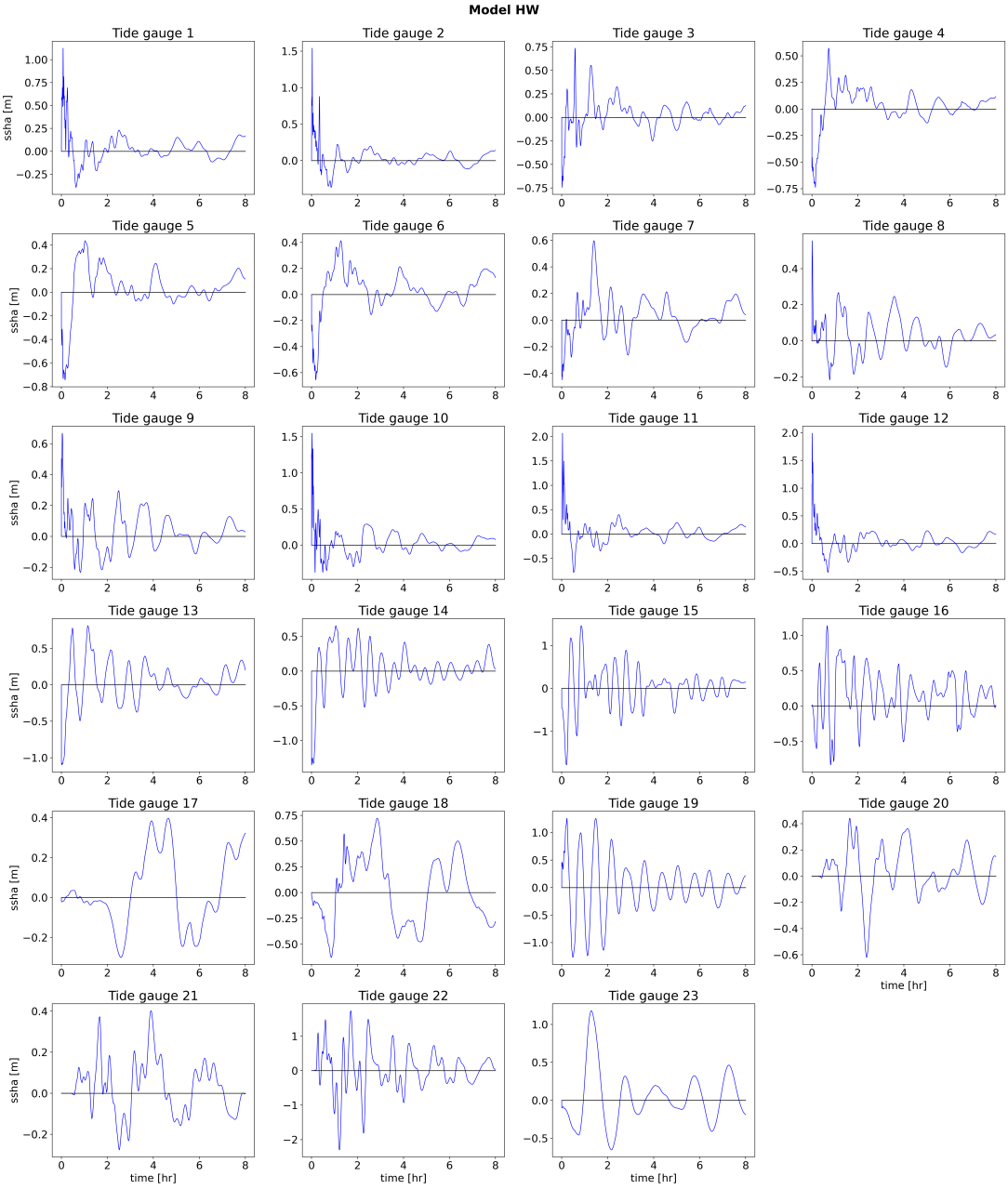



Figure 5.C.8: Synthetic tide gauges showing the sea surface height anomaly (ssha [m]) vs simulation time (8 h) for the one-way-linked model HW (western hypocenter) at 23 stations (Fig. 5.3.5 b).

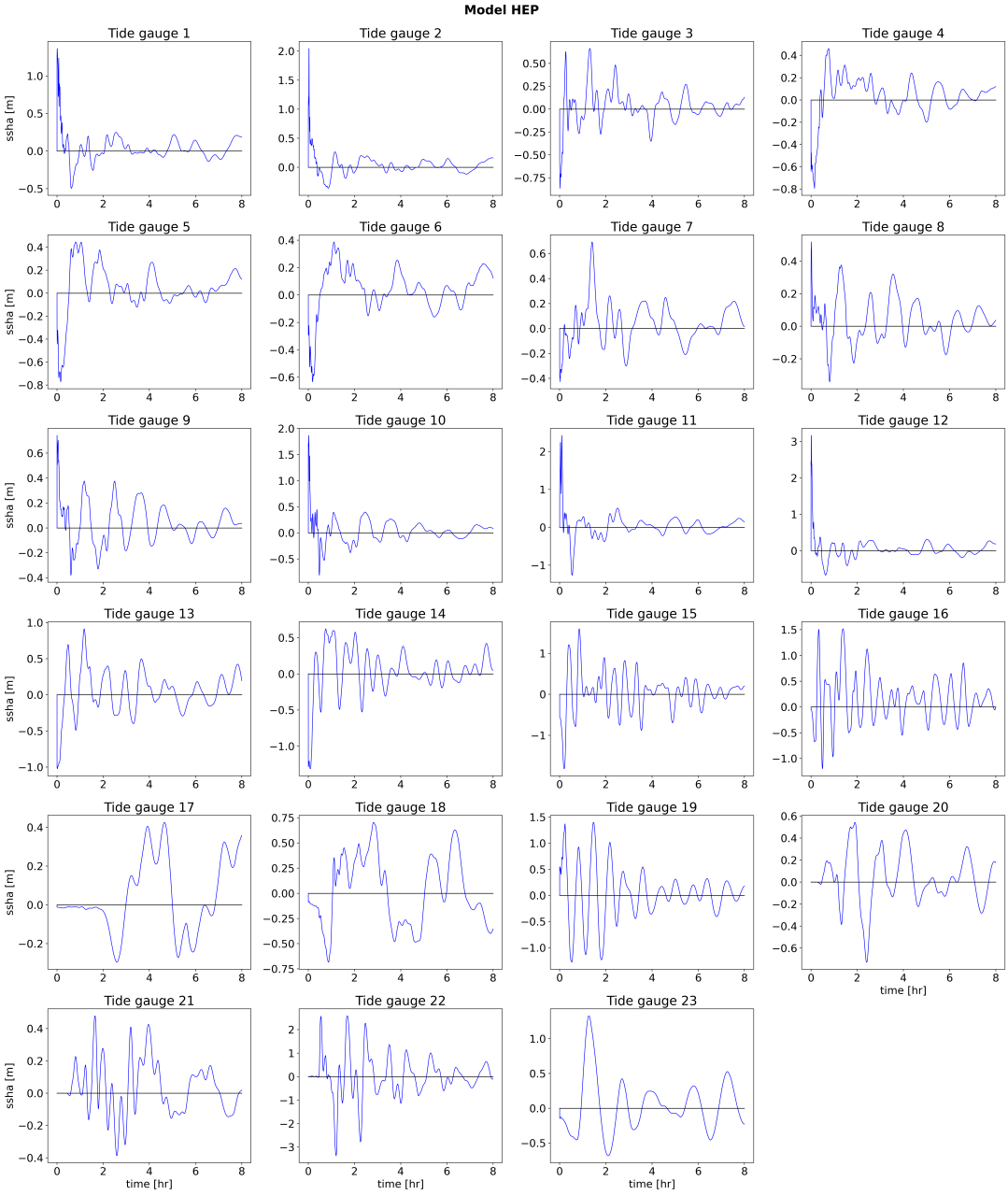



Figure 5.C.9: Synthetic tide gauges showing the sea surface height anomaly (ssha [m]) vs simulation time (8 h) for the one-way-linked model HEP (eastern hypocenter, including plastic deformation) at 23 stations (Fig. 5.3.5 b).

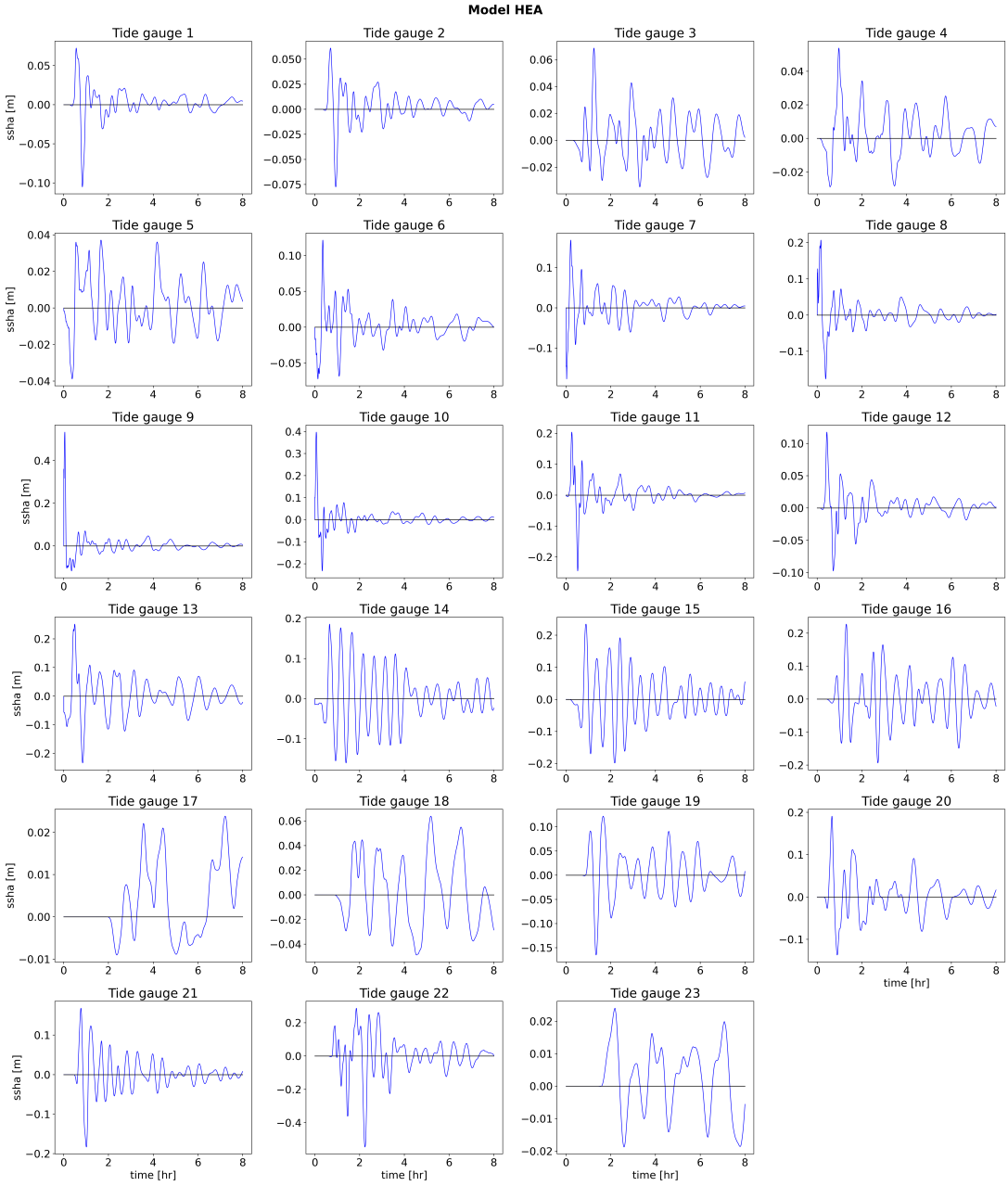



Figure 5.C.10: Synthetic tide gauges showing the sea surface height anomaly (ssha [m]) vs simulation time (8 h) for the one-way-linked model HEA (eastern hypocenter with initial stress asperity) at 23 stations (Fig. 5.3.5 b).

# 5.D Fully-coupled model: tsunami results

We here show tsunami results for the fully-coupled modeling approach after 50 s, 100 s, 200 s, 250 s, and 300 s simulation time, as well as synthetic tide gauges.

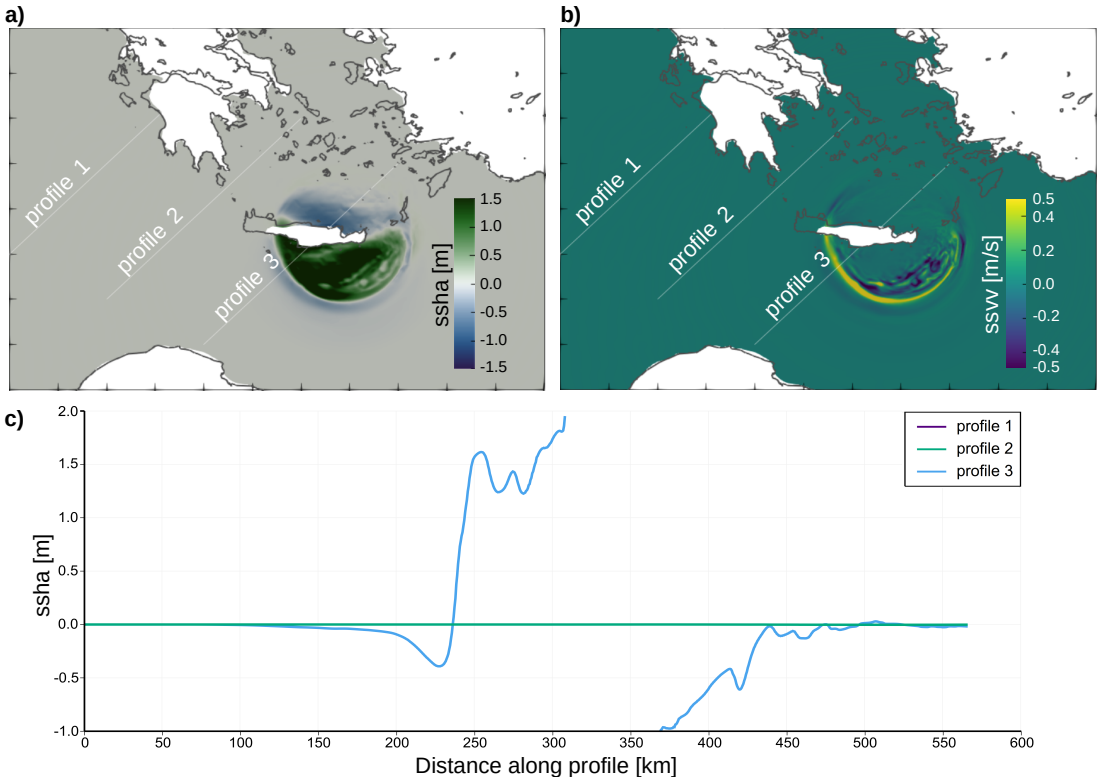



Figure 5.D.1: Results of the fully-coupled earthquake-tsunami simulation: a) ssha [m], b) ssvv [m/s], and c) cross-sections of ssha [m] after 50 s simulation time.

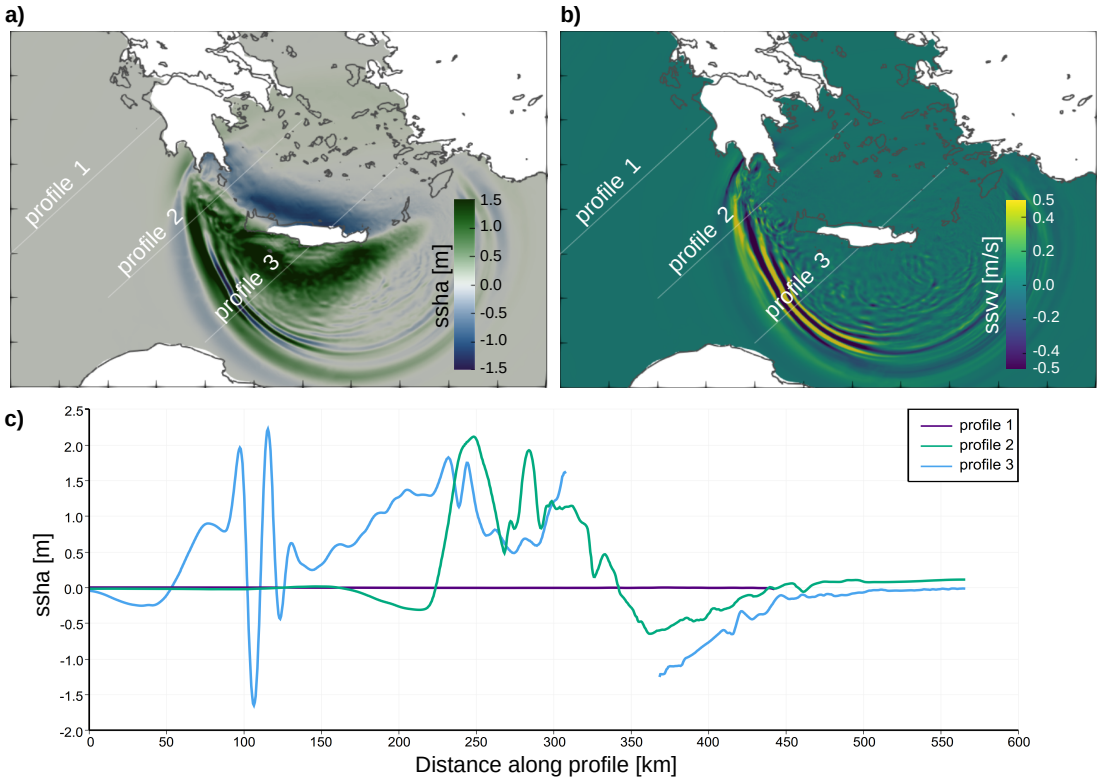



Figure 5.D.2: Results of the fully-coupled earthquake-tsunami simulation: a) ssha [m], b) ssvv [m/s], and c) cross-sections of ssha [m] after 100 s simulation time.

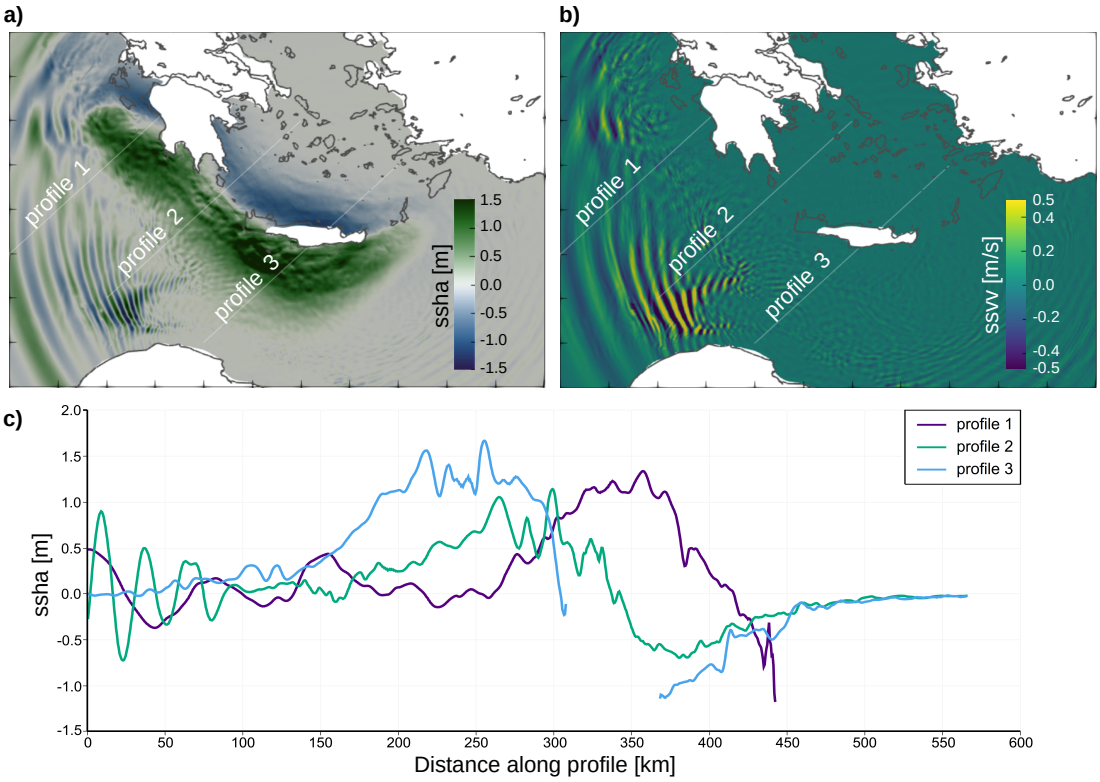



Figure 5.D.3: Results of the fully-coupled earthquake-tsunami simulation: a) ssha [m], b) ssvv [m/s], and c) cross-sections of ssha [m] after 200 s simulation time.

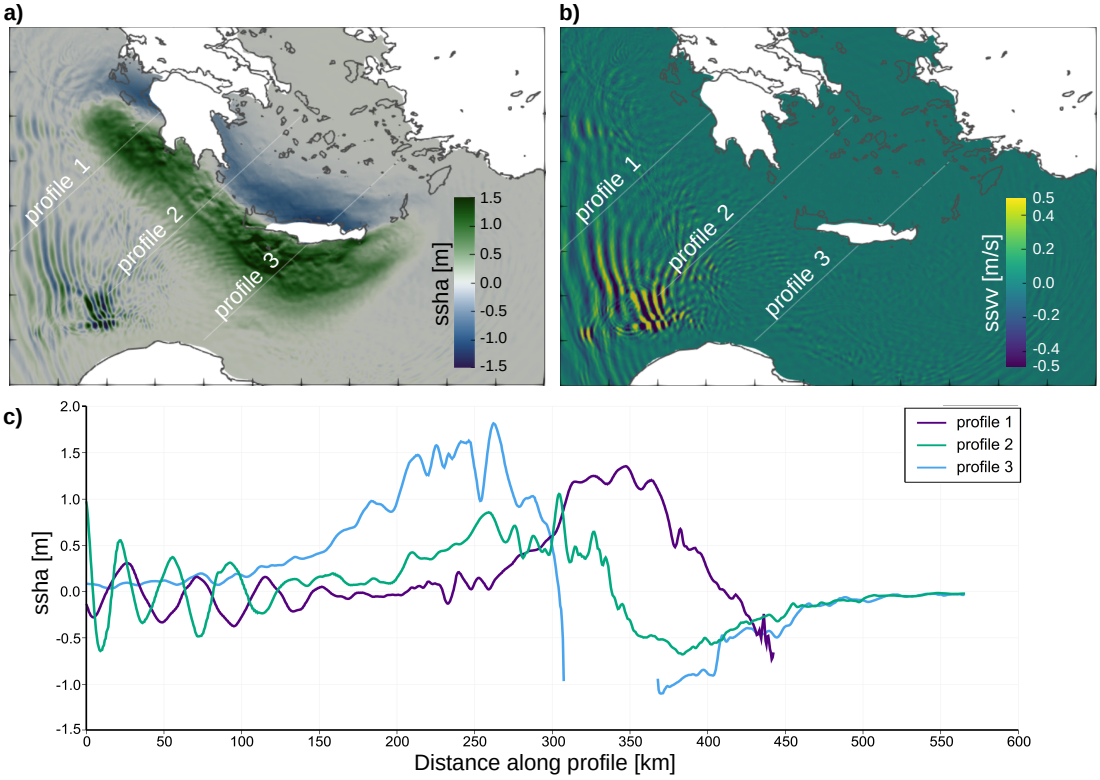



Figure 5.D.4: Results of the fully-coupled earthquake-tsunami simulation: a) ssha [m], b) ssvv [m/s], and c) cross-sections of ssha [m] after 250 s simulation time.

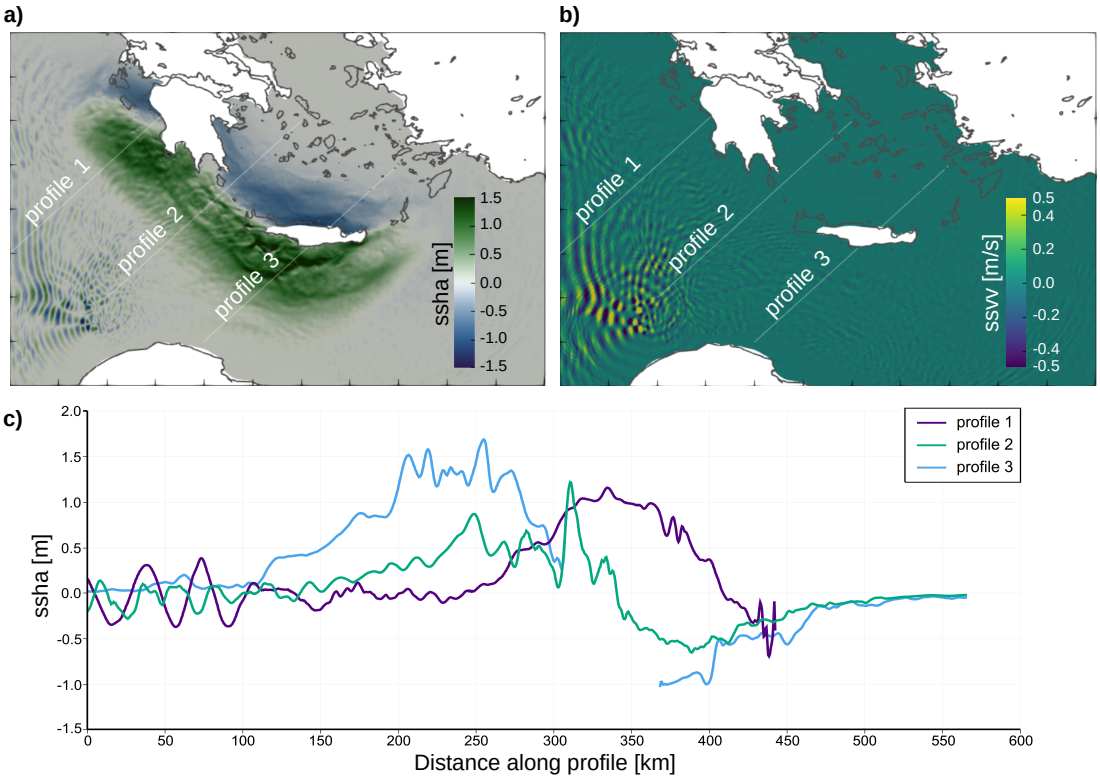



Figure 5.D.5: Results of the fully-coupled earthquake-tsunami simulation: a) ssha [m], b) ssvv [m/s], and c) cross-sections of ssha [m] after 300 s simulation time.

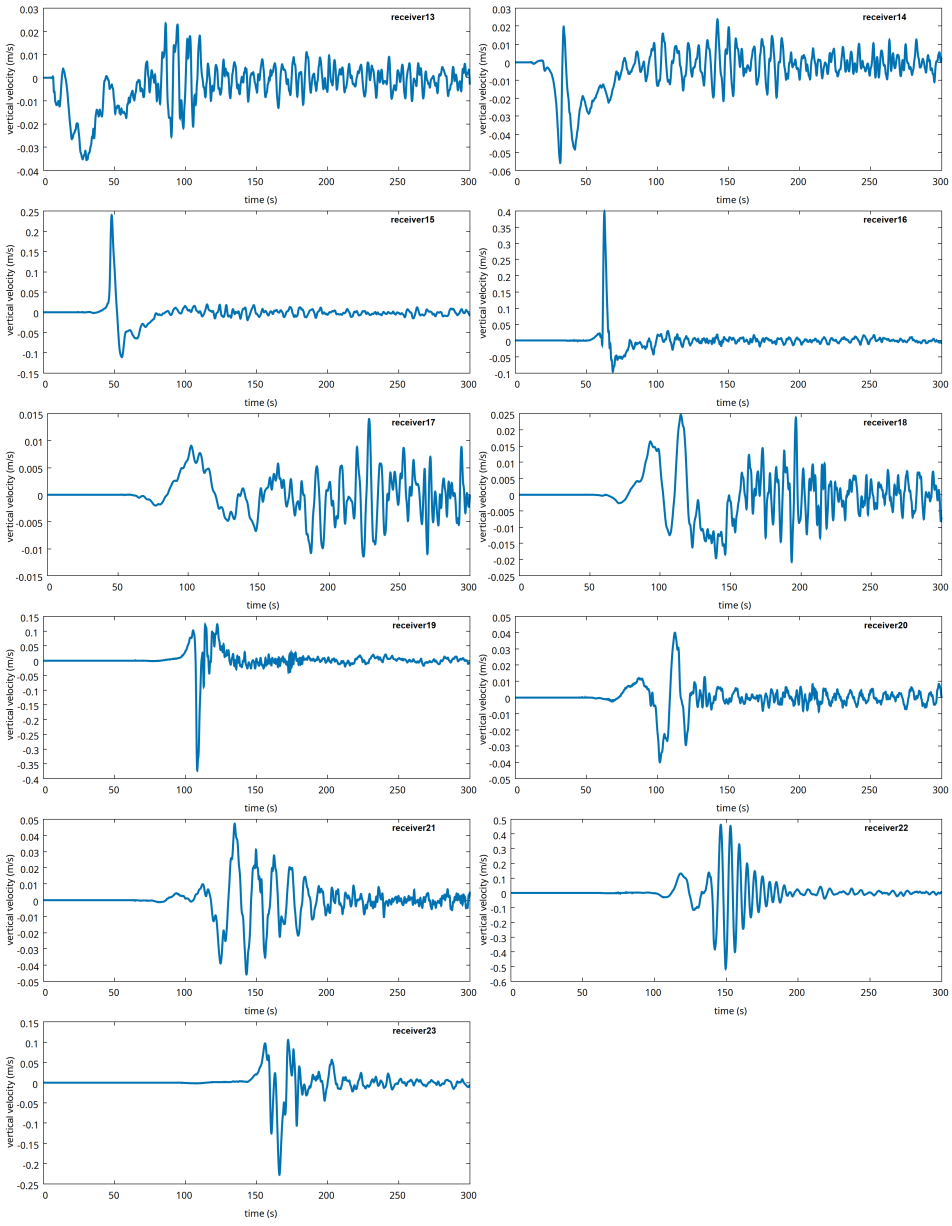



Figure 5.D.6: Synthetic tide gauges showing the sea surface vertical velocity (ssvv [m/s]) vs simulation time (300 s) for the fully-coupled earthquake-tsunami model HE (eastern hypocenter) at stations 13 to 23 (Fig. 5.3.5 b).

# Acknowledgments

We thank Lukas Krenz for useful discussions, and Lauren Abrahams and Eric Dunham for their contributions to the 3D fully-coupled earthquake-tsunami modeling capabilities in SeisSol. This work received funding from the European Union's Horizon 2020 research and innovation program (TEAR ERC Starting grant agreement No. 852992) and Horizon Europe (ChEESE-2P grant No. 101093038, DT-GEO grant No. 101058129, and Geo-INQUIRE grant No. 101058518). AAG acknowledges additional support from the National Science Foundation (CRESCENT, grant no. EAR-2225286, MTMOD, grant no. EAR-2121568, CSA-LCCF, grant no. OAC-2139536, QUAKEWORX, grant no. OAC-2311208) and the National Aeronautics and Space Administration (grant no. 80NSSC20K0495). We appreciate the computing infrastructure of the Department of Earth and Environmental Sciences at LMU, Geophysics (Oeser et al., 2006). The authors gratefully acknowledge the Gauss Centre for Supercomputing e.V. (`www.gauss-centre.eu`, project pn49ha) for funding this project by providing computing time on the GCS Supercomputer SuperMUC at Leibniz Supercomputing Centre (`www.lrz.de`).

# Chapter 6

# Conclusion and Outlook

This thesis links long-term subduction, dynamic rupture, and tsunami models across different spatial and temporal scales to enhance understanding of how various geophysical processes interact in subduction zones. It demonstrates how to generate physically consistent initial conditions for both dynamic forward and tsunami modeling. High-performance computing enables the execution of large-scale models that connect these multiscale processes, such as fully-coupled dynamic rupture-tsunami models, which incorporate elastic-acoustic coupling and accurately represent the full physics of the tsunami generation phase.

## 6.1 Summary of presented work

In Chapter 3, I connect various generic numerical models, from long-term geodynamic subduction and seismic cycling to dynamic rupture and tsunami simulations, spanning different time and spatial scales. This connection provides physically consistent initial conditions for DR and a time-dependent source for the tsunami. With 15 dynamic rupture models, I explore the causes of supershear rupture initiation and how different on-fault hypocentral locations, an increase in Poisson's ratio, or a triplication of fracture energy influence tsunami arrival times and coastal amplitudes.
While the depth of the hypocenter has little effect on tsunami behavior, its lateral position is crucial for tsunami arrival times. Increasing Poisson's ratio results in duplicated shallow fault slip, causing approximately 1.5 m more vertical seafloor uplift and higher coastal tsunami amplitudes. An increase in fracture energy also doubles the shallow fault slip, which in turn doubles the tsunami's potential energy. However, it reduces the peak slip rate, leading to a "tsunami earthquake" that produces the greatest vertical seafloor uplift of 2 m across all models and tsunami amplitudes reaching about 7.5 m.. The inclusion of a complex topobathymetry leads to higher tsunami wave amplitudes at the coast compared to a linearly sloping beach. This study highlights the importance of choosing the correct initial conditions for dynamic rupture. It may help clarify the physical parameters that control rupture dynamics, ultimately resulting in devastating tsunamis.

Chapter 4 examines ten potential earthquake rupture scenarios on the subducting megathrust of the Hellenic Arc region in the eastern Mediterranean. This study demonstrates how initial conditions for DR modeling can be constrained without relying on geodetic locking models, making it applicable to other, mostly "quiet" subduction zones that lack long, complete historical records, such as the Cascadia subduction zone.
Homogeneous initial conditions of uniform along-arc fault pre-stresses lead to worst-case scenarios of margin-wide rupture propagation, generating moment magnitudes $M_W$ ∼9.0. Different hypocentral locations exhibit variations in rupture propagation, with the rupture penetrating the slip-strengthening region of the fault, resulting in shallow slip amplification. The further west the hypocenter, the greater the amount of shallow slip and the larger the localized near-trench seafloor uplift that develops. I demonstrate that a change in the plunge of the maximum principal stress may limit along-arc rupture propagation, and that weak sediments in the upper 15 km, included as off-fault plastic deformation in our model, can double the vertical co-seismic seafloor uplift. The inclusion of a single stress-asperity resembles the historical tsunami-generic $M_W$∼8.0 1303 Crete earthquake.
I progressively increase the model complexity by incorporating varying along-arc shear stress derived from inversion results (Kkallas et al., 2021), leading to events with moment magnitudes of $M_W$∼8.0-8.5, diverse slip rates, and uplift patterns. In an additional model, I implement multiple asperities of varying sizes and a changing critical slip weakening distance. This $M_W$∼8.4 model generates the highest seafloor uplift of approximately 3.5 m, which is more than double the amount of uplift of the $M_W$ ∼9 margin-wide rupture models. The most complex model combines the heterogeneities described above, resulting in the smallest magnitude ($M_W$∼7.5) among all models.
The DR models in this study offer a catalog of physics-based scenarios that can inform future regional Hellenic Arc joint seismic and tsunami hazard assessments.

In Chapter 5, I present tsunami models in the Hellenic Arc region, sourced by the static seafloor deformation of five dynamic rupture earthquake models of Chapter 4.
First, I utilize the static seafloor uplift and subsidence of three $M_W$ ∼9 dynamic rupture models with different hypocentral locations on the Hellenic Arc megathrust to investigate differences in maximum tsunami height and tsunami propagation in the Mediterranean. Then, I examine how the integration of unconsolidated sediments in terms of off-fault plastic deformation contributes to maximum tsunami amplitudes. Additionally, I use the $M_W$ ∼8 stress-asperity model of Chapter 4 to illustrate the tsunami evolution caused by a smaller megathrust earthquake. Finally, I extend one model into a three-dimensional, large-scale, fully-coupled earthquake-tsunami model to demonstrate the complexities of the early time-dependent tsunami generation phase.
The statically sourced non-linear shallow water models show the tsunami evolution in the Mediterranean over an 8 h simulation, with maximum wave heights reaching up to 6.6 m near Crete and a leading wave front approaching the North African coast after 1 h. The northern Aegean and the western Mediterranean mostly remain protected by landmasses in all scenarios. Variations in the epicenter location on the megathrust cause slip to the trench, leading to small bands of near-trench uplift that vary in size. These result in only

minor differences in the maximum tsunami heights in the near field but create different wave arrival times, with the tsunami from a western hypocenter reaching the African coast earlier than the one from a more eastern hypocenter. I demonstrate that incorporating plasticity into the DR model hinders rupture propagation into the slip-strengthening region of the fault, resulting in a 2.27 m higher tsunami amplitude. This suggests that inelastic deformation may have played a key role in historic tsunami-generic earthquakes by increasing the wave amplitude. I show that a non–margin–wide $M_W 8$ scenario can only produce maximum tsunami waves of about 0.5 m, indicating that such an earthquake is unlikely to reproduce the extreme wave heights of past events.
The fully-coupled model runs for 300 s, simultaneously simulating earthquake rupture dynamics, seismic wave propagation in elastic and acoustic media, and tsunami initiation in the compressible ocean. At the early stage of tsunami generation, I model the superimposition of seismic and acoustic waves in the near-fault region. High-amplitude seismo-acoustic waves are generated during the early tsunami stage and can be recorded at synthetic tide gauge stations. For near-fault gauge stations, the signal is strong enough to potentially be extracted and interpreted in real-time, serving as an early warning before the main tsunami arrives.
Incorporating a physically consistent dynamic rupture model into tsunami simulations could help decrease the epistemic uncertainty in tsunami hazard analysis and reduce the variability of stochastic slip models.

## 6.2 Future perspectives

This dissertation offers a guide for establishing physically consistent initial conditions for dynamic rupture and tsunami modeling in primarily "quiet" subduction zones. The first method utilizes generic models to connect simulations across different time frames and scales. This is done by applying material and frictional properties from long-term subduction simulations as initial conditions for dynamic rupture modeling, which then serves to source tsunamis over time. A second, mechanically self-consistent approach is to constrain heterogeneous dynamic rupture initial conditions with increasing complexity by incorporating available observations. These are then utilized to produce tsunami simulations for specific regions, such as the Hellenic Arc. These strategies provide various methods for incorporating dynamic rupture modeling into regional seismic and tsunami hazard assessments for subduction zones. Furthermore, a catalog of physics-based megathrust rupture scenarios for regions where complete and long historical records are absent could be useful for informing hazard assessment and disaster risk management. More computationally intensive, large-scale, fully-coupled earthquake-tsunami simulations can further enhance tsunami hazard assessment by modeling the entire tsunami generation process, capturing early-stage complexities of tsunami formation, and including large-amplitude acoustic and oceanic Rayleigh waves. When recorded by ocean-bottom pressure sensors or hydrophones, they can serve as early warning indicators for tsunamis.

The most obvious next step for extending this work would be to include a larger water layer and more realistic bathymetry to better model tsunami initiation and propagation in the Hellenic Arc region. An example is shown in Figure 6.2.1. A study with this level of detail could help clarify how the tsunami leading front and acoustic waves interact with the shorelines of the Greek Islands. From such a model, even more complex wave interactions might be observed. Extending the simulation area would require significantly more computational resources, as the fully-coupled approach is computationally expensive. Advances in computational optimization and resource management (e.g., Panzera et al., 2016; Li et al., 2023; Folch et al., 2023), along with access to large-scale supercomputing, are essential for running more complex models over a large, realistic domain and longer simulation periods. Solving meshing challenges is also crucial for this endeavor.

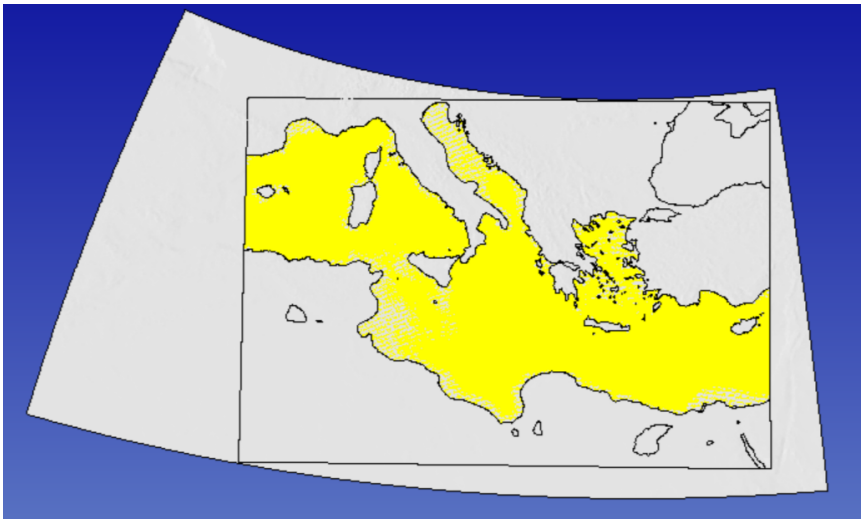


Figure 6.2.1: SimModeler (Simmetrix Inc., 2017) snapshot of the intersection of bathymetry with a water surface for the Mediterranean. The rectangular part would form the modeling domain for a fully-coupled earthquake-tsunami model. The yellow color represents the water layer, and grey represents the solid. Note the many small-scale islands in Greece where the water layer intersects with the topobathymetry.

Future studies could further expand the scope of this thesis by examining the influence of additional subduction zone complexities on tsunami generation and evolution, such as splay faults which are smaller reverse faults (Park et al., 2002; Sibuet et al., 2007; Collot et al., 2008; Brizzi et al., 2020), branching the shallow megathrust or subducted seamounts (McIntosh et al., 2007; Ranero et al., 2008). If included in long-term subduction and seismic cycling models (Fig. 6.2.2), they can serve as physically consistent initial conditions for more realistic dynamic rupture simulations of specific megathrust regions, such as the Southern Chilean margin. Seamounts may act as asperities that trigger rupture propagation (Fig. 6.2.2 a) or as barriers for deep earthquakes. Modeling rupture on megathrusts with seamounts of various geometries on the subducting plate would offer insights into this

complex interaction and improve understanding of potentially tsunamigenic earthquakes.

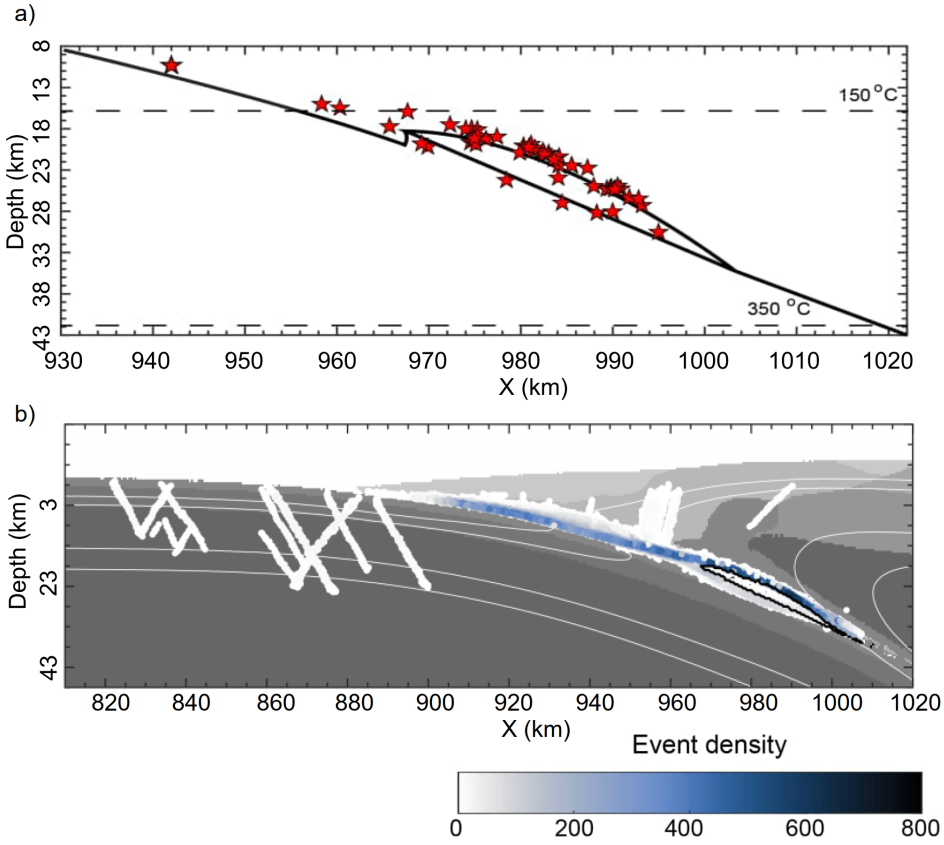



Figure 6.2.2: **Deep subducting seamount in seismo-thermo-mechanical geodynamic seismic cycle model:** Figure is adapted from Fonteijn et al., Tectonophysics (in prep.). a) Subducting interface with imposed deep subducting seamount. Seismic events are displayed as red stars. The events accumulate on top of the seamount. b) Event density in the geodynamic seismic cycling model. High event density is colored dark blue. The event density is high on top of the seamount. Splay faults (white lines) branch the main megathrust. This model could be converted into initial conditions for DR modeling.

Another promising approach would be to perform fully-coupled simulations that incorporate long-term geodynamics and 3D dynamic rupture within a single model. This would eliminate the need for simplifications and corrections of the one-way linking approach, thereby improving simulation accuracy and enabling faster modeling. A first step toward such models was taken by (Jourdon et al., 2024), who loosely coupled geodynamic models with dynamic rupture to provide a mechanically consistent framework for earthquake modeling analysis.

# Bibliography


Aagaard, B. T., Anderson, G., and Hudnut, K. W. (2004). Dynamic rupture modeling of the transition from thrust to strike-slip motion in the 2002 Denali fault earthquake, Alaska. *Bulletin of the Seismological Society of America*, 94(6B):S190–S201.

Abbate, A., Davies, G., Lorito, S., Kalligeris, N., Romano, F., Tonini, R., and Volpe, M. (2025). Importance sampling of seismic tsunami sources with near-field emphasis for inundation PTHA: benchmarking with complete ensembles. *Geophysical Journal International*, 241(1):155–169.

Abbate, A., González Vida, J. M., Castro Díaz, M. J., Romano, F., Bayraktar, H. B., Babeyko, A., and Lorito, S. (2024). Modelling tsunami initial conditions due to rapid coseismic seafloor displacement: efficient numerical integration and a tool to build unit source databases. *Natural Hazards and Earth System Sciences*, 24(8):2773–2791.

Abrahams, L. S., Krenz, L., Dunham, E. M., Gabriel, A.-A., and Saito, T. (2023). Comparison of methods for coupled earthquake and tsunami modelling. *Geophysical Journal International*, 234(1):404–426.

Allgeyer, S. and Cummins, P. (2014). Numerical tsunami simulation including elastic loading and seawater density stratification. *Geophysical Research Letters*, 41(7):2368–2375.

Altinok, Y. and Ş. Ersoy (2000). Tsunamis observed on and near the turkish coast. *Natural Hazards*, pages 185–205.

Ambraseys, N. (2009). *Earthquakes in the Mediterranean and Middle East: a multidisciplinary study of seismicity up to 1900*. Cambridge University Press.

Ambraseys, N. N. (1962). Data for the investigation of the seismic sea-waves in the Eastern Mediterranean. *Bulletin of the Seismological Society of America*, 52:895–913.

Ambraseys, N. N. (1994). Material for the investigation of the seismicity of Libya. *Libyan Studies*, 25:7–22.

Amlani, F., Bhat, H. S., Simons, W. J., Schubnel, A., Vigny, C., Rosakis, A. J., Efendi, J., Elbanna, A. E., Dubernet, P., and Abidin, H. Z. (2022). Supershear shock front contribution to the tsunami from the 2018 Mw 7.5 Palu, Indonesia earthquake. *Geophysical Journal International*, 230:2089–2097.

Ammon, C. J., Kanamori, H., Lay, T., and Velasco, A. A. (2006). The 17 July 2006 Java tsunami earthquake. *Geophysical Research Letters*, 33(24).

Ampuero, J.-P. and Ben-Zion, Y. (2008). Cracks, pulses and macroscopic asymmetry of dynamic rupture on a bimaterial interface with velocity-weakening friction. *Geophysical Journal International*, 173(2):674–692.

Andrews, D. (1980). A stochastic fault model: 1. Static case. *Journal of Geophysical Research: Solid Earth*, 85(B7):3867–3877.

Andrews, D. J. (1976a). Rupture propagation with finite stress in antiplane strain. *Journal of Geophysical Research (1896-1977)*, 81(20):3575–3582.

Andrews, D. J. (1976b). Rupture velocity of plane strain shear cracks. *Journal of Geophysical Research*, 81(32):5679–5687. Publisher: John Wiley & Sons, Ltd.

Andrews, D. J. (2002). A fault constitutive relation accounting for thermal pressurization of pore fluid. *Journal of Geophysical Research: Solid Earth*, 107(B12):ESE 15–1–ESE 15–8.

Andrews, D. J. (2005). Rupture dynamics with energy loss outside the slip zone. *Journal of Geophysical Research: Solid Earth*, 110(B1).

Angelier, J. (1990). Inversion of field data in fault tectonics to obtain the regional stress—III. A new rapid direct inversion method by analytical means. *Geophysical Journal International*, 103(2):363–376.

Antonopoulos, J. (1980). AntData from investigation on seismic sea-waves events in the Eastern Mediterranean from the birth of Christ to 500 AD. *Annals of Geophysics*, 33:141–161.

Aochi, H. and Fukuyama, E. (2002). Three-dimensional nonplanar simulation of the 1992 Landers earthquake. *Journal of Geophysical Research: Solid Earth*, 107(B2):ESE 4–1–ESE 4–12.

Aochi, H. and Madariaga, R. (2003). The 1999 Izmit, Turkey, earthquake: Nonplanar fault structure, dynamic rupture process, and strong ground motion. *Bulletin of the Seismological Society of America*, 93(3):1249–1266.

Aochi, H. and Ulrich, T. (2015). A Probable Earthquake Scenario near Istanbul Determined from Dynamic Simulations. *Bulletin of the Seismological Society of America*, 105(3):1468–1475. Publisher: GeoScienceWorld.

Arcos, M. E. M. and LeVeque, R. J. (2015). Validating velocities in the GeoClaw tsunami model using observations near Hawaii from the 2011 Tohoku tsunami. *Pure and Applied Geophysics*, 172:849–867.

Atkinson, G. M., Bommer, J. J., and Abrahamson, N. A. (2014). Alternative approaches to modeling epistemic uncertainty in ground motions in probabilistic seismic-hazard analysis.

Babeyko, A., Hoechner, A., and Sobolev, S. V. (2010). Source modeling and inversion with near real-time GPS: a GITEWS perspective for Indonesia. *Natural Hazards and Earth System Sciences (NHESS)*, 10(7):1617–1627.

Baglione, E., Lorito, S., Piatanesi, A., Romano, F., Basili, R., Brizuela, B., Tonini, R., Volpe, M., Bayraktar, H. B., and Amato, A. (2021). Characterization of fault plane and coseismic slip for the 2 May 2020, Mw 6.6 Cretan Passage earthquake from tide gauge tsunami data and moment tensor solutions. *Natural Hazards and Earth System Sciences*, 21(12):3713–3730.

Bahrouni, N., Meghraoui, M., Bayraktar, H. B., Lorito, S., Zagrarni, M. F., Polonia, A., Bel Mabrouk, N., and Kamoun, F. (2024). Tsunami deposits in Tunisia contemporaneous of the large 365 CE Crete earthquake and Mediterranean Sea catastrophic event. *Scientific Reports*, 14(1):4537.

Bai, K. and Ampuero, J.-P. (2017). Effect of seismogenic depth and background stress on physical limits of earthquake rupture across fault step overs. *Journal of Geophysical Research: Solid Earth*, 122(12):10–280.

Bao, H., Ampuero, J.-P., Meng, L., Fielding, E. J., Liang, C., Milliner, C. W., Feng, T., and Huang, H. (2019). Early and persistent supershear rupture of the 2018 magnitude 7.5 Palu earthquake. *Nature Geoscience*, 12(3):200–205.

Bartolomeo, M. D., Meziane, A., Massi, F., Baillet, L., and Fregolent, A. (2010). Dynamic rupture at a frictional interface between dissimilar materials with asperities. *Tribology International*, 43:1620–1630.

Basili, R., Brizuela, B., Herrero, A., Iqbal, S., Lorito, S., Maesano, F. E., Murphy, S., Perfetti, P., Romano, F., Scala, A., Selva, J., Taroni, M., Tiberti, M. M., Thio, H. K., Tonini, R., Volpe, M., Glimsdal, S., Harbitz, C. B., Løvholt, F., Baptista, M. A., Carrilho, F., Matias, L. M., Omira, R., Babeyko, A., Hoechner, A., Gürbüz, M., Pekcan, O., Yalçıner, A., Canals, M., Lastras, G., Agalos, A., Papadopoulos, G., Triantafyllou, I., Benchekroun, S., Jaouadi, H. A., Abdallah, S. B., Bouallegue, A., Hamdi, H., Oueslati, F., Amato, A., Armigliato, A., Behrens, J., Davies, G., Bucci, D. D., Dolce, M., Geist, E., Vida, J. M. G., González, M., Sánchez, J. M., Meletti, C., Sozdinler, C. O., Pagani, M., Parsons, T., Polet, J., Power, W., Sørensen, M., and Zaytsev, A. (2021). The Making of the NEAM Tsunami Hazard Model 2018 (NEAMTHM18). *Frontiers in Earth Science*, 8.

Basili, R., Tiberti, M. M., Kastelic, V., Romano, F., Piatanesi, A., Selva, J., and Lorito, S. (2013). Integrating geologic fault data into tsunami hazard studies. *Natural Hazards and Earth System Sciences*, 13:1025–1050.

Bassett, D. and Watts, A. B. (2015). Gravity anomalies, crustal structure, and seismicity at subduction zones: 1. Seafloor roughness and subducting relief. *Geochemistry, Geophysics, Geosystems*, 16(5):1508–1540.

Becerril, C., Sladen, A., Ampuero, J.-P., Preciado-Garbayo, J., Gonzalez-Herraez, M., Kutschera, F., Gabriel, A.-A., and Bouchette, F. (2025). Towards tsunami early-warning with Distributed Acoustic Sensing: expected seafloor strains induced by tsunamis. *ESS Open Archive*.

Becker, D. and Meier, T. (2010). Seismic slip deficit in the southwestern forearc of the Hellenic subduction zone. *Bulletin of the Seismological Society of America*, 100:325–342.

Behrens, J. and Dias, F. (2015). New computational methods in tsunami science. *Philosophical Transactions of the Royal Society A: Mathematical, Physical and Engineering Sciences*, 373(2053):20140382.

Behrens, J., Løvholt, F., Jalayer, F., Lorito, S., Salgado-Gálvez, M. A., Sørensen, M., Abadie, S., Aguirre-Ayerbe, I., Aniel-Quiroga, I., Babeyko, A., Baiguera, M., Basili, R., Belliazzi, S., Grezio, A., Johnson, K., Murphy, S., Paris, R., Rafliana, I., Risi, R. D., Rossetto, T., Selva, J., Taroni, M., Zoppo, M. D., Armigliato, A., Bureš, V., Cech, P., Cecioni, C., Christodoulides, P., Davies, G., Dias, F., Bayraktar, H. B., González, M., Gritsevich, M., Guillas, S., Harbitz, C. B., Kânoğlu, U., Macías, J., Papadopoulos, G. A., Polet, J., Romano, F., Salamon, A., Scala, A., Stepinac, M., Tappin, D. R., Thio, H. K., Tonini, R., Triantafyllou, I., Ulrich, T., Varini, E., Volpe, M., and Vyhmeister, E. (2021). Probabilistic Tsunami Hazard and Risk Analysis: A review of research gaps. *Frontiers in Earth Science*, 9.

Benetatos, C., Kiratzi, A., Papazachos, C., and Karakaisis, G. (2004). Focal mechanisms of shallow and intermediate depth earthquakes along the Hellenic Arc. *Journal of Geodynamics*, 37(2):253–296.

Berger, M. J., George, D. L., LeVeque, R. J., and Mandli, K. T. (2011). The GeoClaw software for depth-averaged flows with adaptive refinement. *Advances in Water Resources*, 34(9):1195–1206. arXiv: 1008.0455.

Bie, L., González, P. J., and Rietbrock, A. (2017). Slip distribution of the 2015 Lefkada earthquake and its implications for fault segmentation. *Geophysical Journal International*, 210(1):420–427.

Biemiller, J., Gabriel, A.-A., and Ulrich, T. (2023). Dueling dynamics of low-angle normal fault rupture with splay faulting and off-fault damage. *Nature Communications*, 14(1):2352.

Bilek, S. L. (2010). Invited review paper: Seismicity along the South American subduction zone: Review of large earthquakes, tsunamis, and subduction zone complexity. *Tectonophysics*, 495(1):2–14. From the trench to the arc: subduction along South America.

Bilek, S. L. and Engdahl, E. R. (2007). Rupture characterization and aftershock relocations for the 1994 and 2006 tsunami earthquakes in the Java subduction zone. *Geophysical Research Letters*, 34(20).

Bilek, S. L. and Lay, T. (1999). Rigidity variations with depth along interplate megathrust faults in subduction zones. *Nature*, 400(6743):443–446.

Bilek, S. L. and Lay, T. (2018). Subduction zone megathrust earthquakes. *Geosphere*, 14(4):1468–1500.

Bilek, S. L., Schwartz, S. Y., and DeShon, H. R. (2003). Control of seafloor roughness on earthquake rupture behavior. *Geology*, 31(5):455–458.

Bird, P. (2003). An updated digital model of plate boundaries. *Geochemistry, Geophysics, Geosystems*, 4.

Bird, P., Kagan, Y. Y., Jackson, D. D., Stein, S., and Freymueller, J. (2002). Plate tectonics and earthquake potential of spreading ridges and oceanic transform faults.

Bizzarri, A. and Cocco, M. (2006). A thermal pressurization model for the spontaneous dynamic rupture propagation on a three-dimensional fault: 1. Methodological approach. *Journal of Geophysical Research: Solid Earth*, 111(B5).

Blaser, L., Krüger, F., Ohrnberger, M., and Scherbaum, F. (2010). Scaling Relations of Earthquake Source Parameter Estimates with Special Focus on Subduction Environment. *Bulletin of the Seismological Society of America*, 100(6):2914–2926.

Bletery, Q., Sladen, A., Jiang, J., and Simons, M. (2016). A Bayesian source model for the 2004 great Sumatra-Andaman earthquake. *Journal of Geophysical Research: Solid Earth*, 121(7):5116–5135.

Bocchini, G. M., Novikova, T., Papadopoulos, G., Agalos, A., Mouzakiotis, E., Karastathis, V., and Voulgaris, N. (2020). Tsunami Potential of Moderate Earthquakes: The July 1, 2009 Earthquake ($M_W$ 6.45) and its Associated Local Tsunami in the Hellenic Arc. *Pure and Applied Geophysics*, 177:1315–1333.

Bohnhoff, M., Harjes, H. P., and Meier, T. (2005). Deformation and stress regimes in the Hellenic subduction zone from focal Mechanisms. *Journal of Seismology 2005 9:3*, 9:341–366.

Bohnhoff, M., Makris, J., Papanikolaou, D., and Stavrakakis, G. (2001). Crustal investigation of the Hellenic subduction zone using wide aperture seismic data. *Tectonophysics*, 343:239–262.

Bommer, J. J. and Scherbaum, F. (2008). The Use and Misuse of Logic Trees in Probabilistic Seismic Hazard Analysis. *Earthquake Spectra*, 24(4):997–1009.

Bormann, P. (2009). Global 1-D Earth models. In *New Manual of Seismological Observatory Practice (NMSOP)*, pages 1–12. Deutsches GeoForschungsZentrum GFZ.

Borrero, J. C., LeVeque, R. J., Greer, S. D., O'Neill, S., and Davis, B. N. (2015). *Observations and Modelling of Tsunami Currents at the Port of Tauranga, New Zealand*. Engineers Australia and IPENZ, Auckland, New Zealand.

Bostock, M. (2013). The moho in subduction zones. *Tectonophysics*, 609:547–557. Moho: 100 years after Andrija Mohorovicic.

Bourgois, J., Martin, H., Lagabrielle, Y., Le Moigne, J., and Frutos Jara, J. (1996). Subduction erosion related to spreading-ridge subduction: Taitao peninsula (Chile margin triple junction area). *Geology*, 24(8):723–726.

Breuer, A., Heinecke, A., and Bader, M. (2016). Petascale local time stepping for the ADER-DG finite element method. In *2016 IEEE International Parallel and Distributed Processing Symposium (IPDPS)*, pages 854–863.

Breuer, A., Heinecke, A., Rannabauer, L., and Bader, M. (2015). High-order ADER-DG minimizes energy- and time-to-solution of SeisSol. *Lecture Notes in Computer Science (including subseries Lecture Notes in Artificial Intelligence and Lecture Notes in Bioinformatics)*, 9137 LNCS:340–357. Publisher: Springer Verlag.

Breuer, A., Heinecke, A., Rettenberger, S., Bader, M., Gabriel, A.-A., and Pelties, C. (2014). Sustained petascale performance of seismic simulations with SeisSol on SuperMUC. In *International Supercomputing Conference*, pages 1–18. Springer.

Brietzke, G. B., Cochard, A., and Igel, H. (2009). Importance of bimaterial interfaces for earthquake dynamics and strong ground motion. *Geophysical Journal International*, 178(2):921–938.

Briseid Storrøsten, E., Ragu Ramalingam, N., Lorito, S., Volpe, M., Sánchez-Linares, C., Løvholt, F., and Gibbons, S. J. (2024). Machine learning emulation of high resolution inundation maps. *Geophysical Journal International*, 238(1):382–399.

Brizzi, S., Becker, T. W., Faccenna, C., Behr, W., van Zelst, I., Dal Zilio, L., and van Dinther, Y. (2021). The role of sediment accretion and buoyancy on subduction dynamics and geometry. *Geophysical Research Letters*, 48(20):e2021GL096266. e2021GL096266 2021GL096266.

Brizzi, S., van Zelst, I., Funiciello, F., Corbi, F., and van Dinther, Y. (2020). How sediment thickness influences subduction dynamics and seismicity. *Journal of Geophysical Research: Solid Earth*, 125(8):e2019JB018964. e2019JB018964 10.1029/2019JB018964.

Bruhat, L., Fang, Z., and Dunham, E. M. (2016). Rupture complexity and the supershear transition on rough faults. *Journal of Geophysical Research: Solid Earth*, 121(1):210–224.

Byerlee, J. and Summers, R. (1976). A note on the effect of fault gouge thickness on fault stability. *International Journal of Rock Mechanics and Mining Sciences & Geomechanics Abstracts*, 13(1):35–36.

Byrne, D. E., Wang, W.-h., and Davies, D. M. (1993). Mechanical role of backstops in the growth of forearcs. *Tectonics*, 12(1):123–144.

Bürgmann, R., Kogan, M. G., Steblov, G. M., Hilley, G., Levin, V. E., and Apel, E. (2005). Interseismic coupling and asperity distribution along the Kamchatka subduction zone. *Journal of Geophysical Research: Solid Earth*, 110(B7).

Calahorrano B., A., Sallarès, V., Collot, J.-Y., Sage, F., and Ranero, C. R. (2008). Nonlinear variations of the physical properties along the southern ecuador subduction channel: Results from depth-migrated seismic data. *Earth and Planetary Science Letters*, 267(3):453–467.

Candela, T., Renard, F., Schmittbuhl, J., Bouchon, M., and Brodsky, E. E. (2011). Fault slip distribution and fault roughness. *Geophysical Journal International*, 187(2):959–968.

Casten, U. and Snopek, K. (2006). Gravity modelling of the Hellenic subduction zone—a regional study. *Tectonophysics*, 417(3):183–200.

Causse, M., Maufroy, E., André, L., and Bard, P. (2023). What Was the Level of Ground Motion across Europe during the Great A.D. 365 Crete Earthquake? *Seismological Research Letters*, 94(5):2397–2410.

Chan, Y. P. B., Yao, S., and Yang, H. (2023). Impact of Hypocenter Location on Rupture Extent and Ground Motion: A Case Study of Southern Cascadia. *Journal of Geophysical Research: Solid Earth*, 128(8):e2023JB026371.

Chapp, E., Taylor, B., Oakley, A., and Moore, G. F. (2008). A seismic stratigraphic analysis of Mariana forearc basin evolution. *Geochemistry, Geophysics, Geosystems*, 9(10).

Chen, K., Wei, G., Milliner, C., Dal Zilio, L., Liang, C., and Avouac, J.-P. (2024). Supershear ruptures steered by pre-stress heterogeneities during the 2023 Kahramanmaraş earthquake doublet. *Nature Communications*, 15(1):7004.

Chester, F. M., Mori, J. J., Toczko, S., Eguchi, N., Kido, Y., Saito, S., Sanada, Y., Anderson, L., Behrmann, J. H., Bose, S., et al. (2012). Integrated ocean drilling program expedition 343/343T preliminary report, Japan Trench Fast Drilling Project (JFAST), 1 April–24 May 2012 and 5–19 July 2012. *Integrated Ocean Drilling Project Preliminary Report*, 343.

Chorozoglou, D. and Papadimitriou, E. (2019). Monitoring earthquake network measures between main shocks in Greece. *Journal of Seismology*, 23:505–519.

Chousianitis, K. and Konca, A. O. (2019). Intraslab Deformation and Rupture of the Entire Subducting Crust During the 25 October 2018 Mw 6.8 Zakynthos Earthquake. *Geophysical Research Letters*, 46(24):14358–14367.

Chousianitis, K. and Konca, A. O. (2021). Rupture Process of the 2020 $M_W$7.0 Samos Earthquake and its Effect on Surrounding Active Faults. *Geophysical Research Letters*, 48(14):e2021GL094162.

Cifuentes, I. L. and Silver, P. G. (1989). Low-frequency source characteristics of the great 1960 Chilean earthquake. *Journal of Geophysical Research: Solid Earth*, 94(B1):643–663.

Cifuentes-Lobos, R., Calisto, I., MacInnes, B., Moreno, M., Quezada, J., San Martín, J., Fernández-Palma, M., and Saavedra, C. (2023). A stochastic approach to the characterization of the seismic sources: a potential method for the assessment of sources of historical and paleo tsunami. *Stochastic Environmental Research and Risk Assessment*, 37(7):2399–2411.

Cirella, A., Romano, F., Avallone, A., Piatanesi, A., Briole, P., Ganas, A., Theodoulidis, N., Chousianitis, K., Volpe, M., Bozionellos, G., Selvaggi, G., and Lorito, S. (2020). The 2018 Mw 6.8 Zakynthos (Ionian Sea, Greece) earthquake: seismic source and local tsunami characterization. *Geophysical Journal International*, 221(2):1043–1054.

Clawpack Development Team (2023). Clawpack v5.9.2.

Cloos, M. (1992). Thrust-type subduction-zone earthquakes and seamount asperities: A physical model for seismic rupture. *Geology*, 20(7):601–604.

Cloos, M. and Shreve, R. L. (1988). Subduction-channel model of prism accretion, melange formation, sediment subduction, and subduction erosion at convergent plate margins: 1. Background and description. *Pure and Applied Geophysics*, 128(3):455–500.

Coban, K. H. and Sayil, N. (2020). Conditional probabilities of Hellenic Arc Earthquakes based on different distribution models. *Pure and Applied Geophysics*, 177(11):5133–5145.

Cocco, M., Aretusini, S., Cornelio, C., Nielsen, S. B., Spagnuolo, E., Tinti, E., and Di Toro, G. (2023). Fracture energy and breakdown work during earthquakes. *Annual Review of Earth and Planetary Sciences*, 51(1):217–252.

Cocco, M., Tinti, E., and Cirella, A. (2016). On the scale dependence of earthquake stress drop. *Journal of Seismology*, 20:1151–1170.

Cockburn, B. and Shu, C.-W. (1998). The Runge–Kutta discontinuous Galerkin method for conservation laws V: multidimensional systems. *Journal of Computational Physics*, 141(2):199–224.

Collot, J.-Y., Agudelo, W., Ribodetti, A., and Marcaillou, B. (2008). Origin of a crustal splay fault and its relation to the seismogenic zone and underplating at the erosional north Ecuador–south Colombia oceanic margin. *Journal of Geophysical Research: Solid Earth*, 113(B12).

Conrad, C. P. and Lithgow-Bertelloni, C. (2002). How mantle slabs drive plate tectonics. *Science*, 298(5591):207–209.

Contreras-Reyes, E. and Carrizo, D. (2011). Control of high oceanic features and subduction channel on earthquake ruptures along the "chile–peru" subduction zone. *Physics of the Earth and Planetary Interiors*, 186(1):49–58.

Contreras-Reyes, E., Grevemeyer, I., Flueh, E. R., and Reichert, C. (2008). Upper lithospheric structure of the subduction zone offshore of southern Arauco peninsula, Chile, at ∼38°S. *Journal of Geophysical Research: Solid Earth*, 113(B7).

Cornell, C. A. (1968). Engineering seismic risk analysis. *Bulletin of the Seismological Society of America*, 58(5):1583–1606.

Crempien, J. G., Urrutia, A., Benavente, R., and Cienfuegos, R. (2020). Effects of earthquake spatial slip correlation on variability of tsunami potential energy and intensities. *Scientific reports*, 10(1):1–10.

Dal Zilio, L. and Gerya, T. (2022). Subduction earthquake cycles controlled by episodic fluid pressure cycling. *Lithos*, 426-427:106800.

Dalguer, L. A., Miyake, H., Day, S. M., and Kikura, K. (2008). Surface rupturing and buried dynamic-rupture models calibrated with statistical observations of past earthquakes. *Bulletin of the Seismological Society of America*, 98:1147–1161.

Das, S. and Aki, K. (1977). Fault plane with barriers: A versatile earthquake model. *Journal of Geophysical Research (1896-1977)*, 82(36):5658–5670.

Davies, G. and Griffin, J. (2019). Sensitivity of probabilistic tsunami hazard assessment to far-field earthquake slip complexity and rigidity depth-dependence: Case study of Australia. *Pure and Applied Geophysics*, pages 1–28.

Davies, G., Griffin, J., Løvholt, F., Glimsdal, S., Harbitz, C., Thio, H. K., Lorito, S., Basili, R., Selva, J., Geist, E., and Baptista, M. A. (2018). A global probabilistic tsunami hazard assessment from earthquake sources. *Geological Society Special Publication*, 456:219–244.

Davies, G., Weber, R., Wilson, K., and Cummins, P. (2022). From offshore to onshore probabilistic tsunami hazard assessment via efficient Monte Carlo sampling. *Geophysical Journal International*, 230(3):1630–1651.

Davies, G. F. and Richards, M. A. (1992). Mantle convection. *The Journal of Geology*, 100(2):151–206.

Day, S. M., Dalguer, L. A., Lapusta, N., and Liu, Y. (2005). Comparison of finite difference and boundary integral solutions to three-dimensional spontaneous rupture. *Journal of Geophysical Research: Solid Earth*, 110(B12):B12307.

de la Puente, J., Ampuero, J.-P., and Käser, M. (2009). Dynamic rupture modeling on unstructured meshes using a discontinuous Galerkin method. *Journal of Geophysical Research: Solid Earth*, 114(B10).

De Martini, P., Barbano, M., Smedile, A., Gerardi, F., Pantosti, D., Del Carlo, P., and Pirrotta, C. (2010). A unique 4000year long geological record of multiple tsunami inundations in the Augusta Bay (eastern Sicily, Italy). *Marine Geology*, 276(1):42–57.

DeDontney, N. and Rice, J. R. (2012). Tsunami wave analysis and possibility of splay fault rupture during the 2004 Indian Ocean earthquake. *Pure and applied geophysics*, 169:1707–1735.

Delouis, B., Nocquet, J.-M., and Vallée, M. (2010). Slip distribution of the February 27, 2010 Mw = 8.8 Maule Earthquake, central Chile, from static and high-rate GPS, InSAR, and broadband teleseismic data. *Geophysical Research Letters*, 37(17).

DeMets, C., Gordon, R. G., Argus, D., and Stein, S. (1990). Current plate motions. *Geophysical journal international*, 101(2):425–478.

DeMets, C., Gordon, R. G., Argus, D. F., and Stein, S. (1994). Effect of recent revisions to the geomagnetic reversal time scale on estimates of current plate motions. *Geophysical Research Letters*, 21(20):2191–2194.

Dias, F., Dutykh, D., O'Brien, L., Renzi, E., and Stefanakis, T. (2014). On the modelling of tsunami generation and tsunami inundation. *Procedia IUTAM*, 10:338–355.

Dieterich, J. H. (1979). Modeling of rock friction: 1. Experimental results and constitutive equations. *Journal of Geophysical Research: Solid Earth*, 84(B5):2161–2168.

DiVita, A. (1979). 80.'I terremoti a Gortina in et{à} romana e proto-bizantina'. *ASA*, pages 61–62.

DiVita, A. (1995). Arcaheologists and earthquakes, the case of the AD365 earthquake. *Ann Geophys*, 38:971–976.

Doglioni, C., Carminati, E., Cuffaro, M., and Scrocca, D. (2007). Subduction kinematics and dynamic constraints. *Earth-Science Reviews*, 83(3):125–175.

Dorozhinskii, R. and Bader, M. (2021). SeisSol on Distributed Multi-GPU Systems: CUDA Code Generation for the Modal Discontinuous Galerkin Method. In *The International Conference on High Performance Computing in Asia-Pacific Region*, pages 69–82.

Du, Y., Ma, S., Kubota, T., and Saito, T. (2021). Impulsive tsunami and large runup along the Sanriku coast of Japan produced by an inelastic wedge deformation model. *Journal of Geophysical Research: Solid Earth*, 126:e2021JB022098.

Dumbser, M. and Käser, M. (2006). An arbitrary high-order discontinuous Galerkin method for elastic waves on unstructured meshes — II. The three-dimensional isotropic case. *Geophysical Journal International*, 167(1):319–336.

Dunham, E. M. (2007). Conditions governing the occurrence of supershear ruptures under slip-weakening friction. *Journal of Geophysical Research: Solid Earth*, 112(B7).

Dunham, E. M. and Archuleta, R. J. (2005). Near-source ground motion from steady state dynamic rupture pulses. *Geophysical Research Letters*, 32(3).

Dunham, E. M., Belanger, D., Cong, L., and Kozdon, J. E. (2011a). Earthquake ruptures with strongly rate-weakening friction and off-fault plasticity, Part 1: Planar faults. *Bulletin of the Seismological Society of America*, 101(5):2296–2307.

Dunham, E. M., Belanger, D., Cong, L., and Kozdon, J. E. (2011b). Earthquake Ruptures with Strongly Rate-Weakening Friction and Off-Fault Plasticity, Part 2: Nonplanar Faults. *Bulletin of the Seismological Society of America*, 101(5):2308–2322.

Dziewonski, A. M. and Anderson, D. L. (1981). Preliminary reference Earth model. *Physics of the earth and planetary interiors*, 25(4):297–356.

Ebinger, C., Ayele, A., Keir, D., Rowland, J., Yirgu, G., Wright, T., Belachew, M., and Hamling, I. (2010). Length and timescales of rift faulting and magma intrusion: The Afar rifting cycle from 2005 to present. *Annual Review of Earth and Planetary Sciences*, 38(Volume 38, 2010):439–466.

El-Sayed, A., Romanelli, F., and Panza, G. (2000). Recent seismicity and realistic waveforms modeling to reduce the ambiguities about the 1303 seismic activity in Egypt. *Tectonophysics*, 328:341–357.

Elbanna, A., Abdelmeguid, M., Ma, X., Amlani, F., Bhat, H. S., Synolakis, C., and Rosakis, A. J. (2021). Anatomy of Strike-Slip Fault Tsunami Genesis. *Proceedings of the National Academy of Sciences of the United States of America*, 118(19):2025632118.

Elliott, J. and Freymueller, J. T. (2020). A block model of present-day kinematics of Alaska and western Canada. *Journal of Geophysical Research: Solid Earth*, 125(7):e2019JB018378.

England, P., Howell, A., Jackson, J., and Synolakis, C. (2015). Palaeotsunamis and tsunami hazards in the Eastern Mediterranean. *Philosophical Transactions of the Royal Society A: Mathematical, Physical and Engineering Sciences*, 373.

Festa, G., Zollo, A., and Lancieri, M. (2008). Earthquake magnitude estimation from early radiated energy. *Geophysical Research Letters*, 35(22):L22307.

Fialko, Y. (2006). Interseismic strain accumulation and the earthquake potential on the southern San Andreas fault system. *Nature*, 441(7096):968–971.

Ficini, E., Cuffaro, M., and Doglioni, C. (2020). Asymmetric dynamics at subduction zones derived from plate kinematic constraints. *Gondwana Research*, 78:110–125.

Fisher, M. A. (1979). Structure and tectonic setting of continental shelf southwest of Kodlak Island, Alaska1. *AAPG Bulletin*, 63(3):301–310.

Flemming, N. C. (1978). Holocene eustatic changes and coastal tectonics in the northeast Mediterranean: implications for models of crustal consumption. *Philosophical Transactions of the Royal Society of London. Series A, Mathematical and Physical Sciences*, 289:405–458.

Folch, A., Abril, C., Afanasiev, M., Amati, G., Bader, M., Badia, R. M., Bayraktar, H. B., Barsotti, S., Basili, R., Bernardi, F., Boehm, C., Brizuela, B., Brogi, F., Cabrera, E., Casarotti, E., Castro, M. J., Cerminara, M., Cirella, A., Cheptsov, A., Conejero, J., Costa, A., de la Asunción, M., de la Puente, J., Djuric, M., Dorozhinskii, R., Espinosa, G., Esposti-Ongaro, T., Farnós, J., Favretto-Cristini, N., Fichtner, A., Fournier, A., Gabriel, A.-A., Gallard, J.-M., Gibbons, S. J., Glimsdal, S., González-Vida, J. M., Gracia, J., Gregorio, R., Gutierrez, N., Halldorsson, B., Hamitou, O., Houzeaux, G., Jaure, S., Kessar, M., Krenz, L., Krischer, L., Laforet, S., Lanucara, P., Li, B., Lorenzino, M. C., Lorito, S., Løvholt, F., Macedonio, G., Macías, J., Marín, G., Martínez Montesinos, B., Mingari, L., Moguilny, G., Montellier, V., Monterrubio-Velasco, M., Moulard, G. E., Nagaso, M., Nazaria, M., Niethammer, C., Pardini, F., Pienkowska, M., Pizzimenti, L., Poiata, N., Rannabauer, L., Rojas, O., Rodriguez, J. E., Romano, F., Rudyy, O., Ruggiero, V., Samfass, P., Sánchez-Linares, C., Sanchez, S., Sandri, L., Scala, A., Schaeffer, N., Schuchart, J., Selva, J., Sergeant, A., Stallone, A., Taroni, M., Thrastarson, S., Titos, M., Tonelllo, N., Tonini, R., Ulrich, T., Vilotte, J.-P., Vöge, M., Volpe, M., Aniko Wirp, S., and Wössner, U. (2023). The EU Center of Excellence for Exascale in Solid Earth (ChEESE): Implementation, results, and roadmap for the second phase. *Future Generation Computer Systems*, 146:47–61.

Frohlich, C. and Wetzel, L. R. (2007). Comparison of seismic moment release rates along different types of plate boundaries. *Geophysical Journal International*, 171(2):909–920.

Fukao, Y. (1979). Tsunami earthquakes and subduction processes near deep-sea trenches. *Journal of Geophysical Research: Solid Earth*, 84(B5):2303–2314.

Fuller, C. W., Willett, S. D., and Brandon, M. T. (2006). Formation of forearc basins and their influence on subduction zone earthquakes. *Geology*, 34(2):65–68.

Gabriel, A.-A., Ampuero, J.-P., Dalguer, L. A., and Mai, P. M. (2012). The transition of dynamic rupture styles in elastic media under velocity-weakening friction. *Journal of Geophysical Research: Solid Earth*, 117(B9):B09311.

Gabriel, A.-A., Ampuero, J.-P., Dalguer, L. A., and Mai, P. M. (2013). Source properties of dynamic rupture pulses with off-fault plasticity. *Journal of Geophysical Research: Solid Earth*, 118(8):4117–4126.

Gabriel, A.-A., Garagash, D. I., Palgunadi, K. H., and Mai, P. M. (2024). Fault size–dependent fracture energy explains multiscale seismicity and cascading earthquakes. *Science*, 385(6707):eadj9587.

Gabriel, A.-A., Li, D., Chiocchetti, S., Tavelli, M., Peshkov, I., Romenski, E., and Dumbser, M. (2020). A unified first order hyperbolic model for nonlinear dynamic rupture processes in diffuse fracture zones. *arXiv preprint arXiv:2007.01026*.

Gailler, A., Charvis, P., and Flueh, E. R. (2007). Segmentation of the Nazca and South American plates along the Ecuador subduction zone from wide angle seismic profiles. *Earth and Planetary Science Letters*, 260(3):444–464.

Galanopoulos, A. G. (1960). Tsunamis observed on the coasts of Greece from antiquity to present time. *Annals of Geophysics*, 13(3-4):369–386.

Galis, M., Pelties, C., Kristek, J., Moczo, P., Ampuero, J.-P., and Mai, P. M. (2015). On the initiation of sustained slip-weakening ruptures by localized stresses. *Geophysical Journal International*, 200(2):890–909.

Gallovič, F. and Valentová, L. (2023). Broadband strong ground motion modeling using planar dynamic rupture with fractal parameters. *Journal of Geophysical Research: Solid Earth*, 128(6):e2023JB026506.

Gallovič, F. and Valentova, L. (2020). Earthquake stress drops from dynamic rupture simulations constrained by observed ground motions. *Geophysical Research Letters*, 47(4):e2019GL085880.

Galvez, P., Ampuero, J. P., Dalguer, L. A., Somala, S. N., and Nissen-Meyer, T. (2014). Dynamic earthquake rupture modelled with an unstructured 3-D spectral element method applied to the 2011 M9 Tohoku earthquake. *Geophysical Journal International*, 198(2):1222–1240.

Galvez, P., Dalguer, L. A., Ampuero, J. P., and Giardini, D. (2016). Rupture reactivation during the 2011 mw9.0 tohoku earthquake: Dynamic rupture and ground-motion simulations. *Bulletin of the Seismological Society of America*, 106:819–831.

Galvez, P., Somerville, P., Petukhin, A., Ampuero, J.-P., and Peter, D. (2019). Earthquake cycle modelling of multi-segmented faults: Dynamic rupture and ground motion

simulation of the 1992 Mw 7.3 Landers earthquake. *Pure and Applied Geophysics*, pages 1–17.

Ganas, A., Briole, P., Bozionelos, G., Barberopoulou, A., Elias, P., Tsironi, V., Valkaniotis, S., Moshou, A., and Mintourakis, I. (2020). The 25 October 2018 Mw = 6.7 Zakynthos earthquake (Ionian Sea, Greece): A low-angle fault model based on GNSS data, relocated seismicity, small tsunami and implications for the seismic hazard in the west Hellenic Arc. *Journal of Geodynamics*, 137:101731.

Ganas, A. and Parsons, T. (2009). Three-dimensional model of Hellenic Arc deformation and origin of the Cretan uplift. *Journal of Geophysical Research: Solid Earth*, 114:6404.

Geist, E. and Yoshioka, S. (1996). Source parameters controlling the generation and propagation of potential local tsunamis along the Cascadia margin. *Natural Hazards*, 13(2):151–177.

Geist, E. L. (2002). Complex earthquake rupture and local tsunamis. *Journal of Geophysical Research: Solid Earth*, 107(B5):ESE 2–1 – ESE 2–15.

Geist, E. L. and Lynett, P. J. (2014). Source processes for the probabilistic assessment of tsunami hazards. *Oceanography*, 27(2):86–93.

Geist, E. L. and Oglesby, D. D. (2014). *Tsunamis: Stochastic Models of Occurrence and Generation Mechanisms*, pages 1–29. Springer New York, New York, NY.

Gercek, H. (2007). Poisson's ratio values for rocks. *International Journal of Rock Mechanics and Mining Sciences*, 44(1):1–13.

Gibbons, S. J., Lorito, S., de la Asunción, M., Volpe, M., Selva, J., Macías, J., Sánchez-Linares, C., Brizuela, B., Vöge, M., Tonini, R., Lanucara, P., Glimsdal, S., Romano, F., Meyer, J. C., and Løvholt, F. (2022). The Sensitivity of Tsunami Impact to Earthquake Source Parameters and Manning Friction in High-Resolution Inundation Simulations. *Frontiers in Earth Science*, 9:1412.

Gibbons, S. J., Lorito, S., Macías, J., Løvholt, F., Selva, J., Volpe, M., Sánchez-Linares, C., Babeyko, A., Brizuela, B., Cirella, A., et al. (2020). Probabilistic tsunami hazard analysis: high performance computing for massive scale inundation simulations. *Frontiers in Earth Science*, 8:591549.

Giraldo, F. X. and Warburton, T. (2008). A high-order triangular discontinuous Galerkin oceanic shallow water model. *International Journal for Numerical Methods in Fluids*, 56(7):899–925.

Glimsdal, S., Løvholt, F., Harbitz, C. B., Romano, F., Lorito, S., Orefice, S., Brizuela, B., Selva, J., Hoechner, A., Volpe, M., et al. (2019). A new approximate method for quantifying tsunami maximum inundation height probability. *Pure and Applied Geophysics*, 176(7):3227–3246.

Goda, K. (2015). Effects of seabed surface rupture versus buried rupture on tsunami wave modeling: A case study for the 2011 Tohoku, Japan, earthquake. *Bulletin of the Seismological Society of America*, 105:2563–2571.

Goda, K., Mai, P., and at all., T. Y. (2014). Sensitivity of tsunami wave profiles and inundation simulations to earthquake slip and fault geometry for the 2011 Tohoku earthquake. *Earth Planet Sp*, 66(105):1–20.

Goldsworthy, M., Jackson, J., and Haines, J. (2002). The continuity of active fault systems in Greece. *Geophysical Journal International*, 148(3):596–618.

Gomez, B. and Kadri, U. (2021). Near real-time calculation of submarine fault properties using an inverse model of acoustic signals. *Applied Ocean Research*, 109:102557.

Gómez Zapata, J. C., Pittore, M., Cotton, F., Lilienkamp, H., Shinde, S., Aguirre, P., and Santa María, H. (2022). Epistemic uncertainty of probabilistic building exposure compositions in scenario-based earthquake loss models. *Bulletin of Earthquake Engineering*, 20(5):2401–2438.

González, F., Geist, E. L., Jaffe, B., Kânoğlu, U., Mofjeld, H., Synolakis, C., Titov, V. V., Arcas, D., Bellomo, D., Carlton, D., et al. (2009). Probabilistic tsunami hazard assessment at seaside, Oregon, for near-and far-field seismic sources. *Journal of Geophysical Research: Oceans*, 114(C11):C11023.

Gonzalez, F. I., LeVeque, R. J., Chamberlain, P., Hirai, B., Varkovitzky, J., and George, D. L. (2011). Validation of the GeoClaw model. *NTHMP MMS Tsunami Inundation Model Validation Workshop*, pages 1–84.

Granot, R. (2016). Palaeozoic oceanic crust preserved beneath the eastern Mediterranean. *Nature Geoscience*, 9:701–705.

Graves, R., Jordan, T. H., Callaghan, S., Deelman, E., Field, E., Juve, G., Kesselman, C., Maechling, P., Mehta, G., Milner, K., et al. (2011). CyberShake: A physics-based seismic hazard model for southern California. *Pure and Applied Geophysics*, 168:367–381.

Green, H. W. and Houston, H. (1995). The mechanics of deep earthquakes. *Annual Review Of Earth And Planetary Sciences, Volume 23, pp. 169-214.*, 23:169–214.

Grezio, A., Babeyko, A., Baptista, M. A., Behrens, J., Costa, A., Davies, G., Geist, E. L., Glimsdal, S., González, F. I., Griffin, J., et al. (2017). Probabilistic tsunami hazard analysis: Multiple sources and global applications. *Reviews of Geophysics*, 55(4):1158–1198.

Grezio, A., Laura, S., Warner, M., Andrea, A., Paolo, G., and Jacopo, S. (2012). Probabilistic tsunami hazard assessment for Messina Strait Area (Sicily, Italy). *Natural Hazards*, 64:329–358.

Griffith, W. A., Nielsen, S., Di Toro, G., and Smith, S. A. F. (2010). Rough faults, distributed weakening, and off-fault deformation. *Journal of Geophysical Research: Solid Earth*, 115(B8).

Group, G. C. (2019). GEBCO 2019 Grid.

Gu, Y., Zhang, Z., Wang, W., and Wang, Z. (2023). Dynamic rupture simulations based on interseismic locking models—taking the Suoerkuli section of the Altyn Tagh fault as an example. *Geophysical Journal International*, 234(3):1737–1751.

Guidoboni, E. and Comastri, A. (1997). The large earthquake of 8 August 1303 in Crete: seismic scenario and tsunami in the Mediterranean area. *Journal of Seismology 1997 1:1*, 1:55–72.

Guidoboni, E., Comastri, A., and nazionale di geofisica e vulcanologia (Italy), I. (2005). *Catalogue of earthquakes and tsunamis in the Mediterranean area from the 11th to the 15th century*. Istituto nazionale di geofisica e vulcanologia.

Guidoboni, E., Traina, G., and Comastri, A. (1994). Catalogue of ancient earthquakes in the Mediterranean sea up to the 10th century. *Ist. Naz. Geofis.*

Hamouda, A. (2006). Numerical computations of 1303 tsunamigenic propagation towards Alexandria, Egyptian Coast. *Journal of African Earth Sciences*, 44(1):37–44.

Hanks, T. C. and Cornell, C. A. (1994). Probabilistic seismic hazard analysis: A beginner's guide. In *Proceedings of the Fifth Symposium on Current Issues Related to Nuclear Power Plant Structures, Equipment and Piping*, volume 1, pages 1–1. North Carolina State University Raleigh.

Hardebeck, J. L. (2015). Stress orientations in subduction zones and the strength of subduction megathrust faults. *Science*, 349(6253):1213–1216.

Harris, R. A., Archuleta, R. J., and Day, S. M. (1991). Fault steps and the dynamic rupture process: 2-D numerical simulations of a spontaneously propagating shear fracture. *Geophysical Research Letters*, 18(5):893–896.

Harris, R. A., Barall, M., Aagaard, B., Ma, S., Roten, D., Olsen, K., Duan, B., Liu, D., Luo, B., Bai, K., Ampuero, J., Kaneko, Y., Gabriel, A., Duru, K., Ulrich, T., , S., Shi, Z., Dunham, E., Bydlon, S., Zhang, Z., Chen, X., Somala, S. N., Pelties, C., Tago, J., Cruz-Atienza, V. M., Kozdon, J., Daub, E., Aslam, K., Kase, Y., Withers, K., and Dalguer, L. (2018). A Suite of Exercises for Verifying Dynamic Earthquake Rupture Codes. *Seismological Research Letters*, 89(3):1146–1162.

Harris, R. A., Barall, M., Andrews, D. J., Duan, B., Ma, S., Dunham, E. M., Gabriel, A.-A., Kaneko, Y., Kase, Y., Aagaard, B. T., Oglesby, D. D., Ampuero, J.-P., Hanks, T. C., and Abrahamson, N. (2011). Verifying a Computational Method for Predicting Extreme Ground Motion. *Seismological Research Letters*, 82(5):638–644.

Harris, R. A. and Day, S. M. (1997). Effects of a low-velocity zone on a dynamic rupture. *Bulletin of the Seismological Society of America*, 87(5):1267–1280.

Harris, R. A. and Day, S. M. (2005). Material contrast does not predict earthquake rupture propagation direction. *Geophysical Research Letters*, 32(23):L23301.

Hayes, G. P., Moore, G. L., Portner, D. E., Hearne, M., Flamme, H., Furtney, M., and Smoczyk, G. M. (2018). Slab2, a comprehensive subduction zone geometry model. *Science*, 362(6410):58–61.

Heidbach, O., Rajabi, M., Cui, X., Fuchs, K., Müller, B., Reinecker, J., Reiter, K., Tingay, M., Wenzel, F., Xie, F., Ziegler, M. O., Zoback, M.-L., and Zoback, M. (2018). The World Stress Map database release 2016: Crustal stress pattern across scales. *Tectonophysics*, 744:484–498.

Heinecke, A., Breuer, A., Rettenberger, S., Bader, M., Gabriel, A., Pelties, C., Bode, A., Barth, W., Liao, X., Vaidyanathan, K., Smelyanskiy, M., and Dubey, P. (2014). Petascale high order dynamic rupture earthquake simulations on heterogeneous supercomputers. In *SC '14: Proceedings of the International Conference for High Performance Computing, Networking, Storage and Analysis*, pages 3–14.

Heki, K. (2011). A Tale of Two Earthquakes. *Science*, 332(6036):1390–1391.

Henneking, S., Venkat, S., Dobrev, V., Camier, J., Kolev, T., Fernando, M., Gabriel, A.-A., and Ghattas, O. (2025). Real-time Bayesian inference at extreme scale: A digital twin for tsunami early warning applied to the Cascadia subduction zone.

Herman, M. W., Furlong, K. P., and Govers, R. (2018). The accumulation of slip deficit in subduction zones in the absence of mechanical coupling: Implications for the behavior of megathrust earthquakes. *Journal of Geophysical Research: Solid Earth*, 123(9):8260–8278.

Heuret, A., Conrad, C. P., Funiciello, F., Lallemand, S., and Sandri, L. (2012). Relation between subduction megathrust earthquakes, trench sediment thickness and upper plate strain. *Geophysical Research Letters*, 39(5).

Hirano, S. (2019). Modeling of unilateral rupture along very long reverse faults. *Journal of Geophysical Research: Solid Earth*, 124(1):1057–1071.

Hok, S., Fukuyama, E., and Hashimoto, C. (2011). Dynamic rupture scenarios of anticipated Nankai-Tonankai earthquakes, southwest Japan. *J. Geophys. Res.*, 116(B12).

Holding, E. P. (2018). GoCad: A computer aided design program for geological applications.

Honal, C. and Rannabauer, L. (2020). Comparing the numerical results in [Vater S., N. Beisiegel, and J. Behrens, 2019] to results produced by the FLASH implementation in Samoa2.

Horspool, N., Pranantyo, I., Griffin, J., Latief, H., Natawidjaja, D., Kongko, W., Cipta, A., Bustaman, B., Anugrah, S., and Thio, H. (2014). A probabilistic tsunami hazard assessment for Indonesia. *Natural Hazards and Earth System Sciences*, 14(11):3105.

Huang, Y. and Ampuero, J.-P. (2011). Pulse-like ruptures induced by low-velocity fault zones. *Journal of Geophysical Research: Solid Earth*, 116(B12).

Iaffaldano, G. and Bunge, H.-P. (2009). Relating rapid plate-motion variations to plate-boundary forces in global coupled models of the mantle/lithosphere system: Effects of topography and friction. *Tectonophysics*, 474(1):393–404. TOPO-EUROPE: The Geoscience of coupled Deep Earth-surface processes.

Ida, Y. (1972). Cohesive force across the tip of a longitudinal-shear crack and Griffith's specific surface energy. *Journal of Geophysical Research*, 77(20):3796–3805.

Ide, S. and Aochi, H. (2005). Earthquakes as multiscale dynamic ruptures with heterogeneous fracture surface energy. *Journal of Geophysical Research: Solid Earth*, 110(B11).

Ide, S., Baltay, A., and Beroza, G. C. (2011). Shallow Dynamic Overshoot and Energetic Deep Rupture in the 2011 $M_w$ 9.0 Tohoku-Oki Earthquake. *Science*, 332(6036):1426–1429.

Ishii, M., Shearer, P. M., Houston, H., and Vidale, J. E. (2005). Extent, duration and speed of the 2004 Sumatra–Andaman earthquake imaged by the Hi-Net array. *Nature*, 435(7044):933–936.

Jackson, J. and Mckenzie, D. (1988). The relationship between plate motions and seismic moment tensors, and the rates of active deformation in the Mediterranean and Middle East. *Geophysical Journal*, 93:45–73.

Jamelot, A., Gailler, A., Heinrich, P., Vallage, A., and Champenois, J. (2019). Tsunami simulations of the Sulawesi Mw 7.5 event: Comparison of seismic sources issued from a tsunami warning context versus post-event finite source. *Pure and Applied Geophysics*, 176(8):3351–3376.

Jeandet Ribes, L., Thomas, M. Y., and Bhat, H. S. (2023). On the importance of setting 3-D stress field in simulations of on- and off-fault deformation. *Geophysical Journal International*, 235(3):2962–2978.

Ji, C., Wald, D. J., and Helmberger, D. V. (2002). Source description of the 1999 Hector Mine, California, earthquake, part I: Wavelet domain inversion theory and resolution analysis. *Bulletin of the Seismological Society of America*, 92(4):1192–1207.

Jia, Z., Shen, Z., Zhan, Z., Li, C., Peng, Z., and Gurnis, M. (2020). The 2018 Fiji Mw 8.2 and 7.9 deep earthquakes: One doublet in two slabs. *Earth and Planetary Science Letters*, 531:115997.

Jolivet, L., Faccenna, C., Huet, B., Labrousse, L., Le Pourhiet, L., Lacombe, O., Lecomte, E., Burov, E., Denèle, Y., Brun, J.-P., Philippon, M., Paul, A., Salaün, G., Karabulut, H., Piromallo, C., Monié, P., Gueydan, F., Okay, A. I., Oberhänsli, R., Pourteau, A., Augier, R., Gadenne, L., and Driussi, O. (2013). Aegean tectonics: Strain localisation, slab tearing and trench retreat. *Tectonophysics*, 597-598:1–33. The Aegean: a natural laboratory for tectonics - Neotectonics.

Jones, I. F., Bloor, R. I., Biondi, B. L., and Etgen, J. T. (2008). Prestack depth migration and velocity model building.

Jongsma, D. (1977). Bathymetry and shallow structure of the Pliny and Strabo Trenches, south of the Hellenic Arc. *GSA Bulletin*, 88(6):797–805.

Jourdon, A., Hayek, J. N., May, D. A., and Gabriel, A.-A. (2024). Coupling 3D geodynamics and dynamic earthquake rupture: fault geometry, rheology and stresses across timescales.

Kagan, Y. Y. and Jackson, D. D. (1991). Seismic Gap Hypothesis: Ten years after. *Journal of Geophysical Research: Solid Earth*, 96(B13):21419–21431.

Kahle, H.-G., Cocard, M., Peter, Y., Geiger, A., Reilinger, R., Barka, A., and Veis, G. (2000). GPS-derived strain rate field within the boundary zones of the Eurasian, African, and Arabian Plates. *JOURNAL OF GEOPHYSICAL RESEARCH*, 105:353–376.

Kajiura, K. (1963). The leading wave of a tsunami. *Bulletin of the Earthquake Research Institute, University of Tokyo*, 41(3):535–571.

Kame, N., Rice, J. R., and Dmowska, R. (2003). Effects of prestress state and rupture velocity on dynamic fault branching. *Journal of Geophysical Research: Solid Earth*, 108(B5):2265.

Kammer, D. S., McLaskey, G. C., Abercrombie, R. E., Ampuero, J.-P., Cattania, C., Cocco, M., Zilio, L. D., Dresen, G., Gabriel, A.-A., Ke, C.-Y., Marone, C., Selvadurai, P. A., and Tinti, E. (2024). Energy dissipation in earthquakes.

Kanamori, H. (1972). Mechanism of tsunami earthquakes. *Physics of the earth and planetary interiors*, 6(5):346–359.

Kanamori, H. (1994). Mechanics of earthquakes. *Annual Review Of Earth And Planetary Sciences, Volume 22, pp. 207-237.*, 22:207–237.

Kanamori, H. (2006). Lessons from the 2004 Sumatra–Andaman earthquake. *Philosophical Transactions of the Royal Society A: Mathematical, Physical and Engineering Sciences*, 364(1845):1927–1945.

Kanamori, H. and Brodsky, E. E. (2004). The physics of earthquakes. *Reports on Progress in Physics*, 67(8):1429.

Kanamori, H. and Kikuchi, M. (1993). The 1992 Nicaragua earthquake: a slow tsunami earthquake associated with subducted sediments. *Nature*, 361(6414):714–716.

Kaneko, Y., Avouac, J.-P., and Lapusta, N. (2010). Towards inferring earthquake patterns from geodetic observations of interseismic coupling. *Nature Geoscience*, 3(5):363–369.

Kaneko, Y. and Fialko, Y. (2011). Shallow slip deficit due to large strike-slip earthquakes in dynamic rupture simulations with elasto-plastic off-fault response. *Geophysical Journal International*, 186(3):1389–1403.

Kaneko, Y., Lapusta, N., and Ampuero, J.-P. (2008). Spectral element modeling of spontaneous earthquake rupture on rate and state faults: Effect of velocity-strengthening friction at shallow depths. *Journal of Geophysical Research: Solid Earth*, 113(B9):B09317.

Kaneko, Y. and Shearer, P. M. (2014). Seismic source spectra and estimated stress drop derived from cohesive-zone models of circular subshear rupture. *Geophysical Journal International*, 197(2):1002–1015.

Karakostas, V. G. and Papadimitriou, E. E. (2010). Fault complexity associated with the 14 August 2003 Mw 6.2 Lefkada, Greece, aftershock sequence. *Acta geophysica*, 58:838–854.

Ke, C.-Y., McLaskey, G. C., and Kammer, D. S. (2018). Rupture termination in laboratory-generated earthquakes. *Geophysical Research Letters*, 45(23):12,784–12,792.

Ke, C.-Y., McLaskey, G. C., and Kammer, D. S. (2022). Earthquake breakdown energy scaling despite constant fracture energy. *Nature communications*, 13(1):1005.

Kelly, G. (2004). Ammianus and the great tsunami*. *The Journal of Roman Studies*, 94:141–167.

Kennett, B., Gorbatov, A., and Kiser, E. (2011). Structural controls on the Mw 9.0 2011 Offshore-Tohoku earthquake. *Earth and Planetary Science Letters*, 310(3):462–467.

Kim, J., Pedersen, G. K., Løvholt, F., and LeVeque, R. J. (2017). A Boussinesq type extension of the GeoClaw model - a study of wave breaking phenomena applying dispersive long wave models. *Coastal Engineering*, 122:75–86.

Kim, Y.-S. and Sanderson, D. J. (2006). Structural similarity and variety at the tips in a wide range of strike–slip faults: a review. *Terra Nova*, 18(5):330–344.

Kiratzi, A. (2013). The January 2012 earthquake sequence in the Cretan Basin, south of the Hellenic Volcanic Arc: Focal mechanisms, rupture directivity and slip models. *Tectonophysics*, 586:160–172.

Kiratzi, A., Papazachos, C., Özacar, A., Pinar, A., Kkallas, C., and Sopaci, E. (2022). Characteristics of the 2020 Samos earthquake (Aegean Sea) using seismic data. *Bulletin of Earthquake Engineering*, 20:7713–7735.

Kiratzi, A. A. and Papazachos, C. B. (1995). Active deformation on the shallow part of the subducting lithospheric slab in the southern Aegean. *Journal of Geodynamics*, 19(1):65–78.

Kirkpatrick, J. D., Edwards, J. H., Verdecchia, A., Kluesner, J. W., Harrington, R. M., and Silver, E. A. (2020). Subduction megathrust heterogeneity characterized from 3D seismic data. *Nature Geoscience*, 13(5):369–374.

Kkallas, C., Papazachos, C. B., Scordilis, E. M., and Margaris, B. N. (2021). Active stress field of the Southern Aegean Sea subduction area from fault-plane solutions on the basis of different stress inversion approaches. *Journal of Geodynamics*, 143:101813.

Klinger, Y., Okubo, K., Vallage, A., Champenois, J., Delorme, A., Rougier, E., Lei, Z., Knight, E. E., Munjiza, A., Satriano, C., Baize, S., Langridge, R., and Bhat, H. S. (2018). Earthquake damage patterns resolve complex rupture processes. *Geophysical Research Letters*, 45(19):10,279–10,287.

Knighton, J. and Bastidas, L. A. (2015). A proposed probabilistic seismic tsunami hazard analysis methodology. *Natural Hazards*, 78:699–723.

Kopp, H. (2013). Invited review paper: The control of subduction zone structural complexity and geometry on margin segmentation and seismicity. *Tectonophysics*, 589:1–16.

Kopp, H., Flueh, E., Petersen, C., Weinrebe, W., Wittwer, A., and Scientists, M. (2006). The Java margin revisited: Evidence for subduction erosion off Java. *Earth and Planetary Science Letters*, 242(1):130–142.

Kopp, H., Klaeschen, D., Flueh, E. R., Bialas, J., and Reichert, C. (2002). Crustal structure of the Java margin from seismic wide-angle and multichannel reflection data. *Journal of Geophysical Research: Solid Earth*, 107(B2):ETG 1–1–ETG 1–24.

Kozdon, J. E. and Dunham, E. M. (2013). Rupture to the Trench: Dynamic Rupture Simulations of the 11 March 2011 Tohoku Earthquake. *Bulletin of the Seismological Society of America*, 103(2B):1275–1289.

Kozdon, J. E. and Dunham, E. M. (2014). Constraining shallow slip and tsunami excitation in megathrust ruptures using seismic and ocean acoustic waves recorded on ocean-bottom sensor networks. *Earth and Planetary Science Letters*, 396:56–65.

Krabbenhoeft, A., Weinrebe, R. W., Kopp, H., Flueh, E. R., Ladage, S., Papenberg, C., Planert, L., and Djajadihardja, Y. (2010). Bathymetry of the Indonesian Sunda margin-relating morphological features of the upper plate slopes to the location and extent of the seismogenic zone. *Natural Hazards and Earth System Sciences*, 10(9):1899–1911.

Kreemer, C. and Chamot-Rooke, N. (2004). Contemporary kinematics of the southern Aegean and the Mediterranean Ridge. *Geophysical Journal International*, 157(3):1377–1392.

Krenz, L., Uphoff, C., Ulrich, T., Gabriel, A. A., Abrahams, L. S., Dunham, E. M., and Bader, M. (2021). 3D Acoustic-Elastic Coupling with Gravity: The Dynamics of the 2018 Palu, Sulawesi Earthquake and Tsunami. *International Conference for High Performance Computing, Networking, Storage and Analysis, SC*. arXiv: 2107.06640 Publisher: IEEE Computer Society ISBN: 9781450384421.

Kutschera, F., Gabriel, A.-A., Wirp, S. A., Li, B., Ulrich, T., Abril, C., and Halldórsson, B. (2024a). Linked and fully coupled 3D earthquake dynamic rupture and tsunami modeling for the Húsavík–Flatey Fault Zone in North Iceland. *Solid Earth*, 15(2):251–280.

Kutschera, F., Jia, Z., Oryan, B., Wong, J. W. C., Fan, W., and Gabriel, A.-A. (2024b). The Multi-Segment Complexity of the 2024 Mw 7.5 Noto Peninsula Earthquake Governs Tsunami Generation. *Geophysical Research Letters*, 51(21):e2024GL109790.

Käser, M. and Dumbser, M. (2006). An arbitrary high-order discontinuous Galerkin method for elastic waves on unstructured meshes — I. The two-dimensional isotropic case with external source terms. *Geophysical Journal International*, 166(2):855–877.

Käser, M., Hermann, V., and Puente, J. d. l. (2008). Quantitative accuracy analysis of the discontinuous Galerkin method for seismic wave propagation. *Geophysical Journal International*, 173(3):990–999.

Laigle, M., Sachpazi, M., and Hirn, A. (2004). Variation of seismic coupling with slab detachment and upper plate structure along the western Hellenic subduction zone. *Tectonophysics*, 391:85–95.

Lallemand, S. and Lallemand, S. (1999). *La subduction océanique*, volume 1999. Gordon and Breach Science Publishers Netherland.

Lambert, V., Lapusta, N., and Faulkner, D. (2021). Scale dependence of earthquake rupture prestress in models with enhanced weakening: Implications for event statistics and inferences of fault stress. *Journal of Geophysical Research: Solid Earth*, 126(10):e2021JB021886.

Langer, S., Weatherley, D., Olsen-Kettle, L., and Finzi, Y. (2013). Stress heterogeneities in earthquake rupture experiments with material contrasts. *Journal of the Mechanics and Physics of Solids*, 61(3):742–761.

Lay, T., Ammon, C. J., Kanamori, H., Yamazaki, Y., Cheung, K. F., and Hutko, A. R. (2011). The 25 October 2010 Mentawai tsunami earthquake (Mw 7.8) and the tsunami hazard presented by shallow megathrust ruptures. *Geophysical Research Letters*, 38(6):L06302.

Lay, T., Kanamori, H., Ammon, C. J., Koper, K. D., Hutko, A. R., Ye, L., Yue, H., and Rushing, T. M. (2012). Depth-varying rupture properties of subduction zone megathrust faults. *Journal of Geophysical Research: Solid Earth*, 117.

Le Pichon, X. and Angelier, J. (1981). The Aegean Sea. *Philosophical Transactions of the Royal Society of London. Series A, Mathematical and Physical Sciences*, 300(1454):357–372.

LeVeque, R. J. and George, D. L. (2008). High-Resolution Finite Volume Methods for the Shallow Water Equations With Bathymetry and Dry States. *Advanced Numerical Models for Simulating Tsunami Waves and Runup*, pages 43–73. Publisher: World Scientific Publishing Co. ISBN: 9789812790910.

LeVeque, R. J., George, D. L., and Berger, M. J. (2011). Tsunami modelling with adaptively refined finite volume methods. *Acta Numerica*, 20:211–289. Publisher: Cambridge University Press.

Li, B., Gabriel, A.-A., Ulrich, T., Abril, C., and Halldorsson, B. (2023). Dynamic Rupture Models, Fault Interaction and Ground Motion Simulations for the Segmented Húsavík-Flatey Fault Zone, Northern Iceland. *Journal of Geophysical Research: Solid Earth*, 128(6):e2022JB025886.

Li, L., Switzer, A. D., Chan, C.-H., Wang, Y., Weiss, R., and Qiu, Q. (2016). How heterogeneous coseismic slip affects regional probabilistic tsunami hazard assessment: A case study in the South China Sea. *Journal of Geophysical Research: Solid Earth*, 121(8):6250–6272.

Liang, Q. and Marche, F. (2009). Numerical resolution of well-balanced shallow water equations with complex source terms. *Advances in water resources*, 32(6):873–884.

Lindsey, E. O., Mallick, R., Hubbard, J. A., Bradley, K. E., Almeida, R. V., Moore, J. D., Bürgmann, R., and Hill, E. M. (2021). Slip rate deficit and earthquake potential on shallow megathrusts. *Nature Geoscience*, 14:321–326.

Liu, H., Gurnis, M., Leng, W., Jia, Z., and Zhan, Z. (2021). Tonga slab morphology and stress variations controlled by a relic slab: Implications for deep earthquakes in the Tonga-Fiji region. *Geophysical Research Letters*, 48(7):e2020GL091331. e2020GL091331 2020GL091331.

Liu, X. and Zhao, D. (2014). Structural control on the nucleation of megathrust earthquakes in the Nankai subduction zone. *Geophysical Research Letters*, 41(23):8288–8293.

Lockner, D. A. and Beeler, N. M. (2002). 32 - rock failure and earthquakes. In Lee, W. H., Kanamori, H., Jennings, P. C., and Kisslinger, C., editors, *International Handbook of Earthquake and Engineering Seismology, Part A*, volume 81 of *International Geophysics*, pages 505–537. Academic Press.

Lorito, S., Behrens, J., Løvholt, F., Rossetto, T., and Selva, J. (2021). Editorial: From tsunami science to hazard and risk assessment: Methods and models. *Frontiers in Earth Science*, Volume 9 - 2021.

Lorito, S., Romano, F., Atzori, S., Tong, X., Avallone, A., McCloskey, J., Cocco, M., Boschi, E., and Piatanesi, A. (2011). Limited overlap between the seismic gap and coseismic slip of the great 2010 Chile earthquake. *Nature Geoscience*, 4(3):173–177.

Lorito, S., Romano, F., and Lay, T. (2016). Tsunamigenic major and great earthquakes (2004–2013): Source processes inverted from seismic, geodetic, and sea-level data. *Encyclopedia of complexity and systems science, Springer, New York, ISBN*, 13:978–0.

Lorito, S., Selva, J., Basili, R., Romano, F., Tiberti, M. M., and Piatanesi, A. (2015). Probabilistic hazard for seismically induced tsunamis: accuracy and feasibility of inundation maps. *Geophysical Journal International*, 200:574–588.

Lorito, S., Tiberti, M. M., Basili, R., Piatanesi, A., and Valensise, G. (2008). Earthquake-generated tsunamis in the Mediterranean Sea: Scenarios of potential threats to Southern Italy. *Journal of Geophysical Research: Solid Earth*, 113.

Lotto, G. C. and Dunham, E. M. (2015). High-order finite difference modeling of tsunami generation in a compressible ocean from offshore earthquakes. *Computational Geosciences*, 19(2):327–340. Publisher: Springer.

Lotto, G. C., Dunham, E. M., Jeppson, T. N., and Tobin, H. J. (2017a). The effect of compliant prisms on subduction zone earthquakes and tsunamis. *Earth and Planetary Science Letters*, 458:213–222.

Lotto, G. C., Jeppson, T. N., and Dunham, E. M. (2018). Fully Coupled Simulations of Megathrust Earthquakes and Tsunamis in the Japan Trench, Nankai Trough, and Cascadia Subduction Zone. *Pure and Applied Geophysics*, 176(9):4009–4041. Publisher: Birkhauser Verlag AG.

Lotto, G. C., Jeppson, T. N., and Dunham, E. M. (2019). Fully coupled simulations of megathrust earthquakes and tsunamis in the Japan Trench, Nankai Trough, and Cascadia Subduction Zone. *Pure and Applied Geophysics*, 176:4009–4041.

Lotto, G. C., Nava, G., and Dunham, E. M. (2017b). Should tsunami simulations include a nonzero initial horizontal velocity? *Earth, Planets and Space*, 69(1):1–14.

Loveless, J. P. and Meade, B. J. (2011). Spatial correlation of interseismic coupling and coseismic rupture extent of the 2011 MW = 9.0 Tohoku-oki earthquake. *Geophysical Research Letters*, 38(17).

Løvholt, F., Kaiser, G., Glimsdal, S., Scheele, L., Harbitz, C. B., and Pedersen, G. (2012). Modeling propagation and inundation of the 11 March 2011 Tohoku tsunami. *Natural Hazards and Earth System Sciences*, 12(4):1017–1028.

Lund, B. and Townend, J. (2007). Calculating horizontal stress orientations with full or partial knowledge of the tectonic stress tensor. *Geophysical Journal International*, 170(3):1328–1335.

Luo, Y. and Liu, Z. (2021). Fault zone heterogeneities explain depth-dependent pattern and evolution of slow earthquakes in Cascadia. *Nature Communications*, 12(1):1959.

Ma, S. (2008). A physical model for widespread near-surface and fault zone damage induced by earthquakes. *Geochemistry, Geophysics, Geosystems*, 9(11).

Ma, S. (2022). Dynamic off-fault failure and tsunamigenesis at strike-slip restraining bends: Fully-coupled models of dynamic rupture, ocean acoustic waves, and tsunami in a shallow bay. *Tectonophysics*, 838:229496. Publisher: Elsevier.

Ma, S. and Andrews, D. J. (2010). Inelastic off-fault response and three-dimensional dynamics of earthquake rupture on a strike-slip fault. *Journal of Geophysical Research: Solid Earth*, 115(B4).

Ma, S. and Beroza, G. C. (2008). Rupture dynamics on a bimaterial interface for dipping faults. *Bulletin of the Seismological Society of America*, 98(4):1642–1658.

Ma, S. and Hirakawa, E. T. (2013). Dynamic wedge failure reveals anomalous energy radiation of shallow subduction earthquakes. *Earth and Planetary Science Letters*, 375:113–122.

Ma, S. and Nie, S. (2019). Dynamic Wedge Failure and Along-Arc Variations of Tsunamigenesis in the Japan Trench Margin. *Geophysical Research Letters*, 46(15):8782–8790.

Macías, J., Castro, M. J., Ortega, S., Escalante, C., and González-Vida, J. M. (2017). Performance benchmarking of tsunami-HySEA model for NTHMP's inundation mapping activities. *Pure and Applied Geophysics*, 174:3147–3183.

MacInnes, B. T., Gusman, A. R., LeVeque, R. J., and Tanioka, Y. (2013). Comparison of earthquake source models for the 2011 Tohoku event using tsunami simulations and near-field observations. *Bulletin of the Seismological Society of America*, 103(2B):1256–1274.

Madariaga, R., Olsen, K., and Archuleta, R. (1998). Modeling dynamic rupture in a 3d earthquake fault model. *Bulletin of the Seismological Society of America*, 88(5):1182–1197.

Madden, E. H., Bader, M., Behrens, J., Dinther, Y. V., Gabriel, A. A., Rannabauer, L., Ulrich, T., Uphoff, C., Vater, S., and Zelst, I. V. (2020). Linked 3-D modelling of megathrust earthquake-tsunami events: From subduction to tsunami run up. *Geophysical Journal International*, 224:487–516.

Madden, E. H., Ulrich, T., and Gabriel, A.-A. (2022). The state of pore fluid pressure and 3-D megathrust earthquake dynamics. *Journal of Geophysical Research: Solid Earth*, 127(4):e2021JB023382.

Maechling, P., Deelman, E., Zhao, L., Graves, R., Mehta, G., Gupta, N., Mehringer, J., Kesselman, C., Callaghan, S., Okaya, D., Francoeur, H., Gupta, V., Cui, Y., Vahi, K., Jordan, T., and Field, E. (2007). *SCEC CyberShake Workflows—Automating Probabilistic Seismic Hazard Analysis Calculations*, pages 143–163. Springer London, London.

Maeda, T., Furumura, T., Noguchi, S., Takemura, S., Sakai, S., Shinohara, M., Iwai, K., and Lee, S.-J. (2013). Seismic- and Tsunami-Wave Propagation of the 2011 Off the Pacific Coast of Tohoku Earthquake as Inferred from the Tsunami-Coupled Finite-Difference Simulation. *Bulletin of the Seismological Society of America*, 103(2B):1456–1472.

Mai, P. M., Schorlemmer, D., Page, M., Ampuero, J. P., Asano, K., Causse, M., Custodio, S., Fan, W., Festa, G., Galis, M., Gallovic, F., Imperatori, W., Käser, M., Malytskyy, D., Okuwaki, R., Pollitz, F., Passone, L., Razafindrakoto, H. N., Sekiguchi, H., Song, S. G., Somala, S. N., Thingbaijam, K. K., Twardzik, C., Van Driel, M., Vyas, J. C., Wang, R., Yagi, Y., and Zielke, O. (2016). The earthquake-source inversion Validation (SIV) project. *Seismological Research Letters*, 87:690–708.

Mai, P. M., Spudich, P., and Boatwright, J. (2005). Hypocenter locations in finite-source rupture models. *Bulletin of the Seismological Society of America*, 95(3):965–980.

Mai, P. M. and Thingbaijam, K. K. (2014). SRCMOD: An online database of finite-fault rupture models. *Seismological Research Letters*, 85(6):1348–1357.

Marafi, N. A., Eberhard, M. O., Berman, J. W., Wirth, E. A., and Frankel, A. D. (2019). Impacts of Simulated M9 Cascadia Subduction Zone Motions on Idealized Systems. *Earthquake Spectra*, 35(3):1261–1287.

Maravelis, A., Pantopoulos, G., Tserolas, P., and Zelilidis, A. (2015). Accretionary prism–forearc interactions as reflected in the sedimentary fill of southern Thrace Basin (Lemnos Island, NE Greece). *International Journal of Earth Sciences*, 104:1039–1060.

Markoulaki, S. (1987). Hospital excavations at Kissamos. *Archaelogikon Deltion*, Ser. B2:558–563.

Marzocchi, W., Taroni, M., and Selva, J. (2015). Accounting for Epistemic Uncertainty in PSHA: Logic Tree and Ensemble Modeling. *Bulletin of the Seismological Society of America*, 105(4):2151–2159.

McCaffrey, R. (1997a). Influences of recurrence times and fault zone temperatures on the age-rate dependence of subduction zone seismicity. *Journal of Geophysical Research: Solid Earth*, 102(B10):22839–22854.

McCaffrey, R. (1997b). Statistical significance of the seismic coupling coefficient. *Bulletin of the Seismological Society of America*, 87(4):1069–1073.

McCann, W. R., Nishenko, S. P., Sykes, L. R., and Krause, J. (1979). *Seismic Gaps and Plate Tectonics: Seismic Potential for Major Boundaries*, pages 1082–1147. Birkhäuser Basel, Basel. Wyss, Max.

McCloskey, J., Antonioli, A., Piatanesi, A., Sieh, K., Steacy, S., Nalbant, S., Cocco, M., Giunchi, C., Huang, J. D., and Dunlop, P. (2008). Tsunami threat in the Indian Ocean from a future megathrust earthquake west of Sumatra. *Earth and Planetary Science Letters*, 265:61–81.

McClusky, S., Balassanian, S., Barka, A., Demir, C., Ergintav, S., Georgiev, I., Gurkan, O., Hamburger, M., Hurst, K., Kahle, H., Kastens, K., Kekelidze, G., King, R., Kotzev, V., Lenk, O., Mahmoud, S., Mishin, A., Nadariya, M., Ouzounis, A., Paradissis, D., Peter, Y., Prilepin, M., Reilinger, R., Sanli, I., Seeger, H., Tealeb, A., Toksöz, M. N., and Veis, G. (2000). Global Positioning System constraints on plate kinematics and dynamics in the eastern Mediterranean and Caucasus. *Journal of Geophysical Research: Solid Earth*, 105:5695–5719.

McClusky, S., Reilinger, R., Mahmoud, S., Ben Sari, D., and Tealeb, A. (2003). GPS constraints on Africa (Nubia) and Arabia plate motions. *Geophysical Journal International*, 155(1):126–138.

McGuire, J. J., Zhao, L., and Jordan, T. H. (2002). Predominance of unilateral rupture for a global catalog of large earthquakes. *Bulletin of the Seismological Society of America*, 92(8):3309–3317.

McIntosh, K. D., Silver, E. A., Ahmed, I., Berhorst, A., Ranero, C. R., Kelly, R. K., and Flueh, E. R. (2007). *9. The Nicaragua Convergent Margin: Seismic Reflection Imaging of the Source of a Tsunami Earthquake*, pages 257–287. Columbia University Press, New York Chichester, West Sussex. Timothy H Dixon and Casey Moore.

McKenzie, D. (1972). Active Tectonics of the Mediterranean Region. *Geophysical Journal International*, 30(2):109–185.

McKenzie, D. (1978). Active tectonics of the Alpine—Himalayan belt: the Aegean Sea and surrounding regions. *Geophysical Journal International*, 55(1):217–254. Publisher: Oxford Academic.

McNally, K. C. (1983). Seismic gaps in space and time. *Annual Review of Earth and Planetary Sciences, Vol. 11, p. 359*, 11:359.

McNeill, L. C., Goldfinger, C., Kulm, L. D., and Yeats, R. S. (2000). Tectonics of the Neogene Cascadia forearc basin: Investigations of a deformed late Miocene unconformity. *GSA Bulletin*, 112(8):1209–1224.

Mei, C. C. and Kadri, U. (2017). Sound signals of tsunamis from a slender fault. *Journal of Fluid Mechanics*, 836:352–373.

Meier, M.-A., Heaton, T., and Clinton, J. (2016). Evidence for universal earthquake rupture initiation behavior. *Geophysical Research Letters*, 43(15):7991–7996.

Meister, O., Rahnema, K., and Bader, M. (2016). Parallel memory-efficient adaptive mesh refinement on structured triangular meshes with billions of grid cells. *ACM Transactions on Mathematical Software (TOMS)*, 43(3):1–27.

Melgar, D. (2025). Consideration of rupture kinematics increases tsunami amplitudes in far-field hazards assessments.

Melgar, D. and Bock, Y. (2013). Near-field tsunami models with rapid earthquake source inversions from land- and ocean-based observations: The potential for forecast and warning. *Journal of Geophysical Research: Solid Earth*, 118(11):5939–5955.

Melgar, D., Williamson, A. L., and Salazar-Monroy, E. F. (2019). Differences between heterogenous and homogenous slip in regional tsunami hazards modelling. *Geophysical Journal International*, 219(1):553–562.

Melnick, D., Moreno, M., Motagh, M., Cisternas, M., and Wesson, R. L. (2012). Splay fault slip during the Mw 8.8 2010 Maule Chile earthquake. *Geology*, 40(3):251–254.

Meng, J., Sinoplu, O., Zhou, Z., Tokay, B., Kusky, T., Bozkurt, E., and Wang, L. (2021). Greece and Turkey shaken by African tectonic retreat. *Scientific Reports*, 11(1):6486.

Meng, L., Inbal, A., and Ampuero, J.-P. (2011). A window into the complexity of the dynamic rupture of the 2011 Mw 9 Tohoku-Oki earthquake. *Geophysical Research Letters*, 38(7):L00G07.

Meng, X., Goulet, C., Milner, K., Graves, R., and Callaghan, S. (2023). Comparison of Nonergodic Ground-Motion Components from CyberShake and NGA-West2 Datasets in California. *Bulletin of the Seismological Society of America*, 113(3):1152–1175.

Miyatake, T. (1992). Dynamic rupture processes of inland earthquakes in Japan weak and strong asperities. *Geophysical research letters*, 19(10):1041–1044.

Mochizuki, K., Yamada, T., Shinohara, M., Yamanaka, Y., and Kanazawa, T. (2008). Weak Interplate Coupling by Seamounts and Repeating M 7 Earthquakes. *Science*, 321(5893):1194–1197.

Mohammad, H. and Riadi, G. A. (2021). Source modeling and spectral analysis of the Crete tsunami of 2nd May 2020 along the Hellenic Subduction Zone, offshore Greece. *Earth, Planets and Space (Online)*, 73(1).

Molina-Ormazabal, D., Ampuero, J.-P., and Tassara, A. (2023). Diverse slip behaviour of velocity-weakening fault barriers. *Nature Geoscience*, 16(12):1200–1207.

Moore, J. C. and Silver, E. A. (1987). Continental margin tectonics: Submarine accretionary prisms. *Reviews of Geophysics*, 25(6):1305–1312.

Moreno, M., Melnick, D., Rosenau, M., Baez, J., Klotz, J., Oncken, O., Tassara, A., Chen, J., Bataille, K., Bevis, M., Socquet, A., Bolte, J., Vigny, C., Brooks, B., Ryder, I., Grund, V., Smalley, B., Carrizo, D., Bartsch, M., and Hase, H. (2012). Toward understanding tectonic control on the Mw 8.8 2010 Maule Chile earthquake. *Earth and Planetary Science Letters*, 321-322:152–165.

Moreno, M., Rosenau, M., and Oncken, O. (2010). 2010 Maule earthquake slip correlates with pre-seismic locking of Andean subduction zone. *Nature*, 467(7312):198–202.

Mori, N., Goda, K., and Cox, D. (2018). Recent process in probabilistic tsunami hazard analysis (PTHA) for mega thrust subduction earthquakes. In *The 2011 Japan Earthquake and Tsunami: Reconstruction and Restoration*, pages 469–485. Springer.

Mori, N., Mai, P. M., Goda, K., and Yasuda, T. (2017). Tsunami inundation variability from stochastic rupture scenarios: Application to multiple inversions of the 2011 Tohoku, Japan earthquake. *Coastal Engineering*, 127:88–105.

Moschetti, M. P., Aagaard, B. T., Ahdi, S. K., Altekruse, J., Boyd, O. S., Frankel, A. D., Herrick, J., Petersen, M. D., Powers, P. M., Rezaeian, S., Shumway, A. M., Smith, J. A., Stephenson, W. J., Thompson, E. M., and Withers, K. B. (2023). The 2023 US National Seismic Hazard Model: Ground-motion characterization for the conterminous United States. *Earthquake Spectra*, page 87552930231223995.

Mulargia, F. (2019). Earthquake occurrence, recurrence, and hazard. In *Mechanics of Earthquake Faulting*, volume 202, pages 211–226. IOS Press.

Murotani, S., Miyake, H., and Koketsu, K. (2008). Scaling of characterized slip models for plate-boundary earthquakes. *Earth, Planets and Space*, 60:987–991.

Murphy, S., Scala, A., Herrero, A., Lorito, S., Festa, G., Trasatti, E., Tonini, R., Romano, F., Molinari, I., and Nielsen, S. (2016). Shallow slip amplification and enhanced tsunami hazard unravelled by dynamic simulations of mega-thrust earthquakes. *Scientific reports*, 6(1):1–12.

Murphy, S., Toro, G. D., Romano, F., Scala, A., Lorito, S., Spagnuolo, E., Aretusini, S., Festa, G., Piatanesi, A., and Nielsen, S. (2018). Tsunamigenic earthquake simulations

using experimentally derived friction laws. *Earth and Planetary Science Letters*, 486:155–165.

Müller, R. D., Sdrolias, M., Gaina, C., and Roest, W. R. (2008). Age, spreading rates, and spreading asymmetry of the world's ocean crust. *Geochemistry, Geophysics, Geosystems*, 9(4).

Nakano, M., Murphy, S., Agata, R., Igarashi, Y., Okada, M., and Hori, T. (2020). Self-similar stochastic slip distributions on a non-planar fault for tsunami scenarios for megathrust earthquakes. *Progress in Earth and Planetary Science*, 7(1):1–13.

Necmioğlu, O. and Özel, N. M. (2014). An earthquake source sensitivity analysis for tsunami propagation in the Eastern Mediterranean. *Oceanography*, 27:76–85.

Nielsen, S. B. (1998). Free surface effects on the propagation of dynamic rupture. *Geophysical Research Letters*, 25:125–128.

Niu, X., Zhao, D., Isozaki, Y., Nishizono, Y., and Inakura, H. (2020). Structural heterogeneity and megathrust earthquakes in Southwest Japan. *Physics of the Earth and Planetary Interiors*, 298:106347.

Noda, A., Saito, T., Fukuyama, E., and Urata, Y. (2021). Energy-based scenarios for great thrust-type earthquakes in the Nankai trough subduction zone, southwest Japan, using an interseismic slip-deficit model. *Journal of Geophysical Research: Solid Earth*, 126(5):e2020JB020417.

Noguchi, S., Maeda, T., and Furumura, T. (2013). FDM Simulation of an Anomalous Later Phase from the Japan Trench Subduction Zone Earthquakes. *Pure and Applied Geophysics*, 170(1-2):95–108. Publisher: Birkhauser Verlag AG.

Nyst, M. and Thatcher, W. (2004). New constraints on the active tectonic deformation of the Aegean. *Journal of Geophysical Research: Solid Earth*, 109(B11).

Oeser, J., Bunge, H.-P., and Mohr, M. (2006). Cluster Design in the Earth Sciences Tethys. In Gerndt, M. and Kranzlmüller, D., editors, *High Performance Computing and Communications*, pages 31–40, Berlin, Heidelberg. Springer.

Oglesby, D. D., Archuleta, R. J., and Nielsen, S. B. (2000). The three-dimensional dynamics of dipping faults. *Bulletin of the Seismological Society of America*, 90(3):616–628.

Ohnaka, M. (2004). Rupture in the laboratory. *Science*, 303(5665):1788–1789.

Okada, Y. (1985). Surface deformation due to shear and tensile faults in a half-space. *Bulletin of the Seismological Society of America*, 75(4):1135–1154.

Okal, E. A., Synolakis, C. E., Uslu, B., Kalligeris, N., and Voukouvalas, E. (2009). The 1956 earthquake and tsunami in Amorgos, Greece. *Geophysical Journal International*, 178(3):1533–1554. Publisher: Oxford Academic.

Oleskevich, D. A., Hyndman, R. D., and Wang, K. (1999). The updip and downdip limits to great subduction earthquakes: Thermal and structural models of Cascadia, south Alaska, SW Japan, and Chile. *Journal of Geophysical Research: Solid Earth*, 104(B7):14965–14991.

Oliver, J. and Major, M. (1960). Leaking modes and the PL phase. *Bulletin of the Seismological Society of America*, 50(2):165–180.

Olsen, K. M., Bangs, N. L., Tréhu, A. M., Han, S., Arnulf, A., and Contreras Reyes, E. (2020). Thick, strong sediment subduction along south-central Chile anditsrole ingreat earthquakes. *Earth and Planetary Science Letters*, 538.

Omira, R., Ramalho, R. S., Kim, J., González, P. J., Kadri, U., Miranda, J. M., Carrilho, F., and Baptista, M. A. (2022). Global Tonga tsunami explained by a fast-moving atmospheric source. *Nature*, 609(7928):734–740.

Oral, E., Ampuero, J. P., Ruiz, J., and Asimaki, D. (2022). A Method to Generate Initial Fault Stresses for Physics-Based Ground-Motion Prediction Consistent with Regional Seismicity. *Bulletin of the Seismological Society of America*, 112(6):2812–2827.

Ott, R. F., Wegmann, K. W., Gallen, S. F., Pazzaglia, F. J., Brandon, M. T., Ueda, K., and Fassoulas, C. (2021). Reassessing eastern Mediterranean tectonics and earthquake hazard from the 365 CE earthquake. *AGU Advances*, 2:e2020AV000315.

Ozer, C., Gok, E., and Polat, O. (2018). Three-Dimensional Seismic Velocity Structure of the Aegean Region of Turkey from Local Earthquake Tomography. *Annals of Geophysics*, 61(1):SE111. Publisher: Editrice Compositori s.r.l.

Pacheco, J. F. and Sykes, L. R. (1992). Seismic moment catalog of large shallow earthquakes, 1900 to 1989. *Bulletin of the Seismological Society of America*, 82(3):1306–1349.

Pacheco, J. F., Sykes, L. R., and Scholz, C. H. (1993). Nature of seismic coupling along simple plate boundaries of the subduction type. *Journal of Geophysical Research: Solid Earth*, 98(B8):14133–14159.

Palgunadi, K. H., Gabriel, A.-A., Ulrich, T., López-Comino, J. Á., and Mai, P. M. (2020). Dynamic Fault Interaction during a Fluid-Injection-Induced Earthquake: The 2017 $M_W$ 5.5 Pohang Event. *Bulletin of the Seismological Society of America*, 110(5):2328–2349.

Panzera, F., Zechar, J. D., Vogfjörd, K. S., and Eberhard, D. A. (2016). A revised earthquake catalogue for South Iceland. *Pure and Applied Geophysics*, 173:97–116.

Papadimitriou, E., Karakostas, V., Mesimeri, M., and Vallianatos, F. (2016). The Mw6.7 12 October 2013 western Hellenic Arc main shock and its aftershock sequence: implications for the slab properties. *International Journal of Earth Sciences*, 105:2149–2160.

Papadimitriou, E. E. and Karakostas, V. G. (2008). Rupture model of the great AD 365 Crete earthquake in the southwestern part of the Hellenic Arc. *Acta Geophysica*, 56:293–312.

Papadopoulos, G. and Chalkis, B. (1984). Tsunamis observed in greece and the surrounding area from antiquity up to the present times. *Marine Geology*, 56(1-4):309–317.

Papadopoulos, G., Minoura, K., Imamura, F., Kuran, U., Yalçiner, A., Fokaefs, A., and Takahashi, T. (2012). Geological evidence of tsunamis and earthquakes at the Eastern Hellenic Arc: correlation with historical seismicity in the eastern Mediterranean Sea. *Research in Geophysics*, 2:12.

Papadopoulos, G. A., Agalos, A., Minadakis, G., Triantafyllou, I., and Krassakis, P. (2020a). Short-term foreshocks as key information for mainshock timing and rupture: The Mw6.8 25 October 2018 Zakynthos earthquake, Hellenic Subduction Zone. *Sensors*, 20(19).

Papadopoulos, G. A., Daskalaki, E., Fokaefs, A., and Giraleas, N. (2010). Tsunami hazard in the eastern Mediterranean sea: Strong earthquakes and tsunamis in the west Hellenic Arc and trench system. *Journal of Earthquake and Tsunami*, 04(03):145–179.

Papadopoulos, G. A., Karastathis, V. K., Koukouvelas, I., Sachpazi, M., Baskoutas, I., Chouliaras, G., Agalos, A., Daskalaki, E., Minadakis, G., Moshou, A., Mouzakiotis, A., Orfanogiannaki, K., Papageorgiou, A., Spanos, D., and Triantafyllou, I. (2014). The Cephalonia, Ionian Sea (Greece), sequence of strong earthquakes of January-February 2014: a first report. *Research in Geophysics*, 4(1).

Papadopoulos, G. A. and Kijko, A. (1991). Maximum likelihood estimation of earthquake hazard parameters in the Aegean area from mixed data. *Tectonophysics*, 185(3):277–294.

Papadopoulos, G. A., Lekkas, E., Katsetsiadou, K.-N., Rovythakis, E., and Yahav, A. (2020b). Tsunami alert efficiency in the Eastern Mediterranean Sea: The 2 May 2020 Earthquake (Mw6.6) and near-field tsunami south of Crete (Greece). *GeoHazards*, 1(1):44–60.

Papadopoulos, N. and Chatziathanasiou, S. (2011). ERT pollution monitoring in areas of olive oil mills' wastes (OOMW): Preliminary results from a disposal site in Crete (Greece). *Berichte Geol. B.-A*, 93:193–197.

Papazachos, B. and Papazachou, C. (2003). The earthquakes of Greece, Ziti Publ. *Co., Thessaloniki, Greece*.

Papazachos, B. C., Karakostas, V. G., Papazachos, C. B., and Scordilis, E. M. (2000). The geometry of the Wadati–Benioff zone and lithospheric kinematics in the Hellenic arc. *Tectonophysics*, 319:275–300.

Papazachos, B. C., Papaioannou, C. A., Papazachos, C. B., and Savvaidis, A. S. (1999). Rupture zones in the Aegean region. *Tectonophysics*, 308:205–221.

Papazachos, C. and Nolet, G. (1997). P and S deep velocity structure of the Hellenic area obtained by robust nonlinear inversion of travel times. *Journal of Geophysical Research: Solid Earth*, 102:8349–8367.

Papazachos, C. B. and Kiratzi, A. A. (1996). A detailed study of the active crustal deformation in the Aegean and surrounding area. *Tectonophysics*, 253(1):129–153.

Papoulia, J., Tsambas, A., Anagnostou, C., Makris, J., Pomonis, A., Gulkan, P., Yalciner, A., Slejko, D., Mascle, J., Papadopoulos, G., others, and Nicolich, R. (2010). Seismic and Tsunami Risk Assessment and Mitigation Scenarios in the Western Hellenic Arc: The SEAHELLARC Project. *14 ECEE*, page 8.

Park, H., Cox, D. T., Alam, M. S., and Barbosa, A. R. (2017). Probabilistic Seismic and Tsunami Hazard Analysis Conditioned on a Megathrust Rupture of the Cascadia Subduction Zone. *Frontiers in Built Environment*, Volume 3 - 2017.

Park, J.-O., Tsuru, T., Takahashi, N., Hori, T., Kodaira, S., Nakanishi, A., Miura, S., and Kaneda, Y. (2002). A deep strong reflector in the Nankai accretionary wedge from multichannel seismic data: Implications for underplating and interseismic shear stress release. *Journal of Geophysical Research: Solid Earth*, 107(B4):ESE 3–1–ESE 3–16.

Park, R. G. (2013). *Geological structures and moving plates*. Springer Science & Business Media.

Peacock, S. M. (2001). Are the lower planes of double seismic zones caused by serpentine dehydration in subducting oceanic mantle? *Geology*, 29(4):299–302.

Pelties, C., de la Puente, J., Ampuero, J.-P., Brietzke, G. B., and Käser, M. (2012). Three-dimensional dynamic rupture simulation with a high-order discontinuous Galerkin method on unstructured tetrahedral meshes. *Journal of Geophysical Research: Solid Earth*, 117(B2):B02309.

Pelties, C., Gabriel, A.-A., and Ampuero, J.-P. (2014). Verification of an ADER-DG method for complex dynamic rupture problems. *Geoscientific Model Development*, 7(3):847–866.

Pichon, X. L. and Angelier, J. (1979). The hellenic arc and trench system: A key to the neotectonic evolution of the eastern mediterranean area. *Tectonophysics*, 60(1):1–42.

Pirazzoli, P. A., Ausseil-Badie, J., Giresse, P., Hadjidaki, E., and Arnold, M. (1992). Historical environmental changes at phalasarna harbor, West Crete. *Geoarchaeology*, 7:371–392.

Pirazzoli, P. A., Laborel, J., and Stiros, S. C. (1996). Earthquake clustering in the Eastern Mediterranean during historical times. *J. Geophys. Res.*, 101:6083–6097.

Pirazzoli, P. A., Thommeret, J., Thommeret, Y., Laborel, J., and Montag-Gioni, L. F. (1982). Crustal block movements from Holocene shorelines: Crete and Antikithera (Greece). *Tectonophysics*, 86:27–43.

Piromallo, C. and Morelli, A. (2003). P wave tomography of the mantle under the Alpine-Mediterranean area. *Journal of Geophysical Research: Solid Earth*, 108.

Polet, J. and Kanamori, H. (2000). Shallow subduction zone earthquakes and their tsunamigenic potential. *Geophysical Journal International*, 142(3):684–702.

Prada, M., Galvez, P., Ampuero, J.-P., Sallarès, V., Sánchez-Linares, C., Macías, J., and Peter, D. (2021). The influence of depth-varying elastic properties of the upper plate on megathrust earthquake rupture dynamics and tsunamigenesis. *Journal of Geophysical Research: Solid Earth*, 126(11):e2021JB022328.

Ramos, M. D. and Huang, Y. (2019). How the transition region along the Cascadia megathrust influences coseismic behavior: Insights from 2-D dynamic rupture simulations. *Geophysical Research Letters*, 46:1973–1983.

Ramos, M. D., Huang, Y., Ulrich, T., Li, D., Gabriel, A.-A., and Thomas, A. M. (2021). Assessing margin-wide rupture behaviors along the Cascadia megathrust with 3-D dynamic rupture simulations. *Journal of Geophysical Research: Solid Earth*, 126(7):e2021JB022005. e2021JB022005 2021JB022005.

Ramos, M. D., Thakur, P., Huang, Y., Harris, R. A., and Ryan, K. J. (2022). Working with dynamic earthquake rupture models: A practical guide. *Seismological Society of America*, 93(4):2096–2110.

Ranero, C. R., Grevemeyer, I., Sahling, H., Barckhausen, U., Hensen, C., Wallmann, K., Weinrebe, W., Vannucchi, P., von Huene, R., and McIntosh, K. (2008). Hydrogeological system of erosional convergent margins and its influence on tectonics and interplate seismogenesis. *Geochemistry, Geophysics, Geosystems*, 9(3).

Reid, H. F. (1929). The forces and movements at the earthquake-focus. *Eos, Transactions American Geophysical Union*, 10-11(1):43–46.

Reilinger, R., McClusky, S., Vernant, P., Lawrence, S., Ergintav, S., Cakmak, R., Ozener, H., Kadirov, F., Guliev, I., Stepanyan, R., Nadariya, M., Hahubia, G., Mahmoud, S., Sakr, K., ArRajehi, A., Paradissis, D., Al-Aydrus, A., Prilepin, M., Guseva, T., Evren, E., Dmitrotsa, A., Filikov, S. V., Gomez, F., Al-Ghazzi, R., and Karam, G. (2006). GPS constraints on continental deformation in the Africa-Arabia-Eurasia continental collision zone and implications for the dynamics of plate interactions. *Journal of Geophysical Research: Solid Earth*, 111.

Ren, C., Yue, H., Cao, B., Zhu, Y., Wang, T., An, C., Ge, Z., and Li, Z. (2022). Rupture process of the 2020 $M_W$=6.9 Samos, Greece earthquake on a segmented fault system constrained from seismic, geodetic, and tsunami observations. *Tectonophysics*, 839:229497.

Rettenberger, S., Meister, O., Bader, M., and Gabriel, A.-A. (2016). ASAGI: A Parallel Server for Adaptive Geoinformation. In *Proceedings of the Exascale Applications and Software Conference 2016*, EASC '16, pages 1–9, New York, NY, USA. Association for Computing Machinery.

Rice, J. R. (1980). The mechanics of earthquake rupture. In Dziewonski, A. and Boschi, E., editors, *Physics of the Earth's Interior, Proc. Int. Sch. Phys. Enrico Fermi, 78*, pages 555–649.

Rice, J. R. (2006). Heating and weakening of faults during earthquake slip. *Journal of Geophysical Research: Solid Earth*, 111(B5).

Rice, J. R. (2017). Heating, weakening and shear localization in earthquake rupture. *Philosophical Transactions of the Royal Society A: Mathematical, Physical and Engineering Sciences*, 375(2103):20160015.

Richardson, R. M., Solomon, S. C., and Sleep, N. H. (1979). Tectonic stress in the plates. *Reviews of Geophysics*, 17(5):981–1019.

Ripperger, J. (2007). *Numerical explorations on stress heterogeneity: dynamic earthquake rupture and near-fault ground motion*. PhD thesis, ETH Zurich.

Ripperger, J., Mai, P., and Ampuero, J.-P. (2008). Variability of near-field ground motion from dynamic earthquake rupture simulations. *Bulletin of the seismological society of America*, 98(3):1207–1228.

Rodriguez-Marek, A., Bommer, J. J., Youngs, R. R., Crespo, M. J., Stafford, P. J., and Bahrampouri, M. (2021). Capturing epistemic uncertainty in site response. *Earthquake Spectra*, 37(2):921–936.

Romano, F., Trasatti, E., Lorito, S., Piromallo, C., Piatanesi, A., Ito, Y., Zhao, D., Hirata, K., Lanucara, P., and Cocco, M. (2014). Structural control on the Tohoku earthquake rupture process investigated by 3D FEM, tsunami and geodetic data. *Scientific reports*, 4(1):1–11.

Roten, D., Olsen, K., Day, S., and Cui, Y. (2018). Quantification of fault-zone plasticity effects with spontaneous rupture simulations. *Best practices in physics-based fault rupture models for seismic hazard assessment of nuclear installations*, pages 45–67.

Roten, D., Olsen, K. B., and Day, S. M. (2017). Off-fault deformations and shallow slip deficit from dynamic rupture simulations with fault zone plasticity. *Geophysical Research Letters*, 44(15):7733–7742.

Roten, D., Olsen, K. B., Day, S. M., Cui, Y., and Fäh, D. (2014). Expected seismic shaking in Los Angeles reduced by San Andreas fault zone plasticity. *Geophysical Research Letters*, 41(8):2769–2777.

Rubin, A. M. and Ampuero, J. P. (2007). Aftershock asymmetry on a bimaterial interface. *Journal of Geophysical Research: Solid Earth*, 112:5307.

Ruff, L. and Kanamori, H. (1980). Seismicity and the subduction process. *Physics of the Earth and Planetary Interiors*, 23(3):240–252.

Ruff, L. and Kanamori, H. (1983). Seismic coupling and uncoupling at subduction zones. *Tectonophysics*, 99(2):99–117. Third Annual Symposium of the Geodynamics Research Program, Texas A & M University.

Ruff, L. J. (1989). Do trench sediments affect great earthquake occurrence in subduction zones? *Subduction Zones Part II*, 129:263–282.

Ruina, A. (1983). Slip instability and state variable friction laws. *Journal of Geophysical Research: Solid Earth*, 88(B12):10359–10370.

Ryan, K. J., Geist, E. L., Barall, M., and Oglesby, D. D. (2015). Dynamic models of an earthquake and tsunami offshore Ventura, California. *Geophysical Research Letters*, 42:6599–6606.

Sachpazi, M., Laigle, M., Charalampakis, M., Diaz, J., Kissling, E., Gesret, A., Becel, A., Flueh, E., Miles, P., and Hirn, A. (2016). Segmented Hellenic slab rollback driving Aegean deformation and seismicity. *Geophysical Research Letters*, 43(2):651–658.

Sage, F., Collot, J.-Y., and Ranero, C. (2006). Interplate patchiness and subduction-erosion mechanisms: Evidence from depth-migrated seismic images at the central Ecuador convergent margin. *Geology*, 34(12):997–1000.

Saito, T., Baba, T., Inazu, D., Takemura, S., and Fukuyama, E. (2019). Synthesizing sea surface height change including seismic waves and tsunami using a dynamic rupture scenario of anticipated Nankai trough earthquakes. *Tectonophysics*, 769:228166.

Saito, T. and Furumura, T. (2009). Three-dimensional tsunami generation simulation due to sea-bottom deformation and its interpretation based on the linear theory. *Geophysical Journal International*, 178(2):877–888.

Sakaguchi, A., Chester, F., Curewitz, D., Fabbri, O., Goldsby, D., Kimura, G., Li, C.-F., Masaki, Y., Screaton, E. J., Tsutsumi, A., Ujiie, K., and Yamaguchi, A. (2011). Seismic slip propagation to the updip end of plate boundary subduction interface faults: Vitrinite reflectance geothermometry on Integrated Ocean Drilling Program NanTro SEIZE cores. *Geology*, 39(4):395–398.

Sallarès, V. and Ranero, C. R. (2019). Upper-plate rigidity determines depth-varying rupture behaviour of megathrust earthquakes. *Nature*, 576:96–101.

Saltogianni, V., Mouslopoulou, V., Oncken, O., Nicol, A., Gianniou, M., and Mertikas, S. (2020). Elastic fault interactions and earthquake rupture along the southern Hellenic subduction plate interface zone in Greece. *Geophysical Research Letters*, 47:e2019GL086604.

Savran, W. H. and Olsen, K. B. (2020). Kinematic Rupture Generator Based on 3-D Spontaneous Rupture Simulations Along Geometrically Rough Faults. *Journal of Geophysical Research: Solid Earth*, 125(10):e2020JB019464.

Scala, A., Festa, G., and Vilotte, J. P. (2017). Rupture dynamics along bimaterial interfaces: a parametric study of the shear-normal traction coupling. *Geophysical Journal International*, 209:48–67.

Scala, A., Lorito, S., Escalante Sánchez, C., Romano, F., Festa, G., Abbate, A., Bayraktar, H. B., Castro, M. J., Macías, J., and Gonzalez-Vida, J. M. (2024). Assessing the optimal tsunami inundation modeling strategy for large earthquakes in subduction zones. *Journal of Geophysical Research: Oceans*, 129(9):e2024JC020941.

Scala, A., Lorito, S., Romano, F., Murphy, S., Selva, J., Basili, R., Babeyko, A., Herrero, A., Hoechner, A., Løvholt, F., et al. (2019). Effect of shallow slip amplification uncertainty on probabilistic tsunami hazard analysis in subduction zones: Use of long-term balanced stochastic slip models. *Pure and Applied Geophysics*, pages 1–24.

Scala, A., Lorito, S., Romano, F., Murphy, S., Selva, J., Basili, R., Babeyko, A., Herrero, A., Hoechner, A., Løvholt, F., Maesano, F. E., Perfetti, P., Tiberti, M. M., Tonini, R., Volpe, M., Davies, G., Festa, G., Power, W., Piatanesi, A., and Cirella, A. (2020). Effect of shallow slip amplification uncertainty on probabilistic tsunami hazard analysis in subduction zones: Use of long-term balanced stochastic slip models. *Pure and Applied Geophysics*, 177:1497–1520.

Scheffers, A. and Scheffers, S. (2007). Tsunami deposits on the coastline of west Crete (Greece). *Earth and Planetary Science Letters*, 259:613–624.

Schlüter, H. U., Gaedicke, C., Roeser, H. A., Schreckenberger, B., Meyer, H., Reichert, C., Djajadihardja, Y., and Prexl, A. (2002). Tectonic features of the southern Sumatra-western Java forearc of Indonesia. *Tectonics*, 21(5):11–1–11–15.

Schmedes, J., Archuleta, R. J., and Lavallée, D. (2010). Correlation of earthquake source parameters inferred from dynamic rupture simulations. *Journal of Geophysical Research: Solid Earth*, 115(B3).

Schmitt, S. V., Segall, P., and Dunham, E. M. (2015). Nucleation and dynamic rupture on weakly stressed faults sustained by thermal pressurization. *Journal of Geophysical Research: Solid Earth*, 120(11):7606–7640.

Scholl, D. W., Kirby, S. H., von Huene, R., Ryan, H., Wells, R. E., and Geist, E. L. (2015). Great (≥Mw8.0) megathrust earthquakes and the subduction of excess sediment and bathymetrically smooth seafloor. *Geosphere*, 11(2):236–265.

Selva, J., Lorito, S., Volpe, M., Romano, F., Tonini, R., Perfetti, P., Bernardi, F., Taroni, M., Scala, A., Babeyko, A., Løvholt, F., Gibbons, S. J., Macías, J., Castro, M. J., González-Vida, J. M., Sánchez-Linares, C., Bayraktar, H. B., Basili, R., Maesano, F. E., Tiberti, M. M., Mele, F., Piatanesi, A., and Amato, A. (2021). Probabilistic tsunami forecasting for early warning. *Nature Communications*, 12.

Selva, J., Tonini, R., Molinari, I., Tiberti, M. M., Romano, F., Grezio, A., Melini, D., Piatanesi, A., Basili, R., and Lorito, S. (2016). Quantification of source uncertainties in Seismic Probabilistic Tsunami Hazard Analysis (SPTHA). *Geophysical Journal International*, 205:1780–1803.

Sementsov, K. and Nosov, M. (2023). Calculation of the Initial Elevation of the Water Surface at the Source of a Tsunami in a Basin with Arbitrary Bottom Topography. *Mathematical Models and Computer Simulations*, 15(4):746–758.

Sementsov, K. A., Baba, T., Kolesov, S. V., Tanioka, Y., and Nosov, M. A. (2024). The effect of earthquake fault rupture kinematics on tsunami generation: a numerical study of real events. *Geophysical Journal International*, 240(2):920–941.

Sepúlveda, I., Haase, J. S., Carvajal, M., Xu, X., and Liu, P. L. (2020). Modeling the sources of the 2018 Palu, Indonesia, tsunami using videos from social media. *Journal of Geophysical Research: Solid Earth*, 125(3):e2019JB018675.

Sepulveda, I., Liu, P. L.-F., and Grigoriu, M. (2019). Probabilistic tsunami hazard assessment in South China Sea with consideration of uncertain earthquake characteristics. *Journal of Geophysical Research: Solid Earth*, 124(1):658–688.

Shaw, B. (2012). *The AD 365 Earthquake: Large Tsunamigenic Earthquakes in the Hellenic Trench*, pages 7–28. Springer Berlin Heidelberg, Berlin, Heidelberg.

Shaw, B., Ambraseys, N. N., England, P. C., Floyd, M. A., Gorman, G. J., Higham, T. F., Jackson, J. A., Nocquet, J. M., Pain, C. C., and Piggott, M. D. (2008). Eastern Mediterranean tectonics and tsunami hazard inferred from the AD 365 earthquake. *Nature Geoscience 2008 1:4*, 1:268–276.

Shaw, B. and Jackson, J. (2010). Earthquake mechanisms and active tectonics of the Hellenic subduction zone. *Geophysical Journal International*, 181:966–984.

Shearer, P. and Bürgmann, R. (2010). Lessons learned from the 2004 Sumatra-Andaman megathrust rupture. *Annual Review of Earth and Planetary Sciences*, 38(Volume 38, 2010):103–131.

Shedlock, K. M., Giardini, D., Grunthal, G., and Zhang, P. (2000). The GSHAP Global Seismic Hazard Map. *Seismological Research Letters*, 71(6):679–686.

Shi, F., Kirby, J. T., Harris, J. C., Geiman, J. D., and Grilli, S. T. (2012). A high-order adaptive time-stepping TVD solver for Boussinesq modeling of breaking waves and coastal inundation. *Ocean Modelling*, 43-44:36–51.

Shi, Z. and Day, S. M. (2013). Rupture dynamics and ground motion from 3-D rough-fault simulations. *Journal of Geophysical Research: Solid Earth*, 118(3):1122–1141.

Shibazaki, B. and Matsu'ura, M. (1992). Spontaneous processes for nucleation, dynamic propagation, and stop of earthquake rupture. *Geophysical Research Letters*, 19(12):1189–1192.

Sibuet, J.-C., Rangin, C., Le Pichon, X., Singh, S., Cattaneo, A., Graindorge, D., Klingelhoefer, F., Lin, J.-Y., Malod, J., Maury, T., Schneider, J.-L., Sultan, N., Umber, M., and Yamaguchi, H. (2007). 26th December 2004 great Sumatra–Andaman earthquake: Co-seismic and post-seismic motions in northern Sumatra. *Earth and Planetary Science Letters*, 263(1):88–103.

Sigmundsson, F. (2006). *Iceland geodynamics: crustal deformation and divergent plate tectonics*. Springer Science & Business Media.

Simmetrix Inc. (2017). SimModeler: Simulation Modeling Suite 11.0 Documentation, Tech. rep.

Simons, M., Minson, S. E., Sladen, A., Ortega, F., Jiang, J., Owen, S. E., Meng, L., Ampuero, J.-P., Wei, S., Chu, R., Helmberger, D. V., Kanamori, H., Hetland, E., Moore, A. W., and Webb, F. H. (2011). The 2011 Magnitude 9.0 Tohoku-Oki Earthquake: Mosaicking the Megathrust from Seconds to Centuries. *Science*, 332(6036):1421–1425.

Singh, S. C., Hananto, N., Mukti, M., Robinson, D. P., Das, S., Chauhan, A., Carton, H., Gratacos, B., Midnet, S., Djajadihardja, Y., et al. (2011). Aseismic zone and earthquake segmentation associated with a deep subducted seamount in Sumatra. *Nature Geoscience*, 4(5):308–311.

Small, D. T. and Melgar, D. (2021). Geodetic coupling models as constraints on stochastic earthquake ruptures: An example application to PTHA in Cascadia. *Journal of Geophysical Research: Solid Earth*, 126(7):e2020JB021149.

Smith, W. H. F. and Sandwell, D. T. (1997). Global sea floor topography from satellite altimetry and ship depth soundings. *Science*, 277(5334):1956–1962.

Socquet, A., Hollingsworth, J., Pathier, E., and Bouchon, M. (2019). Evidence of supershear during the 2018 magnitude 7.5 Palu earthquake from space geodesy. *Nature Geoscience*, 12(3):192–199.

Soloviev, S. L., Solovieva, O. N., Go, C. N., Kim, K. S., and Shchetnikov, N. A. (2000). *Tsunamis in the Mediterranean Sea 2000 B.C.-2000 A.D.*, volume 13. Springer Science & Business Media.

Song, S. G. and Somerville, P. (2010). Physics-based earthquake source characterization and modeling with geostatistics. *Bulletin of the Seismological Society of America*, 100:482–496.

Song, T.-R. A. and Simons, M. (2003). Large trench-parallel gravity variations predict seismogenic behavior in subduction zones. *Science*, 301(5633):630–633.

Souty, V. and Gailler, A. (2021). Fast high-resolution S-PTHA along the western Mediterranean Sea coastlines. Application to the bay of Cannes. *Frontiers in Earth Science*, 9:765610.

Sparkes, R., Tilmann, F., Hovius, N., and Hillier, J. (2010). Subducted seafloor relief stops rupture in South American great earthquakes: Implications for rupture behaviour in the 2010 Maule, Chile earthquake. *Earth and Planetary Science Letters*, 298(1):89–94.

Speranza, F., Minelli, L., Pignatelli, A., and Chiappini, M. (2012). The Ionian Sea: The oldest in situ ocean fragment of the world? *Journal of Geophysical Research: Solid Earth*, 117(B12).

Spratt, T. A. B. (1865). *Travels and Researches in Crete*, volume 2. J. van Voorst.

Stadler, G., Gurnis, M., Burstedde, C., Wilcox, L. C., Alisic, L., and Ghattas, O. (2010). The dynamics of plate tectonics and mantle flow: From local to global scales. *Science*, 329(5995):1033–1038.

Stein, S., Geller, R. J., and Liu, M. (2012). Why earthquake hazard maps often fail and what to do about it. *Tectonophysics*, 562-563:1–25.

Stern, R. J. (2002). Subduction zones. *Reviews of Geophysics*, 40(4):3–1–3–38.

Stiros, S. and Drakos, A. (2006). A fault-model for the tsunami-associated, magnitude $\geq$ 8.5 Eastern Mediterranean, AD365 earthquake. *Z. Geomorphol*, 146:125–137.

Stiros, S. C. (2010). The 8.5+ magnitude, AD365 earthquake in Crete: Coastal uplift, topography changes, archaeological and historical signature. *Quaternary International*, 216:54–63.

Stiros, S. C. (2020). The AD 365 Ammianus tsunami in Alexandria, Egypt, and the Crete ca. 365 fault and tsunami. *Arabian Journal of Geosciences*, 13:1–12.

Stoddard, P. R. (1992). On the relation between transform fault resistance and plate motion. *Journal of Geophysical Research: Solid Earth*, 97(B12):17637–17650.

Strasser, F. O., Arango, M., and Bommer, J. J. (2010). Scaling of the source dimensions of interface and intraslab subduction-zone earthquakes with moment magnitude. *Seismological Research Letters*, 81(6):941–950.

Synolakis, C. E., Bernard, E. N., Titov, V. V., Kânoğlu, U., and González, F. I. (2008). Validation and Verification of Tsunami Numerical Models. *Pure and Applied Geophysics*, 165(11-12):2197–2228.

Sørensen, M. B., Spada, M., Babeyko, A., Wiemer, S., and Grünthal, G. (2012). Probabilistic tsunami hazard in the Mediterranean Sea. *Journal of Geophysical Research: Solid Earth*, 117.

Tadapansawut, T., Okuwaki, R., Yagi, Y., and Yamashita, S. (2021). Rupture process of the 2020 Caribbean earthquake along the oriente transform fault, involving supershear rupture and geometric complexity of fault. *Geophysical Research Letters*, 48(1):e2020GL090899.

Tang, R., Zhu, S., and Gan, L. (2021). Dynamic rupture simulations of the 2008 7.9 Wenchuan Earthquake: Implication for heterogeneous initial stress and complex multi-fault geometry. *Journal of Geophysical Research: Solid Earth*, 126(12):e2021JB022457.

Tanioka, Y., Ruff, L., and Satake, K. (1997). What controls the lateral variation of large earthquake occurrence along the Japan Trench? *Island Arc*, 6(3):261–266.

Tanioka, Y. and Satake, K. (1996). Tsunami generation by horizontal displacement of ocean bottom. *Geophysical research letters*, 23(8):861–864.

Tarasov, B. G. (2014). Hitherto unknown shear rupture mechanism as a source of instability in intact hard rocks at highly confined compression. *Tectonophysics*, 621:69–84.

Tarbali, K., Bradley, B. A., and Baker, J. W. (2018). Consideration and propagation of ground motion selection epistemic uncertainties to seismic performance metrics. *Earthquake Spectra*, 34(2):587–610.

Taufiqurrahman, T., Gabriel, A.-A., Li, D., Ulrich, T., Li, B., Carena, S., Verdecchia, A., and Gallovič, F. (2023). Dynamics, interactions and delays of the 2019 Ridgecrest rupture sequence. *Nature*, 618:308–315.

Taufiqurrahman, T., Gabriel, A.-A., Ulrich, T., Valentová, L., and Gallovič, F. (2022). Broadband dynamic rupture modeling with fractal fault roughness, frictional heterogeneity, viscoelasticity and topography: The 2016 Mw 6.2 Amatrice, Italy earthquake. *Geophysical Research Letters*, 49(22):e2022GL098872.

Taymaz, T., Jackson, J., and Westaway, R. (1990). Earthquake mechanisms in the Hellenic Trench near Crete. *Geophysical Journal International*, 102(3):695–731.

Templeton, E. L. and Rice, J. R. (2008). Off-fault plasticity and earthquake rupture dynamics: 1. Dry materials or neglect of fluid pressure changes. *Journal of Geophysical Research: Solid Earth*, 113(B9).

ten Brink, U., Wei, Y., Fan, W., Granja-Bruña, J.-L., and Miller, N. (2020). Mysterious tsunami in the caribbean sea following the 2010 haiti earthquake possibly generated by dynamically triggered early aftershocks. *Earth and Planetary Science Letters*, 540:116269.

Thakur, P., Huang, Y., and Kaneko, Y. (2020). Effects of Low-Velocity Fault Damage Zones on Long-Term Earthquake Behaviors on Mature Strike-Slip Faults. *Journal of Geophysical Research: Solid Earth*, 125(8):e2020JB019587.

Tinti, E., Casarotti, E., Ulrich, T., Taufiqurrahman, T., Li, D., and Gabriel, A.-A. (2021). Constraining families of dynamic models using geological, geodetic and strong ground motion data: The Mw 6.5, October 30th, 2016, Norcia earthquake, Italy. *Earth and Planetary Science Letters*, 576:117237.

Tinti, S., Armigliato, A., Pagnoni, G., and Zaniboni, F. (2005). Scenarios of giant tsunamis of tectonic origin in the Mediterranean. *ISET Journal of Earthquake Technology, Paper No*, 464:171–188.

Titov, V., Kânoğlu, U., and Synolakis, C. (2016). Development of MOST for real-time tsunami forecasting. *Journal of Waterway, Port, Coastal, and Ocean Engineering*, 142(6):03116004.

Titov, V. V. and Gonzalez, F. I. (1997). Implementation and testing of the method of splitting tsunami (MOST) model. *NOAA Technical Memorandum ERL PMEL-112*.

Tonini, R., Armigliato, A., Pagnoni, G., Zaniboni, F., and Tinti, S. (2011). Tsunami hazard for the city of Catania, eastern Sicily, Italy, assessed by means of Worst-case Credible Tsunami Scenario Analysis (WCTSA). *Natural Hazards and Earth System Sciences*, 11:1217–1232.

Tregoning, P., Brunner, F. K., Bock, Y., Puntodewo, S. S. O., McCaffrey, R., Genrich, J. F., Calais, E., Rais, J., and Subarya, C. (1994). First geodetic measurement of convergence across the Java Trench. *Geophysical Research Letters*, 21(19):2135–2138.

Triantafyllou, I., Agalos, A., Samaras, A. G., Karambas, T. V., and Papadopoulos, G. A. (2024). Strong earthquakes and tsunami potential in the Hellenic subduction zone. *Journal of Geodynamics*, 159:102021.

Ulrich, T. and Aochi, H. (2015). Rapidness and robustness of finite-source inversion of the 2011 Mw 9.0 Tohoku earthquake by an elliptical-patches method using continuous GPS and acceleration data. *Pure and Applied Geophysics*, 172(12):3439–3453.

Ulrich, T., Gabriel, A. A., Ampuero, J. P., and Xu, W. (2019a). Dynamic viability of the 2016 Mw 7.8 Kaikōura earthquake cascade on weak crustal faults. *Nature Communications*, 10(1):1213.

Ulrich, T., Gabriel, A.-A., and Madden, E. H. (2021). GeoClaw input files of the 2004 Sumatra-Andaman tsunami scenarios published in Ulrich et al. (2021). *Zenodo*.

Ulrich, T., Gabriel, A.-A., and Madden, E. H. (2022). Stress, rigidity and sediment strength control megathrust earthquake and tsunami dynamics. *Nature Geoscience*, 15(1):67–73.

Ulrich, T., Vater, S., Madden, E. H., Behrens, J., van Dinther, Y., Van Zelst, I., Fielding, E. J., Liang, C., and Gabriel, A.-A. (2019b). Coupled, physics-based modeling reveals earthquake displacements are critical to the 2018 Palu, Sulawesi Tsunami. *Pure and Applied Geophysics*, 176(10):4069–4109.

Uphoff, C. and Bader, M. (2020). Yet another tensor toolbock for discontinous Galerkin methods and other applications. *ACM Trabsactions on Mathematical Software (TOMS)*, 46(4):1–40.

Uphoff, C., Krenz, L., Ulrich, T., Wolf, S., Knoll, A., David, S., Li, D., Dorozhinskii, R., Heinecke, A., Wollherr, S., Bohn, M., Schliwa, N., Brietzke, G., Taufiqurrahman, T., Anger, S., Rettenberger, S., Simonis, F., Gabriel, A., Pauw, V., Breuer, A., Kutschera, F., Hendrawan Palgunadi, K., Rannabauer, L., van de Wiel, L., Li, B., Chamberlain, C., Yun, J., Rekoske, J., G, Y., and Bader, M. (2022). SeisSol/SeisSol: v1.0.0-rc. Software.

Uphoff, C., Krenz, L., Ulrich, T., Wolf, S., Schneller, D., Kurapati, V., Knoll, A., Li, D., Dorozhinskii, R., Heinecke, A., Wollherr, S., Bohn, M., Schliwa, N., Brietzke, G., Taufiqurrahman, T., Anger, S., Rettenberger, S., Simonis, F., Gabriel, A., Pauw, V., Breuer, A., Kutschera, F., Hendrawan Palgunadi, K., Rannabauer, L., van de Wiel, L., Li, B., Chamberlain, C., Yun, J., Rekoske, J., G, Y., and Bader, M. (2024). SeisSol. version: 202103_Sumatra-1271-gc25ae5d3.

Uphoff, C., Rettenberger, S., Bader, M., Madden, E. H., Ulrich, T., Wollherr, S., and Gabriel, A. A. (2017). Extreme scale multi-physics simulations of the tsunamigenic 2004 Sumatra megathrust earthquake. In *Proceedings of the International Conference for High Performance Computing, Networking, Storage and Analysis, SC 2017*, pages 1–16. Association for Computing Machinery, Inc.

Vallianatos, F., Michas, G., and Papadakis, G. (2014). Non-extensive and natural time analysis of seismicity before the Mw6.4, October 12, 2013 earthquake in the South West segment of the Hellenic Arc. *Physica A: Statistical Mechanics and its Applications*, 414:163–173.

Van Dinther, Y., Gerya, T., Dalguer, L., Mai, P. M., Morra, G., and Giardini, D. (2013). The seismic cycle at subduction thrusts: Insights from seismo-thermo-mechanical models. *Journal of Geophysical Research: Solid Earth*, 118(12):6183–6202.

Van Dinther, Y., Mai, P. M., Dalguer, L., and Gerya, T. (2014). Modeling the seismic cycle in subduction zones: The role and spatiotemporal occurrence of off-megathrust earthquakes. *Geophysical Research Letters*, 41(4):1194–1201.

van Zelst, I., Rannabauer, L., Gabriel, A.-A., and van Dinther, Y. (2022). Earthquake rupture on multiple splay faults and its effect on tsunamis. *Journal of Geophysical Research: Solid Earth*, 127(8):e2022JB024300.

van Zelst, I., Thieulot, C., and Craig, T. J. (2023). The effect of temperature-dependent material properties on simple thermal models of subduction zones. *Solid Earth*, 14(7):683–707.

van Zelst, I., Wollherr, S., Gabriel, A.-A., Madden, E. H., and van Dinther, Y. (2019). Modeling megathrust earthquakes across scales: One-way coupling from geodynamics and seismic cycles to dynamic rupture. *Journal of Geophysical Research: Solid Earth*, 124:11414–11446.

Vannucci, G., Pondrelli, S., Argnani, A., Morelli, A., Gasperini, P., and E., B. (2004). An atlas of Mediterranean seismicity. *Annals of Geophysics*, Suppl. to vol. 47:247 – 306–306.

Vater, S. and Behrens, J. (2014). Well-balanced inundation modeling for shallow-water flows with Discontinuous Galerkin schemes. In Fuhrmann, J., Ohlberger, M., and Rohde, C., editors, *Finite Volumes for Complex Applications VII – Elliptic, Parabolic and Hyperbolic Problems*, volume 78 of *Springer Proceedings in Mathematics & Statistics*, pages 965–973.

Vater, S., Beisiegel, N., and Behrens, J. (2015). A limiter-based well-balanced discontinuous Galerkin method for shallow-water flows with wetting and drying: One-dimensional case. *Advances in Water Resources*, 85:1–13.

Vater, S., Beisiegel, N., and Behrens, J. (2019). A limiter-based well-balanced discontinuous Galerkin method for shallow-water flows with wetting and drying: Triangular grids. *International Journal for Numerical Methods in Fluids*, 91(8):395–418.

Venkataraman, A. and Kanamori, H. (2004). Observational constraints on the fracture energy of subduction zone earthquakes. *Journal of Geophysical Research: Solid Earth*, 109(B5):B05302.

Vernant, P., Reilinger, R., and McClusky, S. (2014). Geodetic evidence for low coupling on the Hellenic subduction plate interface. *Earth and Planetary Science Letters*, 385:122–129.

Vigny, C., Socquet, A., Peyrat, S., Ruegg, J.-C., Métois, M., Madariaga, R., Morvan, S., Lancieri, M., Lacassin, R., Campos, J., Carrizo, D., Bejar-Pizarro, M., Barrientos, S., Armijo, R., Aranda, C., Valderas-Bermejo, M.-C., Ortega, I., Bondoux, F., Baize, S., Lyon-Caen, H., Pavez, A., Vilotte, J. P., Bevis, M., Brooks, B., Smalley, R., Parra, H.,

Baez, J.-C., Blanco, M., Cimbaro, S., and Kendrick, E. (2011). The 2010 $M_w$ 8.8 Maule Megathrust Earthquake of Central Chile, Monitored by GPS. *Science*, 332(6036):1417–1421.

Volpe, M., Lorito, S., Selva, J., Tonini, R., Romano, F., and Brizuela, B. (2019). From regional to local SPTHA: Efficient computation of probabilistic tsunami inundation maps addressing near-field sources. *Natural Hazards and Earth System Sciences*, 19:455–469.

von Huene, R., Miller, J. J., and Weinrebe, W. (2012). Subducting plate geology in three great earthquake ruptures of the western Alaska margin, Kodiak to Unimak. *Geosphere*, 8(3):628–644.

Von Huene, R., Ranero, C. R., Scholl, D. W., Lallemand, S., and Funiciello, F. (2009). Convergent margin structure in high-quality geophysical images and current kinematic and dynamic models. In *Subduction zone geodynamics*, volume 137, pages 137–157. Springer Berlin, Heidelberg.

Vyas, J. C., Gabriel, A., Ulrich, T., Mai, P. M., and Ampuero, J. (2023). How does thermal pressurization of pore fluids affect 3D strike-slip earthquake dynamics and ground motions? *Bulletin of the Seismological Society of America*, 113(5):1992–2008.

Wallace, G., Moore, J., and DiLeonardo, C. (2003). Controls on localization and densification of a modern décollement: Northern Barbados accretionary prism. *GSA Bulletin*, 115(3):288–297.

Wang, D., Liu, X., Liu, T., Shen, K., Welch, D. O., and Li, B. (2017). Constraints from the dehydration of antigorite on high-conductivity anomalies in subduction zones. *Scientific Reports*, 7(1):16893.

Wang, K. and Bilek, S. L. (2014). Invited review paper: Fault creep caused by subduction of rough seafloor relief. *Tectonophysics*, 610:1–24.

Wang, Y., Heidarzadeh, M., Satake, K., Mulia, I. E., and Yamada, M. (2020). A Tsunami Warning System Based on Offshore Bottom Pressure Gauges and Data Assimilation for Crete Island in the Eastern Mediterranean Basin. *Journal of Geophysical Research: Solid Earth*, 125(10):e2020JB020293. _eprint: https://onlinelibrary.wiley.com/doi/pdf/10.1029/2020JB020293.

Wang, Z. and Zhang, Z. (2025). Unexpected rupture triggering behavior of subshear and free-surface-induced supershear ruptures on stepover. *Earth and Planetary Science Letters*, 664:119457.

Wei, X., Liu, Y., Xu, J., Liu, W., and Chen, X. (2024). A detailed understanding of slow self-arresting rupture. *Journal of Geophysical Research: Solid Earth*, 129(8):e2024JB028881. e2024JB028881 2024JB028881.

Wells, R. E., Blakely, R. J., Sugiyama, Y., Scholl, D. W., and Dinterman, P. A. (2003). Basin-centered asperities in great subduction zone earthquakes: A link between slip, subsidence, and subduction erosion? *Journal of Geophysical Research: Solid Earth*, 108(B10).

Wendt, J., Oglesby, D. D., and Geist, E. L. (2009). Tsunamis and splay fault dynamics. *Geophysical Research Letters*, 36(15):L15303.

Weng, H. and Ampuero, J.-P. (2019). The dynamics of elongated earthquake ruptures. *Journal of Geophysical Research: Solid Earth*, 124(8):8584–8610.

Wesnousky, S. G. (2006). Predicting the endpoints of earthquake ruptures. *Nature*, 444(7117):358–360.

White, R. S. (1988). The Earth's crust and lithosphere. *Journal of Petrology*, Special_Volume(1):1–10.

Whittaker, A., Bott, M. H. P., and Waghorn, G. D. (1992). Stresses and plate boundary forces associated with subduction plate margins. *Journal of Geophysical Research: Solid Earth*, 97(B8):11933–11944.

Wilcox, L. C., Stadler, G., Burstedde, C., and Ghattas, O. (2010). A high-order discontinuous Galerkin method for wave propagation through coupled elastic–acoustic media. *Journal of Computational Physics*, 229(24):9373–9396.

Williamson, A., Melgar, D., and Rim, D. (2019). The effect of earthquake kinematics on tsunami propagation. *Journal of Geophysical Research: Solid Earth*, 124(11):11639–11650.

Wilson, A. and Ma, S. (2021). Wedge plasticity and fully coupled simulations of dynamic rupture and tsunami in the Cascadia subduction zone. *Journal of Geophysical Research: Solid Earth*, 126:e2020JB021627.

Wirp, S. A., Gabriel, A. A., Schmeller, M., Madden, E. H., van Zelst, I., Krenz, L., van Dinther, Y., and Rannabauer, L. (2021). 3D Linked Subduction, Dynamic Rupture, Tsunami, and Inundation Modeling: Dynamic Effects of Supershear and Tsunami Earthquakes, Hypocenter Location, and Shallow Fault Slip. *Frontiers in Earth Science*, 9:177.

Wirp, S. A., Gabriel, A.-A., Ulrich, T., and Lorito, S. (2024). Dynamic rupture modeling of large earthquake scenarios at the Hellenic Arc toward physics-based seismic and tsunami hazard assessment. *Journal of Geophysical Research: Solid Earth*, 129(11):e2024JB029320.

Wirp, S. A., Kutschera, F., Gabriel, A.-A., Ulrich, T., Bader, M., and Lorito, S. (2025). Hellenic Arc tsunami generation from $M_W 8+$ 3D margin-wide dynamic rupture earthquake scenarios. *EarthArXiv: Preprint*.

Wirth, E. A., Sahakian, V. J., Wallace, L. M., and Melnick, D. (2022). The occurrence and hazards of great subduction zone earthquakes. *Nature Reviews Earth & Environment*, 3(2):125–140.

Withers, K. B., Olsen, K. B., Shi, Z., and Day, S. M. (2018). Validation of deterministic broadband ground motion and variability from dynamic rupture simulations of buried thrust earthquakes. *Bulletin of the Seismological Society of America*, 109(1):212–228.

Wolf, S., Gabriel, A.-A., and Bader, M. (2020). Optimization and local time stepping of an ADER-DG scheme for fully anisotropic wave propagation in complex geometries. In Krzhizhanovskaya, V. V., Závodszky, G., Lees, M. H., Dongarra, J. J., Sloot, P. M. A., Brissos, S., and Teixeira, J., editors, *Computational Science – ICCS 2020*, pages 32–45. Springer International Publishing.

Wollherr, S. (2018). *Inelastic material response in multi-physics earthquake rupture simulations*. PhD thesis, Ludwig-Maximilians-Universität-München. Geomechanically constrained dynamic rupture models of subduction zone earthquakes with plasticity.

Wollherr, S., Gabriel, A.-A., and Uphoff, C. (2018). Off-fault plasticity in three-dimensional dynamic rupture simulations using a modal Discontinuous Galerkin method on unstructured meshes: implementation, verification and application. *Geophysical Journal International*, 214(3):1556–1584.

Wong, J. W. C., Fan, W., and Gabriel, A.-A. (2023). A quantitative comparison and validation of finite-fault models: The 2011 Tohoku-Oki earthquake. *Authorea Preprints*.

Woo, G. (2018). Counterfactual disaster risk analysis. *Variance. J, Advancing the Science of Risk*, 10:279–291.

Xie, Z., Hu, C., Cai, Y., and Wang, C.-y. (2009). Effect of Poisson's ratio on stress state in the Wenchuan M$S$ 8.0 earthquake fault. *Earthquake Science*, 22(6):603–607.

Xu, S., Ben-Zion, Y., Ampuero, J.-P., and Lyakhovsky, V. (2015). Dynamic ruptures on a frictional interface with off-fault brittle damage: feedback mechanisms and effects on slip and near-fault motion. *Pure and Applied Geophysics*, 172:1243–1267.

Yamamoto, T. (1982). Gravity waves and acoustic waves generated by submarine earthquakes. *International Journal of Soil Dynamics and Earthquake Engineering*, 1(2):75–82.

Yang, H., Yao, S., He, B., Newman, A. V., and Weng, H. (2019). Deriving Rupture Scenarios From Interseismic Locking Distributions Along the Subduction Megathrust. *Journal of Geophysical Research: Solid Earth*, 124(10):10376–10392.

Ye, L., Lay, T., Kanamori, H., and Rivera, L. (2016). Rupture characteristics of major and great (Mw$\geq$ 7.0) megathrust earthquakes from 1990 to 2015: 1. Source parameter scaling relationships. *Journal of Geophysical Research: Solid Earth*, 121(2):826–844.

Yeh, H., Liu, P., Synolakis, C., and editors (1996). Benchmark problem 4. The 1993 Okushiri Data, Conditions and Phenomena. *World Scientific Publishing Co. Pte. Ltd.*

Yolsal, S., Taymaz, T., and Yalçiner, A. C. (2007). Understanding tsunamis, potential source regions and tsunami-prone mechanisms in the Eastern Mediterranean. *Geological Society Special Publication*, 291:201–230.

Yolsal-Çevikbilen, S. and Taymaz, T. (2012). Earthquake source parameters along the Hellenic subduction zone and numerical simulations of historical tsunamis in the Eastern Mediterranean. *Tectonophysics*, 536-537:61–100.

Yomogida, K. (1988). Crack-like rupture processes observed in near-fault strong motion data. *Geophysical Research Letters*, 15(11):1223–1226.

Zhao, D., Huang, Z., Umino, N., Hasegawa, A., and Kanamori, H. (2011). Structural heterogeneity in the megathrust zone and mechanism of the 2011 Tohoku-oki earthquake (Mw 9.0). *Geophysical Research Letters*, 38(17).

Zheng, Y., Zhao, Z., and Chen, Y. (2013). Continental subduction channel processes: Plate interface interaction during continental collision. *Chinese Science Bulletin*, 58:4371–4377.

Zheng, Y.-F. and Chen, Y.-X. (2016). Continental versus oceanic subduction zones. *National Science Review*, 3(4):495–519.

Zielke, O., Galis, M., and Mai, P. M. (2017). Fault roughness and strength heterogeneity control earthquake size and stress drop. *Geophysical Research Letters*, 44(2):777–783.

# Acknowledgments

I offer my sincere thanks to Alice and Heiner, who provided mentorship throughout my Ph.D. I am genuinely grateful for the numerous opportunities Alice provided me, including conferences in Iceland, Durham, and Smolenice, as well as ChEESE meetings in Rome and Bologna.

I would especially like to thank Christine Thomas and the WWU team who aroused my interest in Geophysics, particularly in Seismology.

My special thanks to Thomas, who was my personal "SeisSol expert" on many occasions.

I thank Lukas for his efforts in helping me out with technical issues.

Thank you, Betsy, Ylona, and Iris, for introducing me to the process of coupling geophysical models across different scales.

Thank you, Fabi, for the great time I had mentoring you during your Bachelor's and Master's programs, and for the scientific exchange that continues to this day.

I thank Michael and the TUM group for their outstanding work on SeisSol.

I would like to thank the ChEESE team, especially Stefano, for the scientific discussions that broadened my geophysical understanding.

Thank you, Sabrina, for being the best office mate during my time in Munich.

Thank you, Bille and Harald, for all the hours of baby care that allowed me to complete my Ph.D.

Thank you, Sandra, for your constant backing.

I want to thank all my friends in Munich for the companionship and wonderful memories we've shared.

My deepest gratitude goes to my family, especially the 3 A's, for their unwavering support. This dissertation would not have been possible without your constant encouragement.